The University Of Sheffield.

Investigating and Improving Fracture Resistance of Elastomer O-rings and Spring Seals Exposed to Rapid Gas Decompression

by

Teddy Mbwadzawo

Supervisors: Prof Alma Hodzic and Dr Christopher Pinna

Thesis submitted as a requirement for the degree of

Doctor of Philosophy

Department of Mechanical Engineering,

The University of Sheffield

October, 2015

Abstract

Fracture resistance of elastomeric O-rings and spring seals exposed to rapid gas decompression (RGD) conditions was investigated using both experimental and numerical methods.

Experimental methods included using scanning electron microscopy (SEM) analysis to analyse fractured surfaces of O-rings and spring seals after exposure to RGD. Microcracks were found to initiate from microvoids or inherent flaws present in the centre region of all the O-rings and spring seals tested. These microcracks would propagate slowly towards the inner and outer circumference of the seals and when the crack size reached a critical size, the crack rapidly accelerated resulting in a catastrophic brittle fracture. Results from the SEM analysis prompted for computerised tomography (micro-CT) to be conducted on elastomeric O-rings. The aim was to analyse the void distribution inside the O-rings before exposure to RGD conditions. Results from micro-CT analyses revealed that the O-rings contained a high void density in the centre region.

Numerical methods included using a sequentially coupled structural mass diffusion Finite Element Analysis (FEA) model to evaluate the stress distribution inside an O-ring during RGD. The coupling between mass diffusion and structural deformation of the O-ring was achieved by employing the Peng-Robinson equation of state and two user subroutines to transfer data between the two models. The FEA model revealed that elements in the centre region of the O-ring's cross-section experience the highest tensile strains during RGD.

Hybrid O-rings were proposed to improve fracture resistance of elastomer O-rings exposed to RGD conditions. The hybrid O-rings were created by inserting a second phase material in the form of a "high fracture toughness" layer to create hybrid O-rings. The aim of the reinforcing second phase layer was to improve the O-rings fracture resistance by delaying crack initiation and propagation. Before the hybrid O-rings were constructed, tearing strength and fatigue tests were conducted on hybrid specimens. The aim of these tests was to investigate how the addition of a second phase material affected the static and dynamic behaviour of the hybrid structures. The results showed that it is possible to improve both static and dynamic fracture resistance of elastomeric components using hybrid structures.

Contents

List of Figures

List of Tables

Nomenclature

σ	stress, MPa
ε	strain
μ	shear modulus of material, MPa
λ_i	principal strain ratios
I_i	strain invariants
W	strain energy, N.mm
T	tearing energy, $N.mm^{-1}$
T_c	critical tearing energy, $N.mm^{-1}$
J	J-integral, $N.mm^{-1}$
J_c	critical j-integral, $N.mm^{-1}$
w	strain energy density, $N.mm^{-2}$
A	surface area, mm^2
l	length, mm
K	bulk modulus of material, MPa
D	diffusion coefficient, $mm^2.s^{-1}$
c	mass concentration of gas, $mol.mm^{-3}$
S	solubility coefficient, $mol.mm^{-3}.Pa^{-1}$
k_p	pressure stress factor used to define stress assisted diffusion
Q	gas permeability, $mol.mm^{-1}.s^{-1}.Pa^{-1}$)
GTR	gas transmission rate, $mol.m^{-2}.s^{-1}.Pa^{-1}$
T	temperature, K

S_{ii}	nominal stress in x-direction, y-direction or nominal shear stress, MPa
NE_{ii}	nominal strain in x-direction, y-direction or nominal shear strain
CPRESS	contact pressure between two surfaces, MPa
ESEDEN	Total elastic strain energy density in an element, $N.mm^{-2}$

Acknowledgements

I would like to thank my supervisor Prof Alma Hodzic for her guidance and support that has helped me to get to this point. I would also like to thank the technicians from the University of Sheffield workshop, especially big Dave, Mike Jackson and Dr Austin Lafferty for their help and input in my experiments. I would also like to express my gratitude to the technicians at the Mellanby centre, University of Sheffield for their technical help and support in conducting Computational Tomography analysis. I would like to thank all the other Sheffield University staff who were always friendly and helped me through my time at university. I would also like to thank all the people in the CICS group for being so friendly and easy to get along with.

I would like to thank the staff at James Walker, for their support and guidance throughout this research project. I would especially like to thank Peter Warren and Andrew Douglas for all the advice and support they have shown me throughout the research project. Also a big thank you to all the staff at James Walker for their advice and help in conducting experiments. I would also like to thank Duncan Wheatley and Akash Gupta for their huge contribution in conducting experiments. I would also like thank Duncan Smith for the help and support in FE analysis of elastomer materials.

I would like to thank my family and friends for the love and support they have shown me throughout my PhD course. I couldn't have done it without them. I would like to dedicate this thesis to my mother for believing in me throughout my time at university and also the encouragement she gave me when times were rough. I would like her to know, I could never have been here it if wasn't for her love, support and the sacrifices she made. I would also like to thank my dad and brother for their encouragement throughout. I would also like to take this opportunity to thank my little sister Olivia for the shoes she bought me when l couldn't afford them on my PhD income. To my girlfriend, l would like to say thanks for the love and support you've shown me since we met, and helping me when l was going through rough times.

Above all l would like to thank the Lord for bringing me this far.

List of Publications

Journal Paper

Mbwadzawo, T. and Hodzic, A. (2015) Coupled Mass Diffusion and Structural Deformation of Elastomer Seals Exposed to Rapid Gas Decompression. Plastics, Rubber and Composites: Macromolecular Engineering. Manuscript Number: PRCME3405, Estimated issue publication date 14-Oct-2015.

Conference Paper

Mbwadzawo, T. and Hodzic, A. (2014) Scanning Electron Microscopy Analysis of Elastomeric O-rings and Seals Fractured During Rapid Gas Decompression. ECCM16-16th European Conference on Composite Materials, Seville, Spain, 22-26 June 2014.

1. Introduction

Rapid Gas Decompression (RGD) also known as explosive decompression (ED) is an operational condition during which applied system pressure is released suddenly, resulting in the expansion of absorbed gas damaging elastomer seals (Ho, 2006). It is a common problem in oil and gas industries and other high pressure gas applications. RGD damage has also been observed in other fluid handling devices, including valves and blow-out preventers. Elastomer seals performance in RGD conditions is a major concern for designers. Failure of elastomer seals in service can lead to defects or even bring oilfield machinery or plant to a standstill, which can have serious implications on financial cost, safety and the environment (Schwartz, 2001).

In typical in-service application, elastomeric seals are exposed to fluids at high pressure. Fluids in contact with the seal surface diffuse into the elastomer until the material is fully saturated. In applications where pressure fluctuations are minimal, this may not be perceived as detrimental, and the slight swelling that results from gas absorption may increase the effectiveness of the seal (Cox, 1985). However, in applications where large pressure fluctuations are experienced typically in oil and gas industries, fluid is absorbed into the elastomer seals through permeation. When the external pressure suddenly drops, in an attempt to balance internal and external pressure, the absorbed fluid expands against the elasticity of the rubber causing high internal tensile stresses and strains leading to seal failure in operation.

In working conditions such as the oilfield industry, elastomer seals are also exposed to a broad range of temperatures and a wide variety of chemicals such as CO_2, CH_4 and H_2S (Schwartz, 2001). Long-time exposure to these chemicals at high temperatures can significantly affect an elastomer seal's mechanical strength, thereby resulting in loss of performance. Due to advancement in elastomer compounding techniques, elastomer materials can now be compounded to work in these harsh environments. However, failure of these compounds due to RGD is still a major concern. Also, even though the failure mechanism due to RGD has been greatly researched (Edmond, 2001), there is still yet a numerical model to be developed to accurately evaluate the stress and strain distribution inside elastomer seals during the decompression cycle.

1.1. Aim and Objectives

The aim of this thesis was to investigate and improve fracture resistance of elastomeric O-rings and spring seals exposed to RGD conditions. The investigation of fracture was conducted using both numerical and experimental methods.

i. Experimental analysis included using scanning electron microscopy (SEM) methods to analyse fractured surfaces of O-rings and spring seals after exposure to RGD.
ii. Computerised tomography (micro-CT) was conducted on virgin O-rings before exposure to RGD conditions. This was done to investigate if any inherent flaws present in the O-rings could be responsible for fracture initiation during RGD conditions.
iii. The experimental methods were complimented with a numerical model, which was solved using Abaqus (2011) FEA package. The aim of the numerical model was to investigate fracture of sealing components exposed to RGD in the presence of CO_2. The FEA model had the capability of evaluating the structural deformation of an O-ring due to internal pressure exerted by the rapidly expanding absorbed gas. To achieve this, the FEA model employed the Peng-Robinson equation of state (Peng and Robinson, 1976) and two user subroutines.
iv. Damage resistance was improved through the introduction of a second phase material in the form of a "high fracture toughness" layer to create hybrid O-rings. The aim of the reinforcing second phase layer was to improve the O-ring's fracture resistance by delaying crack initiation and propagation. The concept of including elements to improve fracture resistance was included in a patent application by industrial sponsor James Walker & Co. Ltd.
v. A numerical model was used to investigate how the addition of a second phase material affected the hybrid O-ring's stress and strain distribution and consequently the ability to maintain acceptable sealing properties. Experimental methods such as tear strength tests and fatigue tests were conducted to analyse how the addition of a second phase material influence the hybrid structure's crack initiation and propagation behaviour.

Figure 1.1 and Figure 1.2 are cross-sectional views of an O-ring and a spring seal respectively compressed by their housing gland surfaces. Working fluid enters the system from one side of the housing as shown in Figure 1.1 and Figure 1.2 and diffuses into the elastomer seal.

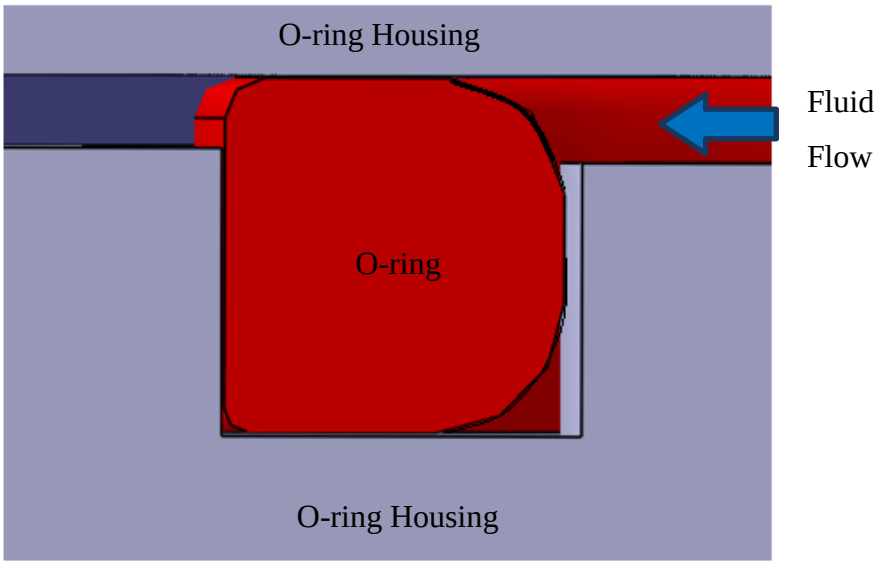

Figure 1.1 Display of a cross-sectional view of an O-ring compressed by the O-ring housing gland surfaces.

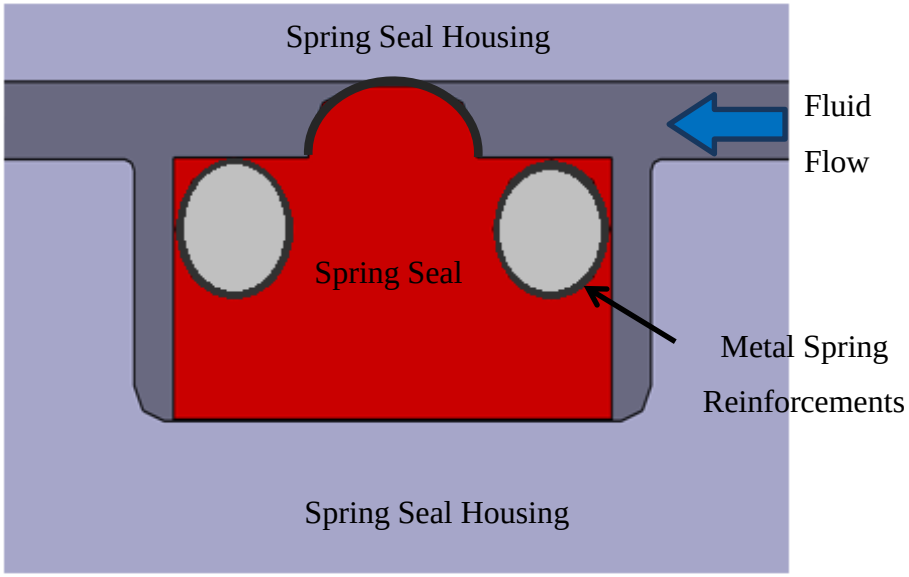

Figure 1.2 Display of a cross-sectional view of a spring seal compressed by the spring seal housing gland surfaces.

2. Literature Review

2.1. Elastomers

Elastomers are used extensively in many industrial applications mainly because of their wide availability and low cost (MSC Software, 2010). Elastomers are identified by their ability to experience large deformations and return to approximately their original configuration upon the release of the deforming forces. Elastomers are defined by Bever (1992) as:

- Containing long chain molecules that are able to rotate freely about the bonds joining neighbouring units.
- The large molecules are joined at a number of sites that form a three dimensional network, either by chemical bonds or by mechanical entanglements to form crosslinks.
- Apart from the crosslinks the molecules move readily past another, meaning that the intermolecular interactions are small.

The crosslinking of the long chain molecules is achieved through a process called vulcanization (Kumar and Nijasure, 1997). During vulcanization, the long chain molecules of the elastomer are chemically linked at intervals along their lengths with adjacent elastomer chains. This process is usually done using sulphur as the crosslinking agent (Lindley, 1984). However, more chemicals have been developed to control the vulcanization process. The properties of the crosslinks are dependent upon the curing conditions, time and temperature as well as the amount and type of vulcanizing ingredients used. The performance of an elastomer can be modified through the addition of fillers. The common use of fillers is for reducing cost or for improving the mechanical and dynamic properties of the elastomer (Rothon, 2001). Carbon black particles and silica are the mostly widely used fillers. Carbon black improves the strength and toughness of elastomers as well as improving resistance to abrasion, tearing and flex fatigue properties of elastomeric materials. (Zhang et al, 2001).

Some of the most common commercially available RGD resistant elastomers are acrylonitrile-butadiene rubber (NBR), hydrogenated acrylonitrile-butadiene rubber (HNBR) and fluorocarbon elastomers (Ho, 2006). NBR elastomers have a working

temperature of up to 100 ^{o}C and have a limited resistance to sour gas (Nagdi, 1993). HNBR's have a working temperature range of -40 ^{o}C to 165 ^{o}C with minimal degradation over long periods of time. HNBR is made through the hydrogenation of NBR compounds which improves the heat and oil resistance (Thavamani and Bhowmick, 1992). During the hydrogenation of NBR compounds to form HNBR elastomers, the double bonds on the polymer chains are converted to single bonds. This gives HNBR elastomers a higher Mooney viscosity (Mezger et al, 2005). Fluorocarbon elastomers have a working temperature range of up to 200 ^{o}C and are considered sour gas resistant, if they are properly formulated (Schwartz, 2001). Fluorocarbons are however, expensive and have processing difficulties. Hence, HNBR compounds were developed to bridge the price and performance gap between general purpose oil resistance elastomers and fluorocarbon elastomers. The development of HNBR was a great triumph in improving almost all major drawbacks on NBR elastomers (Susmita et al, 1993).

2.1.1. Elastic Properties

When an elastomeric material is stretched into a larger strain region for the first time, the response is stiff, however, upon recycling in the same strain region the elastomeric material softens. This behaviour is referred to as stress softening or Mullins effect (Mullins, 1969), named after the rubber scientist Leonard Mullins. In most applications the first few cycles are discarded where it is assumed that repetitive behaviour will dominate. In applications where the first cycle dominates, then only the first cycle's data is recorded and the stress softening effects are ignored.

Elastomer compounds have a nonlinear stress strain relationship and are usually treated as incompressible or nearly incompressible hyperelastic materials. A difference between linear and non-linear carbon filled elastomers is that after loading and subsequent unloading, they do not return to their initial state but exhibit a residual deformation. The permanent deformation combined with the Mullins effects results in complex mechanical behaviour (Guo and Sluys, 2008). Also unlike linear elastic compounds, the stress strain relationship of hyperelastic materials cannot be derived from a constant factor, such as elastic modulus. The stress strain relationship for hyperelastic materials is derived from an energy density function (Li et al, 2009).

2.1.2. Strain Energy Density Functions

There are two different phenomenological methods used to study the elasticity of elastomeric materials. The first method treats the problem from the viewpoint of continuum mechanics. The second method is a statistical approach that derives the elastic properties from some idealized model of the structure of the elastomeric material (Guo and Sluys, 2008). The statistical approach assumes a structure of randomly oriented long molecular chains. A thorough review of the statistical approach is given by Treloar (1975). The continuum mechanics approach begins with the fundamental basis that the strain energy density function must depend on stretch through one or more of the three invariants, $I_{i,}$ of the stretch tensor (Boyce and Arruda, 2000). The invariants are measures of strain and are independent of the coordinate system used to measure the strains and are usually defined as:

$$I_1 = \lambda_1^2 + \lambda_2^2 + \lambda_3^2 \quad [2.1]$$

$$I_2 = \lambda_1^2\lambda_2^2 + \lambda_2^2\lambda_3^2 + \lambda_3^2\lambda_1^2 \quad [2.2]$$

$$I_3 = \lambda_1^2\lambda_2^2\lambda_3^2 \quad [2.3]$$

where $\lambda_1^2,\ \lambda_1^2$ and λ_1^2 are principal stretch ratios and if a material is fully incompressible, I_3 is equal to 1.

These two approaches use a constitutive model to define the deformation of elastomeric materials (Hamzah and Razao, 2013). A constitutive model is a mathematical relation between stress and the corresponding strain. There are several constitutive models used to define the hyperelastic behaviour of elastomer compounds. Rivlin and Saunders (1951) showed that within the accuracy of the experiments, the stress-strain characteristics behaviour for a number of simple types of deformation of rubber can be interpreted in terms of a single form for the stored energy function W, which is defined as a function of two strain invariants I_1 and I_2. Mooney (1940) presented a theory of large elastic deformation under the assumptions the material is isotropic, incompressible and free from hysteresis. Rivlin made modifications to the model proposed by Mooney and the model is generally known as the Mooney-Rivlin model (Ju et al, 2014). The Mooney-Rivlin model can be further expressed using higher order terms of the first invariant I_1 and the second invariant I_2, the Yeoh model (Yeoh, 1993) is an example. The Yeoh model is based on a representation of the strain energy density in a 3-term

expansion of the first invariant I_1. The model has been shown to work well in capturing different deformation states at moderate to large deformations (Boyce and Arruda, 2000).

The strain energy functions mentioned so far are expressed as a function of strain invariants. Odgen (1972) proposed a strain energy function which was based on the principle stretches. The model provided adequate representation of the mechanical response of elastomeric materials and was simple enough to be amenable to mathematical analysis. The Ogden model has been shown to be capable of capturing the state of deformation dependency in elastomeric materials. However, in order to capture this behaviour, the Ogden model requires six parameters (Dorfmann and Muhr, 1999). The Ogden model has been shown to have better flexibility in describing the curvature on the stress-strain curves of elastomeric materials when compared to the Mooney-Rivlin model (Kim et al, 2011). Most of the early strain energy functions assumed incompressibility. Blatz and Ko (1962) presented a new strain energy function to model the deformation of elastomer compounds without assuming incompressibility. They generated a strain energy function from experimental data, obtained in three different stress fields. The new strain energy function was expressed in terms of ν, which has the same significance as the Poisson's ratio in infinitesimal theory. Infinitesimal theory describes the deformation of a solid body in which the displacements of the material particles are assumed to be significantly small compared to the dimensions of the body.

An example of statistical mechanics model is the Arruda and Boyce 8-chain model (Arruda and Boyce, 1993). The model is based on an eight chain representation of the underlying macromolecular network structure of the rubber and the non-Gaussian behaviour of the individual chains in the proposed network. The eight chain model accurately captures the cooperative nature of network deformation while requiring only two material parameters. Furthermore, the 8 chain model provides an accurate model of the larger behaviour under different states of deformation. However, the model fails at small deformations (Mansouri and Darijani, 2014).

Modelling and designing using hyperelastic materials include the selection of an appropriate strain energy function to accurately represent the material behaviour and accurately calibrating the selected strain energy potential using data from suitable

experiments. Some of the common hyperelastic models found in computer simulation FEA packages are:

Mooney-Rivlin model:

$$U = C_{10}(\bar{I}_1 - 3) + C_{01}(\bar{I}_2 - 3) - \frac{1}{D_1}\left(J^{el} - 1\right)^2 \quad [2.4]$$

Neo-Hookean (Simo and Pister, 1984) model:

$$U = C_{10}(\bar{I}_1 - 3) + \frac{1}{D_1}\left(J^{el} - 1\right)^2 \quad [2.5]$$

Ogden model:

$$U = \sum_{i=1}^{N} \frac{2\mu_i}{\alpha_i^2}\left(\bar{\lambda}_1^{\alpha_i} + \bar{\lambda}_2^{\alpha_i} + \lambda_3^{\alpha_i} - 3\right) \sum_{i=1}^{N} \frac{1}{D_i}\left(J^{el} - 1\right)^{2i} \quad [2.6]$$

Polynomial Model:

$$U = \sum_{i+j=1}^{N} C_{ij}(\bar{I}_1 - 3)^i(\bar{I}_2 - 3)^j + \sum_{i=1}^{N} \frac{1}{D_i}\left(J^{el} - 1\right)^{2i} \quad [2.7]$$

where $\bar{\lambda}_i$ are the deviatoric stretches, N is a material parameter. μ_i , α_i and D_i are temperature dependent material parameters. U is the strain energy per unit reference volume, C_{10}, C_{01}, and D_1, are temperature dependent material properties. $\bar{I}_1$ and $\bar{I}_2$ are first and second deviatoric strain invariants. $\mu = \sum_{i=1}^{n} \mu_i$ is the shear modulus, K is the bulk modulus and $j = 1,2,3$ is the Jacobian, equal to 1 for incompressible materials.

2.2. Rapid Gas Decompression (RGD)

Understanding of failure mechanism in RGD has advanced substantially in the past 20 years (Monaghan et al, 2006). Rispin (1985) reported that RGD in seals occurs as blistering, internal splitting or as longitudinal surface splitting referred to as "channelling". Rispin also reported that, blistering is rarely seen in service, due to the time that inevitably elapses between the final depressurisation of the valve and the inspection of the components. Splitting is the most common form of damage that has been frequently observed in service (Rispin, 1985). The splits can either be visible on the seal's surface or located internally with their orientation being classed as transverse or longitudinal to the seal axis. On many occasions, the widths of the longitudinal splits almost equal the diameter of the seal and are normal to the pressure gradient through the

seal. Cox (1985) reported that the RGD resistance of an elastomeric material is dependent both upon the compounding of its base elastomer and upon the composition of the elastomer itself. Outstanding resistance can be achieved in a fluorocarbon elastomer through reinforcement using carbon black particles of optimum size and by curing to a high cross-link density. Cox also reported that RGD resistance is inversely proportional to the cross-sectional area of the elastomer that is exposed to the gas. When specifying elastomer O-rings for rapid gas decompression, it is not sufficient to consider the performance of the seal in isolation (Embury, 2004). The whole system, comprising the housing design, service conditions and the material and seal selection details have to be taken into account. Lorge et al. (1999) investigated the nature of the gas induced damage in a poly (vinylidene fluoride) exposed to explosive decompression in a carbon dioxide environment. Briscoe et al. (1994) published a review that describes the general features of gas induced rupture in elastomers, induced by a reduction in the ambient gas pressure. They proposed that the failure process involved bubble expansion and the subsequent tearing of the interior and exterior of the elastomer. The failure process is a result of at least two stress fields which are simple triaxial tension and by an evolving gas concentration gradient. Gent and Tomkins (1969) conducted a study on the formation and growth of gas bubbles in cross-linked elastomers. They proposed a critical condition which holds true in most cases for bubbles to form: the gas super saturation pressure must exceed 5G/2, where G is the shear modulus of the elastomer. In their experiments, they revealed a cross-sectional display of a collapsed bubble which showed similar features to a flaw observed in a fractured seal (Teesele™) after exposure to RGD conditions. Figures of the two flaws are shown in Appendix A. The similarity of these two flaws suggests the formation of gas bubbles in seals during RGD conditions. Initially the flaw in the Teesele™ was thought to be inherently present within the elastomeric material however, after close inspection the flaw was more likely to represent a collapsed bubble during RGD. Edmond (2001) observed the formation of fatigue rings in seals exposed to RGD conditions and suggested that fatigue is a major failure mechanism in elastomeric seals. Fracture initiates from voids and/or rigid inclusions contained in the raw elastomer material or introduced during the manufacturing process. For instances where fracture initiates from rigid inclusions rather than voids, large inclusions behave as if they were smaller voids causing cracks to grow and inflate under internal pressure (Edmond, 2001).

2.2.1. RGD Test Protocols

To avoid failure of sealing components in operation, there are several industry and customer specific test methods used for validating elastomer sealing components exposed to RGD conditions during service. These tests differ from one another in a number of aspects and hence, the suitability of a particular material accredited under a particular test regime may not necessarily guarantee its suitability if tested using a different test. Some of the common test procedures are:

i. NORSOK M-CR-710 (1994),
ii. NACE TMO 192-98,
iii. SHELL test procedure, as described by Cox, (1985),
iv. TOTALFINA SP-TCS-142 and
v. ISO 23936-2.

Numerical models and experiments conducted in this thesis were based on the Norsok M-710 Rev. 2 (2001) which is a revised version of the Norsok M-CR-710 (1994) standard. The Norsok standards define the requirements for critical elastomer sealing, seat and back up materials for permanent use in subsea environments. According to the Norsok M-710 Rev. 2 test regime, the seals are inserted into the housing grooves and subjected to a pressure of either 15MPa, 20MPa or 30 MPa at temperatures of 100°C, 150°C or 200°C. For both sweet and sour wells, the fluid media is either 3% CO_2 + 97% CH_4 (low CO_2), or 10% CO_2 + 90% CH_4 (High CO_2) and for carbon dioxide injection wells, 100% CO_2 is used. With the test samples in place, pressure is applied for 72 hours to allow the media to permeate into the sealing material. The system is then decompressed to ambient pressure at a rate between 2 MPa and 4 MPa per minute. The sample is held for one hour at ambient, then re-pressurised and soaked at temperature and pressure for 24 hours before further decompression. This cycle is repeated a total of ten times before the test rig is allowed to cool to ambient temperature and left for 24 hours before removing the samples.

2.3. RGD Numerical Model

Routh (1999) proposed a modelling methodology to predict crack initiation in elastomeric seals exposed to RGD. The model used a quantitative approach to predict crack initiation, location and the crack propagation direction in elastomer seals. The

nature of the failure initiation points was determined by microscopic analysis of seal sections. A numerical model was developed by Ho (1993) to model fluid ingress into elastomeric seals, and the resulting long term material property changes caused by volume swell and chemical reaction between elastomer and absorbed fluid. The model was used for calculating the required soak-time in the rig tests, designed to investigate RGD caused by the absorbed fluid in elastomers. However, the model could not be used to predict the stress and strain levels and the stress distribution in the O-ring during the expansion of the absorbed fluid.

The challenge in modelling RGD is analysing the structural deformation of the O-ring due to the pressure exerted by the rapidly expanding gasses. A new FEA model was created by Routh and Ho (1997) in a joint program MODES (Modelling of Decompression in Elastomeric Systems) in order to research the mechanisms and prediction of RGD damage. The model calculates the stress and strain levels caused by seal compression from the housing, thermal expansion and the volumetric expansion upon decompression. The volumetric expansion of the O-ring due to expansion of absorbed gas was taken into account by increasing the temperature of the O-ring in order to produce the required expansion. This method assumes that the expansion of the O-ring due to absorbed fluid is uniform inside the O-ring structure. However, during each decompression cycle the fluid concentration is non-uniform across the O-ring cross-section, and therefore the pressure exerted onto the O-ring by the expanding fluid is also non-uniform. To use the method proposed by the MODES program, the designer has to know the amount of expansion caused by the absorbed fluid during RGD.

Omnes et al. (2010) developed an FEA model to simulate the behaviour of seals during RGD. The structural deformation of the O-ring due to the expansion of the absorbed fluid was taken into account by using the expansion coefficient due to diffusion. The method proposed is capable of modelling the non-uniform expansion of the O-ring due to the non-uniform expansion of the expanding gas. However, the expansion coefficient due to diffusion is quite complex to evaluate.

The numerical model proposed in this thesis evaluates the pressure exerted onto the internal structure of the O-ring by the absorbed gas at various points within the O-ring structure. The O-ring is divided into several finite elements and the pressure exerted onto each element by the absorbed gas in that particular element is evaluated using a

user subroutine. The amount of pressure exerted onto each element inside the O-ring structure is evaluated from the amount of gas concentration contained in the element in the O-ring structure. This pressure is then applied to the model using another user subroutine, which will be explained in more detail in Section 4.3.3. The proposed model has the ability to evaluate the deformation of an O-ring due the non-uniform pressure exerted by the rapidly expanding absorbed gas during RGD.

2.3.1. Peng-Robinson Equation of State

The new RGD numerical model proposed in this thesis evaluates the pressure exerted onto the internal structure of the O-ring due to the expanding gas using an equation of state. An equation of state is a functional relationship between pressure, volume and temperature of a fluid (Anderson, 1989). At present there is no single equation that accurately predicts the properties of all substances under all conditions.

Van Der Waals (1873) proposed an equation of state which can be regarded as a modification of the ideal gas law. The basic assumptions of the Van der Waals theory are contained in two concepts which are: excluded volume (attractive forces) and a homogeneous, isotropic filed potential (repulsive forces) (Heidemann and Prausnitz, 1976). The Van der Waals equation of state is typically written as:

$$\left(\mathrm{p} + \frac{\mathrm{a}}{\mathrm{v}^2}\right)(\mathrm{v} - \mathrm{b}) = \mathrm{NRT} \qquad [2.8]$$

where P is the externally applied pressure, a/v^2 is the molecular pressure generated from the attraction between the molecules, which varies as the square of the density, a, b and c are constants, T is the temperature, R is the ideal gas constant and v is the molar volume.

Beattie and Bridgeman (1928) presented a new equation of state which provided ease and uniqueness of determination of values for the constants of a substance from experimental pressure-volume-temperature measurements. The equation of state provided accurate representation of the pressure-volume-temperature data over wide range of temperature and density. The Beattie-Bridgeman equation is typically written as:

$$\mathrm{P} = \frac{\mathrm{NRT}(1-\varepsilon)}{\mathrm{V}^2}[\mathrm{V} + \mathrm{B}] - \frac{\mathrm{A}}{\mathrm{V}^2} \qquad [2.9]$$

In which

$$A = A_0\left(1 - \frac{a}{V}\right) \quad [2.10]$$

$$B = B_0\left(1 - \frac{b}{V}\right) \quad [2.11]$$

$$\varepsilon = \frac{c}{VT^3} \quad [2.12]$$

Benedict-Webb-Rubin extended the work of Beattie-Bridgeman by increasing the number of constants to eight parameters and was found to provide good results for hydrocarbons (Knag and Mcketta, 1961). The Benedict-Webb-Rubin equation of state is typically written as:

$$P = \frac{RT}{v} + \frac{B_0RT - A_0 - C_0/|T^2}{V^2} + \frac{bRT - a}{v^3} + \frac{a\alpha}{v^6} + \frac{c}{v^3T^2}\left(1 + \frac{\gamma}{v^2}\right)\exp\left(\frac{-\gamma}{v^2}\right) \quad [2.13]$$

where A_0, B_0, C_0, a, b, c, α, and γ are gas dependent coefficients, P is pressure and v is the molar volume.

Peng and Robinson (1976) proposed a new two constant equation of state in which the attractive pressure term of the Van der Waals equation was modified. The proposed model provided both simplicity and accuracy and also showed great advantages in the prediction of liquid phase densities. Among the equations discussed so far, the Peng-Robinson equation is probably the best compromise between mathematical simplicity and accurate representation of data for the range of temperature and pressure to be investigated in this thesis. The Peng-Robinson equation is typically written as:

$$P = \frac{RT}{v-b} - \frac{a(T)}{v(v+b)+b(v-b)} \quad [2.14]$$

At critical temperatures:

$$a(T_c) = 0.45724\ \frac{R^2{T_c}^2}{P_c} \quad [2.15]$$

$$b(T_c) = 0.07780\ \frac{RT_c}{P_c} \quad [2.16]$$

At temperatures other than the critical:

$$a(T) = a(T_c).\alpha(T_r, \omega) \quad [2.17]$$

$$b(T) = b(T_c) \quad [2.18]$$

where *Pc* is the critical pressure, *Tc* the critical temperature, ω the acentric factor, a and b are the corrective terms, $\alpha(T_r, \omega)$ is a dimensionless function of reduced temperature and acentric factor and equals 1 at the critical temperature.

Table 2.1 shows pressure calculated from equations by Peng-Robinson, Beattie-Bridgeman and Benedict-Webb-Rubin compared to the results from Span and Wagner (1994), the uncertainty of the Span and Wagner results ranges from ±0.03 to ±0.05. All the pressure values were calculated at 373.15 K except at the critical conditions.

The Beattie-Bridgeman equation gives the most accurate results at pressures below 100 MPa and densities below 200 kg/m^3, however both Beattie-Bridgeman and Benedict-Webb-Rubin models produce highly inaccurate results at conditions near the critical density. Peng-Robinson model provides results with acceptable accuracy even at conditions near the critical density hence the Peng-Robinson was used in this thesis.

Table 2.1 Pressure calculated by Peng-Robinson, Beattie-Bridgeman and Benedict-Webb-Rubin compared to results by Span and Wagner (1994) at constant temperature of 373.15 K.

Density **(kg/m^3)**	Span and Wagner **(MPa)**	Peng-Robinson **(MPa)**	Beattie-Bridgeman Equation **(MPa)**	Benedict Webb Rubin **(MPa)**
1.44	1.01	1.012	1.013	1.013
		0.20 %	0.3 %	0.30 %
45.82	30	29.801	29.996	30.098
		-0.66 %	0.01 %	0.33 %
62.75	40	39.685	39.985	40.256
		-0.7875 %	-0.04 %	0.64 %
80.65	50	49.569	49.963	50.545
		-0.86 %	-0.08 %	1.09 %
99.63	60	59.474	59.934	61.035
		-0.87 %	-0.11 %	1.73 %
119.80	70	69.423	69.901	71.812
		-0.82 %	-0.14 %	2.59 %
128.23	74	73.423	73.891	76.229
		-0.78 %	-0.15 %	3.01 %
141.28	80	79.445	79.877	82.992
		-0.69 %	-0.15 %	3.61 %
188.56	100	99.798	99.927	107.191
		-0.20 %	-0.07 %	7.19 %
332.35	150	154.024	154.273	190.683
		2.68 %	2.85 %	27.12 %
467*	73.77*	73.885	114.400	167.049
		0.16 %	55.05 %	126.45%

*Critical point and where the critical temperature is 304.12 K.

Key:

Pressure
Error

2.4. Fracture Analysis

Fractography is the study of fractured surfaces in order to determine the relation between the microstructure and the failure mechanism (Hayes et al. 2015). In this research, fractography was conducted using SEM to analyse fractured surfaces of seals exposed to RGD conditions. Fracture of rubber begins at inherent flaws or inclusions where the local stress exceeds a critical level. On a macroscopic scale all fractures belong to one of the two categories: brittle fracture or ductile fracture. Brittle fractures require less energy to form and there is relatively little or no macroscopic visible plastic deformation during failure. Ductile fractures are characterised by material tearing and exhibit gross plastic deformation. Ductile fractures result when stresses exceed the materials yield strength.

Fractography can provide important clues about the failure of a material, the initiation point of failure and the propagation pattern of the fracture. Furthermore fractography can be used to provide valuable information about the local service environment or stress state responsible for crack initiation and propagation (ASM International, 2003). The fracture surfaces of rubber as observed through optical or electron microscopy can be divided into three regions (Collyer, 1994):

i. Mirror region: This region normally surrounds the origin of failure and is associated with slow crack propagation as the incipient crack grows. In brittle fractures as the incipient crack increases in size, a critical size is eventually reached at the point when the crack becomes unstable and grows rapidly.
ii. Mist region: As the fracture accelerates, a smooth, matt region called ‘mist’ is generated, containing the beginnings of scarps and riverlines. In polymers, mist regions are not necessarily confined to the vicinity of the fracture origin but can be observed elsewhere on the fracture surface.
iii. Hackle region: Ultimately, as the fracture accelerates towards its terminal velocity, the ‘hackle’ fracture surface is formed, consisting of distinct riverlines. These regions tend to appear in areas where the stress field is changing rapidly (either in direction or magnitude) or when the stress state changes from one of plane strain to plane stress. The crack propagation direction can be easily determined from the structure of the hackle lines.

Scarps are a result of multiple fractures initiating along a crack front propagating on several different planes subsequently converging onto one plane. Riverlines are valuable features for diagnosing the direction of crack growth (Greenhalgh, 2009). These are natural development of scarps and the convergence of crack planes. The convergence of pairs of planes forms the tributaries of rivers, ultimately converging into one crack and the direction of crack growth is the direction in which the riverlines converge.

2.4.1. Scanning Electron Microscopy (SEM)

In this thesis, SEM is used to study the mode of failure in fractured O-rings and spring seals after exposure to RGD conditions. SEM is the most widely used technique for analysing fracture surfaces to understand the failure modes of elastomers exposed to various service conditions. Furthermore SEM can be used to compare the mode of fracture with the type of fillers or compounding technique used in the elastomeric compound.

Mathew and De (1983a) used SEM to analyse fractured surfaces of natural rubber and natural rubber/polybutadiene rubber blends that had been tested for fatigue resistance separately under bending and tension. They reported that the presence of carbon black resulted in a brittle fracture surface and in tension fatigue, the fracture surface of the filled vulcanizates showed two zones, a rough zone and a tear zone. Setua and De (1984) conducted SEM analysis on fracture surfaces obtained from tensile, tear, abrasion and heat build-up testing to evaluate the failure mode on short fibre-reinforced elastomer composites. They also conducted SEM analysis on fractured styrene-butadiene vulcanizates (Setua and De, 1983). The aim was to investigate how different curing systems affect the fracture behaviour of styrene-butadiene rubber vulcanizates. They reported that fillers help to arrest crack growth and increase stress dissipation, thereby increasing tear resistance. They observed that unfilled peroxide-cured styrene butadiene rubber underwent brittle fracture. Whereas the optimum cross-linked sulphur-cured unfilled vulcanizates underwent fracture in the shear planes and with branching of the tear path.

To identify the stress state responsible for fracture in elastomeric seals exposed to RGD conditions, the SEM results are compared to fracture surfaces from literature. Mathew et al. (1982) used SEM to study the tensile rupture of natural rubber (NR) and styrene-butadiene rubber, vulcanized by sulphur and peroxide systems, both with and without

fillers. They found that the fracture surfaces of filler-reinforced NR and SBR vulcanizates were characterised by their roughness and by the presence of short and curved tear lines. Peroxide-cured SBR underwent brittle fracture, and sulphur-cured SBR showed a smooth surface with a few straight tear lines.

Agarwal et al. (2005) used SEM analysis to study the influence of temperature on tear strength and failure mechanism of natural rubber vulcanizates. Kurian et al. (1989) studied the fracture surfaces of natural rubber vulcanizates filled with different quantities of high density polyethylene after they had been subjected to tension fatigue tests. They reported that thermoplastic filler loading increased the strain energy density of the vulcanizates and reduced the fatigue life.

2.4.1. Computerised Tomography Scan (Micro-CT)

Rispin (1985) reported that the propagation direction of cracks in O-rings exposed to RGD conditions is always normal to the pressure gradient direction as shown in Figure 2.1. Also optical microscopy on fractured surfaces of seals exposed to RGD conditions have revealed cracks initiating through the centre of O-rings and spring seals.

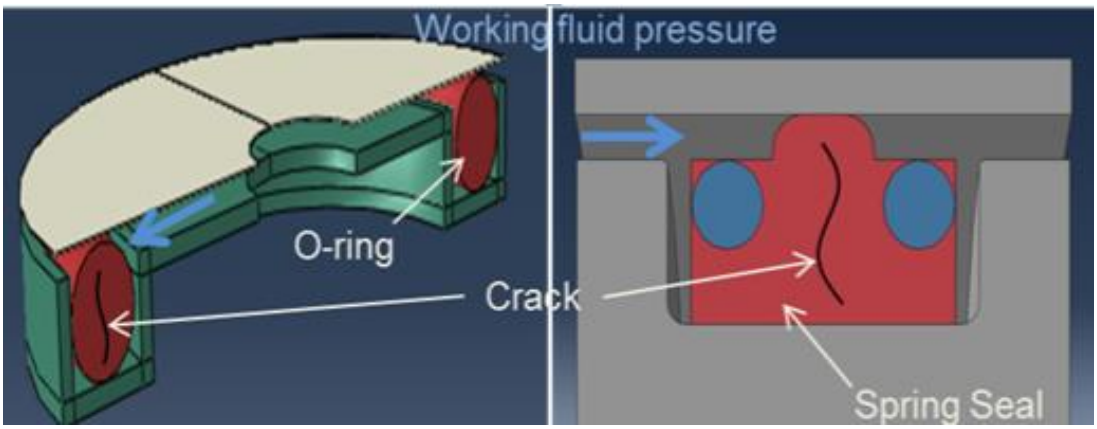

Figure 2.1 A cross – sectional view of an O-ring and Spring Seal inside their housing gland surfaces; cracks are known to propagate normal to the working fluid pressure direction.

The reason for cracks initiating through the centre region of elastomer seals is either because high stress levels are experienced in this region during RGD, or simply because more voids or inherent flaws are located in this region. Voids and rigid inclusions contained in the elastomer material can be a major contributing factor to failure under RGD conditions (Ho, 2006). It is recommended that elastomer seals exposed to RGD conditions should not contain voids and/or rigid inclusions larger than 10 μm (Flitney,

1999). Therefore it is useful to analyse the internal microstructure of elastomer seals before they are exposed to RGD conditions.

The most convenient way to analyse the internal microstructure of an elastomer O-ring without damaging or introducing any defects into the material is by non-destructive morphological analysis using computerised tomography (micro-CT). Micro-CT is a non-destructive technique capable of examining internal features of an object to obtain 2D or 3D computed tomography (CT) images (Harara, 2008). Micro-CT involves passing X-rays from a source through an object and the X-rays are collected by a detector.

The X-rays are attenuated as they pass through the object forming shadow images. From these shadow images, cross-section images of the object are reconstructed using an appropriate algorithm. The main principle of image reconstruction in all computerized tomography applications is the reconstruction of the internal structure of the object from a set of its projections obtained at different angles (Kontaxakis and Strauss, 1998). A variety of reconstruction algorithms have been developed to implement the process of reconstructions of a 3D object from its projections. The algorithms are formed based on the Radon transform and its inversions (Deans, 2000). Note that Radon transform is an integral transform whose inverse is used to reconstruct images from micro-CT scans (Deans, 1983). The reconstructed images are stored and can be viewed and analysed as 2D or 3D images.

Micro-CT has been used in many industrial applications to measure the internal structure of several materials. However, there is not a lot of work reported on using micro-CT in analysing the internal structure of elastomer materials. Bugani et al. (2008) used micro-CT methods to measure the porosity, pore size, pore distribution and the degree of interconnection of the pores in biocalcarenite (Lecce stones). The results were used to study the effect of conservation treatments on stone materials. Apart from measuring voids in materials, micro-CT has been used to study the interaction between optical fibre sensors embedded in fibre-reinforced polymers (Chiesura, 2015). Micro-CT has also been used to characterize 3D textile ceramic composites using micro-CT (Bale et al. (2012). The micro-CT images provided comprehensive geometric information about the matrix voids, individual fibres and fibre coatings. However, they reported that image artifacts can compromise interpretation of the data.

The main challenge in using micro-CT to evaluate the porosity of materials is image processing, to evaluate areas of interest, and in this case to identify voids and/or rigid inclusions. This can be achieved through image segmentation which is a process of partitioning a digital image into multiple segments. Each segment corresponds to different properties. The simplest method of image segmentation is the threshold method, which is used to extract or identify an object from its background on the basis of the distribution of grey levels or texture in image objects (Ping-Sung et al. 2007).

2.5. Fracture Characterisation

The structural integrity of toughened rubber compounds is typically limited by their resistance to fracture. When rubber is loaded, the local stress in the vicinity of a flaw is amplified. When the local stress reaches a critical level, the crack extends causing the rubber to tear. Fracture mechanics analysis can be applied to rubber structures to predict critical loads a rubber component can withstand before failure occurs. However, the main difficulty with fracture characterisation of rubber compounds is due to their large non-linear deformation. It was observed that the stress field in the vicinity of a crack tip for rubber type materials becomes fairly complex, and can vary dramatically with the material models. Numerical calculation of the stress field is thus difficult and not practical (Chang and Ye, 1997).

2.5.1. Tearing Strength

Fracture resistance of a rubber compound can be evaluated through the tearing strength of the material when subjected to continuous stretching. Tearing can be defined as the formation of new surfaces by application of a force in such that it is concentrated at the tip of a sharp indentation or cut in the sample. In many industrial applications, most of the damage to rubber compounds is due to growth of micro cracks generated from static or cyclic loads or due to the manufacturing processes (Luong et al. 2007). A rubber compound with a high tearing strength offers better toughness.

Tear tests have been used extensively in the study of the effects of fillers on elastomers, particularly in trying to determine why gas black greatly improves tear resistance while other pigments, such as clay and whiting reduce (Busse, 1934). Rattanasom et al. (2009) used tear strength tests to study the effects of using different fillers in elastomer

compounds. They reported that at equal loading of fillers, clay filled elastomer compounds exhibit a higher tear strength than carbon black and silica filled elastomer compounds. Tearing strength tests have also been used by Egwaikhide et al. (2013) to compare the tear strength between two natural rubbers with different fillers. One was filled with palm kernel husk carbon obtained from agriculture waste and the other filled with commercial reinforcing filler, carbon black (N330). In this thesis, tear strength tests were used to investigate the effect of combining to different elastomer compounds, in a bid to improve the fracture resistance of the hybrid structure.

Tear strength however, cannot be used as a material property because the tear strength is a function of geometry and boundary conditions. Therefore the results obtained in a tear test can only be regarded as a measure under the conditions of that particular test, and may not have any direct relation to service performance.

The two most common methods used to study fracture of rubber, are the strain energy release rate commonly known as tearing energy developed by Rivlin and Thomas (1953) and the J-integral method developed by Rice (1968). Both methods characterise the fracture properties of rubber materials by assuming a critical amount of energy is required to propagate a crack by a unit area. Although both methods are based on energy concepts, they are different in methods of calculation. These two methods can be applied in Finite Element Analysis (FEA) to characterise the fracture of elastomers.

2.5.2. Tearing Energy

The tearing energy concept is the extension of Griffith's criterion for growth of a crack in brittle materials (Griffith, 1920). In the case of vulcanised rubber, it is described by Rivlin and Thomas (1953) as the rate of decrease of elastically stored energy in a cracked body per unit virtual increment of the crack surface energy:

$$T = -\left[\frac{\partial W}{\partial A}\right]_l \qquad [2.19]$$

where T is the tearing energy, W is the elastic energy stored in the specimen, A is the area of one fracture surface of the crack, and l is the suffix indicating that the derivation is made under constant displacement. A crack in rubber will propagate if the tearing energy T, reaches the critical tearing energy, T_C. The critical tearing energy, T_C is independent of the geometry and dimensions of the test piece and can be considered as a

material parameter (Wang, 1973). This makes the tearing energy concept a strong candidate for characterising fracture of elastomer materials. For component design, the tearing energy is calculated for a hypothetical crack, and is compared to the T_C to determine if the crack will propagate.

There are several tests used to evaluate the tearing energy of simple geometry test specimens. The trousers specimen can be used to evaluate the out of plane mode-III critical energy for elastomers. The test specimen is a thin rectangular piece cut centrally along its length, forming two legs. During the test, the two legs are stretched in opposite directions out of plane of the test piece. The tearing energy equation for a trousers test specimen can be written as (Gdoutos, 2013):

$$T = \frac{2\lambda P}{h} - 2bw \qquad [2.20]$$

where P is the force on the legs of the specimen λ is the strain in the legs, h is the specimen thickness, b is the width of the legs and w is the strain energy density in the legs.

The pure shear tear test piece was introduced by Rivlin and Thomas (1953) to evaluate the characteristic energy for tearing. The pure shear test specimen consists of a flat rectangular sheet of rubber with a high aspect ratio of more than 20. Loading is applied normal to the direction with the longest side. Employing the pure shear test piece, the taring energy can be evaluated from (Kim and Joe, 1989):

$$T_C = w_0 L_0 \qquad [2.21]$$

where T_C is the critical tearing energy, w_0 is the strain energy density in the pure shear region at the displacement at which tearing occurs and L_0 is the distance between the grips before loading.

2.5.3. J-Integral

The J-integral approach was proposed by Rice (1968) as a two dimensional energy line integral that can be used as an analytical tool to calculate the strain energy release rate, or work per unit fracture surface area in a material. The J-integral is similar to the classical strain energy release rate by Griffith. Both theories use a global energy balance approach. The main difference is that, the J-integral is derived from the rate of energy

absorption, while Griffith's energy approach measures the energy release rate for creation of unit new surface area, A. The J-integral approach is theoretically based on a path independent integral:

$$J = \int_{\Gamma} \left(wdy - t\frac{du}{dx}ds \right) \quad [2.22]$$

where J is the J-integral, Γ is any path surrounding the crack tip, w is the local strain energy density, which is the area under the stress-strain curve, y is the coordinate axis parallel to the line of action of the external force, $\frac{du}{dx}$ is the displacement gradient, t is the traction vector, and s is the length.

The J-integral also has a critical value J_C and can be considered a material parameter similar to T_C. A crack will propagate only if the value of the J-integral reaches a critical value of J_C. Wang (1973) used the critical J-integral as the fracture criterion to calculate the critical load for crack growth in uni-axial stretching of nicked rubber vulcanizates sheets. The fracture energy of elastomeric materials can be determined, in terms of J_C, with a single pure shear specimen using the equation (Kim and Joe, 1989):

$$J_C = U_i/B(W - a) \quad [2.23]$$

where J_C is the critical energy for fracture, U_i is the area under the loading curve of a pure shear specimen up to crack initiation point, W is the specimen width, B is the specimen thickness and a is the crack length.

Oh (1976) observed that for the edge cracked specimens of rubber the J-integral approach yielded similar results as the tearing energy method at deformations less than necessary to initiate crack growth. Rice showed that this integral is path independent and it assumes the same value for any choice of path around the crack, and may be interpreted as the potential energy drop in the body per unit virtual extension of the crack. Oh (1976) postulated that, where the crack extends at fixed external boundaries, J is exactly T. Consequently, J may be used to measure T. The computation of T remains limited to specimens with simple geometries and failure modes such that the crack remains self-similar. For more complex geometries such as O-rings, the J-integral is an ideal candidate to characterise fracture.

2.6. Literature Review Summary

This literature review has covered most of the topics that are investigated in this thesis. The elastic properties literature review has shown that, the stress strain relationship of elastomeric materials cannot be derived from a constant factor, such as the elastic modulus. The stress strain relationship for hyperelastic materials is derived from an energy density function. There are several strain energy density functions available in literature. Modelling and designing using elastomeric materials include the selection of an appropriate strain energy function to accurately represent the material behaviour. The strain energy function is accurately calibrated using stress strain results obtained from suitable experiments.

The choice of a suitable strain energy function is dependent on the stress states and the strain range to be modelled. For instance, the Ogden model has been shown to offer better flexibility in describing the curvature on the stress strain curves of elastomeric materials when compared to the Mooney-Rivlin model. However, in applications were the curvature of the stress strain curve is minimal, the Mooney-Rivlin or other higher order models of the Mooney-Rivlin model provide a more accurate representation of the material behaviour. Some applications are only interested in modelling uni-axial stress strain response of elastomeric materials. In these applications, it is cheaper and easier to use strain energy potentials that only require stress strain data from tensile tests only to calibrate them.

Failure of elastomeric seals has been greatly covered in literature, and the most common fracture was reported to be splitting. The splits can either be visible on the seal's surface or located internally with their orientation being classed as transverse or longitudinal to the seal axis. However, there is not much literature on numerical models of elastomeric seals exposed to RGD conditions. The main challenge in modelling RGD is analysing the structural deformation of the O-ring due to the pressure exerted by the rapidly expanding gasses. Two numerical models researched in literature modelled the expansion of the elastomeric seal due to the pressure exerted by the rapidly expanding gas. The first model assumes that the pressure exerted by the absorbed gas is uniform. The volumetric expansion of the O-ring due to expansion of absorbed fluid is taken into account by increasing the temperature of the O-ring in order to produce the required expansion. The second method is capable of capturing the non-uniform deformation of

the O-ring due to the pressure exerted by the absorbed fluid. In this method, the structural deformation of the O-ring due to the expansion of the absorbed fluid is taken into account by using the expansion coefficient due to diffusion. However, the expansion coefficient due to diffusion is quite complex to evaluate.

The numerical model proposed in this thesis evaluates the pressure exerted onto the internal structure of the O-ring by the absorbed gas at various points within the O-ring structure. The O-ring is divided into several finite elements and the pressure exerted onto each element by the absorbed gas in that particular element is evaluated using a user subroutine. The amount of pressure exerted onto each element inside the O-ring structure is evaluated from the amount of gas concentration contained in the element in the O-ring structure. This pressure is then applied to the model using another user subroutine. The proposed model has the ability to evaluate the deformation of an O-ring due the non-uniform pressure exerted by the rapidly expanding absorbed gas during RGD.

The pressure exerted by the rapidly expanding gas is evaluated using an equation of state. There are a number of equations of state available in literature and at present there is no single equation that accurately predicts the properties of all substances under all conditions. However, it was shown in Section 2.3.1 that the Peng-Robinson equation is the best compromise between mathematical simplicity and accurate representation of data for the range of temperature and pressure to be investigated in this thesis.

Table 2.1 compared pressure values evaluated from the equations by Peng-Robinson, Beattie-Bridgeman and Benedict-Webb-Rubin to the results presented by Span and Wagner. The accuracy of the Span and Wagner results ranges from ±0.03 to ±0.05. All the pressure values were calculated at 373.15 K except at the critical conditions. The Beattie-Bridgeman equation produced the most accurate results at pressures below 100 MPa and densities below 200 kg/m^3, however both Beattie-Bridgeman and Benedict-Webb-Rubin models tend to produce highly inaccurate results at conditions near the critical density. Peng-Robinson model provides results with acceptable accuracy even at conditions near the critical density hence the Peng-Robinson was used in this thesis.

SEM analysis of fractured elastomer compounds is extensively covered in literature. Fractography can provide important clues about the failure of a material, the initiation points of failure and the propagation pattern of the fracture. Furthermore fractography

can be used to provide valuable information about the local service environment or stress state responsible for crack initiation and propagation. The SEM analysis covered in literature is used in this thesis to provide important clues about the mode of fracture or the stress state responsible for fracture in elastomeric O-rings and spring seals exposed to RGD conditions. This is conducted by comparing the features observed in the fracture analysis from this research to the fracture surfaces reported in literature.

Fracture characterisation of elastomeric materials is significantly covered in literature. In this thesis, tearing strength tests are used to investigate how the geometry and location of the second phase material affected the components fracture resistance. Tear strength cannot be used as a material property because the tear strength is a function of geometry and boundary conditions. Therefore the results obtained in the tear tests are only regarded as a measure under the conditions of that particular test, and may not have any direct relation to service performance. However, tearing tests have been used extensively in literature for comparing the effects of adding different fillers to elastomeric compounds. The different fillers investigated include carbon black, clay and silica particles.

3. Materials and Experimental Procedure

3.1.1. RGD Fracture Analysis

3.1.2. Scanning Electron Microscopy

This section describes the experimental set-up for conducting fracture analysis on fractured O-rings and spring seals using SEM. Three fractured fluorocarbon FKM type 3 O-ring surfaces shown in Figure 3.1 were examined after being exposed to RGD conditions according to the Norsok M-710 rev.2 (2001) Annex B standards. The fractured O-rings were split internally and their orientation acting longitudinal to the seal axis.

Figure 3.1 Fractured Fluorocarbon FKM type 3 O-ring specimens, the silver paint increases the specimen's conductivity.

Table 3.1 shows the conditions in which the fractured O-ring specimens were tested. The external pressure was released at a rate of 20 bars per minute during each decompression cycle and each O-ring was subjected to 10 decompression cycles.

Table 3.1 Conditions in which fractured O-rings were tested.

Compound	Test Pressure (bar)	Test Temperature (°C)	Test Conditions
FKM type 3	600	100	90% CO_2 in methane
FKM type 3	600	100	90% CO_2 in methane
FKM type 3	400	100	70% CO_2 in methane

Three fractured HNBR101 spring seals were also examined after being exposed to RGD conditions according to the ISO 23936 – 2 standards at a temperature of 120 ^{o}C. Figure 3.2 shows carbon coated fractured surfaces of spring seals after they were exposed to RGD conditions.

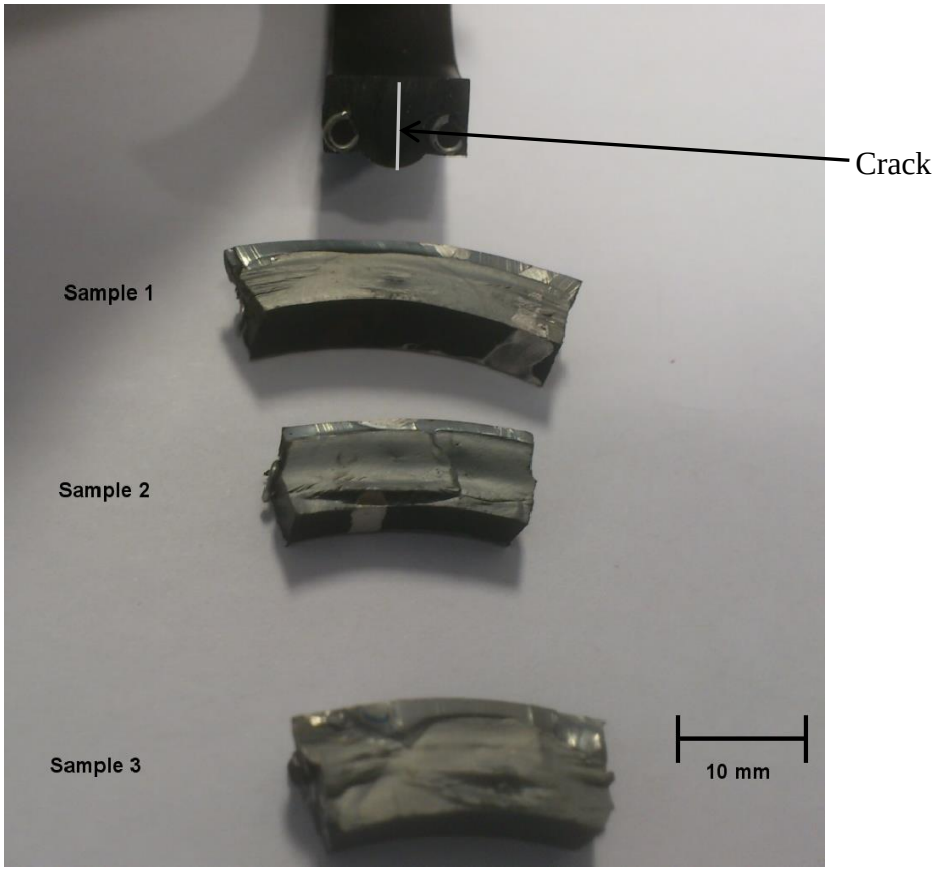

Figure 3.2 Carbon coated fractured surfaces of spring seals, were the grey colour is carbon coating making the surfaces more conductive.

Fractured surfaces of both O-rings and spring seals are non-conductive and therefore they are required to be coated with carbon or gold. Gold coating prevents charging on the surface, which results in poor images being produced. Gold coating promotes the emission of secondary electrons making the specimens conduct evenly and producing a homogeneous surface for analysis and imaging (Leslie and Mitchell, 2007). However gold coating can interfere with elemental analysis. Elemental analysis is used to identify the material composition in a specimen. It can be used to identify the composition of any impurities that may be contained on a fractured surface. In this investigation the fractured surfaces were carbon coated in case elemental analysis needed to be conducted to identify the composition of any inclusions. Carbon coating was conducted by using a carbon source in the form of a rod fitted in a vacuum system between two high current

electrical terminals. The specimens were placed directly underneath the carbon source as shown in Figure 3.3. The carbon source was heated to its evaporation temperature, and a fine stream of carbon was deposited onto the elastomer specimens. The coating process was conducted under vacuum conditions and the carbon rods were heated using an electric current. The coating process was monitored by a white paper strip located next to the specimens inside the vacuum chamber. The change in colour of the white paper strips due to the carbon depositing on it during the coating process was used to indicate how much carbon was deposited onto the fractured specimens. The coating process was stopped when the white strips colour changed to a shade of light grey, which indicated a sufficient carbon thickness on the fracture specimens.

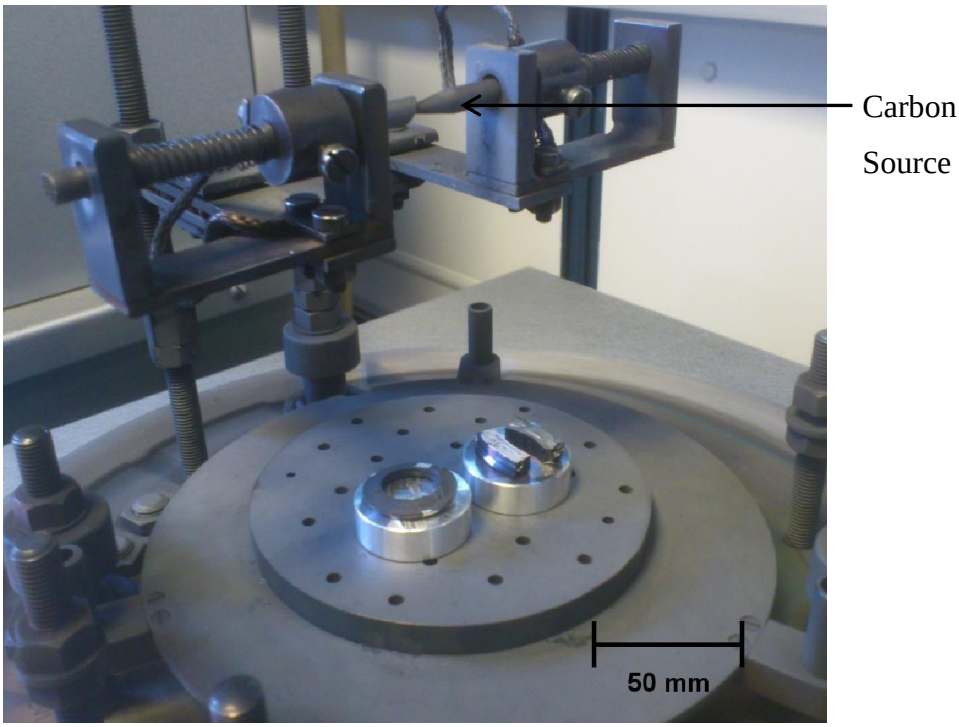

Figure 3.3 Experimental set-up for conducting carbon coating procedures for both O-rings and spring seals.

Before conducting SEM analysis, the fractured surfaces were examined under an optical microscope. This was to identify any visible areas of interest, and to save time during the SEM analysis. Instead of scanning all fractured surfaces using SEM, only a few samples were selected. The selection criterion was based on results from the optical microscope analysis. Samples containing areas of interest such as crack initiation points and crack propagation regions were selected to be analysed using SEM.

3.1.3. Computerised Tomography Scan

This section describes the experimental set-up for conducting computational tomography analysis on elastomer O-rings. Three 6.99 mm HNBR101 O-rings were analysed using a Sky Scan 1172. Two of the O-rings were manufactured the conventional way and the third O-ring was manufactured differently in a bid to reduce void content.

Sky Scan 1172 works by obtaining multiple x-ray "shadow" images of the O-ring as the O-ring is rotated by 180 degrees on a high-precision stage between the radiation source and detector as shown in Figure 3.4. The shadow images are then used to create cross-section images of the O-ring using a modified Feldkamp cone-beam algorithm (Feldkamp et al. 1984), thereby creating a complete 3D representation of the internal microstructure of the O-ring. The O-rings were sectioned careful using a sharp blade as shown in Figure 3.5 and taking caution not to introduce any artificial defects into the O-ring samples. Also as a precaution the first few layers at the top and bottom of the O-rings were not analysed. The reason for the sectioning was because the O-rings were too large to scan as a whole and also sectioning allowed for a more uniform scanning of the sample.

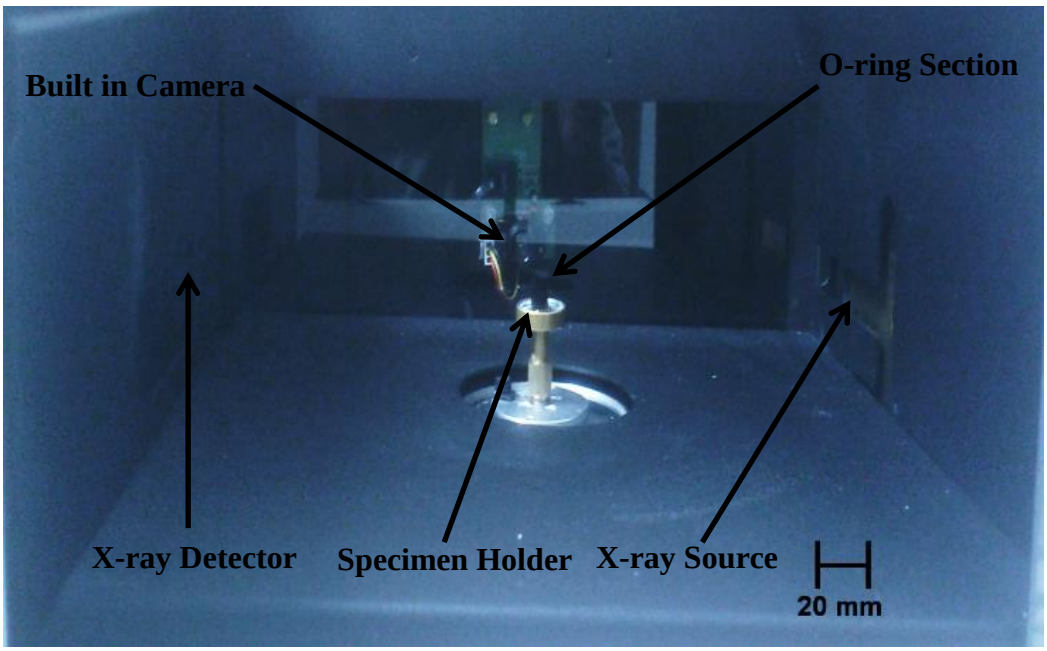

Figure 3.4 Display of an O-ring cross-section inside the Sky Scan 1172, X-rays are emitted from the source and are collected by a detector.

Figure 3.5 A sectioned O-ring specimen analysed using computerised tomography.

After scanning the images, dedicated software "Bruker – micro CT" CT-analyser was used to analyse the internal microstructure of the sample. CT-Analyser is software used for measuring quantitative parameters and constructing visual models from scanned 3D datasets obtained from micro-CT instruments (Bruker Micro-CT, 2013). The reconstructed images can then be displayed by slice-by-slice scrolling, or three orthogonal sections centred at any selected point of the reconstructed space or by conversion to realistic 3D models. The software can also be used to process and analyse datasets and accurately generating quantitative data in this case identifying any voids and/or rigid inclusions.

3.2. Materials Characterisation

3.2.1. Materials

This section gives a brief introduction about the two materials used throughout this thesis. The two elastomer compounds used are hydrogenated nitrile butadiene rubber (HNBR101) and LRCM888. LRCM888 was used as the reinforcing second phase material during the construction of hybrid O-rings. HNBR101 was used as the main core material. Each material was chosen for its specific characteristics. The aim was to design hybrid O-rings that can benefit from each material's strength.

3.2.1.1. Hydrogenated Nitrile Butadiene Rubber (HNBR)

HNBR is common for its physical strength and retention properties after long-term exposure to heat and chemicals. The particular HNBR compound used in this thesis is a compound formulated by the industrial sponsor James Walker & Co. Ltd and is referred to as HNBR101. This compound was specifically developed for RGD resistance and contains 36 % acrylonitrile (ACN), reinforced with carbon black and is peroxide cured. HNBR101 has a working temperature range of -29 °C to +160 °C.

Typical physical features of HNBR101 include (James Walker & Co. Ltd):

- Tensile strength: 32 MPa
- Hardness: 89 IRHD
- Modulus at 50 % elongation : 6.9 MPa
- Modulus at 100 % elongation: 13.5 MPa
- Elongation at break: 210 %
- Tear resistance: 41000 N/m
- Compression set after 24 hours at 150 °C: 16%
- Compression set after 70 hours at 150 °C: 32%

Note that the formulation of HNBR101 is confidential and industrial sponsor James Walker & Co. Ltd does not release the chemical formulation of the compound.

3.2.1.2. LRCM 888

LRCM888 is a compound formulated by the industrial sponsor James Walker & Co. Ltd and it was specifically formulated for its high fracture toughness characteristics. LRCM is short for Lab Report Cockermouth and it is an HNBR compound. Individually LRCM888 has poor sealing capabilities however it has a higher elongation at break than HNBR101. LRCM888 was chosen for its compatibility with HNBR101 in terms of thermal expansion coefficient and creep characteristics. The thermal expansion coefficient and the creep behaviour for both materials are covered in Section 6.2 and Section 6.3.

LRCM 888 contains:

- Zeptol 202L,
- Titanium Dioxide,

- Ultrasil VN3, a precipitated silica used as reinforcing filler and is used to improve elastomeric materials mechanical performance,
- Polyethylene Glycol (PEG) 4000,
- Stearic Acid,
- Struktol® EF 44 A, which is a blend of fatty acid derivatives and improves processing behaviour of elastomeric materials, and
- Ricon ® 153D, which is a liquid polybutadiene resin used to improve materials properties during curing of elastomeric materials.

3.2.2. Hyperelastic Material Properties

Elastomeric material's stress-strain behaviour is quite complex and does not exhibit linear stress-strain behaviour like metals. This is because their stress-strain behaviour is highly nonlinear and they need to be analysed as nonlinear hyperelastic materials using a strain energy potential function. In this thesis, hyperelastic materials are analysed by obtaining stress-strain data for HNBR101 and LRCM888 under uni-axial, pure-shear and bi-axial loading, and using the least squares procedure to calibrate the strain energy potential function.

This section describes the experimental procedures conducted to evaluate the stress-strain data for HNBR101 and LRCM 888 under multi-axial loading. The experiments were conducted according to the ISO D412 (2008) standard, which covers procedures used to investigate tensile properties of vulcanized thermoset rubbers and thermoplastic elastomers. In service, the seals investigated in this research are exposed to high temperatures and the temperature varies with the particular service. In this research, the seals were analysed at 100 °C. Therefore the elastomer material properties were evaluated at the same temperature of 100 °C. In each test all the specimens were preheated for more than ten minutes before each test and the grips which were made of mild steel were preheated for more than thirty minutes before each test. All the tests were performed at 30 mm per minute. This is because elastomers exhibit viscoelastic material properties therefore tests conducted at different strain rates will yield different results. To reduce the error caused by strain rate dependency, all the tests conducted in this research which were strain rate dependent were performed at a rate of 30 mm per minute. 30 mm per minute was chosen because it is slow enough to allow the user to

observe the change in material characterises during each test and make sure the test is proceeding according to the test requirements.

3.2.2.1. Uni-axial Stress

Both HNBR101 and LRCM888 dumbbell specimens were prepared by using a specialised die used for punching out dumbbell specimens. Each dumbbell specimen's dimensions conformed to the requirements outlined in ISO D-412 (2008) standard. The dumbbell specimens analysed are shown in Figure 3.6.

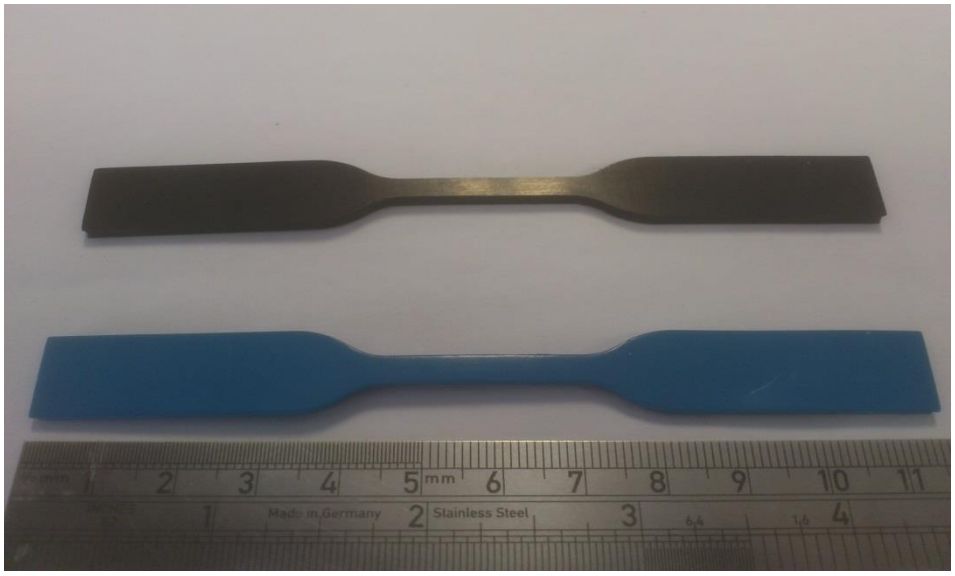

Figure 3.6 Geometry of test specimens used in the uni-axial tests.

The nominal uni-axial stress was evaluated using:

$$\sigma_{Tensile} = F/A \qquad [3.1]$$

where *F* is the average force normal to the width and height of the specimen and *A* is the cross-sectional area through which force is acting.

3.2.2.2. Planar Shear Stress

Both HNBR101 and LRCM888 planar shear test specimens were prepared by using a specialised die. The objective of this experiment is to create an experiment where the specimen is perfectly constrained in the lateral direction such that the entire specimen thinning occurs in the thickness direction (MSC Software, 2010). Therefore, the test specimen is required to have an aspect ratio of more the 10. Since rubber is nearly incompressible, a state of planar shear exists in the specimen at 45 degrees to the

applied force direction. The strain is measured away from the clamp edges where pure strain state is occurring. The two white strips in Figure 3.7 represent the region where strain is measured.

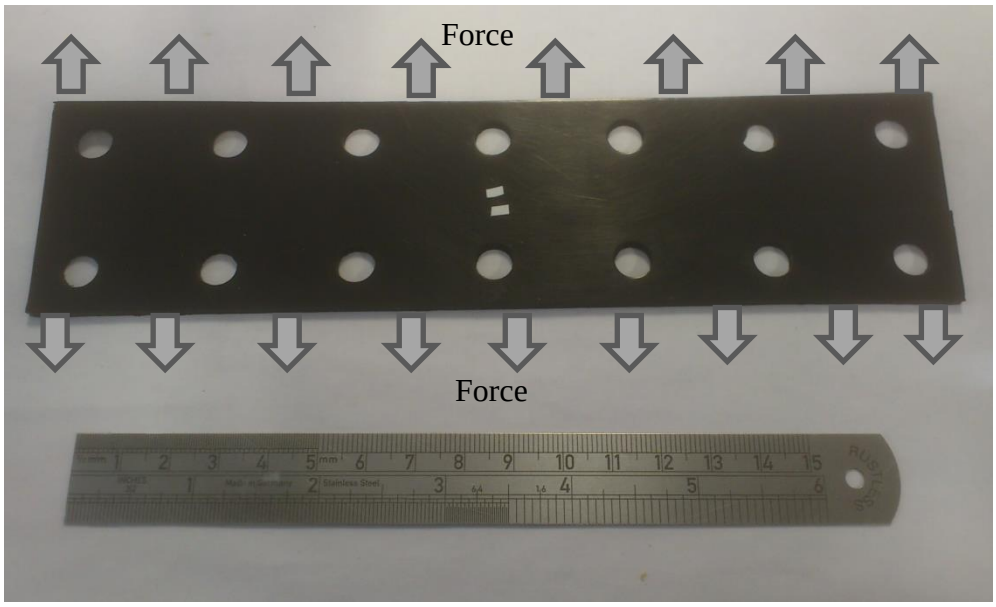

Figure 3.7 Geometry of the planar shear specimen, the white strips in the centre are used to measure strain and the holes on the edges are used for clamping the specimen by the grips.

The nominal uni-axial stress was evaluated using:

$$\sigma_{Shear} = F/A \qquad [3.2]$$

where F is the average force normal to the width and height of the specimen and A is the cross-sectional area through which force is acting.

3.2.2.3. Equibiaxial Stress

The test specimens for equibiaxial tests were prepared by carefully cutting out square rubber samples from a flat sheet and then punching out small holes along the edges of each specimen as shown in Figure 3.8. The aim of this test specimen configuration is to achieve equal equibiaxial strain state by radially stretching the square sheet. The strain is measured in the middle of the test specimen well away from the clamp edges.

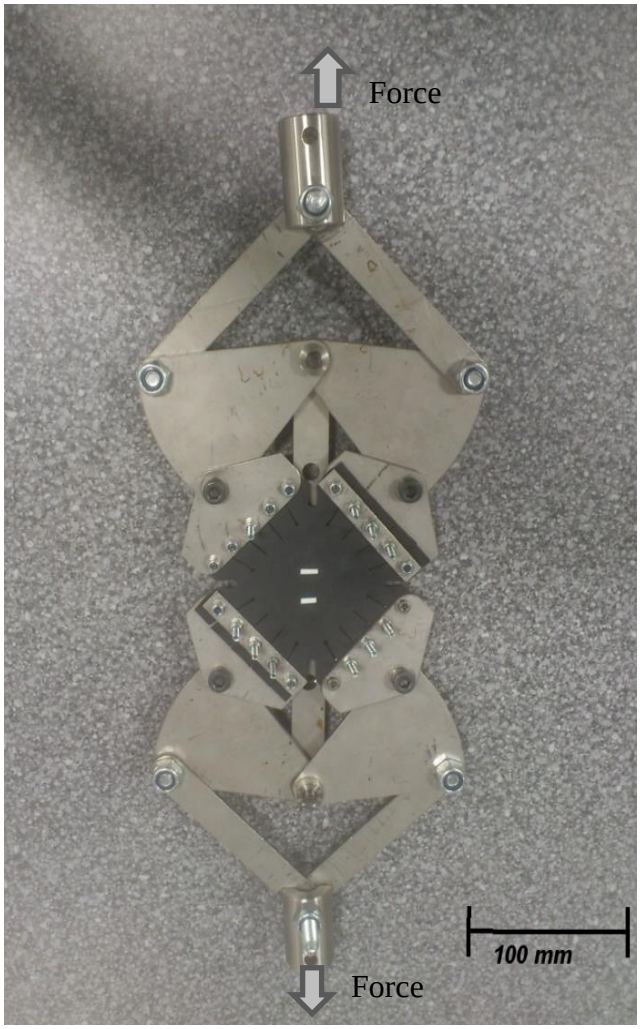

Figure 3.8An experimental set-up for the bi-axial experiment, where a normal force is applied to each side of the square specimen.

The nominal equal equibiaxial stresses inside the specimens are calculated as (Schubert and Harrison, 2015):

$$\sigma_{Bi-axial} = F \cos 45 \, / A \qquad [3.3]$$

where *F* is the average force normal to the width and height of the specimen and *A* is the cross-sectional area through which force is acting.

3.2.3. Viscoelasticity

Pure hyperelastic materials deform instantaneously when they are subjected to an external load and they return to their original configuration almost instantly when the external load is removed. Most elastomers do not exhibit pure hyperelastic material properties. They exhibit gradual deformation and recovery when they are subjected to

loading and unloading and their response is dependent upon the rate at which the load is applied and removed. The time dependency material behaviour is referred to as viscoelasticity. Viscoelastic materials possess both viscous and elastic properties. The material behaviour of viscoelastic materials can be expressed as (Ozkaya et al. 2012):

$$\sigma = \sigma(\varepsilon, \dot{\varepsilon}) \quad [3.4]$$

where σ is the stress, ε is the strain and $\dot{\varepsilon}$ is the strain rate. According to Equation 3.4, stress is not only a function of strain, but also a function of strain rate. This section describes the experiments conducted to evaluate the viscoelastic properties of both HNBR101 and LRCM888. Since the two materials will be used to construct hybrid O-rings, it was important to characterise the two material's dynamic behaviour to ensure compatibility.

3.2.3.1. Glass Transition Temperature and Loss Factor (tan δ)

The glass transition temperature (T_g) and loss factor (tan δ) for both LRCM888 and HNBR101 were measured using a Dynamic Mechanical Analyser (DMA). The T_g represents a major transition in elastomers. The T_g represents the region where the properties of an elastomer change significantly as the material state changes from glassy state to a rubbery state. It can be used to determine the temperature range over which elastomers can operate. When constructing hybrid O-rings, it is imperative that the two materials have the same working temperature range. This is because if they have different working temperatures the two materials will have different properties from each other during service.

The loss factor is the ratio between the loss modulus and the storage modulus. It is a measure of a materials energy damping characteristics. The loss factor can be used to measure an elastomer's ability to absorb energy. The loss factor varies with the state of material, temperature and frequency. Both the glass transition temperature and the loss factor were measured according to the ISO 6721 (2011) standard. The glass temperature and loss factor were determined by conducting a frequency scan for both HNBR101 and LRCM888 in tension mode. The testing was conducted at three different frequencies, 0.1 Hz, 1 Hz and 10 Hz. The tension experiment setup is shown in Figure 3.9. Table 3.2 shows the tensile specimen dimensions used in measuring the glass transition

temperature. The gauge length was measured as the length between the grips in the DMA machine.

Table 3.2 The tensile specimen dimensions used in the creep analysis using DMA.

	Gauge Length (mm)	Thickness (mm)
HNBR101	10	2.5
LRCM 888	10	2.2

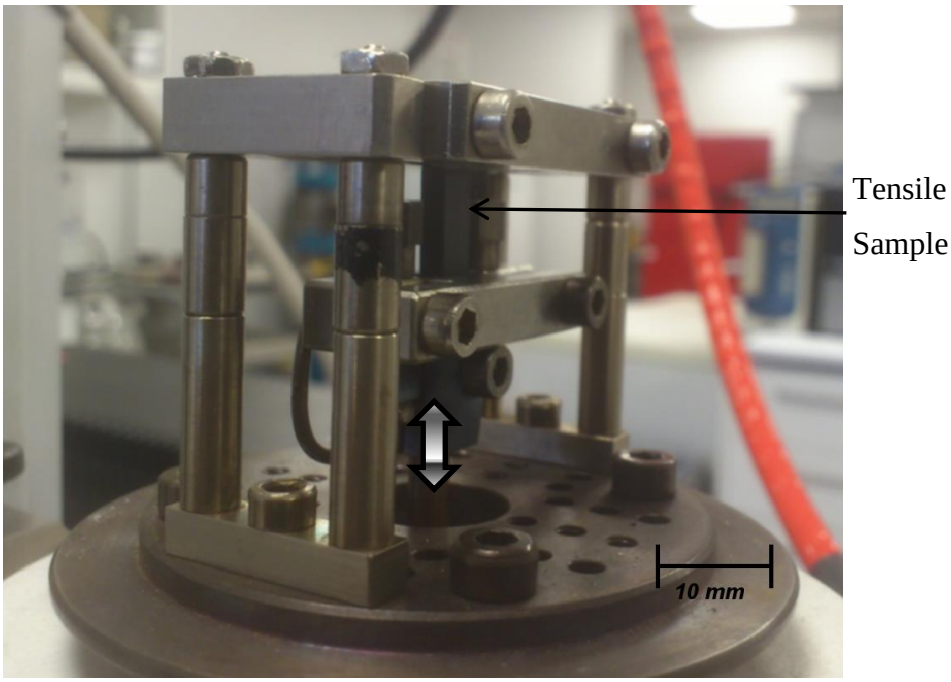

Figure 3.9 Experimental set-up to measure the glass transition temperature for both HNBR101 and LRCM888 in tensile mode.

3.2.3.2. Creep Behaviour

When elastomers are subjected to a constant stress, the deformation is not constant but increases gradually with time and this behaviour is known as creep. The creep tests were conducted according to ISO 8013 (2012) standard. Creep in elastomers can be a result of physical or chemical processes, and under normal conditions both processes can occur simultaneously. However, at normal or low temperatures and/or short time exposure, creep is dominated by physical processes, at high temperature and/or long time exposure time creep is dominated by chemical processes. Creep testing allows the user to examine a material's response to a constant load and its behaviour on removal of that load.

Creep experiments were conducted under shear loading as shown in Figure 3.10 using a DMA machine. The creep tests were performed at 100 °C. The shear specimens were soaked at 100 °C for at least ten minutes before testing and this was to allow the material to uniformly heat to testing temperature. Each specimen was subjected to a constant load of 3 N for more than 40 hours and the change in displacement was recorded at specified intervals as a function of time. The displacement was measured from the distance travelled by the DMA cross head. Table 3.3 shows the shear specimen dimensions used in the creep analysis using DMA.

Table 3.3 The shear specimen dimensions used in the creep analysis using DMA.

	Length (mm)	Thickness (mm)
HNBR101	5	2.5
LRCM 888	5	2.2

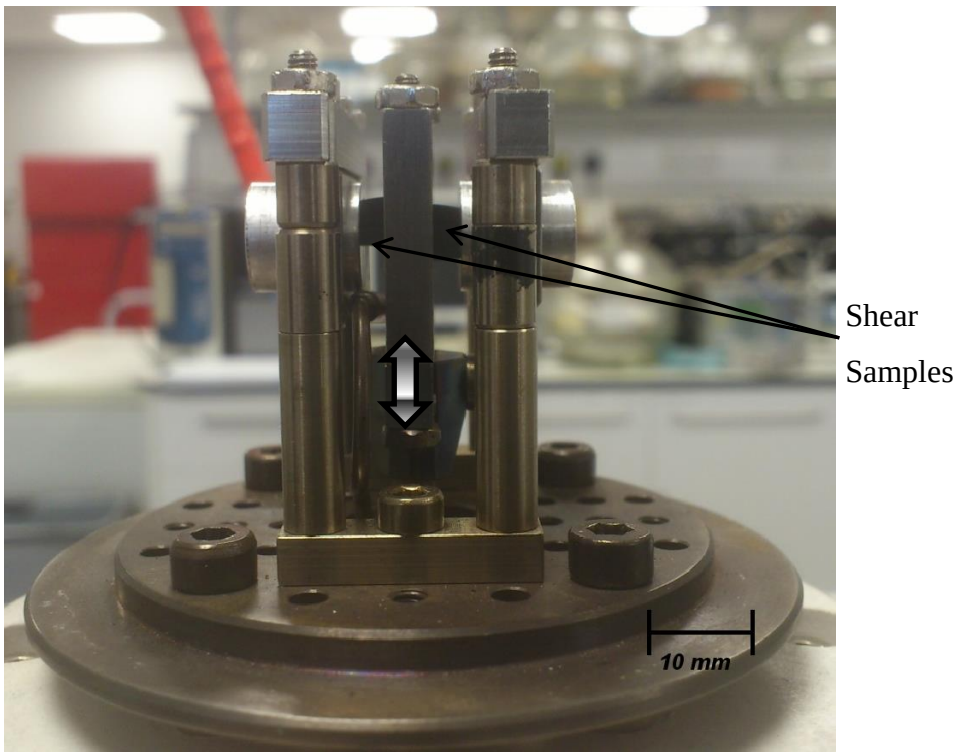

Figure 3.10 Experimental set-up to measure creep behaviour, where the specimen is clamped in shear mode and the change in strain at a constant load is measured.

3.2.4. Coefficient of Thermal Expansion

Thermal expansion coefficient is a material property that is indicative of the extent to which materials expand and/or contract upon heating. Different materials expand or contract by different amounts upon heating. The methodology used to measure thermal expansion in this research is a relatively simple technique and has been proven to give accurate expansion coefficients (Perkin, 2007). The thermal expansion coefficient is evaluated by running the DMA in Thermal Mechanical Analyser (TMA) Mode. DMA normally works by applying an oscillating load to a material and measuring the resultant displacement. However when the DMA is running in TMA mode, the oscillating force function is turned off. The experimental set-up for measuring the coefficient of thermal expansion is the same as the one shown in Figure 3.9, used for measuring the glass transition temperature.

When measuring the thermal coefficient, the sample is clamped into the DMA machine and the displacement of the sample is measured as it expands or contract as a function of temperature. The specimens used had the same dimensions as the samples used for measuring the glass transition temperature in Section 3.2.3.1. The displacement of the specimen while in tensile mode gives an indication of how much the material will expand or contract across the given temperature range.

When the temperature is raised, the material being measured expands and so do the driveshaft and the clamps, therefore it is essential to calibrate the instrument. The calibration was carried out using aluminium strips because the expansion coefficient of the aluminium was known. The thermal expansion of the driveshaft and clamps was then subtracted from the specimen data to give an expansion curve relating to the specimen alone. The expansion coefficient can then be calculated from a plot of displacement as a function of temperature change.

3.2.5. Coefficient of Friction

Friction involving rubber compounds is quite complex, the coefficient of friction is dependent on the contact geometry, velocity, normal load and the test temperature. According to the BS ISO 15113 (2015) standard the coefficient of friction is defined as the ratio of the frictional force opposing motion between two surfaces to the normal between the surfaces under specified test conditions. The friction coefficient is

determined in this research to be used in the FEA model of an O-ring compressed by its housing gland surfaces. In the FEA analysis the speed is kept constant at 30 mm per minute, therefore the friction coefficient was also evaluated at this speed. Also the temperature is kept constant at 100 °C in the FEA analysis, so the friction coefficient was also evaluated at this temperature. The coefficient of friction was measured according to the BS ISO 15113 (2005) standard. According to the standard, two test pieces are brought together under the action of a measured normal load. One surface is slid across the other surface at a measured velocity, and the resistance force is monitored and recorded at specified intervals. The ratio of the frictional/resistant force to the normal load at any instant is the coefficient of friction under the specified test conditions. As the tests proceeds, the contact surfaces may change due to the forces acting on them and this will bring change to the measured coefficient of friction. Therefore the coefficient of friction will not be constant during the test. In this research, the coefficient of friction was taken as the average in the first few minutes of testing. The testing was conducted on a CETR friction tester. The friction coefficient was measured between an HNBR101 flat sheet and a steel ball of diameter 6 mm.

3.2.6. FEA Validation Compression Test

This experiment was conducted on a MTS testing machine at a temperature of 100 °C on 6.99 mm HNBR101 O-rings. The O-rings were placed in a groove in the bottom plate of the O-ring housing shown in Figure 3.11.

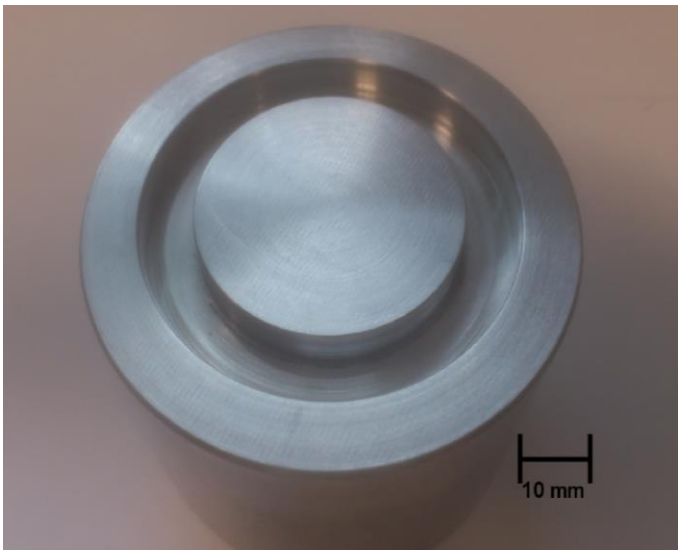

Figure 3.11 An O-ring housing bottom surface containing a 7.6 mm wide groove to fit in the O-ring.

The O-rings were subjected to a compression force at a rate of 30 mm/minute by the top plate shown in Figure 3.12. Force as a function of displacement was measured when the O-ring was subjected to compression force. The O-ring housing was designed based on the test rig used for testing O-rings subjected to rapid gas decompression according to the Norsok M-710 Rev.2 standards. Before testing, the O-rings were subjected to a temperature of 100 °C for more than 10 minutes and before testing began, the O-ring housing made of mild steel was subjected to a temperature for up to an hour.

The aim of this experiment was to validate the FEA model by comparing the evolution of force with displacement. Note that the resultant force is calculated as the average force from all five O-ring samples tested. To remove any stress softening, the O-rings were subjected to three successive compression cycles. However after analysing the force displacement graphs for three consecutive cycles, it was observed there was no significant stress softening or loss of stiffness under compression.

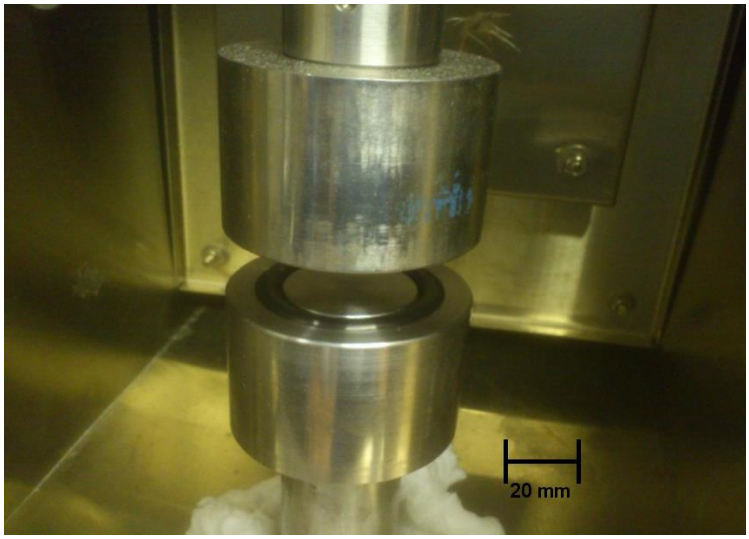

Figure 3.12 O-ring housing with O-ring inserted in the bottom groove.

3.3. Hybrid O-rings

3.3.1. Tearing Strength

Tearing tests were conducted on crescent tear samples containing a second phase material at different locations. The aim was to investigate how the geometry and location of the second phase material affected the samples static fracture resistance. The crescent tear samples used are shown in Figure 3.13 and the hybrid tear samples

analysed comprised of two materials, HNBR101 and LRCM888. Tear tests were conducted according to the BS ISO 34-2 (2011) standard and three samples were tested for each experiment. This test method measures the force per unit thickness required to initiate or propagate a tear through a sheet of rubber. A tearing strain is applied to a test specimen by means of a tensile testing machine at a constant rate of crosshead traverse until the specimen fails.

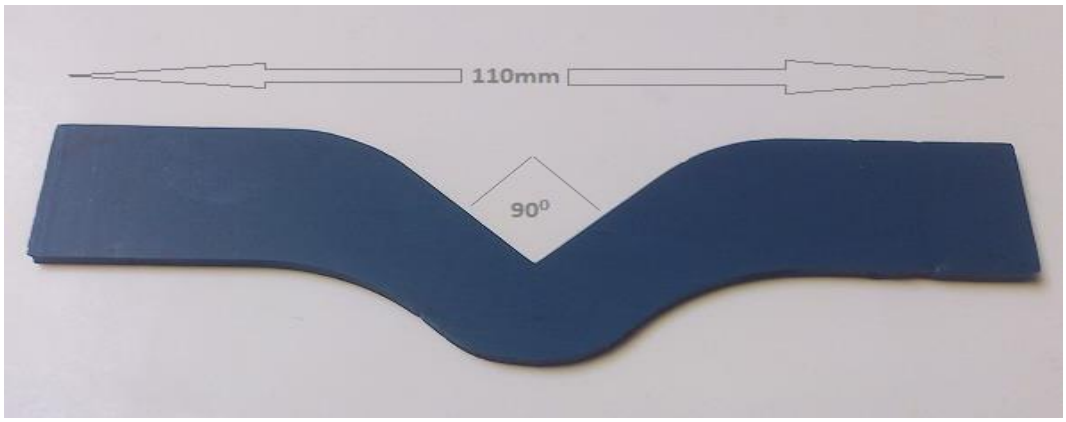

Figure 3.13 Geometry of the test specimen used for tear tests.

Since the operating temperature of O-rings in service is 100 ^{o}C, the tear tests were conducted at the same temperature. Hybrid samples were prepared by moulding a test sheet of HNBR 101 and inserting sections of LRCM888 at specific locations to produce a hybrid tear sample test sheet, as shown in Figure 3.14.

Figure 3.14 A hybrid tear sample test sheet before and after being cured for 12 minutes at 170 ^{O}C.

The main reason for curing the two materials together was to strengthen the bond between the two materials. Traditionally HNBR101 is post-cured for 6 hours at 180 °C to improve the material's properties. Note that 6 hours at 180 °C is the time and temperature used by industrial sponsor James Walker & Co. Ltd to post cure HNBR101. However, post-curing LRCM888 for 6 hours at 180 °C will reduce the material's fracture toughness qualities. To maintain HNBR101 properties and LRCM888 fracture toughness qualities, the hybrid samples were post cured at 150 °C for 3 hours and 45 minutes. Table 3.4 compares different properties of the conventionally post cured HNBR101 and HNBR101 post cured for 3 hours 45 minutes at 150 °C.

Table 3.4 Material properties of HNBR101 and LRCM888 post cured in different conditions.

	Tensile Strength (MPa)	**Maximum Elongation %**	**Compression Set %**	**Hardness, IRHD**
HNBR101 (Post cure 6 hours at 180 °C)	32.9	160	15.5	92
HNBR101 *(*Post cure 3 hours 45 minutes at 150 °C)	33.2	247	25	90
LRCM888 (No post cure)	13.2	653	N/A	N/A
LRCM888 (Post cure 3 hours 45 minutes at 150 °C)	14.4	385	N/A	N/A
Limits	27 minimum	150 minimum	25 maximum	90±5

Post curing HNBR101 at 150 °C for 3 hours 45 minutes improved the rubbers tensile strength and maximum elongation but reduced the elastomers compression set and hardness properties. However the compression set and hardness values were still within the accepted limits. The limits were obtained from industrial sponsor James Walker & Co. Ltd, and the limits presented in Table 3.4 are used for elastomeric seals exposed to RGD conditions. Post curing LRCM888 resulted in the reduction of the maximum elongation however the tensile strength slightly increased. The tensile strength and maximum elongation were determined according to the ISO D-412 standards at room

temperature using dumbbell specimens described in Section 3.2.2.1. Compression set and hardness were determined by industrial sponsor.

Figure 3.15 shows a hybrid tear sample with a horizontal strip located below the crack initiation region. The aim of this hybrid configuration was to investigate the effect of LRCM888 on crack propagation behaviour, especially in arresting crack propagation. Figure 3.16 shows a hybrid tear sample with the LRCM888 material located in the crack initiation region. The aim of this hybrid configuration was to investigate the effect of LRCM888 material on crack initiation. The results from the different configurations will be compared to the control experiment, which is a plain HNBR101 tear sample with no reinforcing layer.

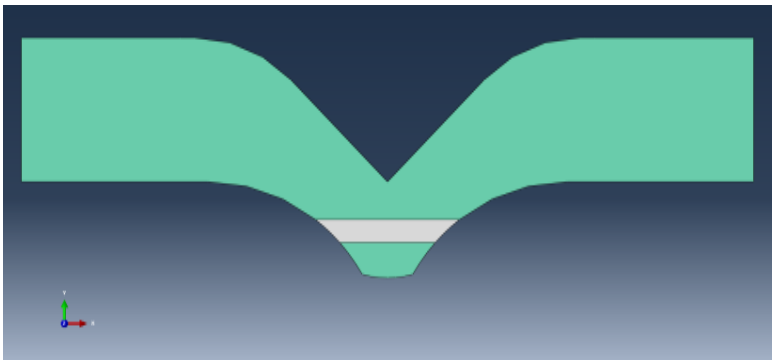

Figure 3.15 A hybrid_3 with horizontal energy absorbing strip below initiation point.

Figure 3.16 A hybrid_4 with energy absorbing layer located at the point of crack initiation.

3.3.1. Fatigue Tests

The results from the tearing strength tests can only investigate the performance of the LRCM888 layer under static loading conditions only. However, since elastomeric seals in operation are exposed to dynamic loading, it was important to understand how the LRCM888 layer would perform under dynamic loading. This investigation was

performed by conducting uni-axial fatigue tests to analyse how the addition of a second phase material affected the dynamic behaviour of the hybrid structure. The fatigue experiments were conducted on a MTS testing machine according to the ASTM D430 standards at 100 °C. To reduce self-heating effects, the experiments were conducted at 1Hz. The fatigue experiments were displacement controlled with an initial pre-strain condition of 16 %. Each sample was fatigued between 16 % minimum and 50 % maximum strain up to failure. The cyclic loading was based upon a sine wave function. Force and displacement data were given out as output as a function of time.

Figure 3.17 shows the fatigue samples test sheet before being cured for 12 minutes at 170 °C. The test sheet was then post-cured for 3 hours 45 minutes at 150 °C. Hybrid fatigue samples were then cut out of the test sheet using a specialised die cutter. Figure 3.18 shows the control sample containing no second phase material. Figure 3.19 shows a hybrid fatigue sample containing a second phase layer located below the crack initiation point. The aim of this configuration was to investigate the effect of the LRCM888 layer on crack propagation under dynamic loading. Figure 3.20 shows a hybrid fatigue sample with a second phase material located at the point of crack initiation. The aim of this configuration was to understand the effect of the LRCM888 layer on crack initiation when the hybrid structure is subjected to dynamic loading. Figure 3.21 shows a hybrid 3 fatigue sample with the second phase material located in the region of high stress concentration. Results from the fatigue tests will be used to understand how the addition of a second phase material affects the dynamic behaviour of the structure. Three samples were tested during each experiment and the average was calculated.

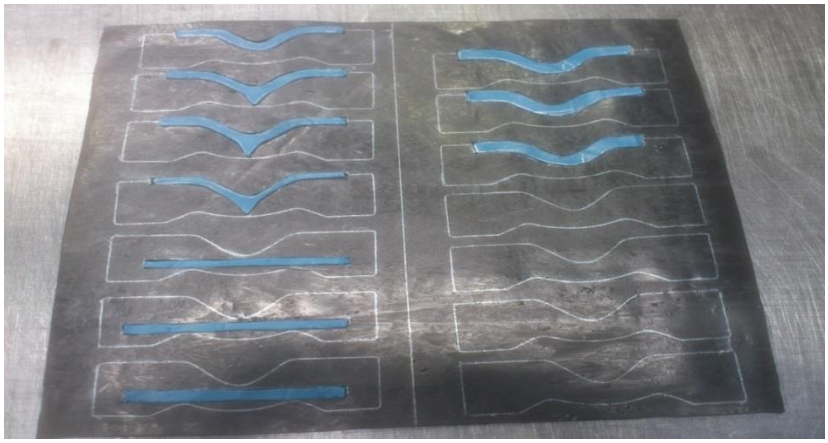

Figure 3.17 Hybrid fatigue samples test sheet before being cured for 12 minutes at 170 ˚C.

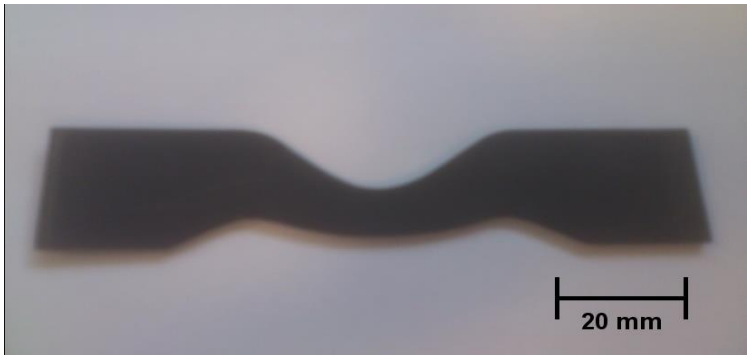

Figure 3.18 A control fatigue sample with no second phase material (HNBR101 only).

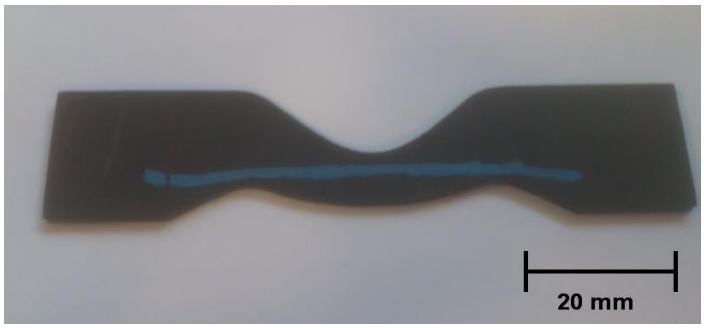

Figure 3.19 Hybrid fatigue sample 1 with a second phase material located below the initiation point.

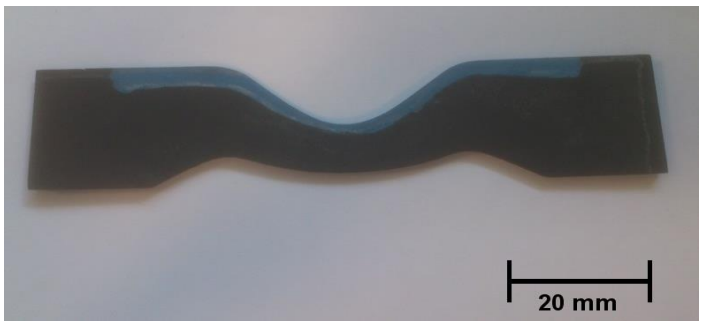

Figure 3.20 Hybrid fatigue sample 2 with a second phase layer located at the point of high stress concentration during loading.

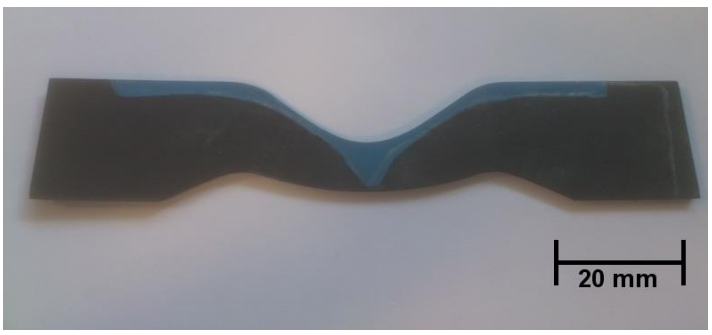

Figure 3.21 Hybrid fatigue sample 3 with a second phase material located in the region of high stress concentration.

These fatigue tests will also investigate how the thickness of the second phase material affects the performance of a rubber component. Figure 3.22 shows different fatigue samples with varying thicknesses of the second phase material.

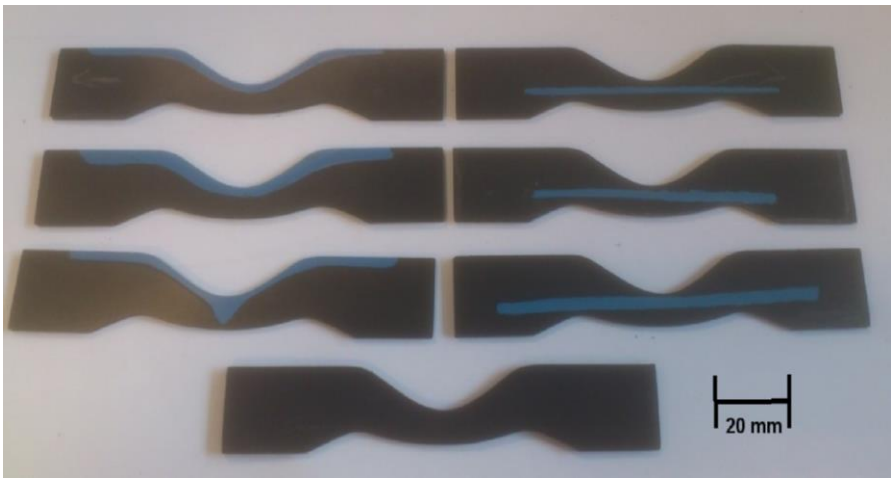

Figure 3.22 A collection of hybrid fatigue samples with varying thicknesses of the second phase material layer.

Uni-axial fatigue tests were conducted on a MTS testing machine according to the ASTM D430 standards at 100 ^{o}C and to reduce self-heating effects, the experiments were conducted at a frequency of 1 Hz. The fatigue experiments were displacement controlled with an initial pre-strain condition of 16 %. Each sample was fatigued between 16 % minimum and 50 % maximum strain up to failure. The cyclic loading was based upon a sine wave function.

3.3.2. FEA Hybrid O-rings

Before making hybrid O-rings, it was essential to analyse how the addition of a second phase material affected the stress and strain distribution in the O-rings. The analysis was conducted using FEA software provided by Abaqus. The setup of the FEA analysis is similar to the set-up of the structural model discussed later in Section 4.1. The only difference is that, the O-ring in this section contains an insert of a LRCM888 layer to make a hybrid O-ring structure. The hybrid O-ring's analysed are shown in Figure 3.23 to Figure 3.26.

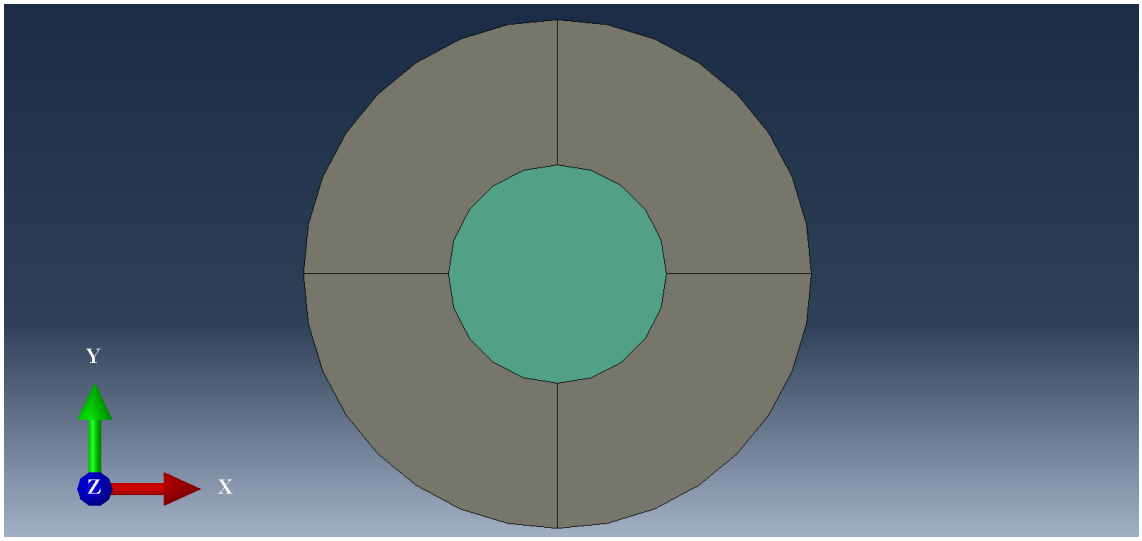

Figure 3.23 FEA model of hybrid_1 O-ring with a circular second phase material located in the centre region of the O-ring.

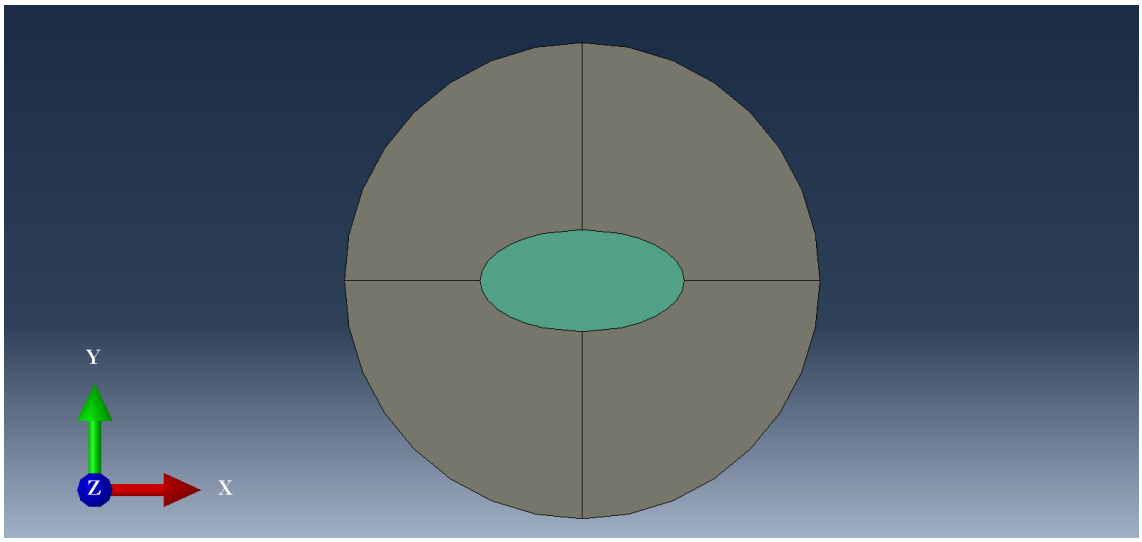

Figure 3.24 FEA model of hybrid _2 O-ring with a horizontal oval second phase material located in the centre region of the O-ring.

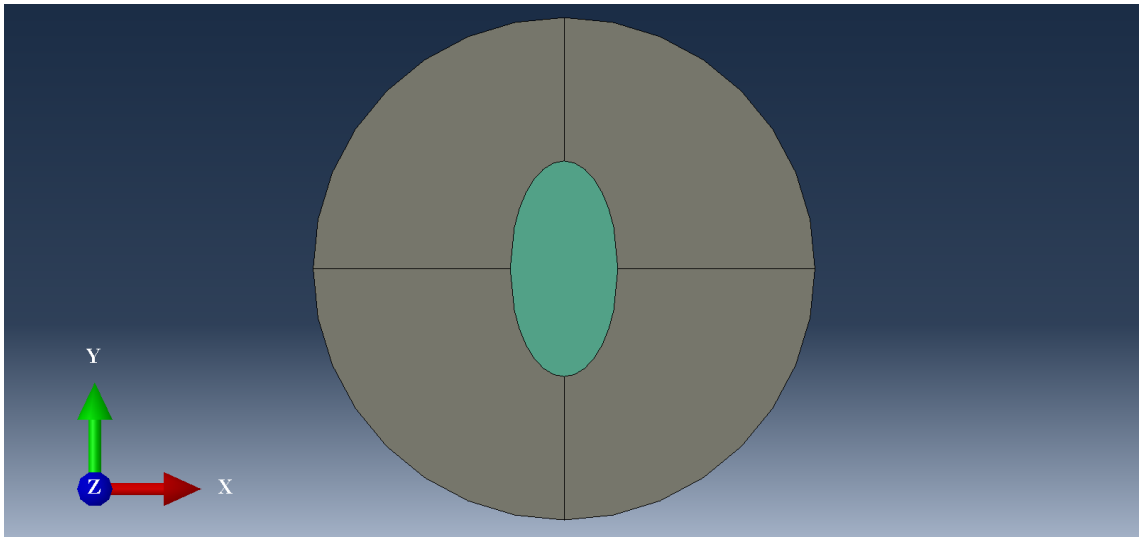

Figure 3.25 FEA model of hybrid _3 O-ring with a vertical oval second phase material located in the centre region of the O-ring.

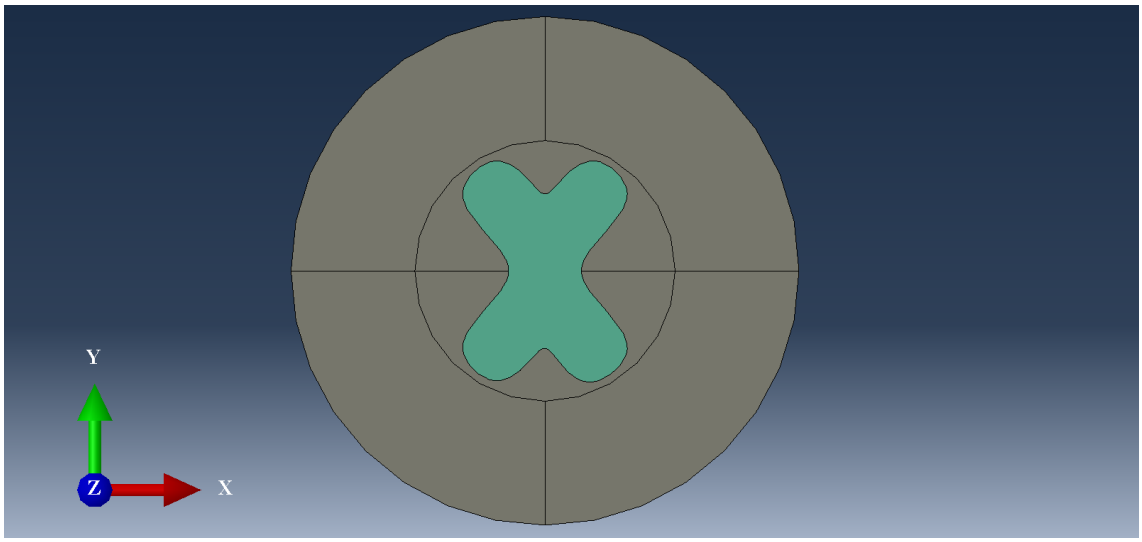

Figure 3.26 FEA model of hybrid _4 O-ring with an X-shape second phase material located in the centre region of the O-ring.

These configurations were designed based on the results from the fractography analysis, tearing strength tests and results from the numerical FEA model used for analysing RGD in elastomer O-rings. The reasons for choosing each of these hybrid configurations are explained in more detail in Section 8.3. The different hybrid O-rings were be compared to the control O-ring containing no second phase inserts. This is done to evaluate whether the addition of the second phase layer improved the O-ring's performance before constructing the actual hybrid O-rings.

3.3.3. Hybrid O-rings

At present there is no conventional technique for manufacturing hybrid O-rings. 6.99 mm hybrid O-rings were manufactured by extruding two different elastomer structures and combining them to form hybrid O-rings. The four hybrid O-rings shown in Figure 3.23 to Figure 3.26 were created by extruding LRCM888 through the extrusion dies displayed in Figure 3.27. The oval shaped die was used to make both the vertical and horizontal oval LRCM888 insert. The X-shape configuration shown in Figure 3.26 was too complicated to manufacture, therefore it was neglected.

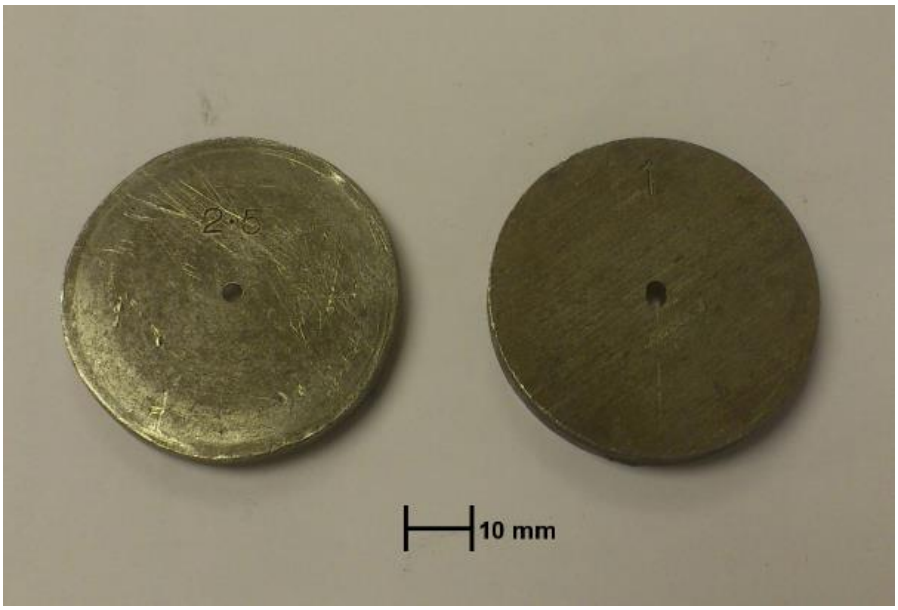

Figure 3.27 Display of extrusion dies used for manufacturing the three hybrid O-rings, the oval shaped die was used to make both the vertical and horizontal oval LRCM insert.

After extruding the three LRCM888 inserts, the HNBR101 component was extruded using a die with a circular diameter of 7.2 mm. The HNBR101 extrusion was cut into several lengths which, were then cut in half as shown in Figure 3.28. A circular or oval section was carved out of the HNBR101 section and the LRCM888 extrusion was fitted into the carved out section as shown in Figure 3.28.

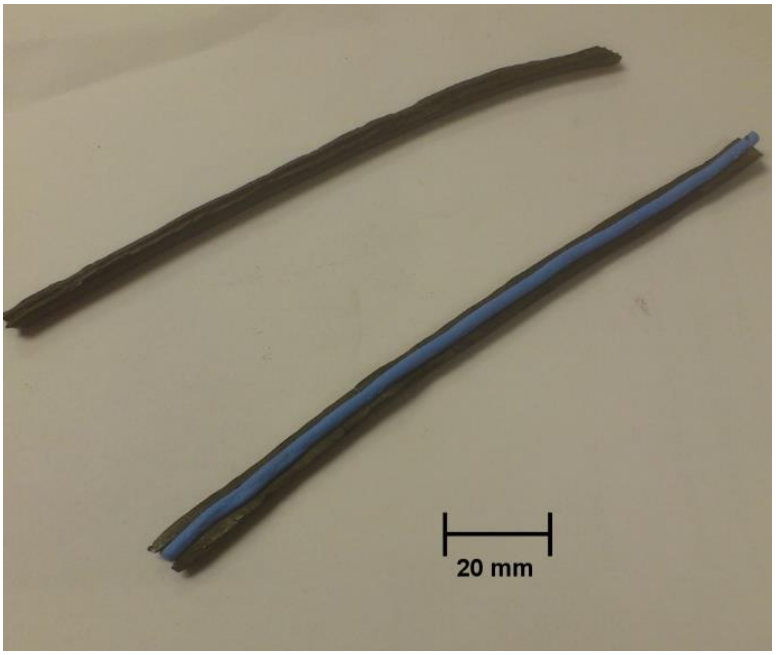

Figure 3.28 Line strips of hybrid O-rings before they were compression cured to form hybrid O-rings.

The hybrid O-rings were then cured under compression at 180 °C for 6 minutes using a compression mould under pressure. Note that the hybrid O-rings were cured using the same conditions used to cure conventional HNBR101 O-rings by industrial sponsor James Walker & Co. Ltd. Figure 3.29 shows the bottom half of a hybrid O-ring with a circular insert in the centre before curing the hybrid O-ring.

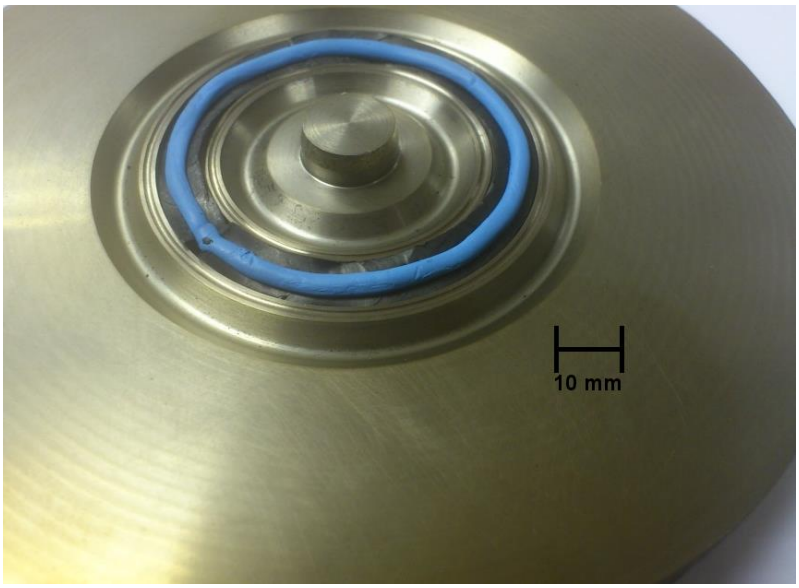

Figure 3.29 Bottom half of a hybrid O-ring with a circular insert in the centre contained in a compression mould before being cured for 6 minutes at 180 °C.

The problem with the first manufacturing technique discussed so far, is that during the curing process there is a high possibility that the second phase material could flow and lose its profile. To avoid this phenomenon, the compression mould was packed with a high quantity of HNBR101 material to make sure that LRCM888 will not find any room to flow thereby keeping its profile.

Another technique was also proposed to stop the second phase material from losing its profile shape. The second technique was similar to the first technique for manufacturing two phase hybrid O-rings, except that the LRCM888 insert was initially pre-cured. The reason for pre-curing LRCM888 was to make sure that when LRCM888 cured together with HNBR101 the material will not flow and lose its profile. The LRCM888 inserts were pre-cured using a compression mould under pressure similar to the one shown in Figure 3.29.

4. Numerical Model Methods and Procedure

The numerical model was broken down into three parts:

i. structural model which was used to evaluate the interaction between the O-ring and the housing gland surfaces;
ii. mass diffusion model which was used to analyse gas diffusing in and out of the O-ring; and
iii. Coupled Structural-Mass Diffusion model which was used to evaluate the structural deformation of the O-ring due to RGD.

4.1. Structural model

The structural model was used to analyse the interaction between the O-ring and its housing gland surfaces. The structural model was validated using results from the compression tests. The deformed O-ring from the structural model analysis will later be used in the mass diffusion analysis as the input geometry. This section discusses the setup of the structural model. The structural model in this section only investigates the compression of the O-ring by its housing gland surfaces. The deformation of the O-ring structure due to the expanding absorbed gas is described in Section 4.3.

4.1.1. Geometry and Boundary Conditions

The geometry of the O-ring housing was modelled based on the RGD test rig which was designed to subject O-rings to RGD conditions according to the Norsok M-710 Rev.2 standard. The O-ring was analysed as a full 3D model, this model was then used to validate the quarter model which was designed to save computing time. The full 3D model is shown in Figure 4.1, only three quarters of the 3D model is shown for easier visualisation.

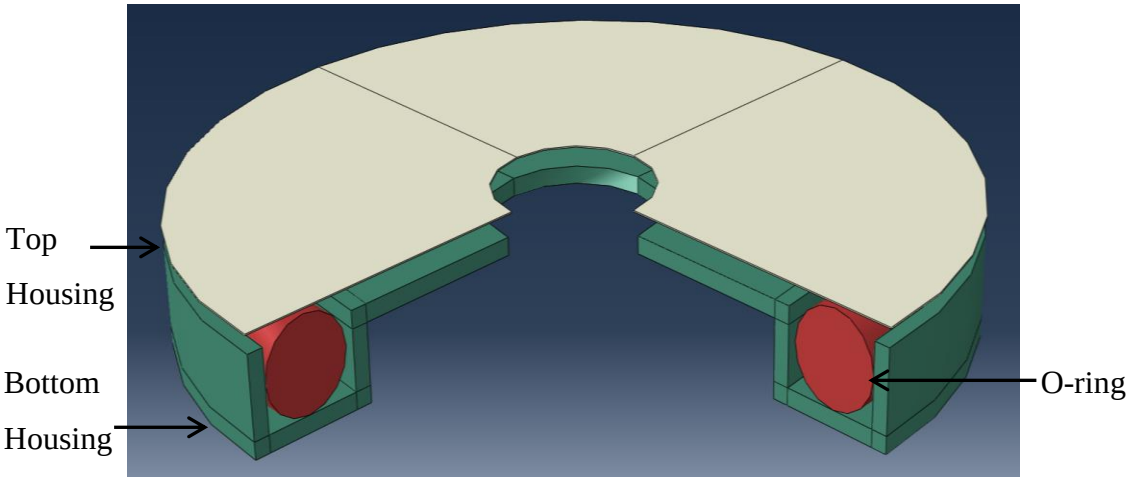

Figure 4.1 A 3D model of an O-ring contained in its housing gland surfaces.

Appropriate boundary conditions were applied to the quarter model shown in Figure 4.2. In the RGD experiments, the O-rings have a larger diameter than the bottom O-ring housing. When the O-rings are fitted into the housing they are in a pre-stressed state before they are compressed by the top housing. To achieve a similar pre-stressed state for O-rings in the FEA analysis, the bottom O-ring housing was designed with a larger diameter than usual. After the O-ring was fitted into the bottom housing, the housing contracted by a specific distance, thereby creating a pre-stress state in the FEA O-rings similar to the experiments.

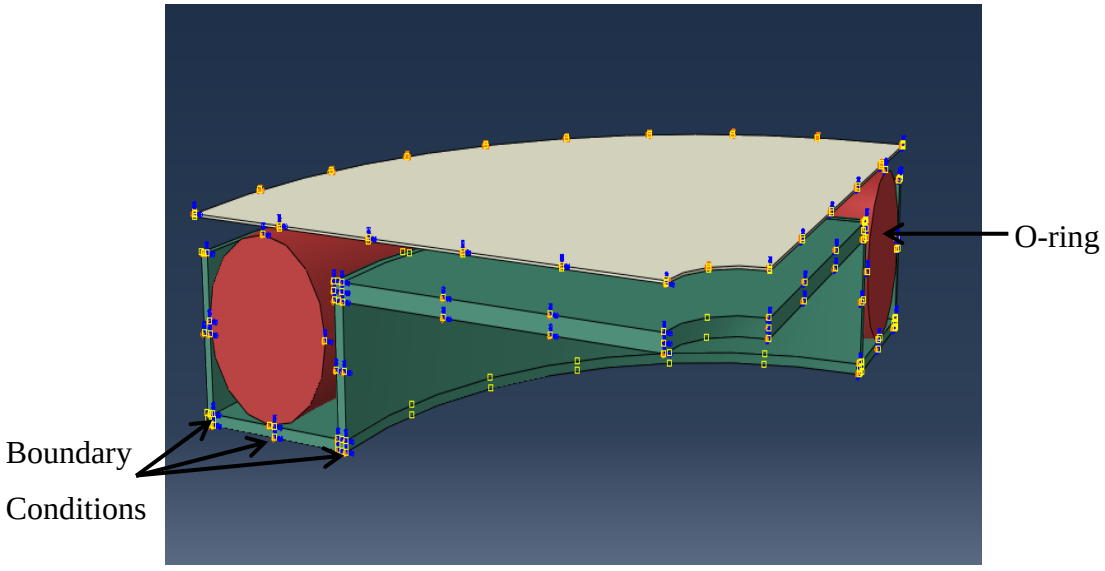

Figure 4.2 3D Quarter model of an O-ring contained in its housing gland surfaces with appropriate boundary conditions.

After preloading the O-ring, the temperature for both the O-ring and its housing gland surfaces was raised and kept constant at 100 °C. The O-ring was then subjected to a 14

% compression by the top housing. The structural model was also modelled as an axisymmetric model shown in Figure 4.3. The initial preloading condition could not be achieved in the axisymmetric model. This is because the axisymmetric model could not be constrained to stop the O-ring from shifting position when subjected to thermal loading. However after comparing results from the axisymmetric model to the 3D models, the difference was small.

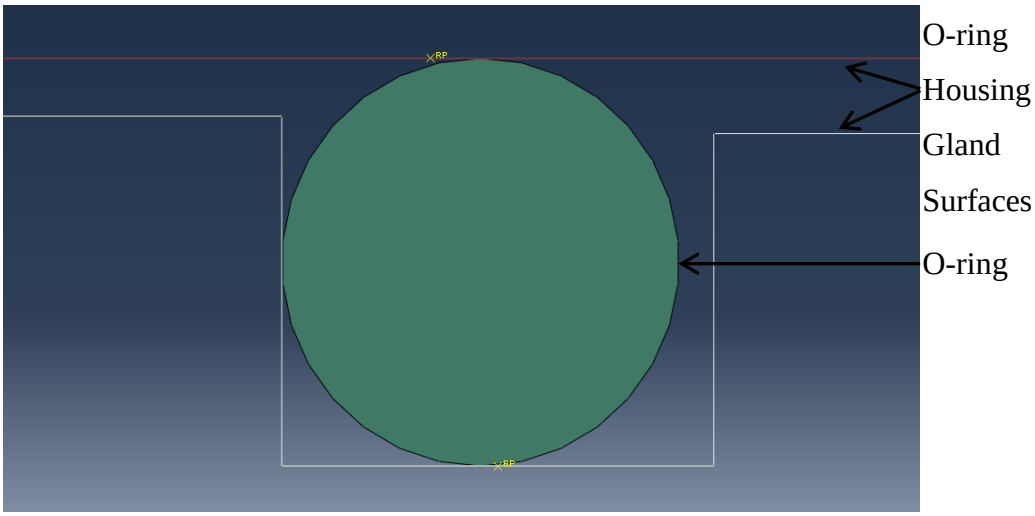

Figure 4.3 Axisymmetric model of an O-ring contained in its housing gland surfaces with appropriate boundary conditions.

The coefficient of friction from the friction tests was found to be 0.37 and the results are shown in Appendix E. The coefficient of friction value was used to define the contact properties between the elastomer O-ring and it housing gland surfaces.

4.1.2. Material Model

A material model describes the behaviour of a material and in this case the material model will define the behaviour of the O-ring and the housing gland surfaces. A material model can be defined by specifying the properties of the material. For instance, the housing gland surfaces in the test rig are made of mild steel, therefore in the FEA model they are defined by specifying their elastic properties such as the Young's modulus and the Poisson's ratio shown in Table 4.1

Table 4.1 Physical properties of mild steel used to define the material model in FEA (Raghavan, 1998).

	Density kg/m^3	**Thermal Expansion K^{-1}**	**Young's Modulus MPa**	**Poisson's Ratio**
Mild Steel	7860	1.17e-5	21000	0.3

Also since the analysis involved thermal expansion, the thermal expansion of mild steel had to be specified in the material model. The density of the housing surfaces can be included in the model, to take into account the mass of the housing. When the housing gland surfaces were modelled as rigid surfaces, there was no need to define a material model since rigid surfaces do not deform but can undergo rigid body motions.

4.1.2.1. Hyperelastic Model

Unlike metals which exhibit a linear stress-strain behaviour, elastomers stress-strain behaviour is quite complex. This is because their stress-strain behaviour is highly nonlinear and they need to be modelled as nonlinear hyperelastic materials. When using the hyperelasticity theory, stress is not directly calculated from the corresponding strain, which is the case with linear elastic materials. Instead, stress is evaluated from the principle of virtual work using the stored strain energy potential function. In FEA, the mechanical response of a hyperelastic material is described in terms of a strain energy potential, U (ε), which describes the strain energy stored in the material per unit volume as a function of strain at that point in the material. Therefore the hyperelastic model in this thesis was calibrated using stress-strain data form uni-axial, pure-shear and equibiaxial tests. The least squares procedure provided in Abaqus was then used to obtain the coefficients of the strain energy potential model.

4.1.3. Mesh Analysis

It is important to choose the appropriate meshing technique and element type when performing FEA. Poor choice of the meshing technique or element type can result in an inaccurate solution. The two 3D models were meshed using quadratic Hex elements, shown in Figure 4.4. Hex elements provide a more uniform mesh distribution with elements with an appropriate aspect ratio. An inappropriate element aspect ratio can lead to element distortion during the analysis and this can lead to inaccurate results.

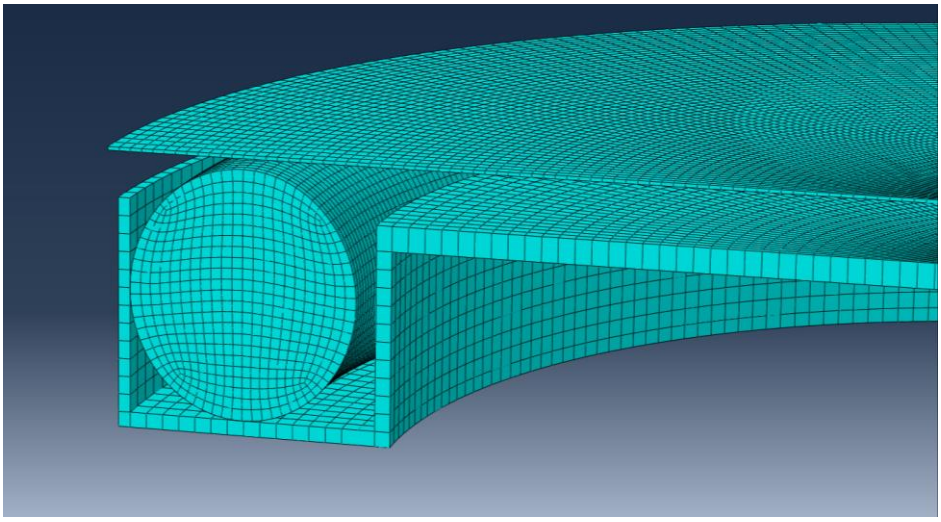

Figure 4.4 3D Quarter model of a meshed O-ring contained in its housing gland surfaces; the full 3D model was meshed using a similar structured technique.

The housing gland surfaces were modelled using 8-node linear brick, reduced integration with hourglass control (C3D8R) stress elements. Reduced integration was used to save computational resources and quadratic elements were used improve the accuracy of the model especially in high stress concentration regions and contact regions. When the initial contraction of the housing gland surfaces was ignored, the surfaces were modelled using rigid elements and this saved computational time. The axisymmetric O-ring was modelled using both structured quad elements and mapped quad elements shown in Figure 4.5. A structured mesh technique produces a uniform mesh pattern and a mapped mesh is used when a structured mesh quality cannot be achieved. A mapped mesh technique produces a randomly distributed mesh pattern. This meshing technique was chosen because it provided less distorted elements after the O-ring was deformed. It was important to maintain a non-distorted mesh after compressing the O-ring because the deformed O-ring was imported into the mass diffusion analysis as the input geometry and mesh.

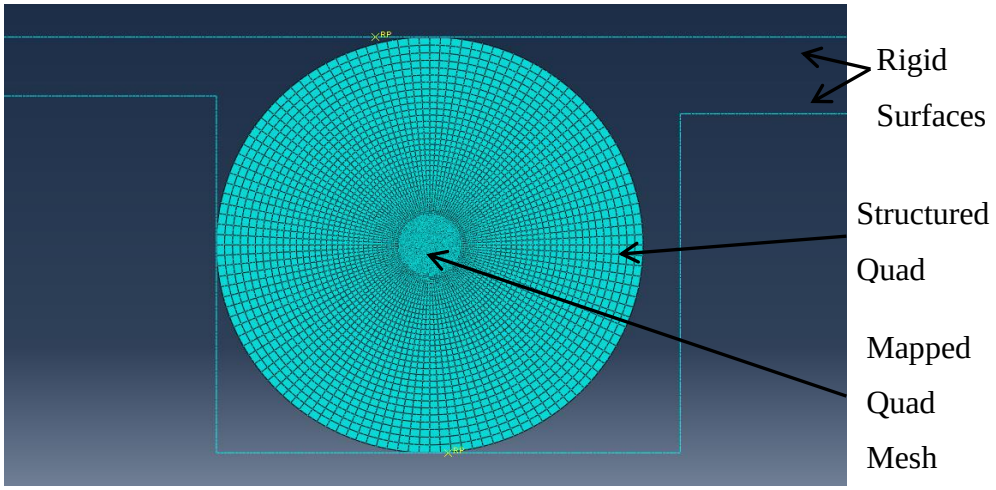

Figure 4.5 Mesh of an axisymmetric model of an O-ring contained in its housing gland surfaces.

A mesh analysis was performed for all the models. In the mesh analysis, the mesh density of the model was gradually increased and the strain energy density was measured. The reason for the mesh analysis was to evaluate the optimum mesh density that will give the most accurate solution without wasting computational resources. Figure 4.6 shows a plot of a mesh analysis conducted on the axisymmetric model. The number of elements in the model was increased until the maximum ESEDEN value converged as shown in the graph. ESEDEN is the total elastic strain energy density in an element. It was chosen in this thesis because one of the objectives of the FEA model is to analyse how the addition of a second phase material affects the strain energy density distribution. Figure 4.7 shows a plot of a mesh analysis conducted on the axisymmetric model. The contact pressure (CPRESS) between the O-ring and the housing gland surfaces was measured as a function of number of elements. CPRESS was chosen because the model will be used to investigate how the addition of a second phase material affects the sealing capabilities of an O-ring over time. Both plots show that the results begin to converge as the number of elements in the O-ring approaches 4000.

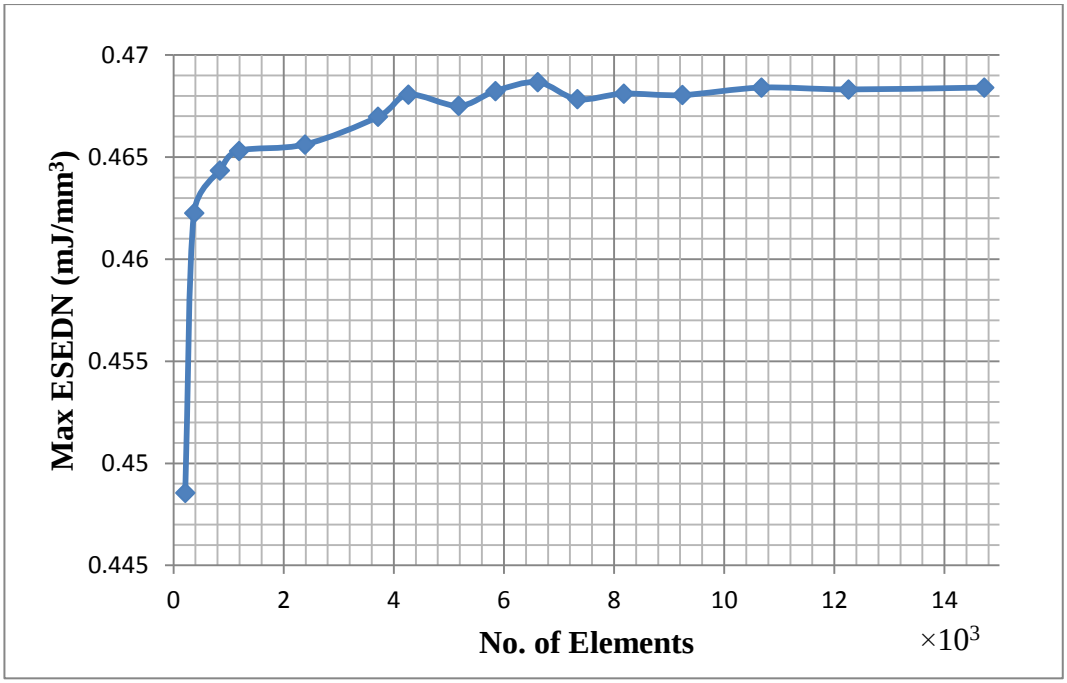

Figure 4.6 Mesh analysis conducted for the axisymmetric model, ESEDEN is the total elastic strain energy density in an element.

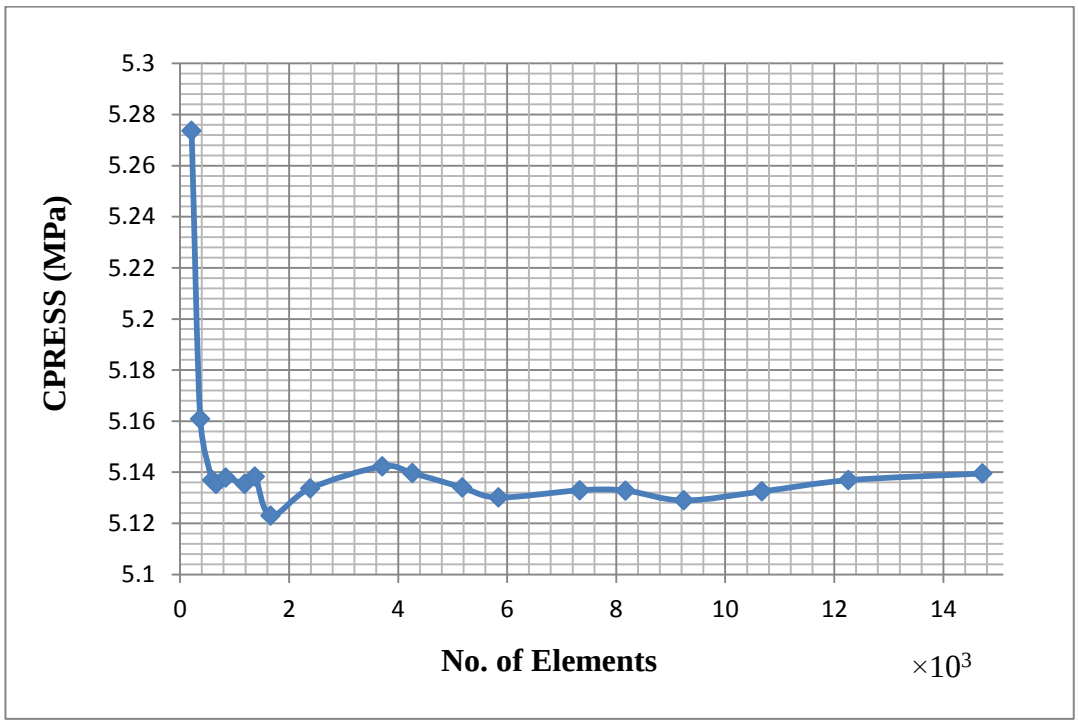

Figure 4.7 Mesh analysis conducted for the axisymmetric model, CPRESS is the contact pressure between the O-ring and the O-ring housing gland surfaces.

4.2. Mass Diffusion Model

The mass diffusion model was designed based on the Norsok M-710 RGD test regime, however since damage is known to occur during the decompression stage, the mass diffusion model only focused on the decompression stage. This stage is modelled in two steps:

i. The first step is a steady-state step which allows gas to diffuse into the O-ring until full saturation.
ii. The second step is a transient step which models the diffusion of gas out of the O-ring during the decompression cycle, as a function of time.

During the transient step, the external pressure is reduced from 8 MPa to 0 MPa at a rate of 2 MPa, 4 MPa and 8 MPa per minute and subsequently the O-ring is allowed to rest for 1 hour. The mass concentration values in each element during the transient step are written to an external file using a user subroutine. The subroutine is discussed in more detail in Section 4.3.

The exported file is used in the coupled structural-diffusion analysis to evaluate the pressure exerted onto each element's surfaces by the expanding diffusing gas. Figure 4.8 shows the cross-section of a deformed O-ring subjected to a compression force by the O-ring housing gland surfaces. Gas is assumed to diffuse in and out of the O-ring through one side of the O-ring shown by the red surface.

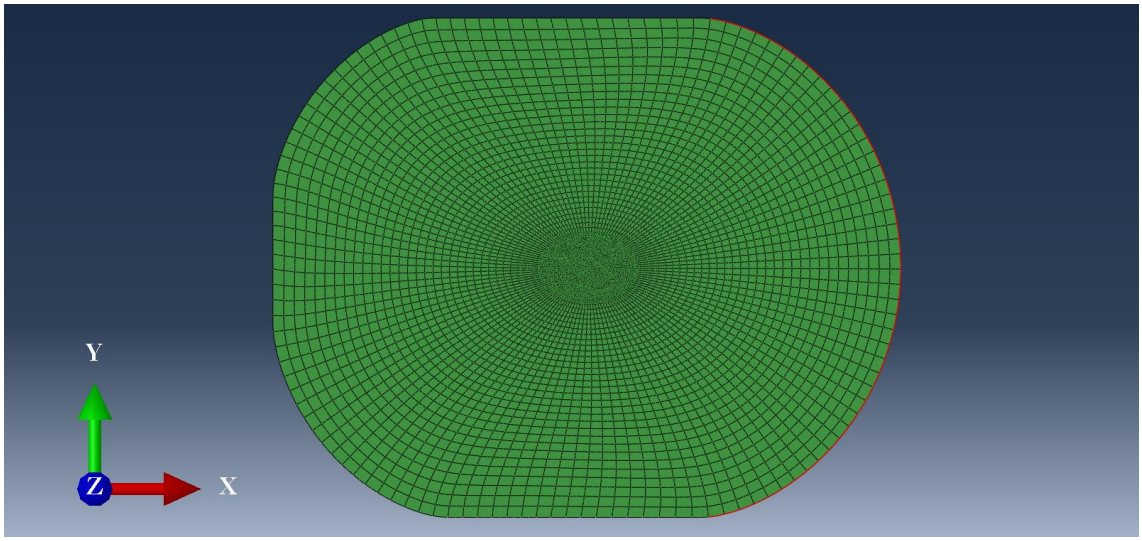

Figure 4.8 Display of a cross-sectional view of a deformed O-ring imported from the structural analysis into the mass diffusion analysis.

The mass diffusion model is solved using the FEA package from Abaqus 6.11-3. The diffusing gas is modelled using the governing equations for mass diffusion, which are an extension of Fick's law. These equations allow non-uniform solubility of the diffusing gas in the base material and for mass diffusion driven by gradients of pressure and temperature. The mass diffusion behaviour is taken into account using an extended Fick's law, (Crank, 1956):

$$\mathrm{J} = -\mathrm{D}\left(\frac{\partial \mathrm{c}}{\partial \mathrm{x}} + \mathrm{sk_p}\frac{\partial \mathrm{p}}{\partial \mathrm{x}}\right) \qquad [4.1]$$

where: J is the diffusion flux, *D* is the diffusion coefficient, *c* is the mass concentration of the diffusing material, *s* is solubility in the base material, and k_P is the pressure stress factor used to define stress-assisted diffusion.

4.2.1. Material Model

Assuming steady state diffusion, the time lag method by Daynes (1920) can be applied to evaluate the diffusion coefficient (D) and the solubility coefficient (S) from the permeation test at different temperature and pressure according to the BS ISO 2782 (2012) standard. The standard test involves separating the cavity of a test cell into a high-pressure and a low pressure side using a disc test piece and in this case a flat rubber sheet. The temperature in the cell is kept constant and for this thesis it was kept constant at 100 °C. The high pressure side is connected to a constant pressure gas

supply. As the gas permeates into the low pressure side, the volume change or pressure is measured on the low pressure side. The change in pressure on the lower side is plotted against time, and the permeability and diffusion coefficient are calculated from the data. A typical gas transmission curve is shown if Figure 4.9.

The gas permeability is calculated from (BS ISO 2782-1, 2012):

$$Q = GTR \times d \qquad [4.2]$$

where *Q i*s the gas permeability coefficient, *GTR* is the gas transmission rate and *d* is the thickness of the test piece (m).

The gas transmission rate is calculated from (BS ISO 2782-1, 2012):

$$GTR = \frac{T_0 \times (V_S - V_b) \times k}{0.0227 \times T \times A \times t \times p_h} \qquad [4.3]$$

where *T* is the test temperature, T_0 is the standard-state temperature in Kelvin, *t* is the time during which test gas was collected in the sampling loop, V_S is the amount of test gas collected in the sampling loop, p_h is the pressure on the high pressure side of the test cell, *A* is the gas transmission area and 0.0227 is the volume, in m^3, of 1 mol of gas at a pressure of 0.1 MPa.

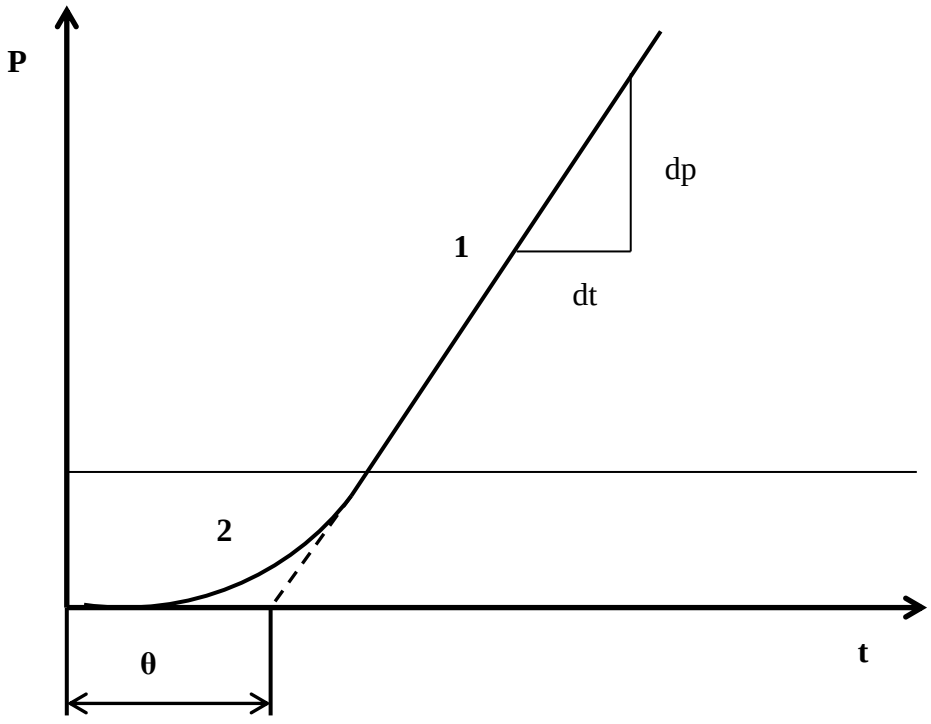

Figure 4.9 A typical Gas transmission curve for evaluating steady state permeation.

P is the Pressure, t is the time in seconds, 1 is the steady state region and 2 is the non-steady state region. The mass diffusion coefficient is calculated from (BS ISO 2782-1, 2012):

$$D = \frac{d^2}{6\theta} \quad [4.4]$$

where D is the gas diffusion coefficient, Θ is the delay time obtained from the gas transmission curve (s) and d is the thickness of the test piece.

The solubility coefficient is calculated from (BS ISO 2782-1, 2012):

$$Q = SD \quad [4.5]$$

where Q is the gas permeability coefficient, D is the mass diffusion coefficient and S is the solubility coefficient.

Table 4.2 The permeability test results measured by external company Smithers Rapra for Carbon Dioxide permeation into HNBR101 and LRCM888 using the method described in Section 4.2.1.

Pressure Bar	**Temperature (K)**	**D (mm^2/s)**	**S [$mol/(mm^3 \cdot Pa$]**	**Q [$mol \cdot m/(m^2 \cdot s \cdot Pa)$]**
1	23	1.081e-5	1.0473e-7	2.57e-17

The permeation data presented in Table 4.2 was measured at 1 bar and room temperature, and these values will be different if they were measured at RGD conditions. Therefore the time taken for gas to diffuse out of the O-ring during RGD from the numerical model will not be representative of the actual time taken by carbon dioxide to diffuse out of the O-ring. However the mass diffusion behaviour should be similar and also since the aim of this thesis is to present a new novel numerical technique for modelling coupled structural – mass diffusion, the permeation data will suffice.

4.3. Sequentially Coupled Structural Mass Diffusion Model

The Coupled Structural Diffusion model is solved as a sequentially coupled model:

i. Initially the O-ring is subjected to a compression force by the O-ring housing gland surfaces.

ii. The deformed O-ring is then imported into the mass diffusion model and used as input geometry in the mass diffusion analysis.

iii. The carbon dioxide distribution inside the O-ring during RGD evaluated by the mass diffusion model is exported to the structural model and used to set boundary conditions.

iv. The structural model is used to analyse the structural deformation of the O-ring due to the rapidly expanding gas.

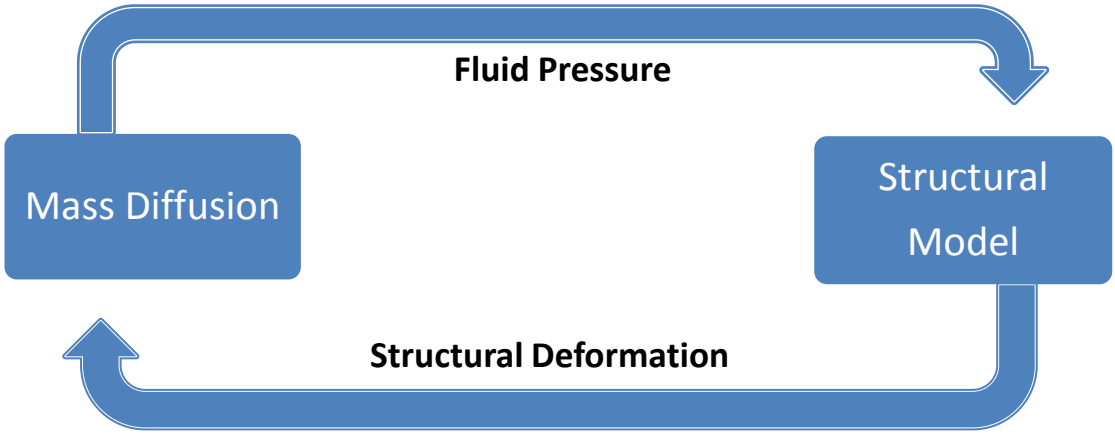

The coupling between the structural deformation of the O-ring and the mass diffusion is achieved by using user subroutines to evaluate the pressure exerted onto each element surface during the decompression period. A user subroutine imports data from the mass diffusion analysis and uses the data to evaluate the pressure exerted onto the internal surfaces of each element by the absorbed gas. During RGD testing, the temperature in the system is kept constant at 100 °C however as the absorbed gas expands due to external pressure drop, the local temperature is likely to change. For simplicity, the coupled structural-mass diffusion model assumes the temperature is constant for both gas and structure hence there is no temperature difference at the gas-structure interface.

As discussed in Section 2.2, there might be possible bubble formation in the elastomer material during the decompression process. The model proposed in this thesis focuses on the coupling between the absorbed expanding gas and the structural deformation of the O-ring and therefore the formation of bubbles will be neglected. However since the coupling process is a local process at different sections within the O-ring, it is possible to expand the model to include gas bubble formation and also the chemical interaction between the elastomer material and the diffusing gas.

4.3.1. Geometry and Boundary Conditions

The geometry conditions and material properties of the coupled structural mass diffusion model were similar to the structural model. Only the boundary conditions were updated by adding two extra steps in the structural model.

The coupled structural mass diffusion model was solved in four steps:

i. The first step allowed the O-ring to expand due to temperature rise, the housing surfaces were modelled as rigid surfaces hence they did not expand or contract due to temperature change.
ii. The second step was a compression step, in which the O-ring was compressed by its housing gland surfaces.
iii. The third step was the gas absorption step, in which gas permeate and diffuse into the O-ring until full saturation. Also in this step, the external compressive pressure acting on the O-ring is applied.
iv. The fourth step is the decompression step, in which a user subroutine is applied to evaluate the internal pressure exerted onto the internal structure of the O-ring as the absorbed gas diffuses out.

In the fourth step, the external pressure acting on the O-ring is reduced at different rates of 2 MPa, 4 MPa, and 8 MPa per minute. The coupled structural mass diffusion model assumes that pressure is the only significant force exerted onto the internal structure of the O-ring due to the diffusing gas. Pressure is applied onto each elements walls and the pressure is acting normal to the internal walls of each element as shown in Figure 4.10. Figure 4.11 shows a summation of the forces acting on an O-ring during the decompression process. These are the forces which will be modelled by the coupled structural mass diffusion model.

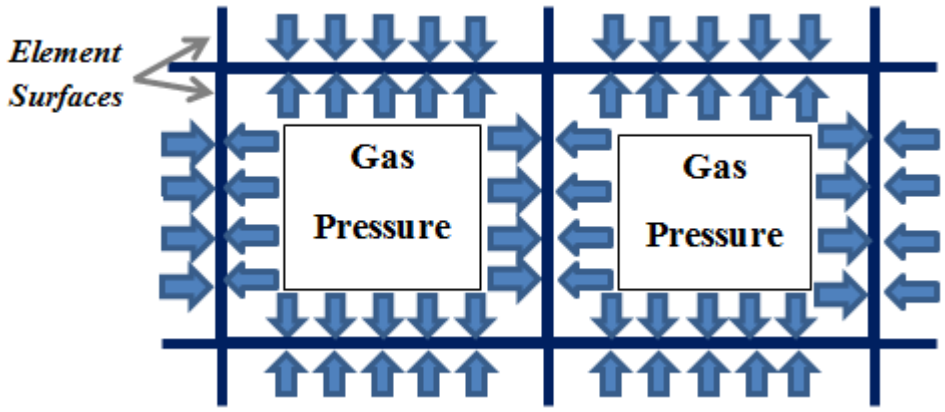

Figure 4.10 Two elements subjected to pressure from the absorbed gas.

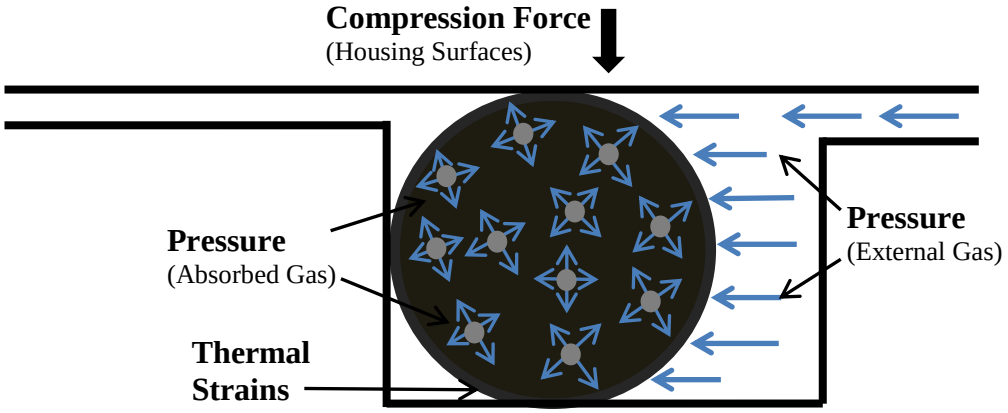

Figure 4.11An axisymmetric view of an O-ring in service under compression forces from the housing gland surfaces and the working fluid, and tensile forces from the absorbed gas.

4.3.2. URDFIL User Subroutine

The results from the mass diffusion analysis were imported into the structural model through the use of the subroutine URDFIL. This subroutine can be used to access the results file during the analysis, and in this case it was used to record the mass concentration values in each element as a function of time. The URDFIL is called at the end of each increment in which new information is written to the results file. After accessing the results file, another subroutine DBFILE has to be called to read the records from the results file and for this particular thesis the records read were the mass concentration values and the corresponding element number. The URDFIL can also be used to call another utility subroutine POSFIL to read the results file starting at a specified step and increment.

The URDFIL subroutine interface:

```
SUBROUTINE URDFIL (LSTOP, LOVRWRT, KSTEP, KINC, DTIME, TIME)
C
    INCLUDE 'ABA_PARAM.INC'
C
    DIMENSION ARRAY (513), JRRAY (NPRECD, 513), TIME (2)
    EQUIVALENCE (ARRAY (1), JRRAY (1, 1))
    User coding to read the results file

    RETURN
    END
```

LSTOP is a flag used to indicate whether an analysis should continue and LOVRWRT is a flag used to indicate results for the increment can be overwritten. DTIME is the time increment, NSTEP is the step containing file to be read and NINC is the increment number to start reading the results file.

The full user subroutine and comments are found in Appendix C. The mass concentration values in each element and the corresponding element number were written to an external file.

The results file was written in a format shown below:

Heading:	Increment Number	Time (s)
Data:	*Element Numbers*	*Concentration values (moles/mm^3)*

4.3.3. DLOAD User Subroutine

The pressure exerted onto each element surface was calculated and applied in the model through the use of a user subroutine Dload. This subroutine can be used to define the variation of the distributed load magnitude as a function of position, time and element number. The subroutine is called at each increment and is used to define the magnitude of load acting on an elements surface. In this thesis, the Dload was used to read the concentration values and the corresponding element number from an external file. The concentration values are then used to calculate the corresponding pressure in each element and this pressure is then applied onto the coupled structured-mass diffusion model. The pressure is entered as negative pressure so that the pressure from the

absorbed gas is pushing outwards, similar to pressurised gas in a bottle pushing on the bottle walls.

The Dload Subroutine interface consists of the following code:

```
SUBROUTINE DLOAD (F, KSTEP, KINC, TIME, NOEL, NPT, LAYER, KSPT,
    1 COORDS, JLTYP, SNAME)
C
    INCLUDE 'ABA_PARAM.INC'
C
    DIMENSION TIME (2), COORDS (3)
    CHARACTER*80 SNAME

    User coding to define F


    RETURN
    END
```

F is the magnitude of the load, KSTEP is the step number and KINC is the increment number. Time (1) is used to define the current value of step time and Time (2) is used to describe the current value of total time. NOEL is called into the user subroutine and defines the element number. JYTYP is the load type for which this call to DLOAD is being made. COORDS is an array containing the coordinates of the load integration points for each element and SNAME is the surface name for a surface based load.

The DLOAD subroutine utilises the Peng-Robinson equation of state to calculate the pressure in each element as a function of time during the decompression cycle. The full subroutine is contained in Appendix D.

The coding to define load in the Dload subroutine is structured as follows:

i. Initially the subroutine reads the external file containing the concentration values. The subroutine reads the concentration values as a function of the element number, increment number and step time.
ii. The second step is a series of commands instructing the subroutine to locate the step number in the analysis followed by locating the increment number in that particular step. The subroutine then locates each element in that particular step and increment number using the assigned element numbers. The subroutine then locates the surface on each element and the load integration point on each surface.

iii. The third step involves converting the concentration values into molar volume and evaluating the amount of pressure corresponding to each concentration value.

iv. The calculated pressure is then applied to the corresponding load integration point on each elements surface as a function of step time.

The subroutine was also programmed to output data to an external results file and the format of the results file is shown below:

Data: *Element Number* *Concentration* *Pressure* *Increment Number*

The output results file was used to verify the subroutine is performing as required.

5. RGD Fracture Analysis Results and Discussion

5.1. Scanning Electron Microscopy Results

O-rings and spring seals exposed to rapid gas decompression were analysed using SEM to identify the initiation points and the mode of crack propagation. This chapter discusses the results obtained from the SEM analysis.

5.1.1. O-rings

Three fractured O-rings were analysed using SEM analysis after they were exposed to RGD conditions explained in Section 3.1.1. The O-rings suffered from internal splits, which is one of the most common fractures in elastomeric seals reported by Rispin (1985). The splits were oriented longitudinal to the seal axis. Figure 5.1 shows the location of three sections in fractured O-rings containing crack initiation and crack propagation regions.

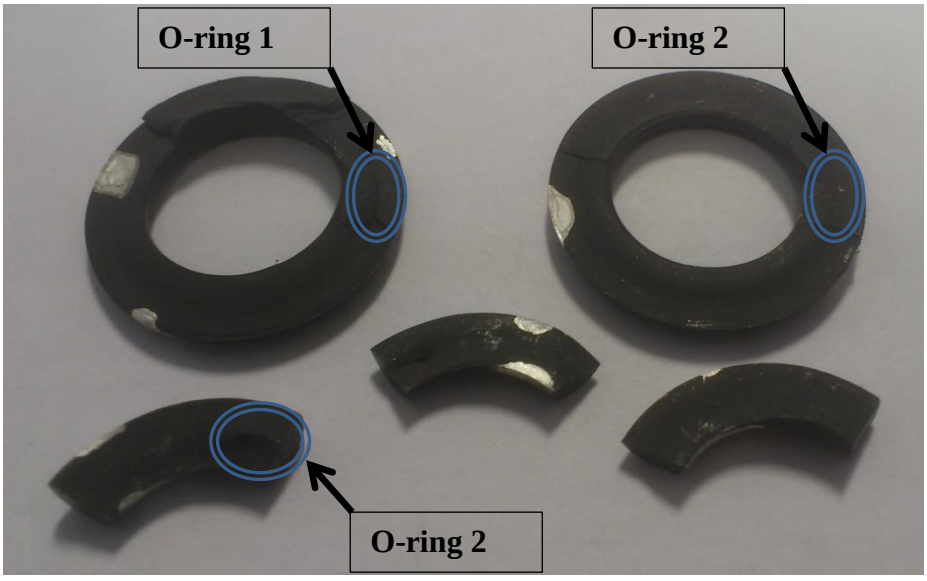

Figure 5.1 Fractured O-ring specimens showing the location of three sections containing crack initiation and crack propagation regions.

5.1.1.1. O-ring 1

Figure 5.2 shows the SEM image for the fracture surface region highlighted in Figure 5.1 O-ring 1. Figure 5.2 displays three different distinct regions of the fracture surface, regions A, B and C. Regions A and B are characterised by many small tearing lines

obstructing one another and the fracture surface is microscopically rough. Regions A and B are associated with slow crack propagation and usually contain the initiation zone. A microscopically rough region was described by Mathew and De (1983a) and Kurian (1989) as the region where failure initiates and propagates in slow increments during each cycle of deformation. Region C displays a macroscopically smooth region with no visible gross plastic deformation. These regions are normally associated with rapid crack propagation. Cracks initiated in regions A and B and propagated in slow increments. When the crack reached a critical size, the crack became unstable and grew at a faster rate leading to a catastrophic brittle fracture displayed by region marked C. The crack propagation direction can typically be identified from the direction in which riverlines converge, as described by Greenhalgh (2009).

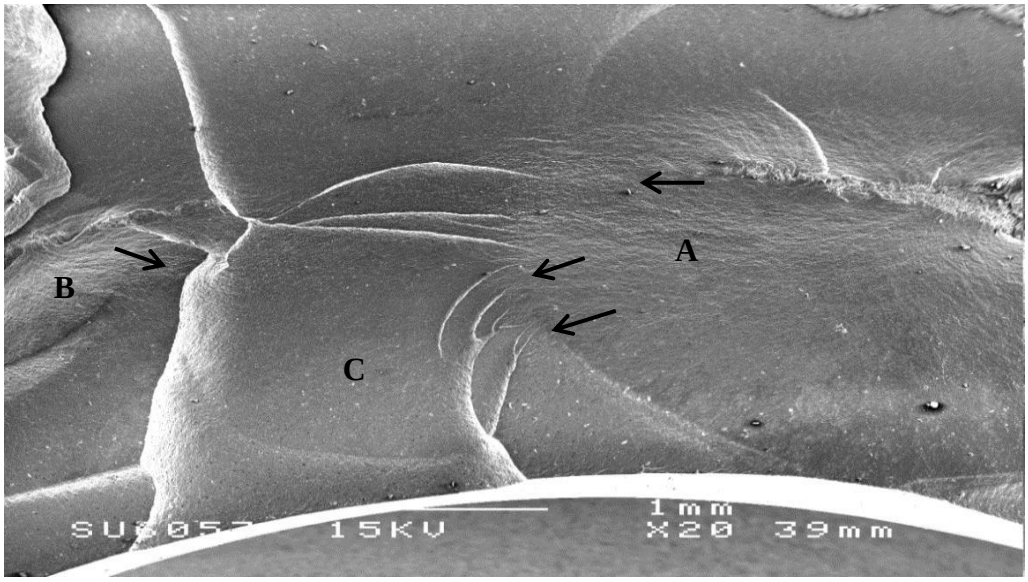

Figure 5.2 SEM image showing fractured surface of O-ring tested in 90 % CO_2 in methane, crack direction propagation was derived from the convergence direction of the riverlines.

Figure 5.3 displays the mirror, mist and hackle areas in region A and the crack direction is indicated by the direction in which the riverlines converge to form hackles. The mirror region is associated with slow crack propagation, and the boundary of the mirror region marks the transition of crack speed from a slow and stable speed to rapid acceleration. Hackle lines are formed as a result of smaller cracks branching into one crack. Hackle regions tend to appear in regions where the stress field is changing rapidly or when the stress state changes from tension to compression.

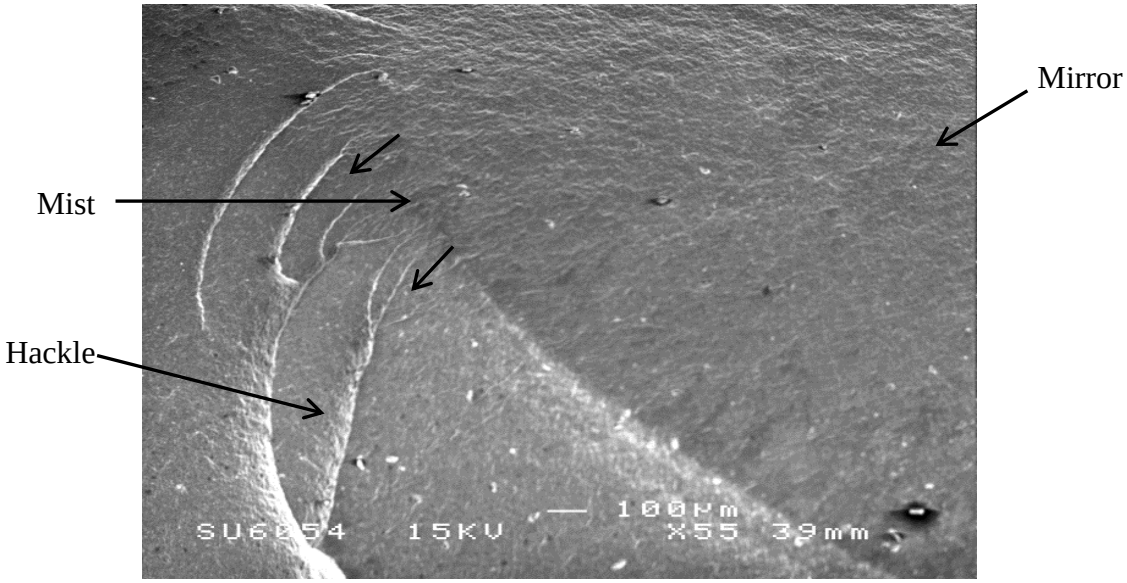

Figure 5.3 A magnified image showing the mirror, mist and hackle morphology of the fractured surface of O-ring tested in 90 % CO_2.

Figure 5.4 is a magnification of the mirror region displayed in Figure 5.3. The fracture surface displays a rough fracture surface with the formation of pits. A similar fracture surface was observed by Mathew and De (2009a) when they conducted tearing tests on natural rubber reinforced with clay particles. They observed a rough fracture surface containing pits/cavities similar to the fracture surface displayed in Figure 5.4. They postulated that the formation of these pits on the surface was a result of reinforcing agglomerates, coming out of the matrix and these loose agglomerates in the matrix act as stress raisers and offer an easy path for the tear to follow, thereby reducing the overall strength of the material.

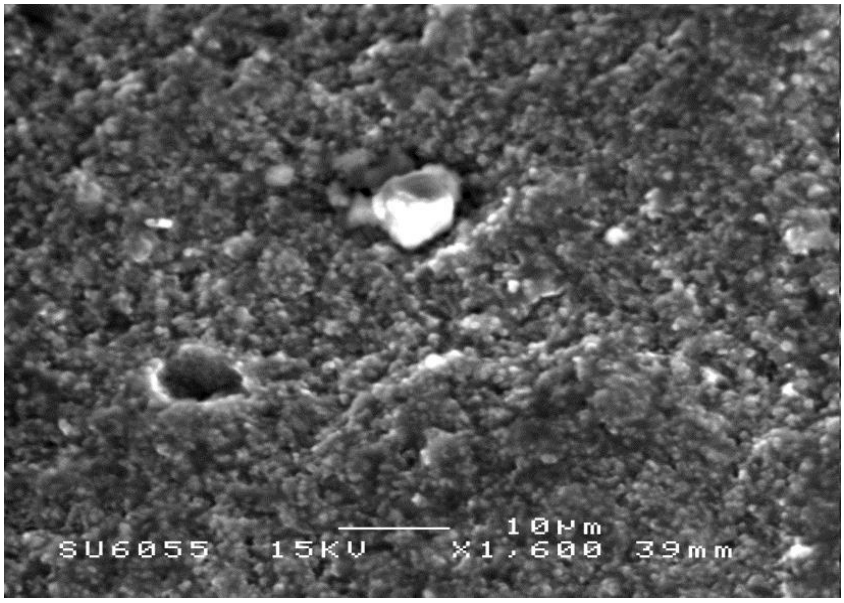

Figure 5.4 SEM image showing mirror region of the fractured surface of O-ring tested in 90 % CO_2 in methane.

5.1.1.2. O-ring 2

Figure 5.5 shows the SEM image for the fracture surface region highlighted in Figure 5.1 O-ring 2. The fracture surface of the second O-ring tested in 90 % CO_2 in methane also contains two distinct regions similar to the previous O-ring. In Figure 5.5 stable crack growth is more pronounced on the inner circumference of the O-ring whilst the outer region displays a rapid crack propagation fracture surface. The direction of the converging hackles indicate that cracks initiated in the centre region and propagated towards the inner circumference of the O-ring and once the cracks reached a critical size, the crack accelerated resulting in rapid crack propagation fracture.

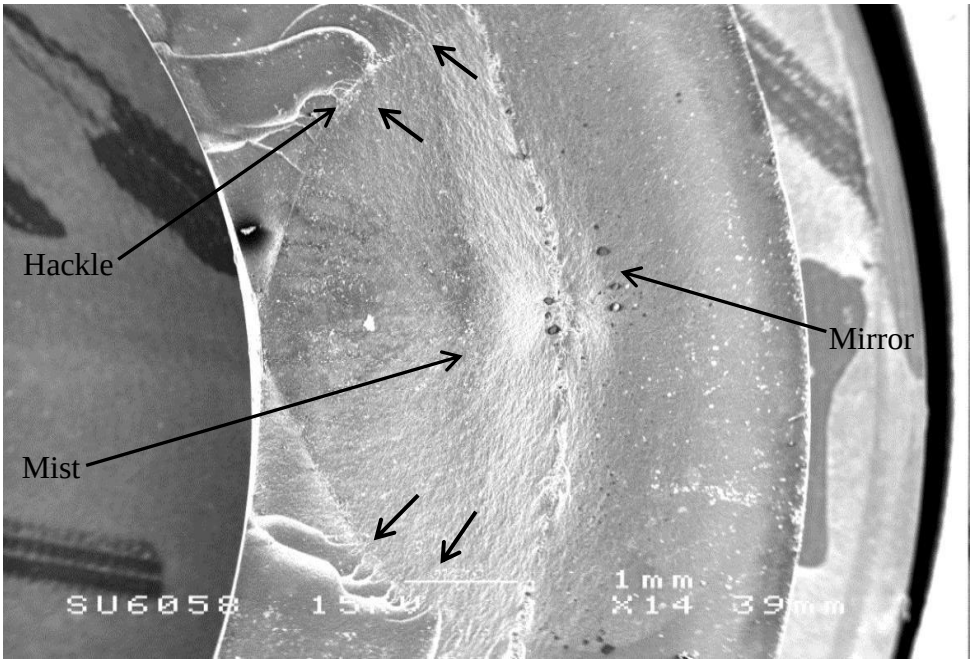

Figure 5.5 Mirror, mist and hackle morphology of the fractured surface of O-ring tested in 90 % CO_2 in methane, the crack direction is indicated by the arrows.

Figure 5.6 shows the centre region of the fractured surface shown in Figure 5.5. Cracking was more pronounced in this region and this is an indication that higher stress levels could have been experienced in this region of the O-ring during R.G.D or this region could be the point of weakness in the O-ring structure. Figure 5.7 is a magnification of the centre region. The fracture surface shows cracks propagating from cavities and these open cavities were a result of inherent voids present in the material, rupturing during rapid gas decompression. These cavities act as crack initiation sites in the O-ring thereby reducing the materials strength.

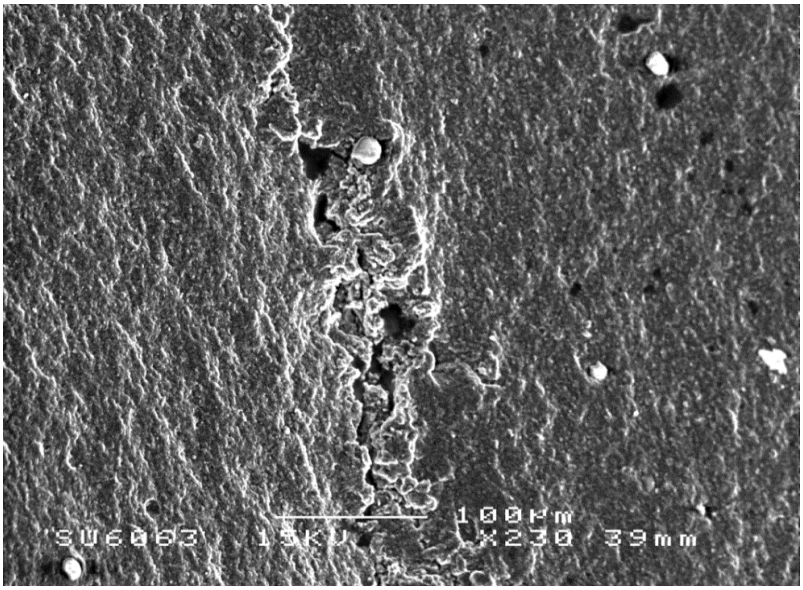

Figure 5.6 SEM image of the centre region in O-ring tested in 90 % CO_2 in methane, cracking was more pronounced in this region.

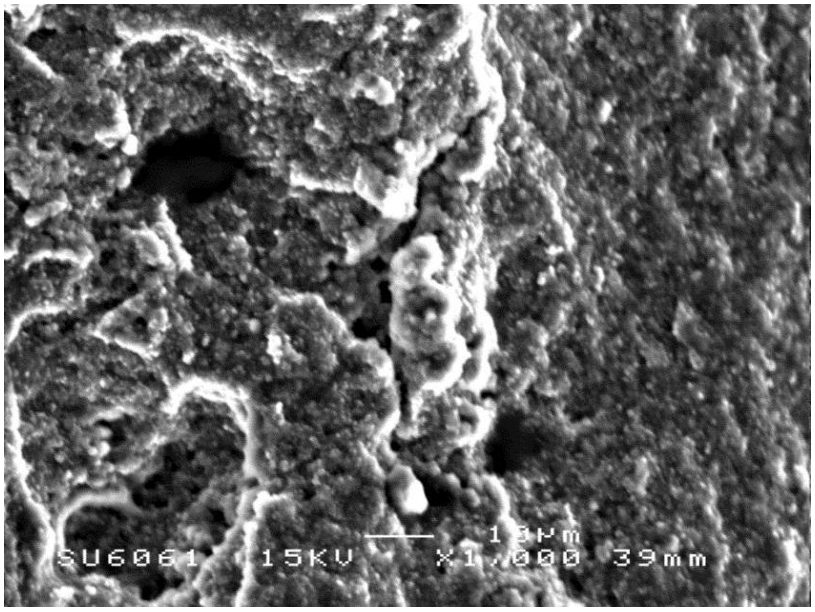

Figure 5.7 SEM image of the centre region in O-ring tested in 90 % CO_2 in methane, displaying cracks propagating from cavities.

5.1.1.3. O-ring 3

Figure 5.8 shows the SEM image for the fracture surface region highlighted in Figure 5.1 O-ring 3. Figure 5.8 shows the top and bottom fracture surfaces of an O-ring tested in 70 % CO_2 in methane. Figure 5.9 shows cracks initiating and propagating from an inherent inclusion contained in the material.

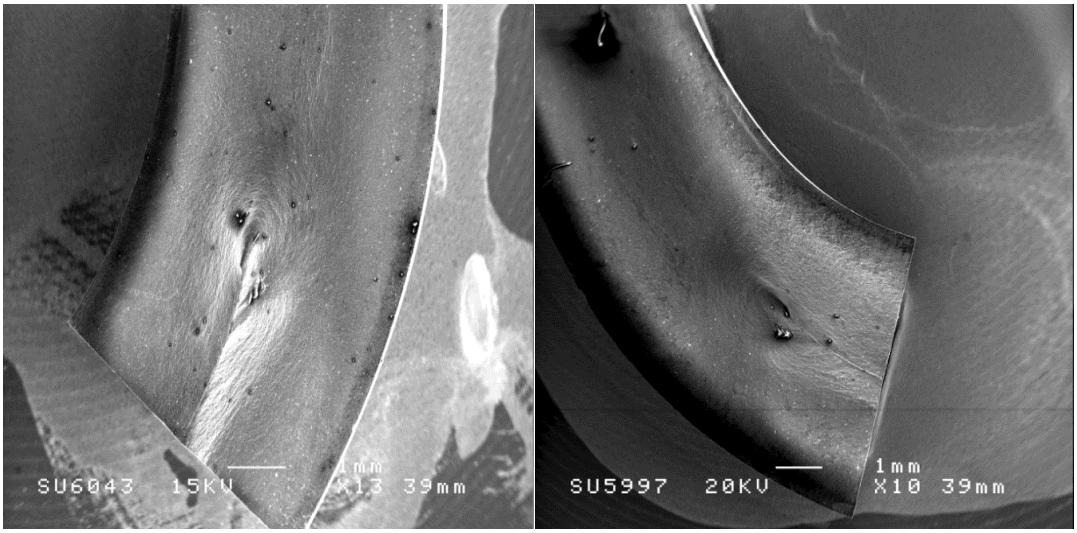

Figure 5.8 Fracture surfaces of O-ring tested in 70 % CO_2 in methane, displaying the top and bottom surfaces of the fracture.

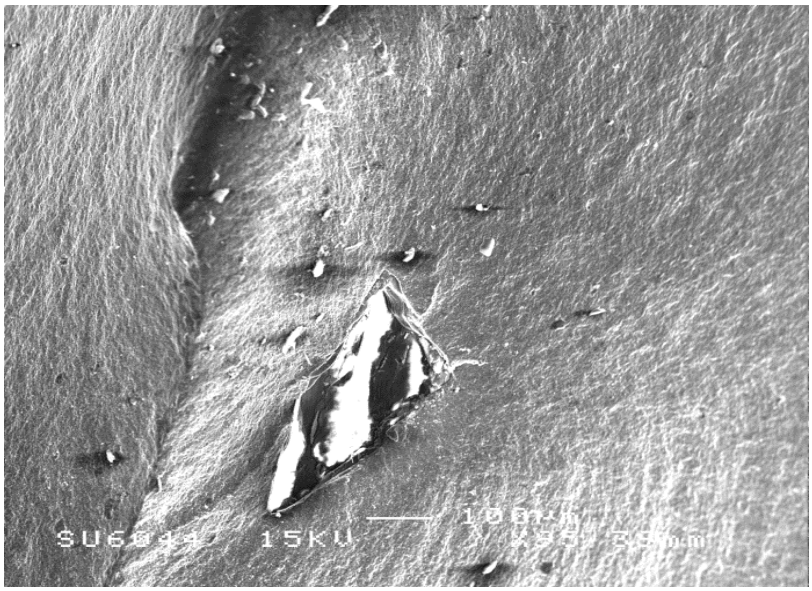

Figure 5.9 SEM image showing microcracks initiating from an inclusion O-ring tested in 70 % CO_2 in methane.

To identify the inclusion, the fracture surface was analysed using energy-dispersive spectroscopy (EDS) and the inclusion was identified to be a compound containing silicon. The inclusion is most likely silica. The inclusion must have got embedded into the rubber during the manufacturing process or contained in the elastomer raw material. The initiation region in the third O-ring is small in comparison to the previous O-rings, indicating the crack reached terminal velocity (critical speed) more rapidly in the third specimen compared to the previous specimens.

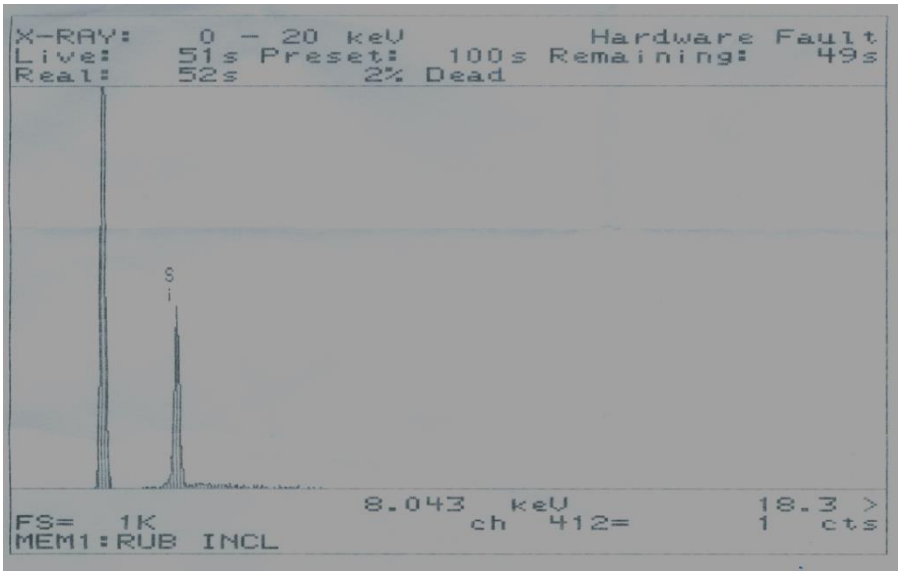

Figure 5.10 Energy-dispersive spectroscopy results conducted to identify the composition of the inclusion.

5.1.2. Spring Seals

This section shows results from SEM analysis conducted on elastomeric spring seals. Three fractured HNBR101 spring seals were examined after being exposed to RGD conditions according to the ISO 23936 – 2 standards at a temperature of 120 ^{o}C. The spring seals suffered from internal splits, which is one of the most common fractures in elastomeric seals reported by Rispin (1985). The splits were oriented longitudinal to the seal axis. Figure 5.11 shows the location of three sections in fractured O-rings containing crack initiation and crack propagation regions.

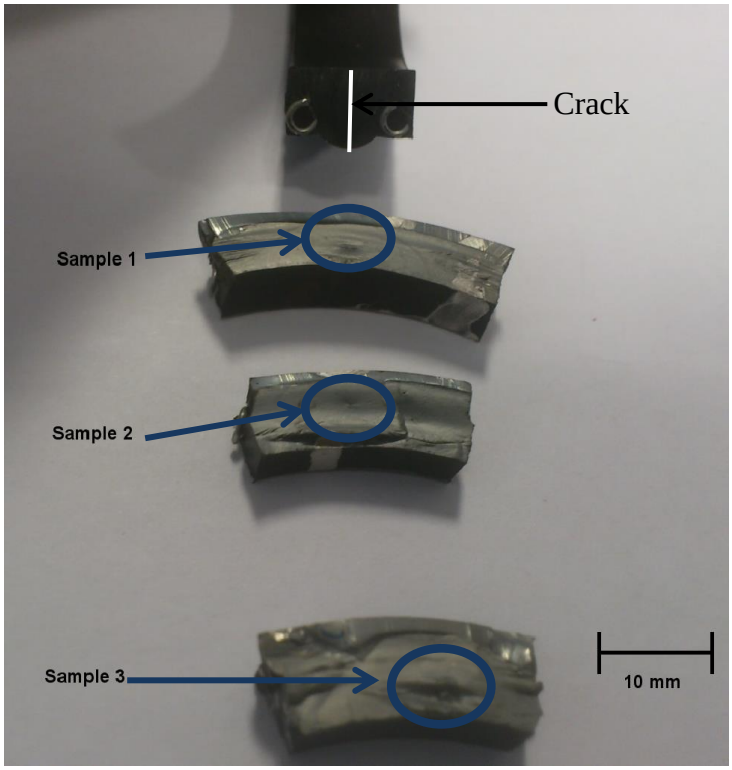

Figure 5.11 Fractured spring seals showing the location of three sections containing crack initiation and crack propagation regions.

5.1.2.1. Spring Seal 1

Figure 5.12 shows the SEM image for the fracture surface region highlighted in Figure 5.11. Figure 5.12 displays the fracture surface of a spring seal containing small multiple cracks propagating from an initiation point in the centre of the spring seal. The relatively rough and bright region is the slow propagation region, which is mainly characterised by small multiple cracks propagating away from an initiation point. Similar to O-rings, the spring seals have a larger slow crack propagation region towards the inner circumference compared to the outer circumference. Figure 5.13 displays a magnified image of an inherent flaw with cracks propagating at a 90^{o} angle from the flaw. The flaw region contains multiple irregular shaped cavities of different sizes. This type of flaw was likely a result of multiple voids in close proximity rupturing during the decompression cycle and coalescing to form bigger wider voids.

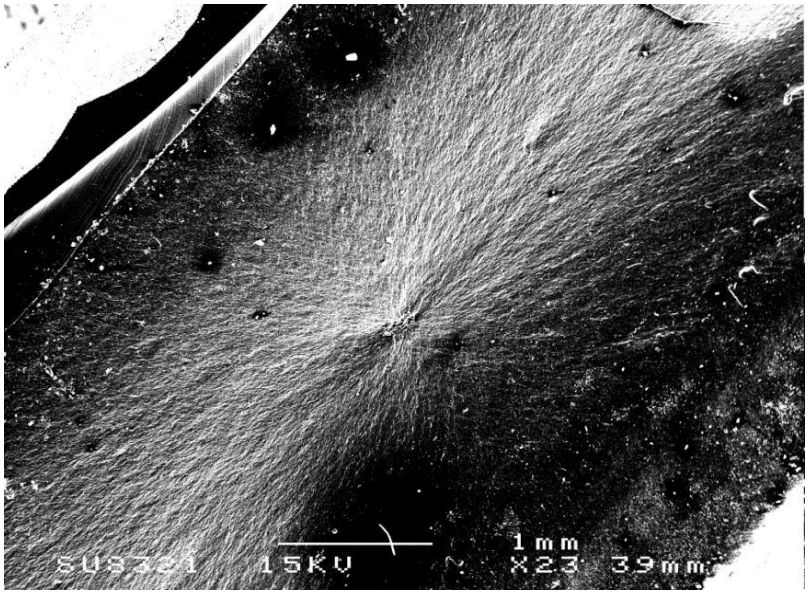

Figure 5.12 A fracture surface of a spring seal displaying multiple small cracks initiating from an inherent flaw.

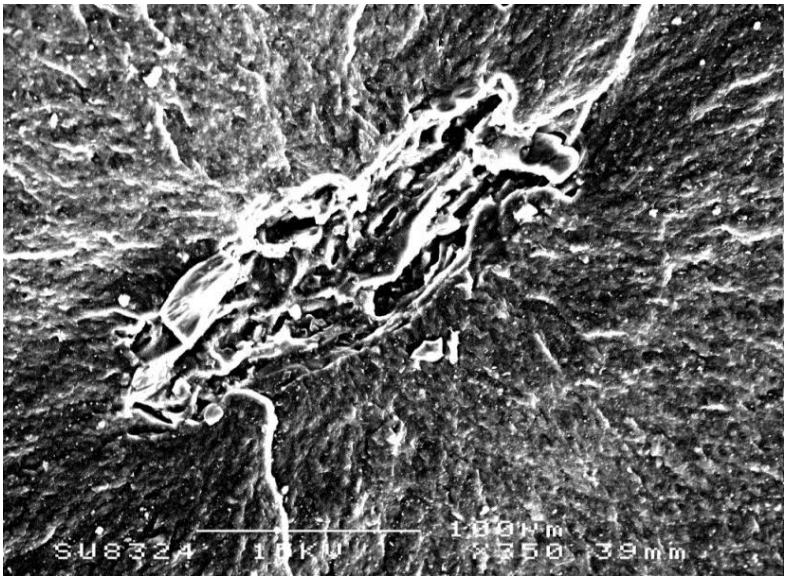

Figure 5.13 A magnified fracture surface showing microcracks propagating from an inherent flaw.

Figure 5.14 shows the fracture surface of the spring seal in the slow crack propagation region, the surface contains tearing lines and an open void of diameter 7.14 nm. Voids are usually introduced into O-rings and springs seals during processing and are almost impossible to avoid. During rapid gas decompression the voids inflate resulting in tensile stresses or strains in the void walls. If the stresses are higher than the strength of the elastomer, cracks initiate and propagate. The void in Figure 5.14 is not the cause for

crack initiation in the spring seal, however these open voids in the matrix act as stress raisers and offering a crack propagation path, thereby reducing the overall strength of the material.

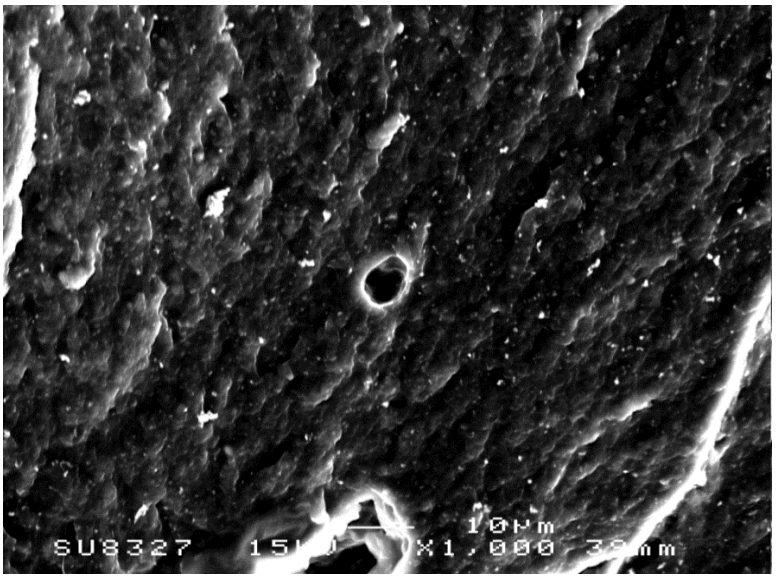

Figure 5.14 A fracture surface of a spring seal displaying tear lines and a void present on the fracture surface.

5.1.2.2. Spring Seal 2

Figure 5.15 shows the crack initiation region of a fracture in a spring seal. The fracture surface contains small multiple cracks propagating in various directions from a flaw and these small cracks coalesce to form bigger cracks. Slow crack propagation was more pronounced towards the inner circumference of the spring seal. Figure 5.16 displays two smaller cracks combining to form a bigger crack in the hackle region. Loose particles are present on the fracture surface these loose particles also act as stress raisers offering an easy path for cracks to propagate.

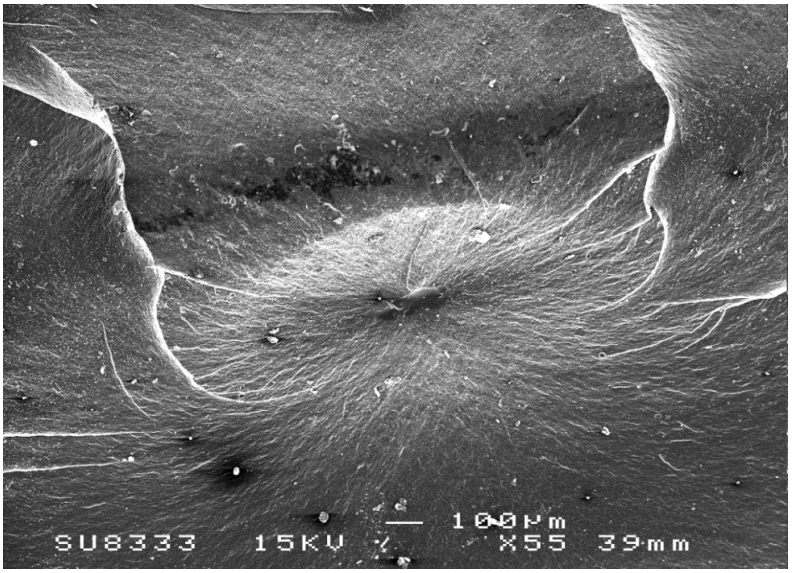

Figure 5.15 Fracture surface of a spring seal, small multiple cracks initiating from a flaw and combining to form bigger cracks.

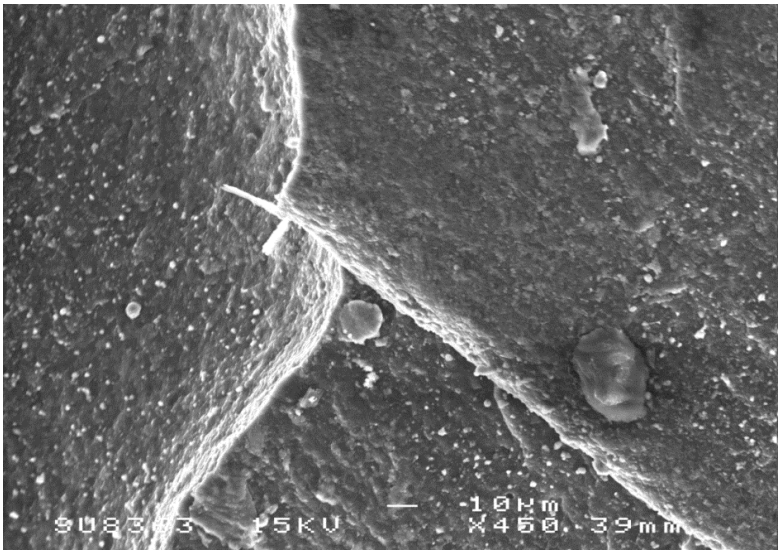

Figure 5.16 An SEM image of a fracture surface showing two small cracks combining to form a bigger crack.

Figure 5.17 is a magnification of a flaw shown in Figure 5.15 with a length size of 0.67 µm. This flaw could have been a result of three processes:

i. It could have been an inherent flaw present within the rubber compound.
ii. It could have been a flaw introduced during the manufacturing process.
iii. It could have been produced during rapid gas decompression.

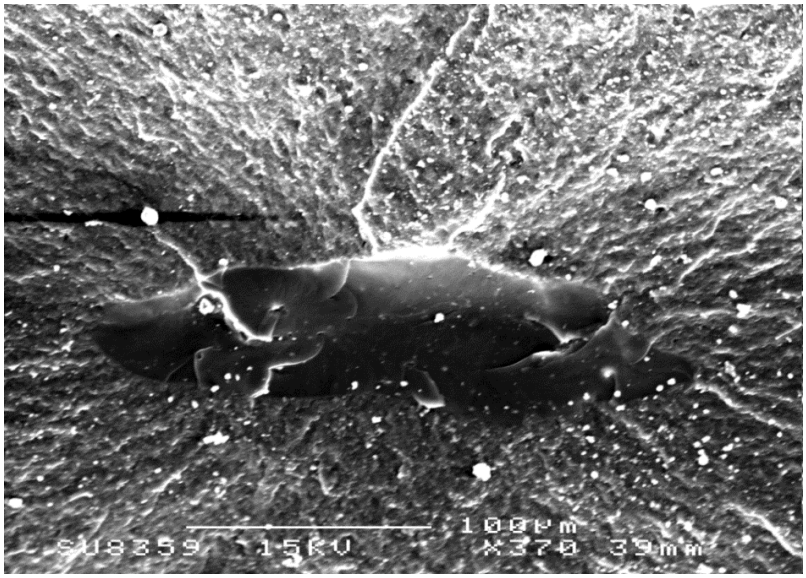

Figure 5.17 An SEM image showing a flaw present in a spring seal with cracks propagating in different directions from the flaw.

Figure 5.18 is the fracture surface of a spring seal in the rapid crack propagation fracture region, these regions are characterised by relatively little or no macroscopic visible plastic deformation and they require relatively less energy to form. The fracture surface contains pits and particles with varying diameter sizes between 0.736 nm to 9.6 nm. Fracture surfaces containing surface debris are typically associated with energy driven failure mode. The white particles shown in Figure 5.18 are reinforcement particles added to the elastomer compound during processing. The reinforcement particles are used to accelerate the cross-linking process, while other particles improve processing and others improve the properties of the finished product.

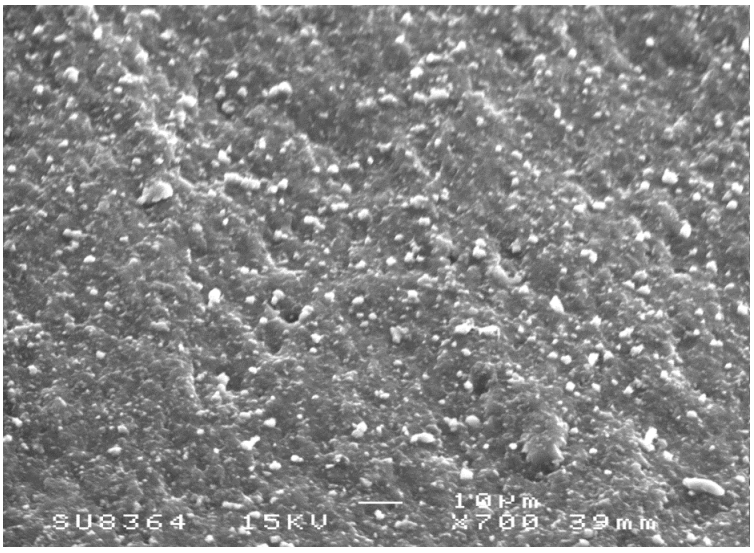

Figure 5.18 A Fracture surface of a spring seal with surface debris and pits.

5.1.2.3. Spring Seal 3

Figure 5.19 shows the initiation region of a crack in a spring seal with small multiple cracks propagating in different directions from a flaw. The fracture surface also contains surface debris with diameters up to 14.2 µm, however these surface particles do not seem to be responsible for the crack initiation or to have assisted in the crack propagation process since there are no visible cracks initiating or propagating from these particles.

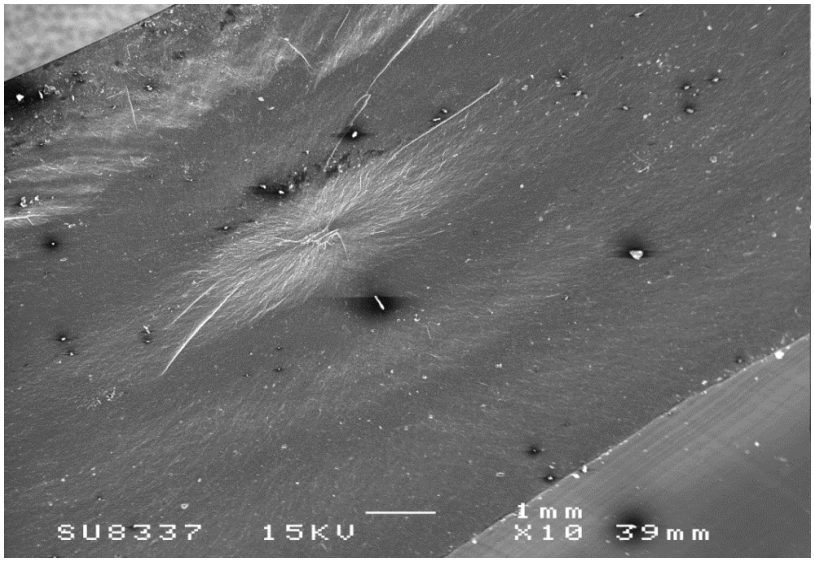

Figure 5.19 A Fracture surface of a spring seal showing small multiple cracks propagating from an inherent flaw.

Figure 5.20 shows the magnification of a flaw in a spring seal with small multiple cracks and bigger lines of around 1.5 µm propagating from the inherent flaw.

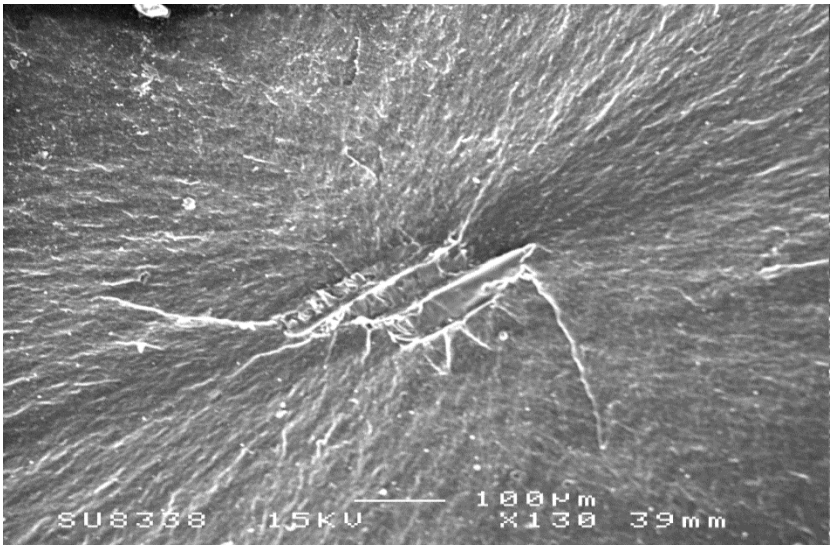

Figure 5.20 An SEM image of an inherent in a spring seals with multiple cracks propagating from the flaw.

5.2. Computerised Tomography Scan Results

After reconstructing datasets from Sky Scan 1172, 3D x-ray images of the O-ring sections were constructed and are shown in Figure 5.21, Figure 5.22 and Figure 5.23. The O-ring sections contain white randomly distributed spots, which after close inspection the white spots were found to be surrounding or adjacent to randomly distributed voids of varying dimensions between 30 to 60 micrometres. The determination of voids and the white spots is shown later in this chapter.

These randomly distributed white spots can also be viewed on 2D images at different levels along the height of the O-ring section. These white spots were probably a result of reinforcement particles added to the elastomeric compound to aid in processing or to improve the material properties of the elastomeric compound. Figure 5.21 contained more randomly distributed white specs compared to the other two O-ring cross-sections.

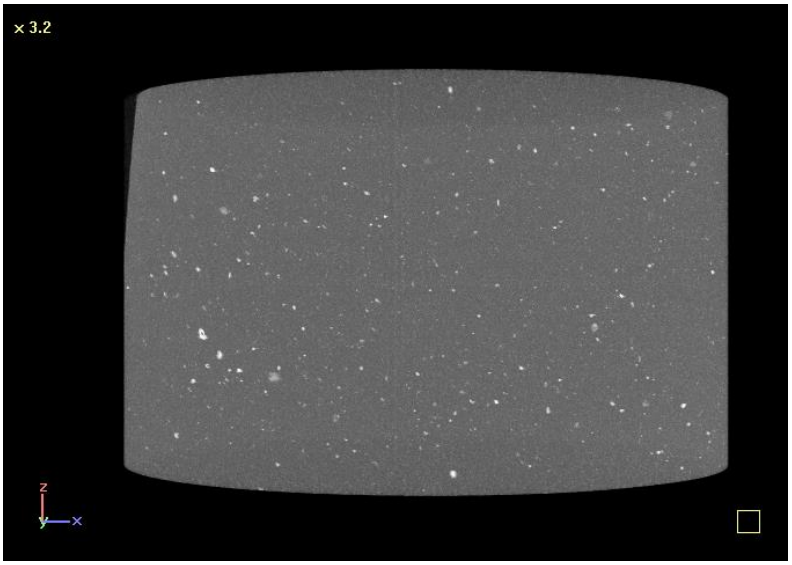

Figure 5.21 3D x-ray display of an O-ring section from a conventionally manufactured 6.99 mm O-ring, were the randomly distributed white specs are voids inside the O-ring cross-section.

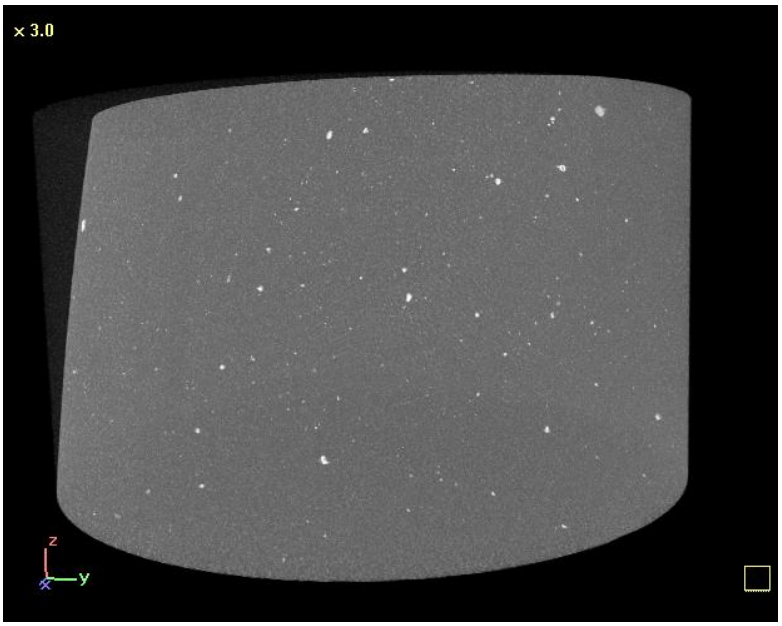

Figure 5.22 A 3D x-ray display of an O-ring section from a conventionally manufactured 6.99 mm O-ring. The section contains less white specs compared to the previous section from a conventionally manufactured O-ring.

Figure 5.23 3D x-ray display of an O-ring section from a differently manufactured 6.99 mm O-ring, were the randomly distributed white specs are voids inside the O-ring cross-section.

The reconstructed images can also be viewed as a shadow projection of the O-ring as shown in Figure 5.24. The red line indicates the height or location of the 2D cross-sectional images. This is important when identifying the points along the O-ring's height where the voids are contained. The first few images at the top and bottom of the O-ring sample were ignored because any voids in that area could have been introduced during the sectioning of the O-ring.

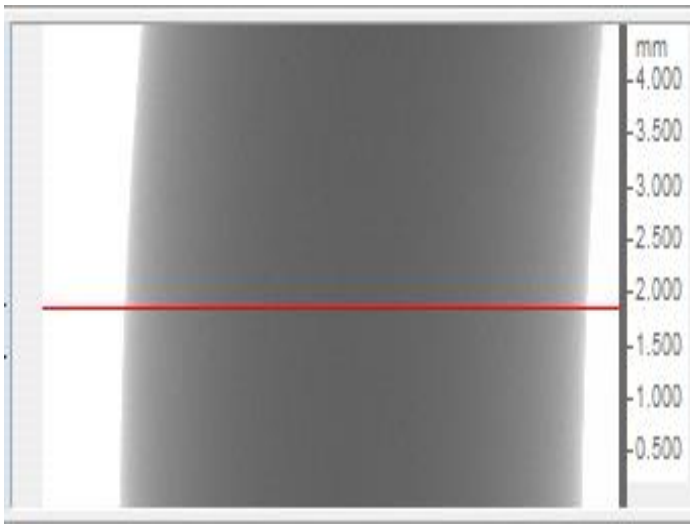

Figure 5.24 Display of the shadow projection of a standardly manufactured O-ring cross-section. The red line indicates the height or location of the displayed 2D cross-section images.

Figure 5.25 shows a 2D image of an O-ring with a void in the top right of the image. The 2D image was taken at a height of 1.88 mm of the O-ring section as shown by the red line in Figure 5.24. The voids space and solid particles in the reconstructed images have different densities and different atomic numbers. Therefore, the void spaces and the solid particles will have different levels of X-ray attenuation (Taylor et al. (2015). The 8-bit reconstructed images contain 256 grey scales and each voxel has greyscale intensity from 0 to 255, where 0 is black and 255 is white on the grey scale. A pixel value of 0 represents the material with the minimum relative density. The scanned O-rings compose of voids, solid elastomeric material and reinforcement particles such as carbon black. Therefore, the black regions in the micro-CT images were judged to correspond to void spaces and the brightest regions represent the material with the highest relative density.

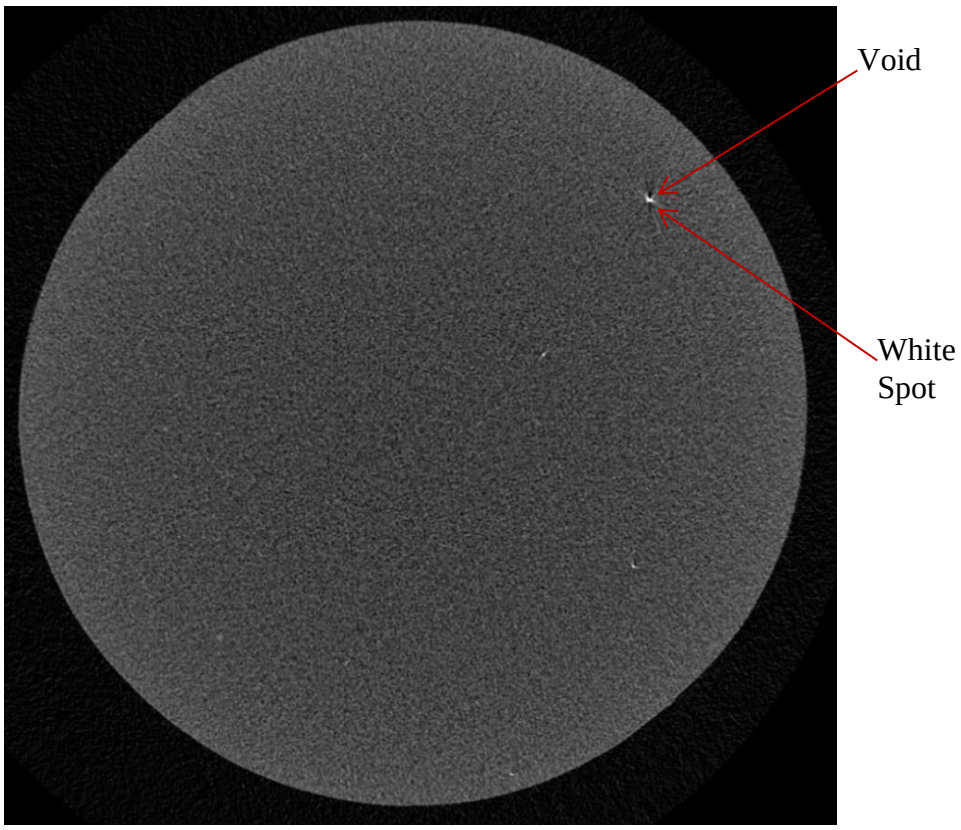

Figure 5.25 Display of a 2D image of the O-ring taken at a height of 1.88 mm. The image contains a visible void on the top right of the 2D image with a white spot attached to the void.

Figure 5.26 shows a 2D image of an O-ring with a void in the centre region of the image. The 2D image was taken at a height of 3.68 mm of the O-ring section. The voids

shown in Figure 5.25 and Figure 5.26 are just two of many randomly distributed voids found in all the O-ring sections analysed. There was no distinct shape of the voids and they were of different shapes and sizes.

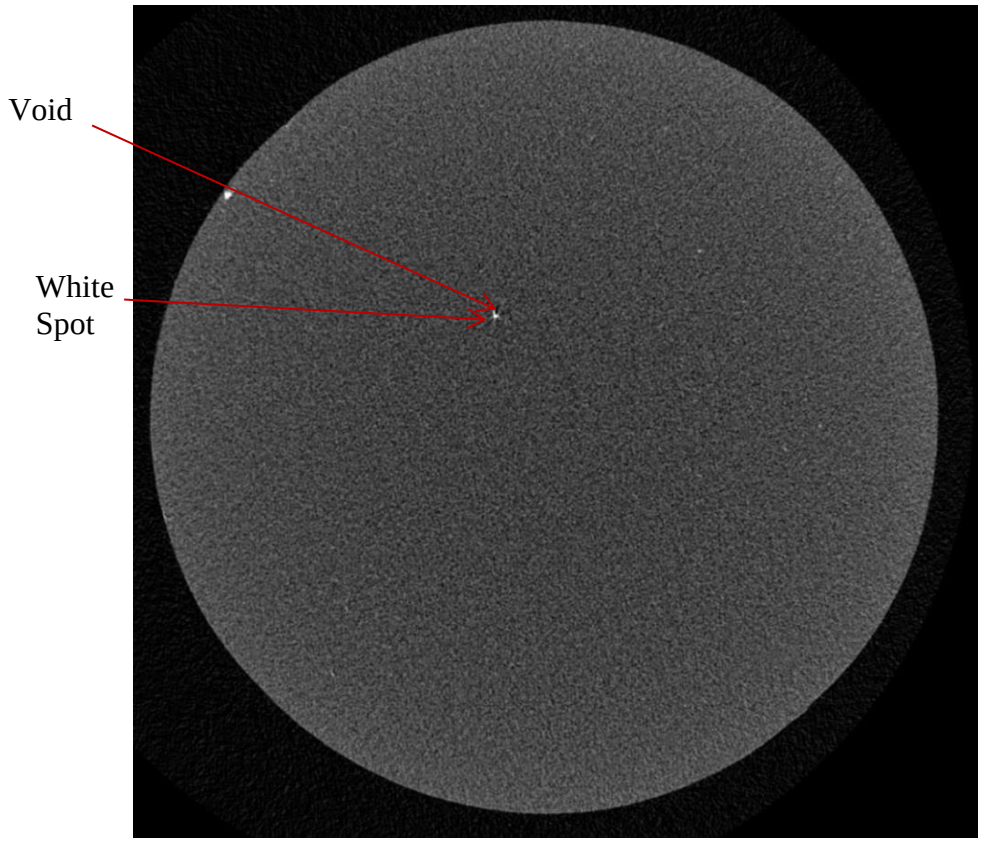

Figure 5.26 Display of a 2D image of the O-ring taken at a height of 3.68 mm. The image contains a visible void in the centre region of the 2D image with a white spot attached to the void.

Figure 5.27 shows a magnified display of a void shown in Figure 5.26. The image is too distorted and cannot be used to provide an accurate quantitative analysis of void sizes and distribution. However, the distorted image revealed that apart from the large voids present in the tomography images, there were also multiple smaller voids present in the images. In the magnified images, the smaller voids appear randomly distributed and the size of the images does not allow deducing the distribution of these small multiple voids.

In order to evaluate the void distribution for both large visible voids and smaller voids, the images were viewed as binary images. In these images, white colour represents areas with brightness within the range of the binary threshold selection, and colour black represent areas outside the binary threshold.

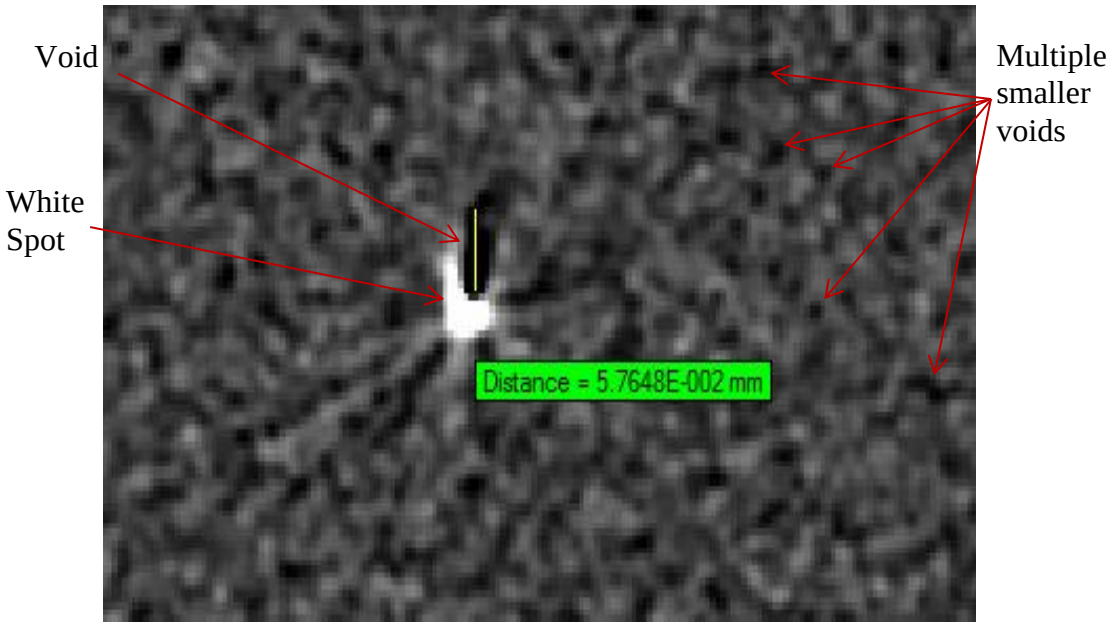

Figure 5.27 A magnified display of a void in shown Figure 5.26 and the void has a length of approximately 58 micrometres with a white spot attached to the void.

Figure 5.28 shows the image displayed in Figure 5.26 as a binary image were the white regions represents solid rubber sections and the black regions represent voids present in the O-ring section. Image segmentation was achieved by using the automatic threshold function provided in the CT-Analyser package. Image segmentation is the process of separating the solid material from the void spaces. During the segmentation process, a threshold value is selected. Voxels with a grey value higher than this value become white and represent the solid rubber sections and voxels with a grey value below the threshold will become black and will represent the void spaces or background. The binary images were also compared to the corresponding raw images to make sure the black regions corresponded to the visible voids in the raw images.

Figure 5.28 also shows an analysis which was conducted to evaluate the area with the highest void density. The amount of voids per area in five different regions shown in Figure 5.28 were measured and compared. The amount of voids per area tends to increase towards the centre region of the O-ring. This void distribution trend was observed in every layer along the O-ring's cross-section and also in all three O-rings analysed. This void distribution trend was likely introduced into the O-rings during the manufacturing process.

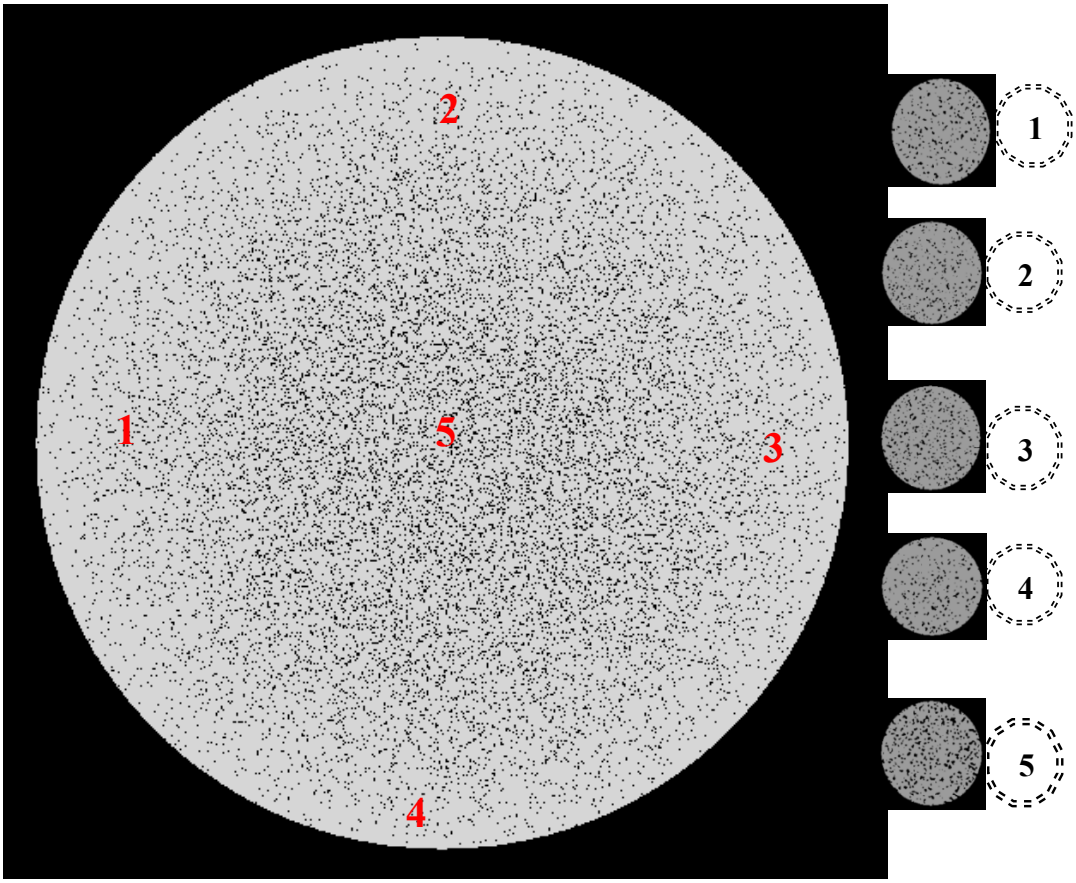

Figure 5.28 A binary image of the 2D image shown in Figure 5.26, white areas represent the solid rubber sections and black areas represent voids. The smaller circles represent five different regions in the image with region five showing the highest void density.

The void distribution shown in Figure 5.28 is probably the reason why cracks in HNBR101 O-rings initiate and propagate from the centre region of the O-rings. In service gas in contact with the O-ring surface diffuse into the material until the O-ring is fully saturated. Due to a high void density ratio in the centre region, more gas nucleates in this region in comparison to other regions. When the external pressure is released, higher stress levels are experienced in the centre region of the O-ring due to a higher concentration of compressed gas expanding. Even though the O-ring contains larger voids which are randomly distributed through-out the O-ring's cross-section, it is the small multiple voids concentrated in the centre region which are likely responsible for fracture. Therefore improving the distribution of the voids can improve the O-ring's RGD resistance in service.

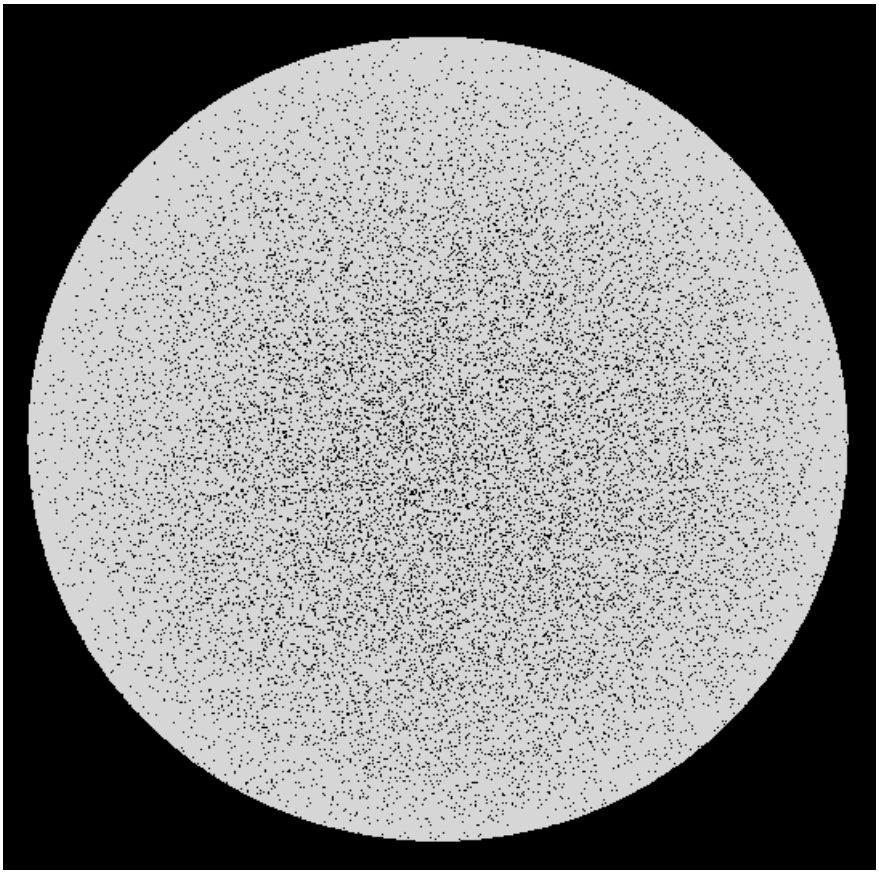

Figure 5.29 A binary image from an O-ring section manufactured conventionally. The image has a total porosity of 7.55 %.

Figure 5.29 and Figure 5.30 display 2D binary images from a standard O-ring and a further processed O-ring respectively. The two O-rings had a similar void distribution trend, with a higher void ratio located in the centre region of the image.

The porosity level inside the 2D binary images was measured. To measure porosity in the 2D images, a region of interest was created. The region of interest is created to separate the O-ring section from the surrounding space. This is done so that the porosity ratio does not include the surrounding space and the porosity percentage is only for the void space inside the O-ring cross section. After creating the region of interest, the selected region is shown as a binary image. A morphometry analysis was performed on the binarised region of interest. The morphometry analysis measures the volume of any void spaces fully surrounded by solid material, as a percentage of the volume of solid material.

The total porosity in each 2D image was evaluated. The total porosity in the image from the standard O-ring was 7.55 % whilst the one from the further processed O-ring was

6.11 %. The total porosity in the 2D images is given as the area of all open and closed pores as a percent of the total section area. The total porosity is not constant for every 2D image and varies along the height of the O-ring's section. Therefore the total porosity from a 2D image is not a true measure of whether the further processed O-ring has reduced porosity.

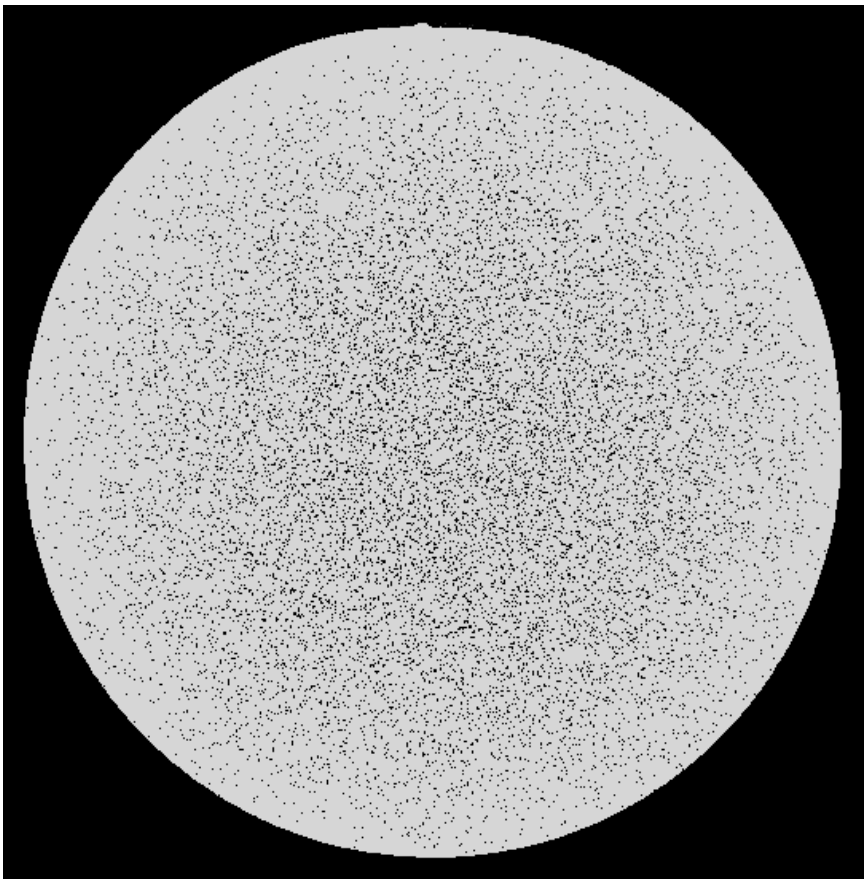

Figure 5.30 A binary image from an O-ring section manufactured differently from the conventional way. The 2D image has a total porosity of 6.11 %.

A better way to compare the porosity of the three O-ring sections was to evaluate the porosity of the whole section volume. However evaluating the porosity of the whole section is time consuming and requires a large amount of computational resources. To save computational time, each O-ring section was divided into three equal separate subsections. Each subsection was taken at a different height of the O-ring's section and each 3D subsection comprised of a 100 2D images. The total porosity in each subsection was evaluated and the total porosity is given as the volume of all open and closed pores as a percent of the total subsection volume.

The total porosity in each O-ring was evaluated as the average porosity of the three subsections from each O-ring. Table 5.1 shows the average total porosity for three different O-rings analysed. The porosity in the further processed O-ring section was reduced however the reduction was small.

Table 5.1 The average total porosity for three different O-ring sections analysed.

	Volume_1 Porosity (%)	Volume_2 Porosity (%)	Volume_3 Porosity (%)	Average Porosity (%)
Conventionally manufactured O-ring_1	6.93	6.52	6.77	6.74
Conventionally manufactured O-ring_2	6.82	6.86	7.13	6.94
Further Processed O-ring	6.54	6.52	6.49	6.51

5.3. RGD Fracture Analysis Summary

Scanning electron microscopy was conducted on fractured Fluorocarbon elastomer O-rings and Hydrogenated Nitrile Butadiene spring seals after being exposed to rapid gas decompression. All fractured surfaces contained two distinct regions; rough region which is associated with slow crack propagation, and a smooth region which is normally associated with fast brittle crack propagation. Microcracks initiated from microvoids or inherent flaws in the centre region of the elastomer seals and propagated towards the inner and outer circumference of the seal. When the crack reached a critical size, the crack rapidly accelerated resulting in a catastrophic fracture. Both spring seals and O-rings fracture surfaces contained hackle lines which tend to appear in regions where the stress field is changing rapidly or when the stress state changes from tension to compression or vice versa.

All fracture surfaces for both O-rings and spring seals displayed more pronounced relatively stable crack growth towards the inner circumference. This indicated that higher stress levels were experienced on this side of the specimen during RGD, or this region maybe a point of weakness in both the O-rings and spring seals structures.

All the flaws in the spring seals where located in the centre region of the seals. This indicates that these flaws could have been introduced during the manufacturing process

and were not necessarily inherent flaws contained in the elastomer raw material. The fracture surface of both O-rings and spring seals specimens contained pits on the surface and these pits were a result of reinforcing agglomerates, coming out of the matrix. These loose agglomerates in the matrix can act as stress raisers also offering an easy path for a tear to follow thereby reducing the overall strength of the material.

Computerised tomography (micro-CT) was conducted on HNBR101 O-rings to evaluate the void density and distribution. Micro-CT scanning was carried out using Sky Scan 1172 and the images were analysed using CT-analyser software from Bruker micro-CT. The micro-CT images revealed multiple randomly distributed voids of varying dimensions from 30 to 60 micrometres along the length of the O-ring sections scanned. All the voids had various shapes and dimensions and they could have been introduced during the manufacturing process or contained in the elastomer raw material. The O-ring sections also contained smaller multiple voids which were only visible in binary images or after zooming in on the raw images.

The binary mode images revealed that all 2D cross-section images of the O-ring contained a high void density in the centre region. This distribution of small voids could be one of the reasons why cracks in HNBR101 O-rings always initiate and propagate through the centre regions. This is because during service there is a higher concentration of absorbed gas at the centre of the O-ring due to high void density in this region. When the external pressure suddenly drops during RGD, higher stress levels are experienced in this region due to the high concentration of compressed gas expanding.

The total porosity in all the three O-ring sections was evaluated. The total porosity in the further processed O-ring was slightly reduced however the reduction was very small and was less than 0.23 %. This investigation has however shown that it is possible to use non-destructive methods to evaluate the void density and distribution inside elastomer O-rings and can be used a tool in the design of elastomer seals with improved void distribution.

6. Material Characterisation Results and Discussion

6.1. Hyperelastic Material Model Results

Both HNBR101 and LRCM888 were characterised by evaluating their stress-strain behaviour under uni-axial, planar shear and equibiaxial loading. The stress-strain curves for both materials were used to define the material model in the FEA. The strain was measured using a video extensometer based on the experiments explained in Section 3.2.2. Figure 6.1 shows the uni-axial stress-strain behaviour for both HNBR101 and LRCM888. Figure 6.2 displays the planar shear stress-strain curves for both HNBR101 and LRCM888. Figure 6.3 shows the stress-strain behaviour of both HNBR101 and LRCM888 under bi-axial loading.

The stress strain plots show that LRCM888 has a lower stiffness under uni-axial, planar shear and equibiaxial loading when compared to HNBR101. Three samples were tested for each test and the averages were calculated in Microsoft Excel. The raw data for all the experiments conducted is shown in Appendix I. The raw data was processed in Microsoft Excel, by taking the average of the tests performed. The raw data, stress was recorded at random strain intervals. To get an average of the stress – strain curves for each type of loading, a polynomial function of the raw data was found using non-linear regression supplied in the Microsoft Excel package (2010) and each polynomial had an R-squared value of more than 0.999. Using these polynomials the average curve was found.

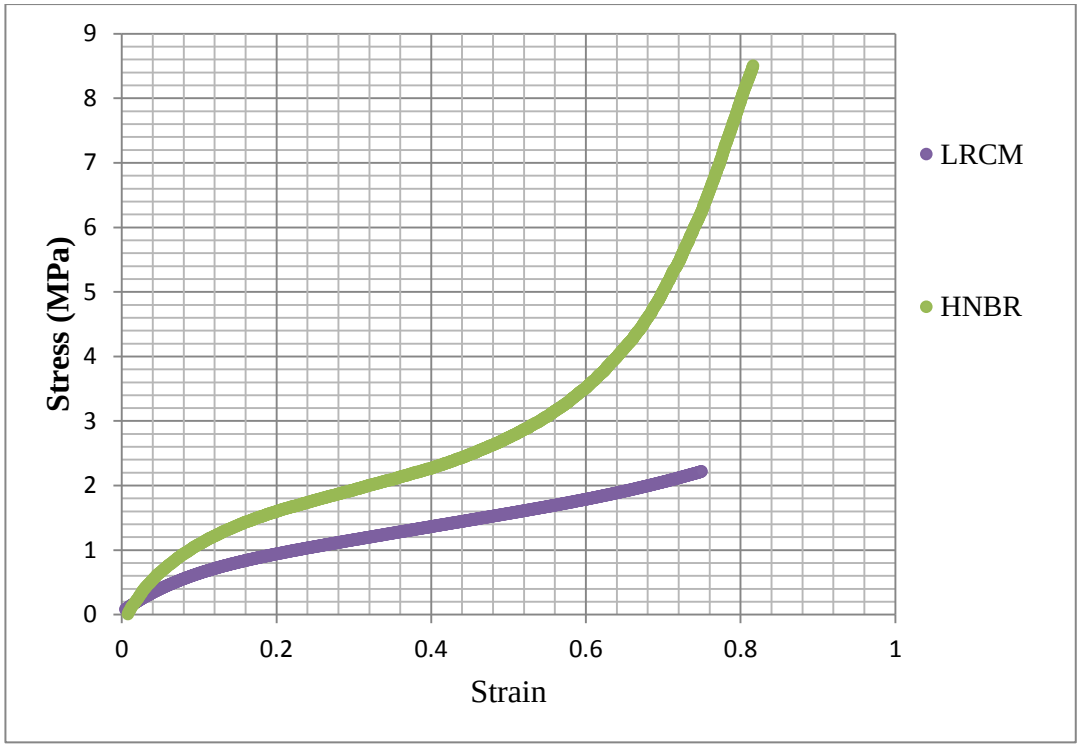

Figure 6.1 Uni-axial stress-strain results for both HNBR101 and LRCM888.

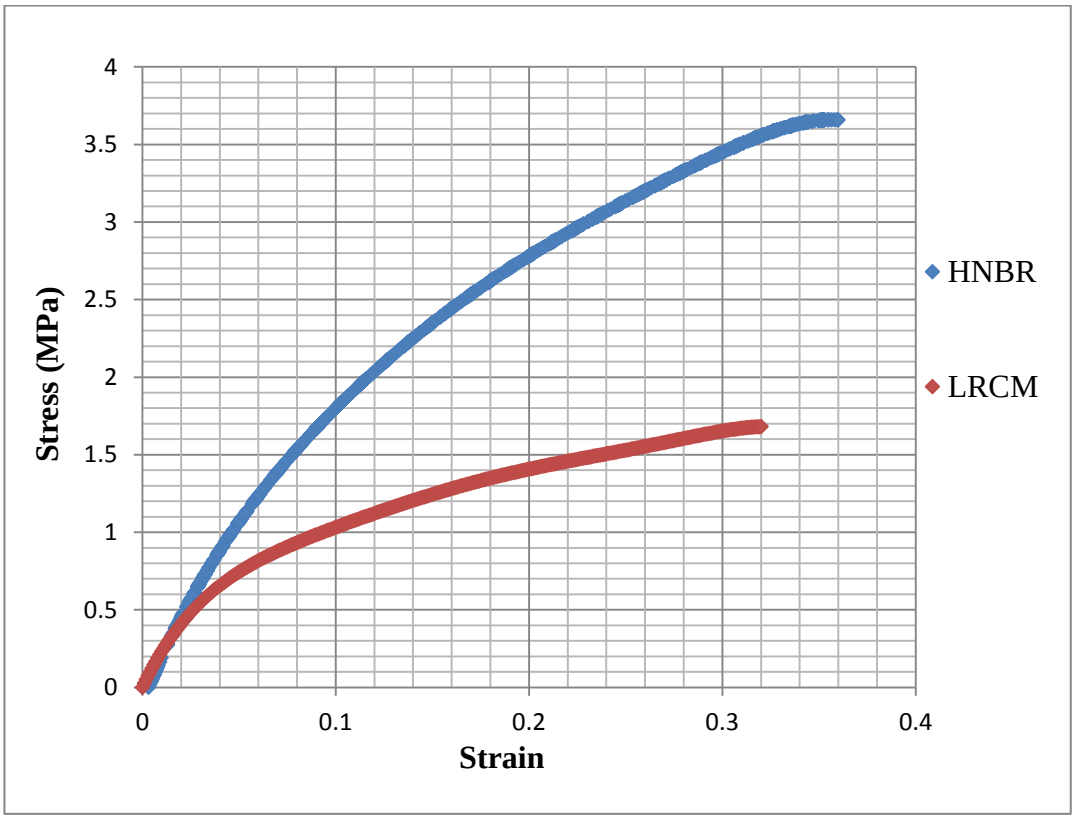

Figure 6.2 The planar shear stress-strain results for both HNBR101 and LRCM888.

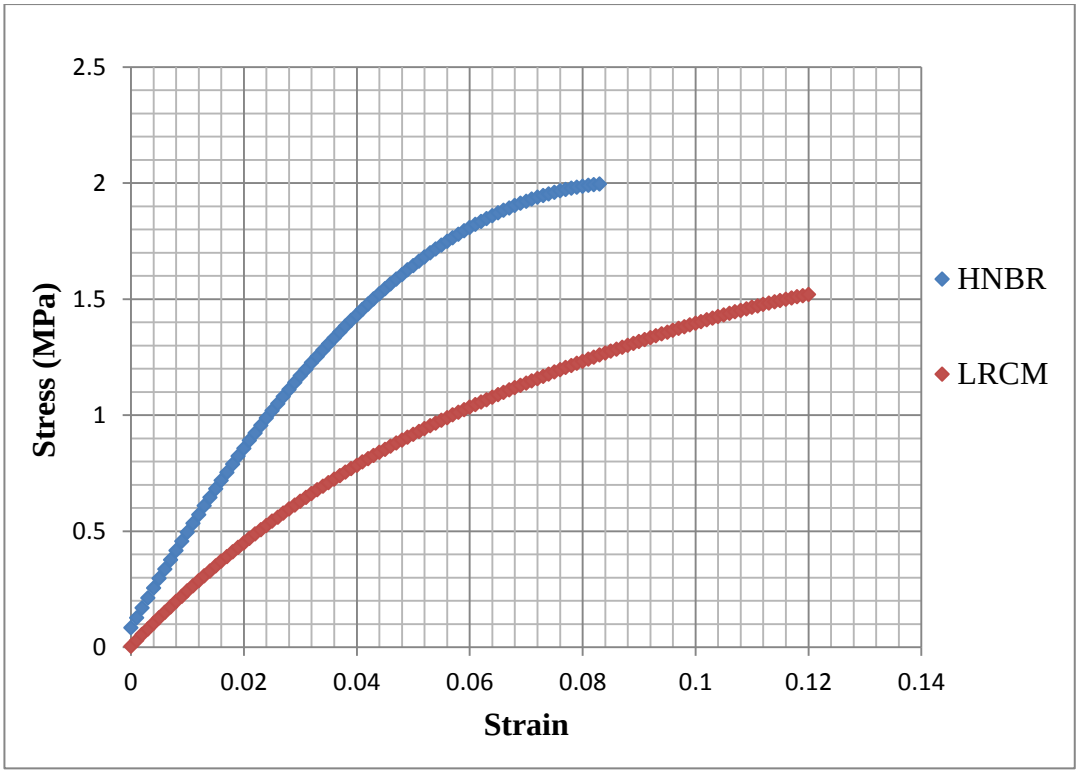

Figure 6.3 The equibiaxial stress-strain results for both HNBR101 and LRCM888.

6.2. Thermal Expansion Results

The thermal expansion coefficient was evaluated using a dynamic mechanical analyser (DMA). In the thermal expansion experiments, a tensile specimen was held in the DMA machine using tensile grips and the change in length of the rubber specimen due to thermal expansion was recorded. A plot of change in displacement with temperature was plotted and used to evaluate the thermal coefficient for HNBR101 and LRCM888.

6.2.1. HNBR101

Figure 6.4 shows the evolution of displacement with temperature for an aluminium strip and the DMA instruments. The DMA instruments refer to the driveshaft and the grips, which also expand upon heating. The displacement plot for the DMA instruments was evaluated by subtracting the aluminium curve from the aluminium + DMA instruments curve. The curve for the DMA instruments is the calibration curve which is subtracted from the elastomer + DMA instruments to give the thermal expansion curve for the elastomer material alone. The thermal expansion curve for HBNR101 is shown in

Figure 6.5. The thermal expansion coefficient of HNBR101 is given by the gradient of its thermal expansion curve divided by the specimen's length.

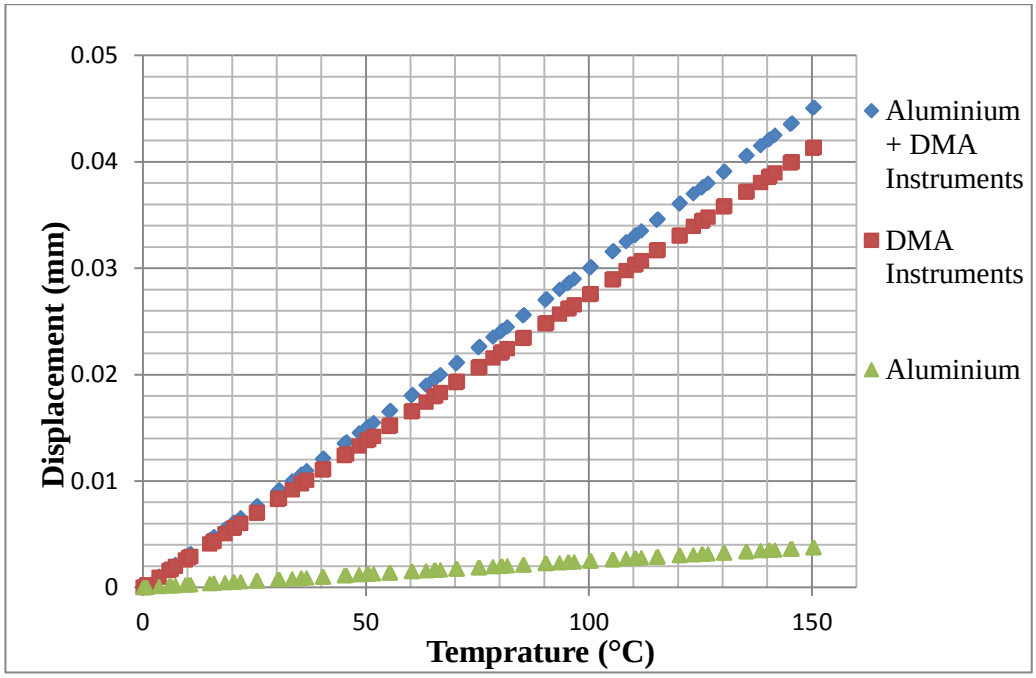

Figure 6.4 The thermal expansion curves for an aluminium strip and DMA instruments, DMA instruments refer to the grips and driveshaft.

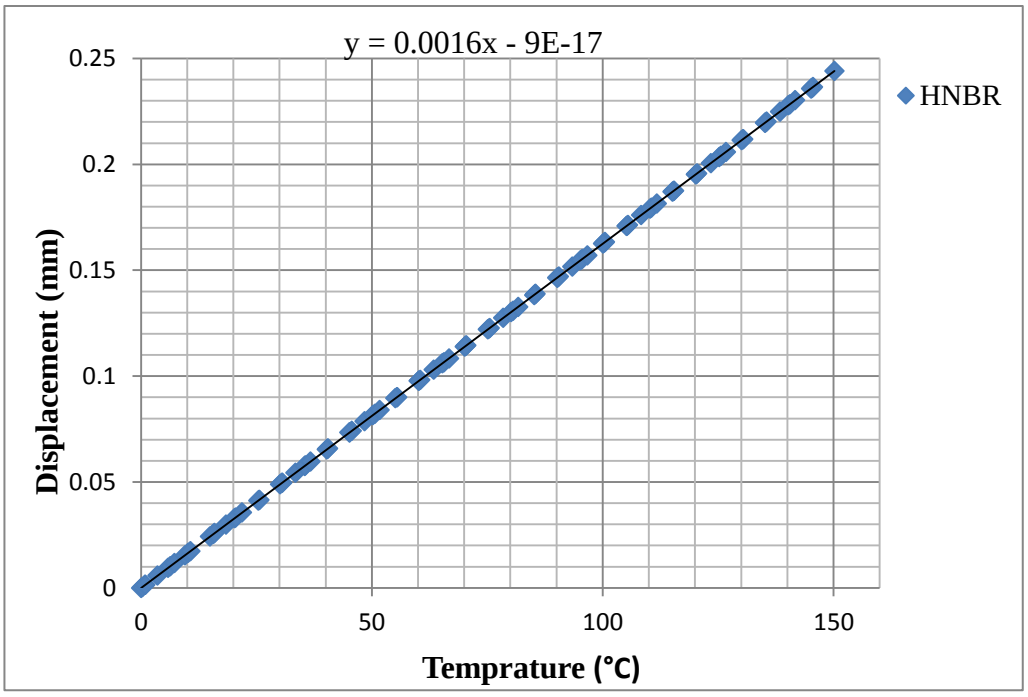

Figure 6.5 The thermal expansion curve for HBNR101 and the thermal coefficient is given by the gradient of the curve divided by length of sample.

6.2.2. LRCM888

The thermal expansion coefficient for LRCM888 was evaluated the same way as the thermal expansion for HNBR101. This involved calibrating the DMA instruments, by subtracting the thermal expansion curve of a known material from the thermal expansion curve for both the known material plus DMA instruments.

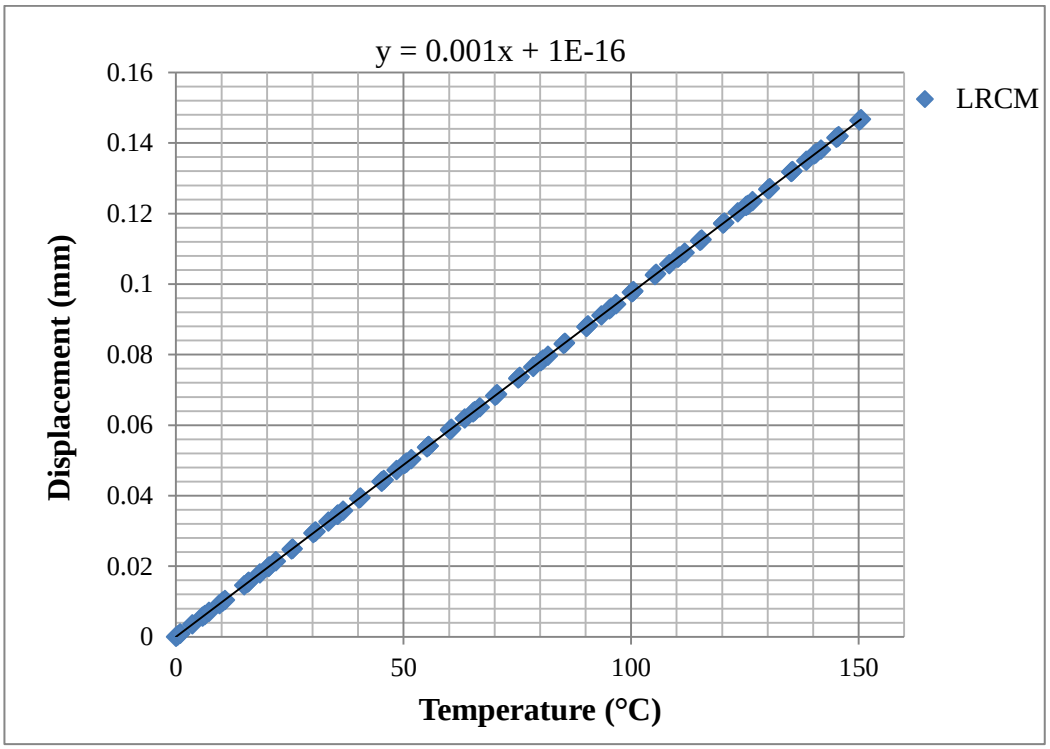

Figure 6.6 The thermal expansion curve for LRCM888 and the thermal coefficient is given by the gradient of the curve divided by length of sample.

The thermal expansion coefficient is then calculated by evaluating the gradient of the thermal expansion curve for LRCM888 as shown in Figure 6.6 and dividing the gradient by the samples gauge length which was 10 mm for both HNBR and LRCM samples.

6.3. Viscoelastic Behaviour

6.3.1. Glass Transition Temperature and Loss Factor (tan δ) Results

The transition temperature represents the region where the properties of an elastomer change significantly as the material state changes from glassy state to a rubbery state. The glass transition temperature in this thesis is given as the peak on the graph of the

loss factor against temperature. Figure 6.7 shows the evolution of the loss factor with temperature. Figure 6.7 shows the average of the three tests conducted for each sample. The raw data for all the tests conducted can be found in Appendix H. The glass transition temperature is found to be -14.6 °C for HNBR101 and -22.7 °C for LRCM888 at a frequency of 1 Hz.

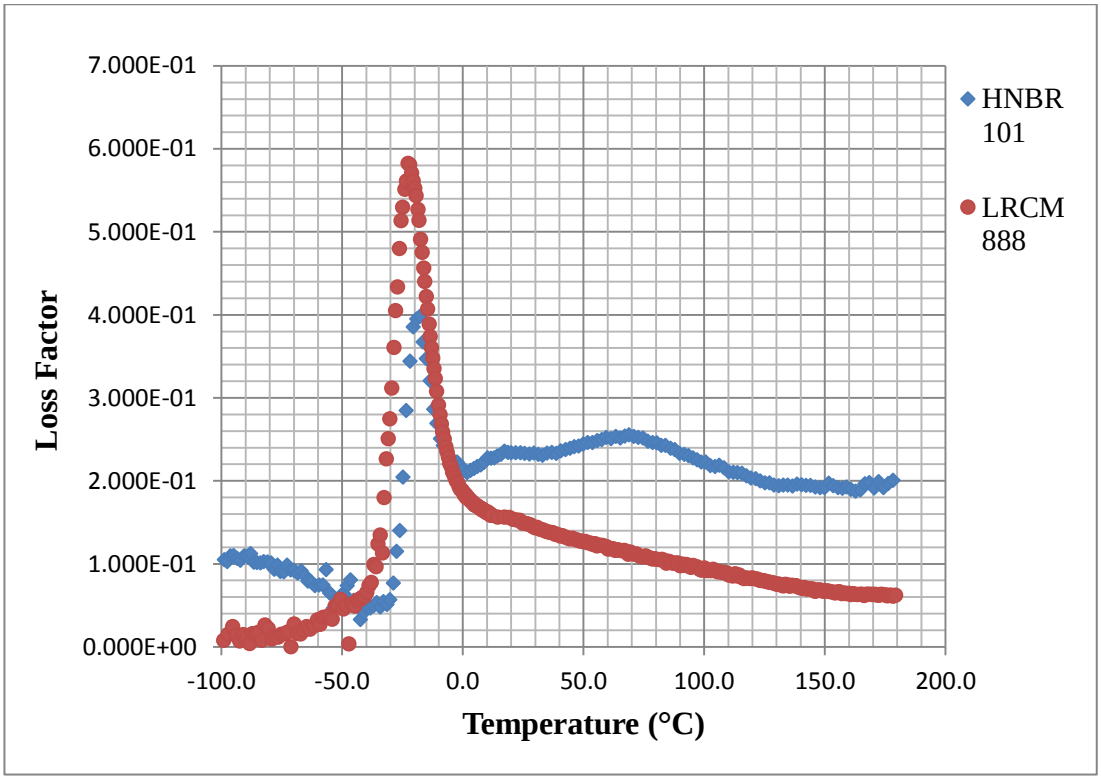

Figure 6.7 The evolution of loss factor with temperature at 1 Hz, the glass transition temperature is given by the peak of the slope.

The loss factor against temperature plot shows that HNBR101 and LRCM888 have a similar working temperature range, since they follow the same trend. At temperatures below -40 °C both materials are in a glassy state and above 10 °C the materials are in a rubbery state. Also Figure 6.7 shows that at T_g, LRCM888 has a loss factor of 0.58 while HNBR101 has a loss factor of 0.41. This means that at transition, LRCM888 has a higher energy damping factor than HNBR101. However at room temperature or working temperature of 100 °C, HNBR101 has a higher loss factor. The transition temperature for both materials was found to vary with the test frequency. At higher frequencies, the T_g shifts to the right towards higher temperatures. At lower frequencies, the T_g shifts to the left towards lower colder temperatures. The graph showing this trend for both materials can be found in Appendix H.

6.3.2. Creep Behaviour Results

Creep tests were conducted on HNBR101 and LRCM888 and the aim was to examine the materials response when subjected to a constant load. Figure 6.8 shows the creep test results for both LRCM888 and HNBR101. The two materials display similar creep characterises and this is likely because they are compounded from the same base polymer.

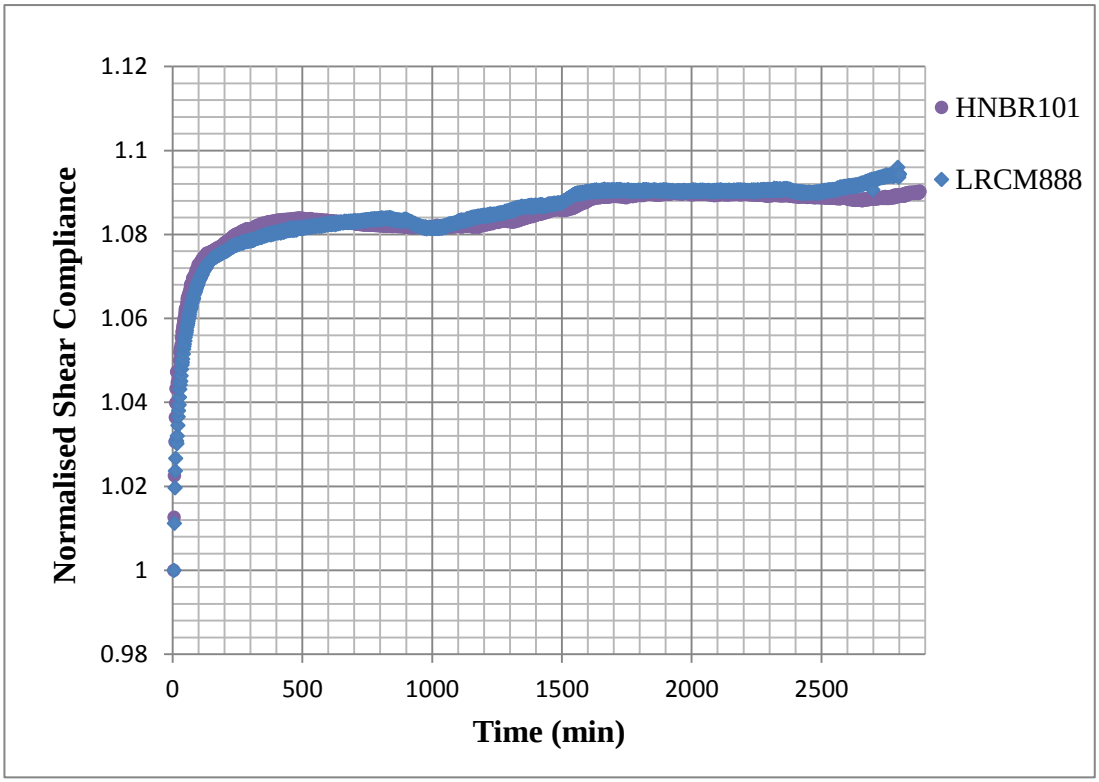

Figure 6.8 The creep test results showing the evolution of the normalised shear compliance with time for both HNBR101 and LRCM888.

Figure 6.8 shows that when both HNBR101 and LRCM888 are exposed to the same constant load for up to 48 hours both materials will creep by almost the same amount. The normalised shear compliance is defined as:

$$j_s(t) = G_0 J_S(t) \qquad [6.1]$$

where $J_S(t) = \gamma(t) / \tau_0$ is the shear compliance, $\gamma(t)$ is the total shear strain, τ_0 is the constant shear stress in a shear creep test and G_0 is the instantaneous shear modulus. The instantaneous shear modulus was measured as the shear modulus at the beginning of the experiment.

6.4. FEA Validation Compression Test Results and Discussion

6.99 mm O-rings were subjected to a compression force at a rate of 30 mm/minute and force as a function of displacement was measured. The aim of the experiment was to validate an FEA model which was used to evaluate the contact pressure between an O-ring and its housing gland surfaces. Figure 6.9 shows the evolution of force with displacement of an O-ring under compression from its housing gland surfaces. The graph is an average of five tests performed on five different O-ring samples. The curve shown in Figure 6.9 is an average of five tests performed. The graph showing results from all the five tests performed can be found in Appendix K.

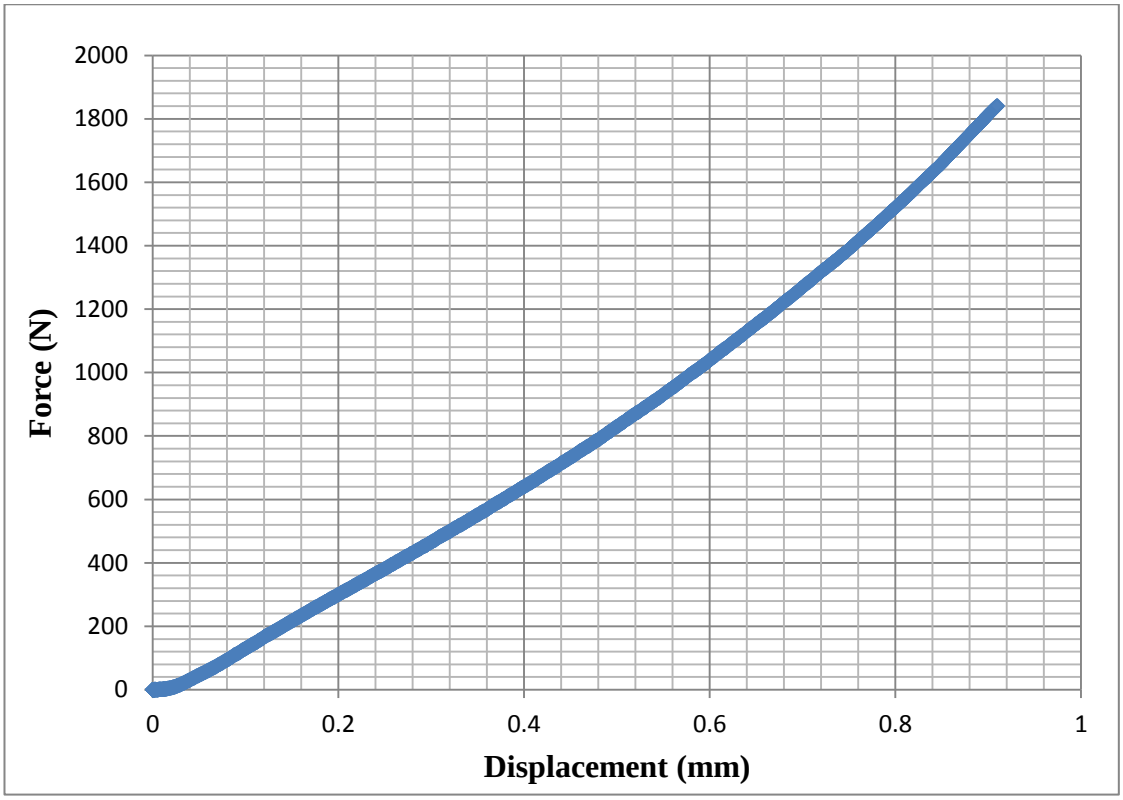

Figure 6.9 Evolution of force with displacement for an O-ring under compression from its housing gland surfaces.

6.5. Material Characterisation Results and Discussion Summary

Both HNBR101 and LRCM888 were characterised by evaluating their stress-strain behaviour under multiaxial loading. The stress strain curves showed that LRCM888 has a lower stiffness than HNBR101. The stress strain curves will be used to calibrate a strain energy potential that defines the hyperelastic behaviour for each material. The thermal expansion coefficient for both materials was also evaluated using a dynamic mechanical analyser (DMA). In the thermal expansion experiments, a tensile specimen was held in the DMA using tensile grips and the change in length of the rubber specimen due to thermal expansion was recorded. The thermal expansion coefficient for each material will be used to calibrate a material model for each material in Finite Element Analysis.

The glass transition temperature and loss factor for both HNBR101 and LRCM888 were evaluated. At T_g LRCM888 has a higher loss factor, however in the rubbery state, HNBR101 has a higher loss factor. Also the two materials have a similar working range, at temperatures below -40 °C both materials are in a glassy state and above 10 °C the materials are in a rubbery state. The T_g for both materials was found to be dependent on strain rate, at lower strain rates the T_g shifts towards the low temperature region and at higher strain rates T_g shifts towards the higher temperature region. Shear creep experiments revealed that HNBR101 and LRCM888 had similar creep characteristics and this is likely because they are compounded from the same base polymer.

7. Numerical Model Results and Discussion

7.1. Structural Model Results

The structural model was used to analyse the interaction between an O-ring and its housing gland surfaces. The O-ring was modelled as a hyperelastic material. The structural model was validated using results from the O-ring compression experiments. To save computational time only a quarter of the O-ring and its housing gland surfaces were modelled using appropriate boundary conditions. In the experiments, the O-rings have a larger diameter than the bottom O-ring housing. When the O-rings are fitted into the housing they are in a pre-stressed state before they are compressed by the top housing. To achieve a similar pre-stress state in the 3D FEA models, the bottom O-ring housing in FEA analysis was designed with a larger diameter than usual and after the O-ring was fitted into the bottom housing, the housing contracted by a specific distance, thereby creating a pre-stress state in the FEA O-rings similar to the experiments. The structural model was also modelled as an axisymmetric model, which was used in the coupled structural mass diffusion analysis.

7.1.1. Material model

The mechanical response of a hyperelastic material is described in terms of a strain energy potential, which describes the strain energy stored in the material per unit volume as a function of strain at that point in the material. Stress-strain data generated using two different strain energy potentials was compared to the experimental stress-strain data. The two strain energy potentials compared were the Ogden and the polynomial N-2 functions. These two models were chosen because they gave the best fit when compared to other strain energy potentials provided in Abaqus (2011). Figure 7.1 and Figure 7.2 shows the stress-strain curves generated from the Odgen and the polynomial functions being compared to experimental data. Both models can be seen to accurately model the behaviour of HNBR101 and LRCM888.

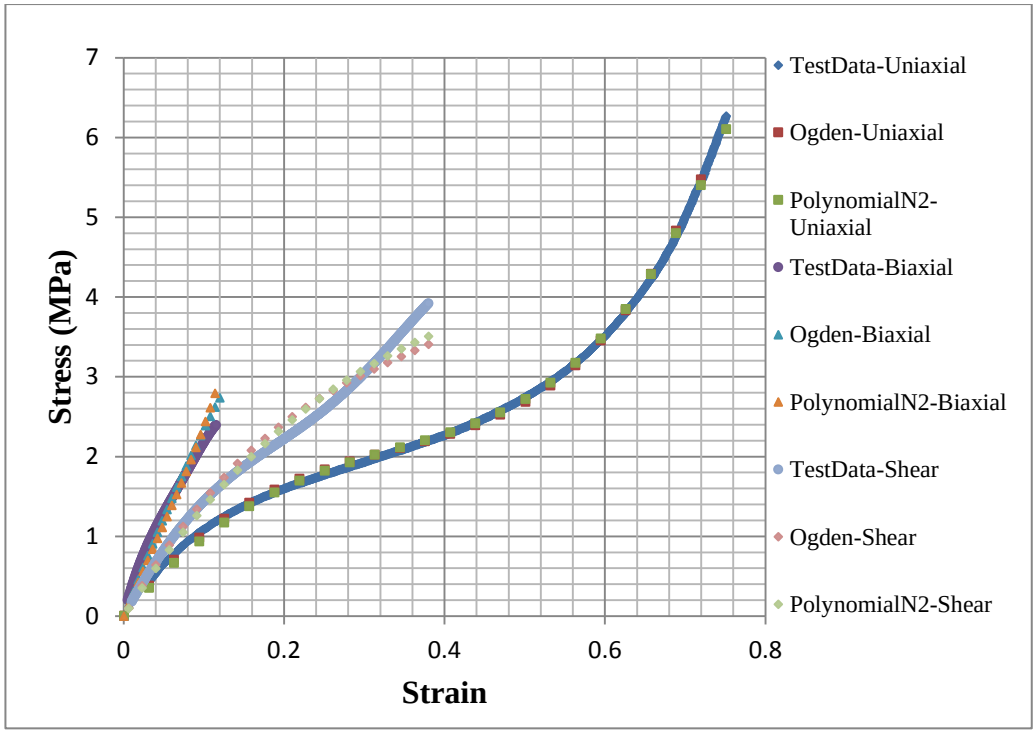

Figure 7.1: HNBR101 stress-strain curves generated from the Ogden and the Polynomial_N2 material model compared to test data measured under multi-axial.

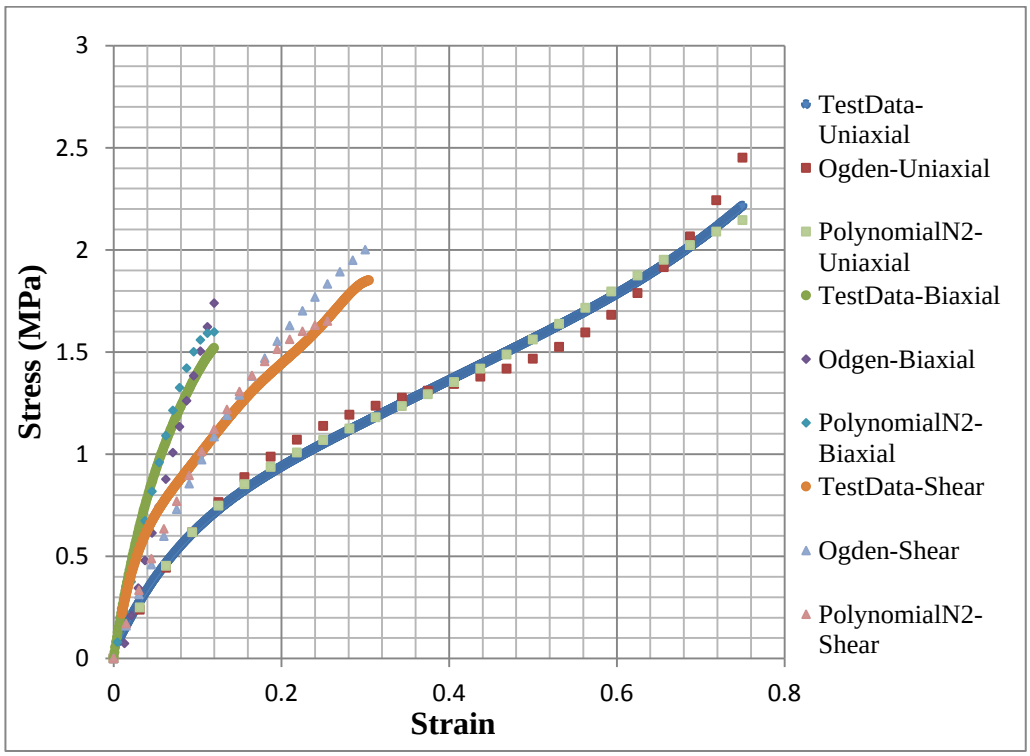

Figure 7.2: LRCM888 stress-strain curves generated from the Ogden and the Polynomial_N2 material model compared to test data measured under multi-axial.

The polynomial N-2 material model was chosen in this thesis because it provided the best fit to the experimental data. Both the Ogden model and the polynomial function were able to predict the uniaxial deformation on both HNBR101 and LRCM 888 elastomers. However, the polynomial function provides a better fit to the planar shear and equibiaxial data. This is because the Ogden model has been shown to have better flexibility in describing the curvature on the strain-stress curves than the polynomial function. However, when the curvature is minimal, the polynomial function provides a better fit which was the case for the planar shear and equibiaxial data. Therefore, the polynomial function provided a better fit to the data from all three different load cases. The strain energy potential was calibrated using test data conducted under multi-axial loading. Figure 7.3, Figure 7.4 and Figure 7.5 show the stress-strain curves generated from the polynomial material model compared to the experimental data. The material model seems to predict the stress values at various strain levels with acceptable accuracy. The error between the stress-strain curves obtained from the experiments and the stress-strain curves generated from the material model was quantified using the root mean square error (RMSE). The root mean square error is a measure between values predicted by a model and the actual values observed.

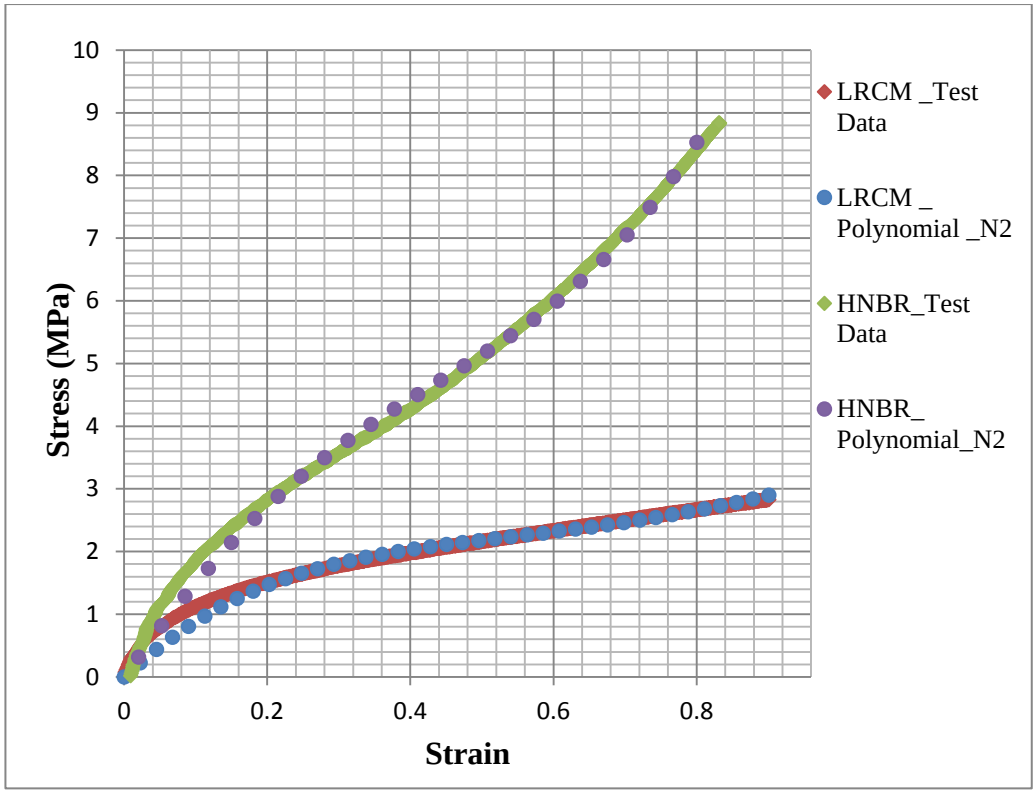

Figure 7.3: Stress-Strain curves generated from Polynomial_N2 material model compared to test data measured under uni-axial loading for both HNBR101 and LRCM888.

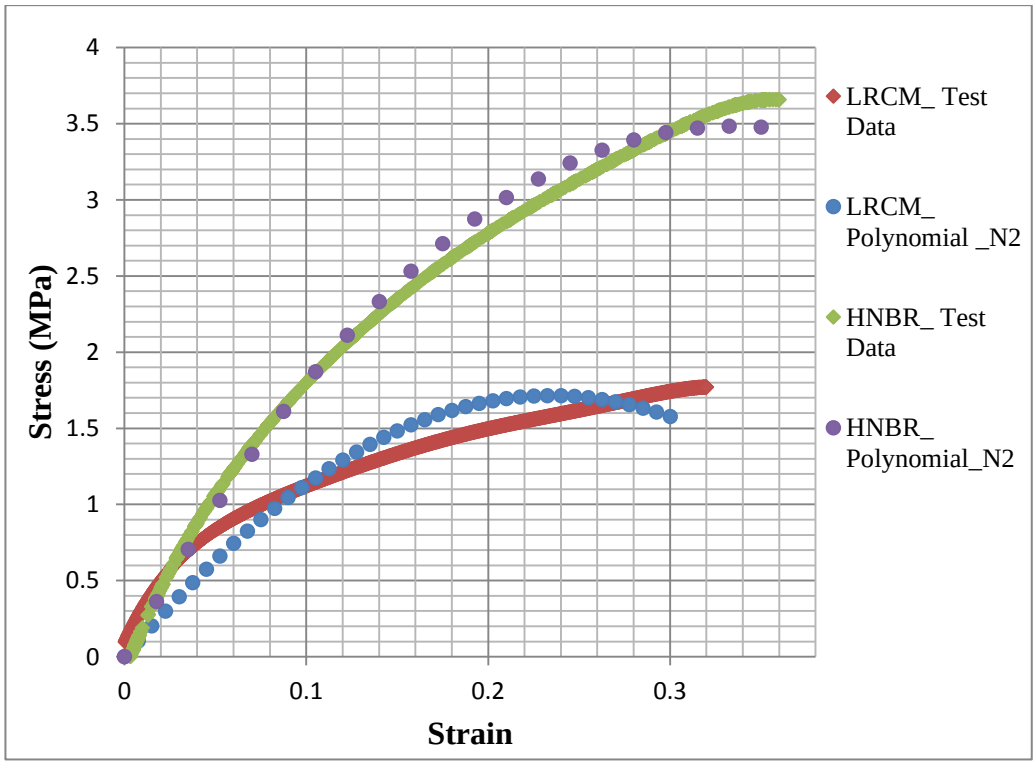

Figure 7.4 Stress-Strain curves generated from a Polynomial_N2 material model compared to test data measured under shear loading for both HNBR101 and LRCM888.

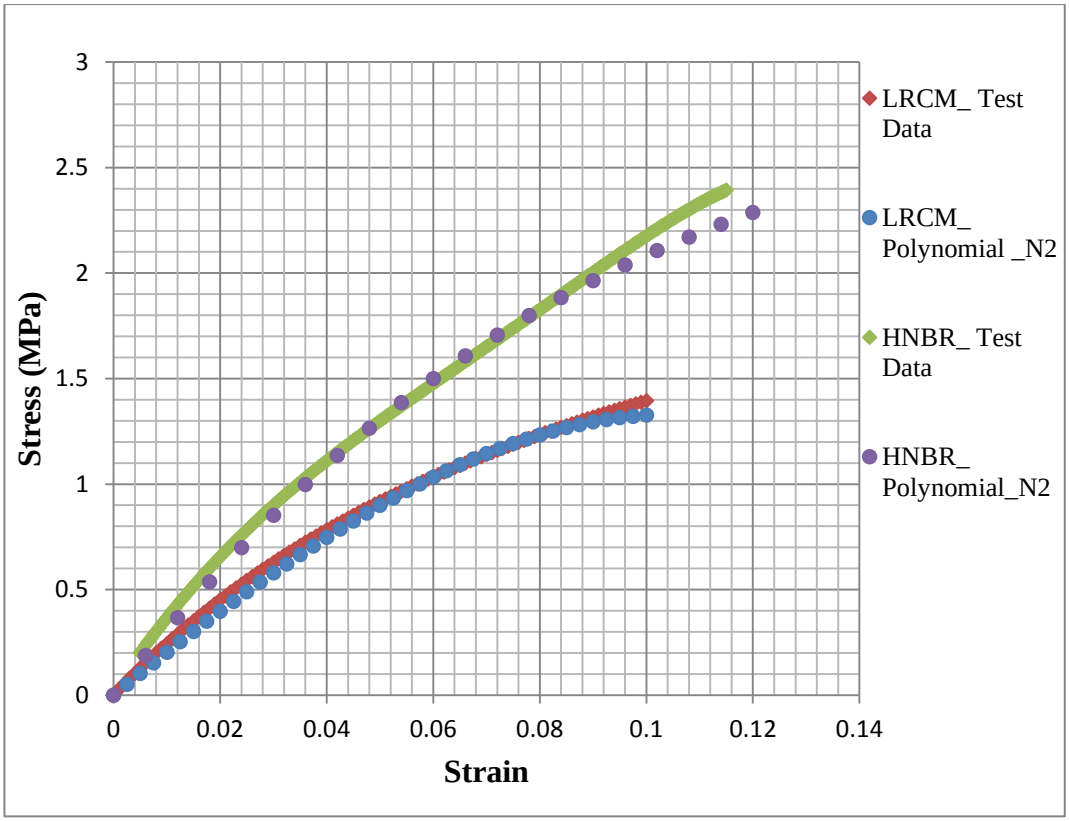

Figure 7.5 Stress-Strain curves generated from a Polynomial_N2 material model compared to test data measured under equibiaxial loading for both HNBR101 and LRCM888.

RMSE values were calculated to measure the accuracy of the material model using, the equation shown in 7.1.

$$RMSE = \sqrt{\frac{1}{n}\sum_{i=1}^{n}(y_i - \hat{y}_i)^2} \qquad [7.1]$$

where y_i and $\hat{y}_i$ represent stress values from experiments and the material model respectively, n is the total number of points and the RMSE value is expressed using the same units as the quantity being predicted, in this case the quantity is stress and the units are MPa. The RMSE value indicates the average error that the material model over predicts or under predicts the actual stress value. Table 7.1 shows the RMSE values produced by the Polynomial N-2 material model for different loading conditions and the average RMSE. The average RMSE values were calculated from adding up all the RMSE values for different loading conditions and dividing by the number of loading conditions. The material model for HNBR101 was able to predict stress with an average error of ±0.109 MPa and the material model for LRCM888 was able to predict stress values with an average error of 0.107 MPa.

Table 7.1 Root mean square error values from the Polynomial N-2 material model whilst predicting multi axial stress values.

	Material	RMSE (MPa)
Uni-axial	HNBR101	0.164
	LRCM888	0.099
Equibiaxial	HNBR101	0.055
	LRCM888	0.071
Planar Shear	HNBR101	0.107
	LRCM888	0.151
Average (RMSE)	HNBR101	0.109
	LRCM888	0.107

The aim of the numerical model is to analyse the stress distribution inside an O-ring during RGD and also to evaluate the maximum sealing pressure of an O-ring in its housing gland surfaces. Both aims are mostly interested in the higher stress region. Therefore the average RMSE values of 0.109 MPa and 0.107 MPa are acceptable because at high stresses the errors are not significant. The errors are only significant at lower stresses. For instance at 5 MPa an error of ±0.109 MPa is less than 3 %, however at 0.2 MPa an error of ± 0.109 is more than a 50 % error. Therefore caution must be taken at lower stress levels.

7.1.2. Compression Test Results

FEA results of evolution of force with displacement during the compression of an O-ring by its gland surfaces were compared to the experimental results. FEA results from both the axisymmetric model and the 3D quarter model were found to be in close agreement with the experimental results as shown in Figure 7.6. A RMSE value was calculated to evaluate the numerical models accuracy.

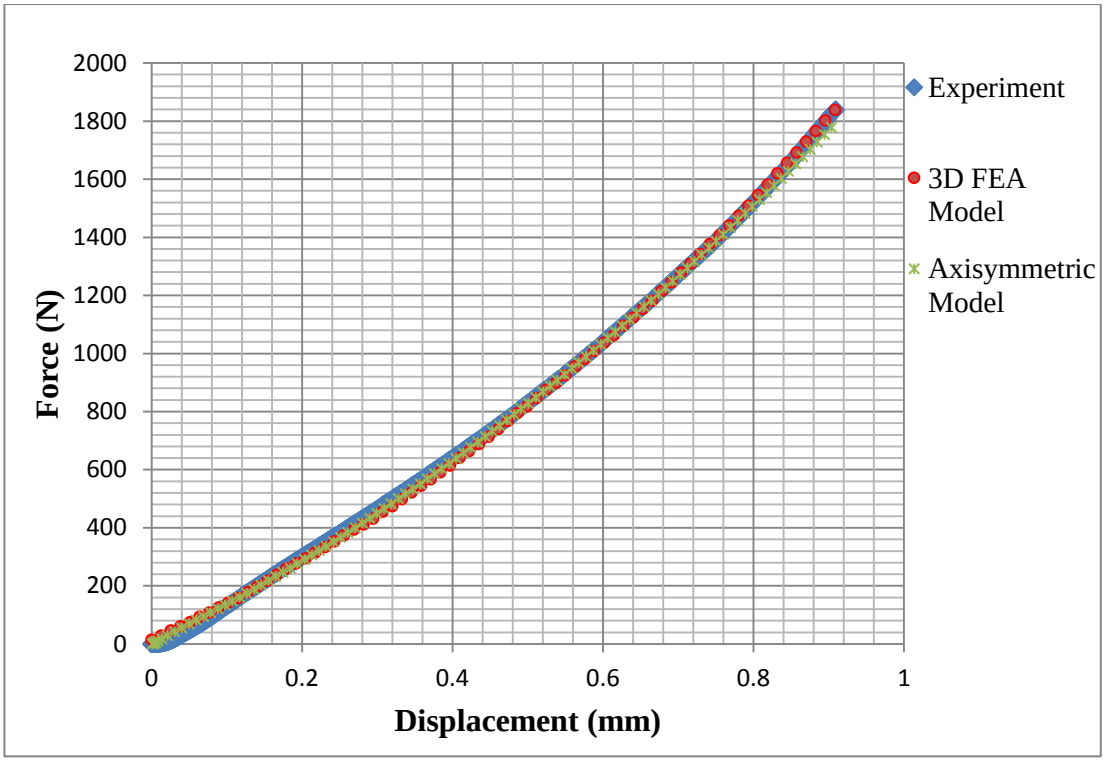

Figure 7.6 A comparison of the evolution of force with displacement between experimental data and data from the FEA analysis.

Table 7.2 shows the root mean square error (RMSE) values for the 3D FEA model and an axisymmetric model. The RMSE value indicates the average error value which the numerical model under predict or over predict the actual force values by. Both models have a RMSE value of less than 14 N. This value is only significant at low strains and because of the high forces generated during the loading of the O-ring, an error of 14 N can be neglected.

Table 7.2: Root mean square error value for the 3D Quarter FEA model and an Axisymmetric.

	RMSE (N)
3D Quarter FEA Model	13.91
Axisymmetric Model	13.34

This shows the numerical model is capable of modelling an O-ring under compression from its housing gland surfaces with acceptable accuracy. However caution should be taken when analysing results at strains lower than 2 % as shown in Figure 7.7. Figure 7.7 shows the evolution of error with strain for the 3D quarter FEA model. The error was calculated by dividing the RMSE value by force at each strain level to evaluate the

amount of error expected at that strain level. As mentioned before the model is capable of predicting the experimental results within reasonable accuracy. However the numerical model has poor accuracy at strain levels lower than 2 %.

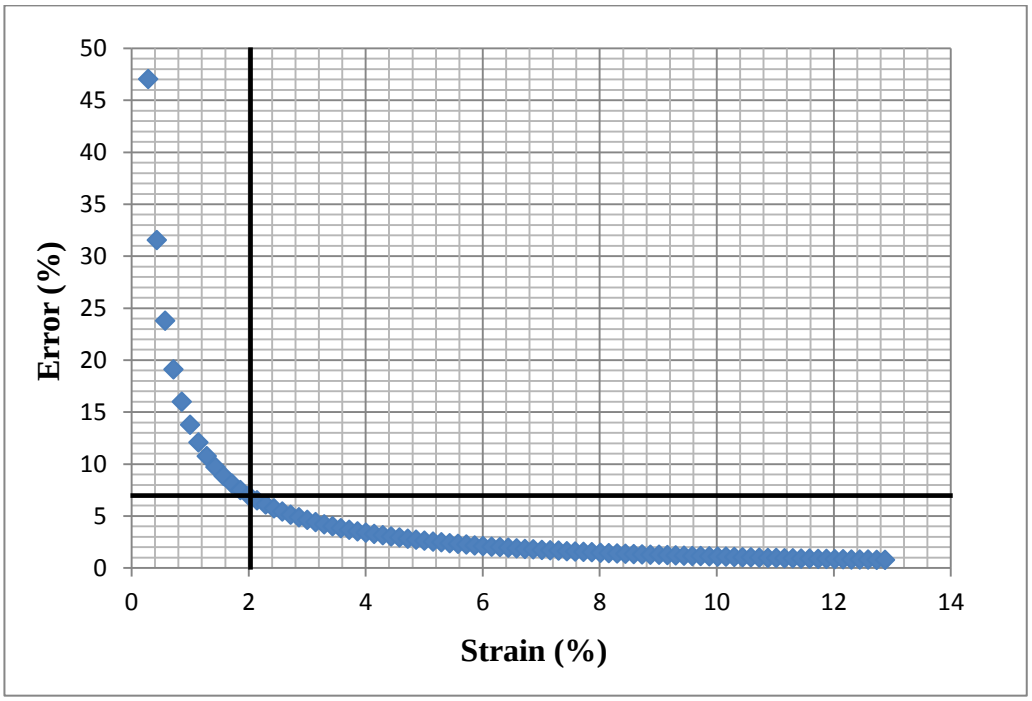

Figure 7.7 The evolution of error with strain between data from the 3D Quarter FEA model and data from the experimental analysis.

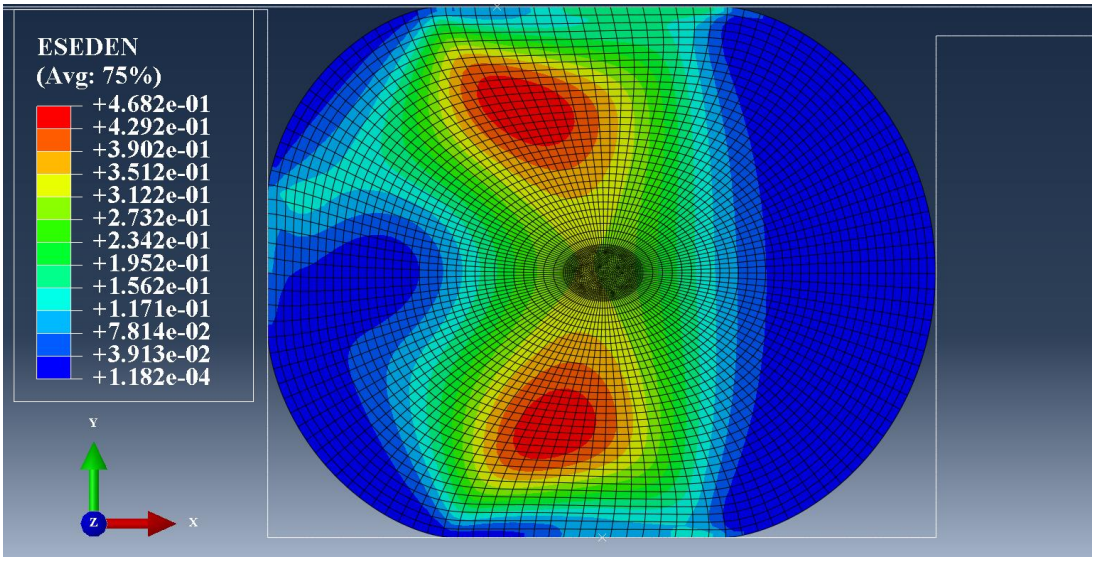

Figure 7.8 Total elastic strain energy density distribution in an axisymmetric model of an O-ring contained in its housing gland surfaces.

Figure 7.8 shows the total elastic strain energy density in the elements, after compression from the housing gland surfaces. Elements above and below the centre region in the O-ring, display the highest elastic strain energy density.

7.2. Mass Diffusion Analysis Results

A mass diffusion model was designed based on the Norsok M-710 RGD test regime. The mass diffusion model only focused on analysing the decompression cycle. The model involved allowing gas to diffuse into the O-ring until full saturation. Then release the external pressure and record the change in mass concentration with time in the O-ring as gas diffuses out. The external pressure was released at three different rates of 2 MPa, 4 MPa and 8 MPa per minute. The mass concentration values in each element during the decompression stage were written to an external file using a user subroutine.

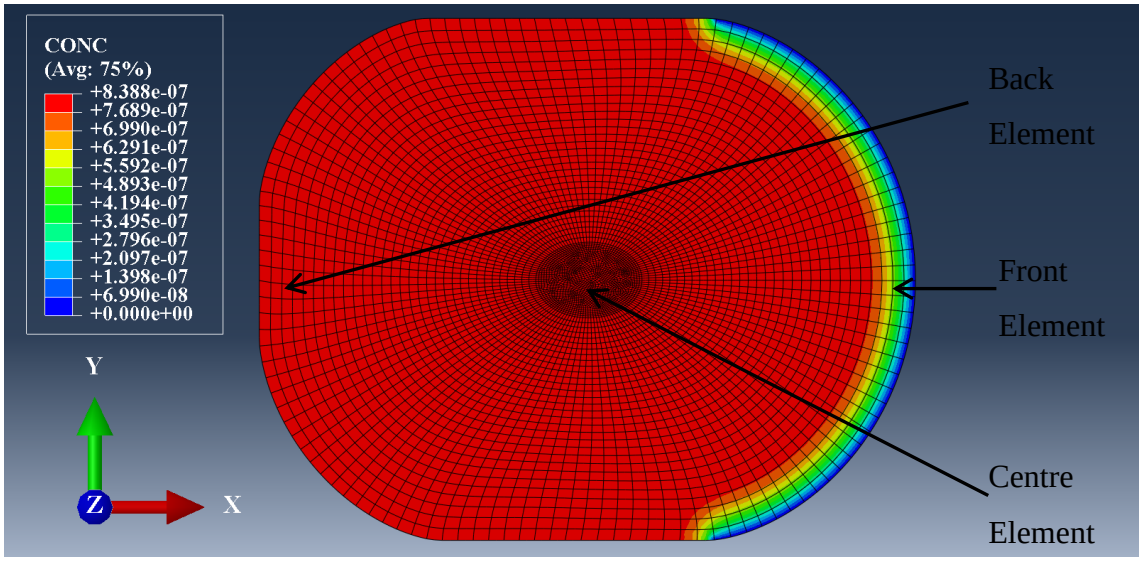

Figure 7.9 The mass concentration distribution inside an O-ring after an hour during the decompression cycle at a rate of 4 MPa per minute.

Figure 7.9 shows the carbon dioxide mass concentration distribution inside the O-ring after an hour during the decompression cycle at a rate of 4 MPa per minute. There is a concentration difference across the O-ring and this concentration difference results in an internal pressure difference across the O-ring. After an hour during RGD, only a small percentage of absorbed carbon dioxide had diffused out of the O-ring. The time taken for carbon dioxide to diffuse out of the O-ring in the numerical model is not exactly representative of the actual time it takes for carbon dioxide to diffuse out of the O-ring in the experiments. This is because the permeation data used in this analysis was

measured at different conditions than those experienced during the RGD process. However the mass diffusion behaviour should be similar. Figure 7.10 shows the evolution of mass concentration with time in three elements across the cross-section of an O-ring shown in Figure 7.9. The rate of change in mass concentration with time in each element is affected by the position of the element and also by the diffusion and solubility coefficients. The higher the diffusion coefficient, the higher the rate of change in mass concentration in each element as the absorbed gas diffuses out of the O-ring.

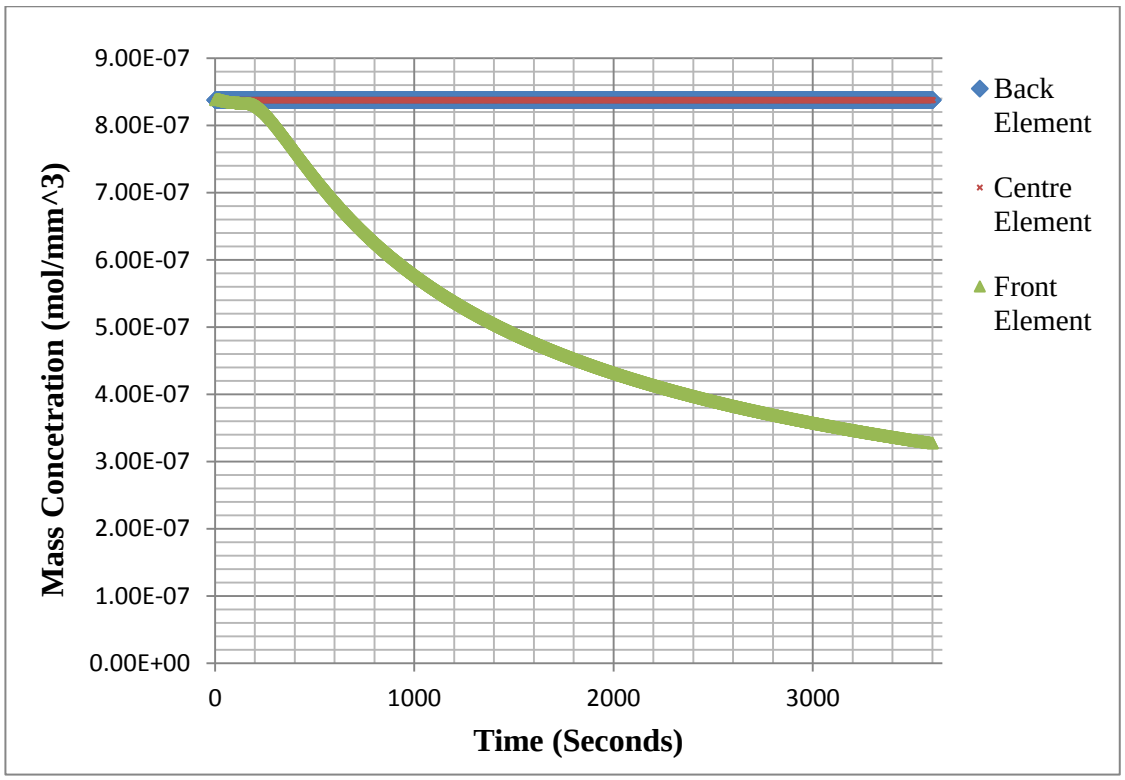

Figure 7.10 Evolution of mass concentration with time at three different points across the O-ring's cross-section.

The concentration values during the decompression stage were written to an external file using a user subroutine. Table 7.3 shows the mass concentration values of the first ten elements at increment equal to 1 and time equal to 1 second. The first row contains the increment number and time in seconds respectively. The first column in the second row contains the element number and the second column in the second row contains the corresponding concentration values in each element. The full external file contains concentration values for up to 5520 elements and for a time of 3600 seconds. The full external file is too big to show in this thesis. The external file which is written in a

format shown in Table 7.3 is written in such a way that it is easier to read the values into another user subroutine.

Table 7.3 Concentration values of the first five elements at the first increment and time equal to 1 second.

Element Number	Concentration (mol/mm^3)
1	0.000000837840
2	0.000000837840
3	0.000000837840
4	0.000000837840
5	0.000000837840

7.3. Coupled Structural – Mass Diffusion Model Results

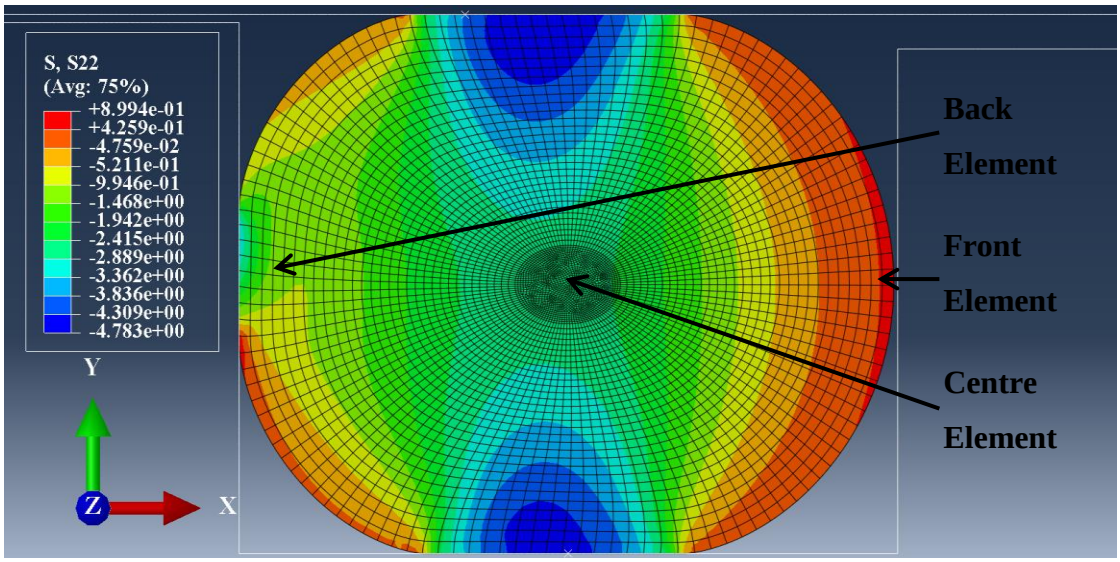

Figure 7.11 The stress distribution (S_{22}) inside the O-ring due to compression load from the O-ring housing gland surfaces and thermal expansion.

Figure 7.11 shows the stress distribution inside an O-ring after being subjected to a compression force by its housing gland surfaces and thermal expansion only. The stress (S_{22}) is non-uniform across the O-ring cross-section. Elements in the centre and the back regions are under compressive stress ($-S_{22}$) whilst some elements in the front

regions are under tension stress. Figure 7.12 shows the evolution of stress (S_{22}) in three different elements across the O-ring cross-section due to compression force from the housing gland surfaces and thermal expansion only. The highest compressive stress was experienced by elements in the centre region of the O-ring. The least compressive stresses were experienced by the elements in the front region of the O-ring as shown in Figure 7.11.

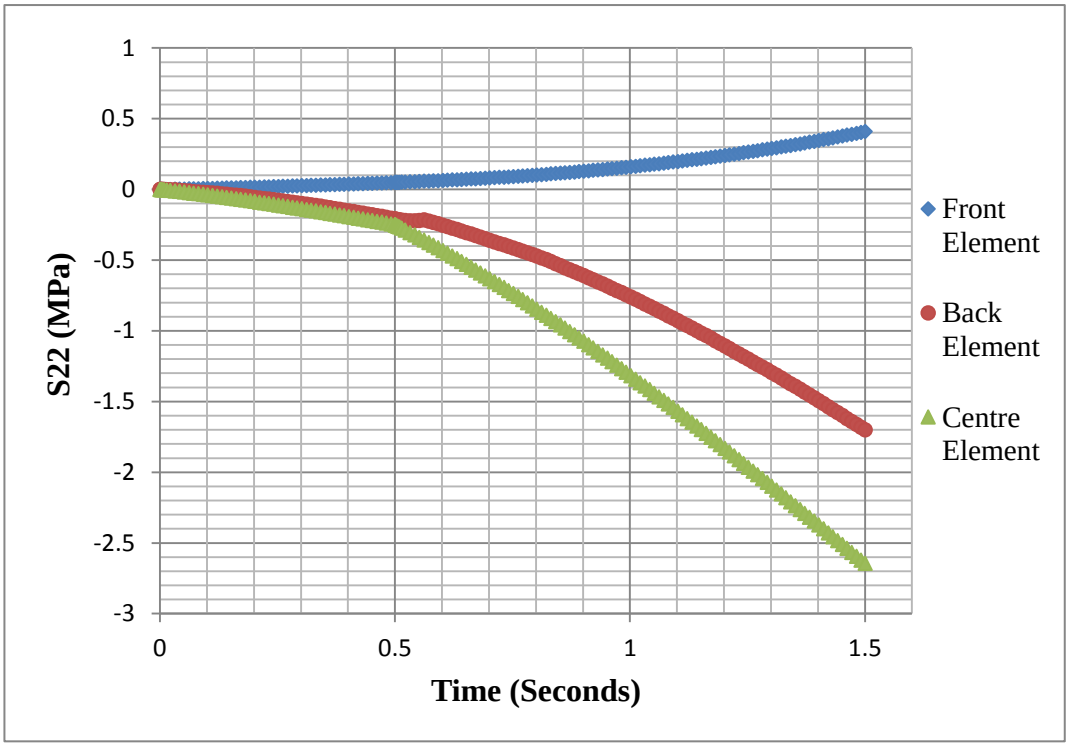

Figure 7.12 The evolution of stress (S_{22}) in three different elements across the O-ring cross-section due to compression force from the O-ring housing gland surfaces and thermal expansion.

Figure 7.13 shows the stress distribution (S_{22}) inside the O-ring after 1 second during the decompression cycle. At this stage the forces acting on the O-ring are:

- Compression force from the housing gland surfaces,
- Stresses due to thermal expansion,
- Pressure from the external working fluid and,
- Internal pressure from the absorbed gas.

Most of the elements in the O-ring are under compression in the y-direction. However as the external pressure from the working fluid is reduced most of the elements will

experience a stress state change from compression to tension as the decompression cycle continues.

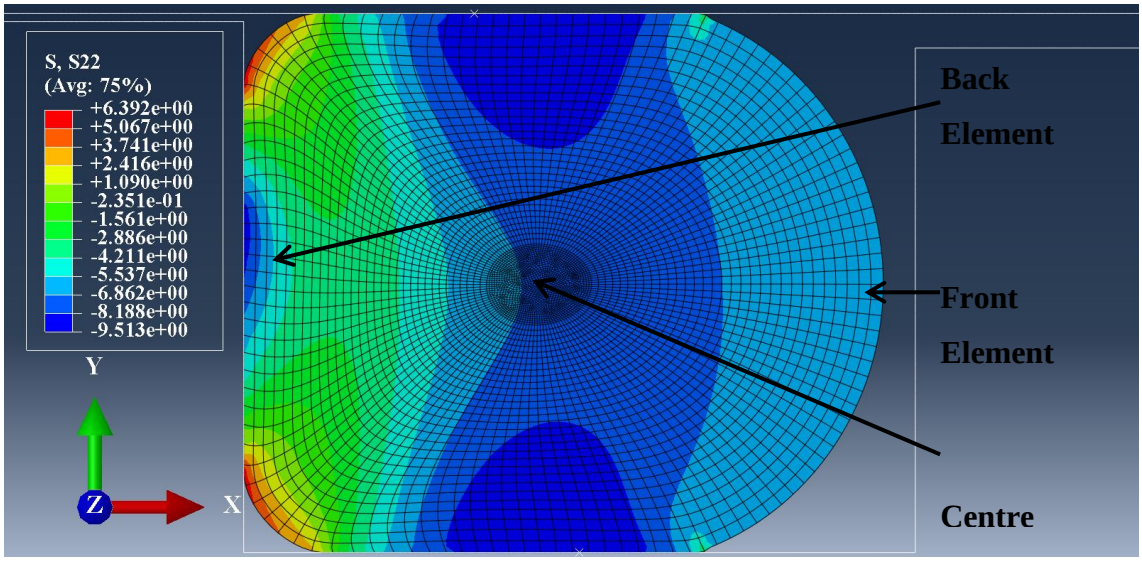

Figure 7.13 The stress distribution (S_{22}) inside the O-ring after 1 second during the decompression cycle.

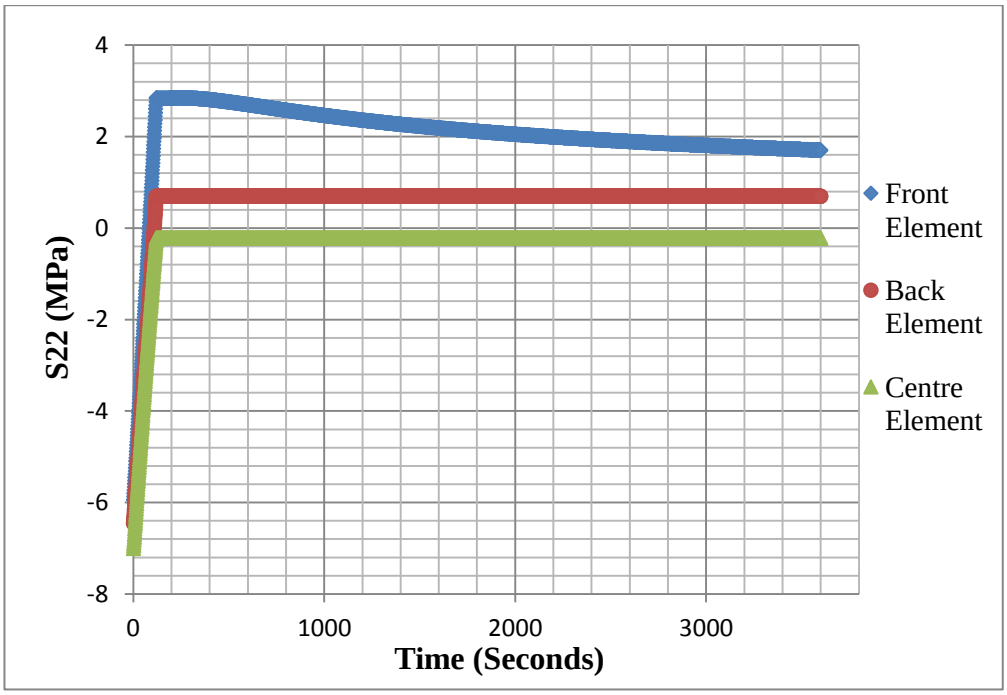

Figure 7.14 The evolution of stress (S_{22}) with time in three different elements across the O-ring cross-section during the decompression cycle.

Figure 7.14 shows the evolution of stress in the y-direction with time in three different elements shown in Figure 7.13. The stress values are averaged values at the centroid of each element. The plot shows that the stress (S_{22}) changes from compression to tension

during the first few minutes of the decompression cycle. The stress state change is a result of the reduction of external pressure from the working fluid. This stress state change is probably the reason for the formation of hackle lines on the fracture surfaces of failed O-rings and spring seals as observed in section 5.1. The front elements showed the highest tensile stresses (S_{22}) however, as the gas diffused out more rapidly in the front elements, the stress in the front elements dropped rapidly compared to other elements.

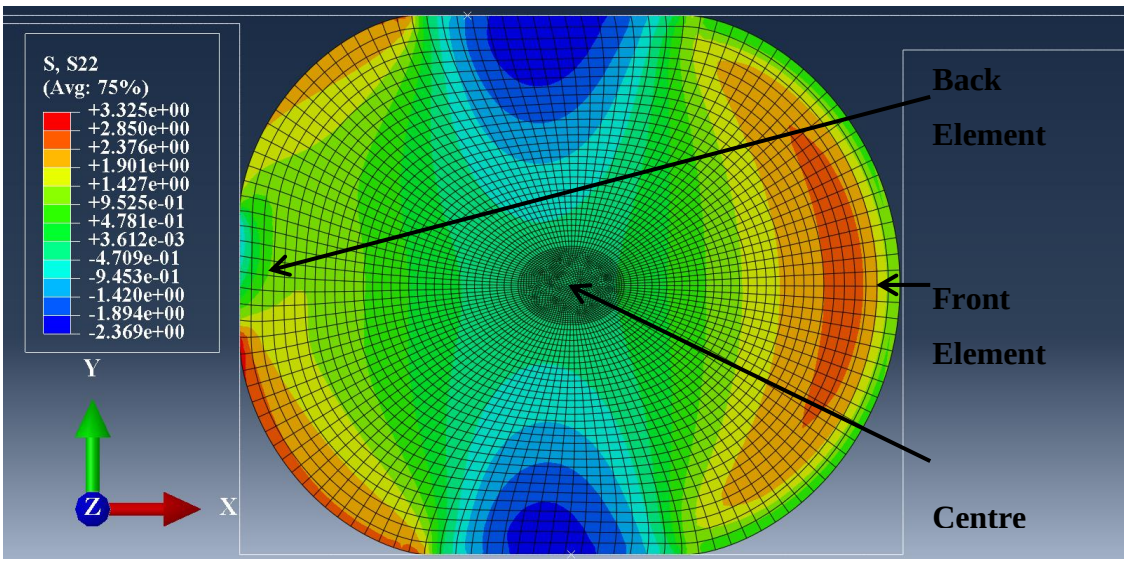

Figure 7.15 The stress distribution (S_{22}) inside the O-ring after an hour during the decompression cycle.

Figure 7.15 shows the stress (S_{22}) distribution inside the O-ring after an hour during the decompression cycle. At this stage the external pressure has dropped to zero hence there is no external pressure acting on the O-ring from the working fluid. The only forces acting on the O-ring are compressive stresses from the housing gland surfaces, thermal stresses and tensile stresses from the absorbed fluid. At this stage most of the elements in the O-ring are under tensile stress except elements at the top and bottom of the middle section. Elements in the front region display the highest tensile stresses.

Figure 7.16 shows the evolution of stress (S_{22}) with time in the centre element at three different decompression rates. The plot shows that the higher the decompression rate, the higher the stress rate during the first few minutes of the decompression cycle. All the other elements showed a similar trend to the one shown in Figure 7.16. This high stress rate during the first few minutes of the decompression cycle is likely the reason why elastomer O-rings fails when the external pressure is released at a faster rate. RGD

experiments conducted at James Walker & Co. Ltd (Industrial sponsor) have shown that cracks in elastomer seals occur when the external pressure is released at a faster rate and no cracks were found when external pressure is released at slower rates.

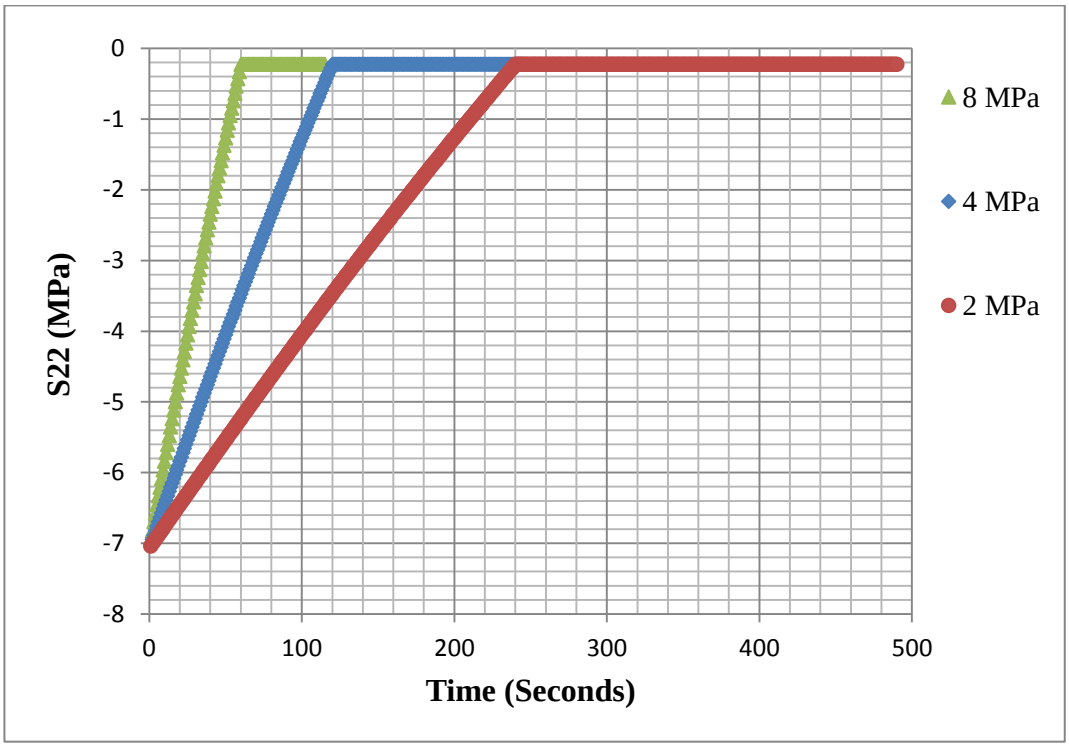

Figure 7.16 The evolution of stress (S_{22}) with time in a centre element during the decompression cycle at three different decompression rates.

Figure 7.17 shows the nominal strain (NE_{22}) distribution inside an O-ring after an hour during the decompression cycle. The highest compression strains ($-NE_{22}$) were experienced by elements in the centre region during RGD. Elements in the front and back regions of the O-ring are under small tensile strains (NE_{22}). Figure 7.18 shows the evolution of nominal strain with time in three different elements across the O-ring cross-section. The centre element displays the highest compression strains whilst the front and back elements are in tension.

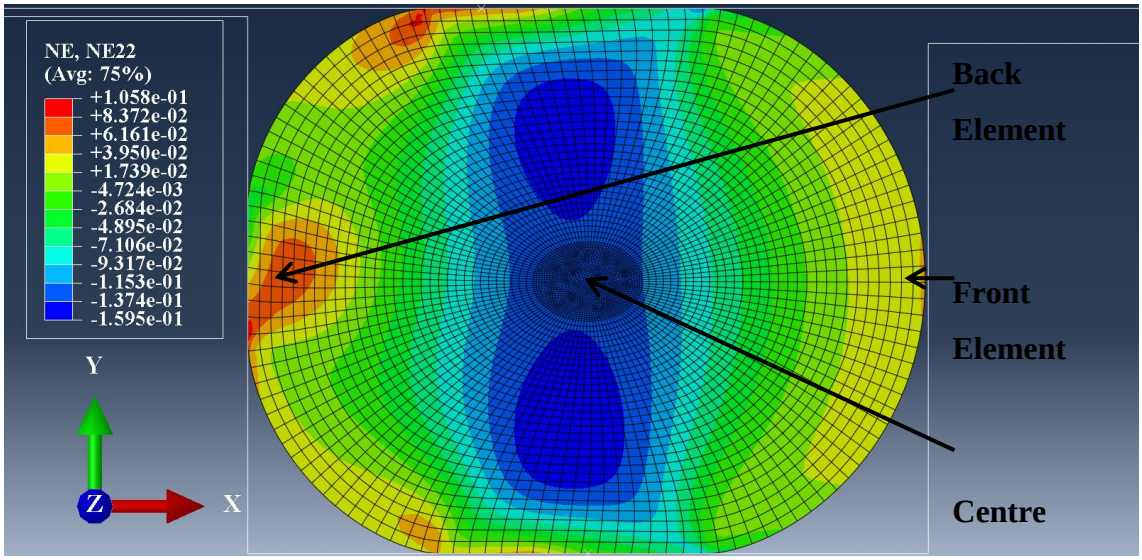

Figure 7.17 The nominal Strain (NE_{22}) distribution inside the O-ring after an hour during the decompression cycle.

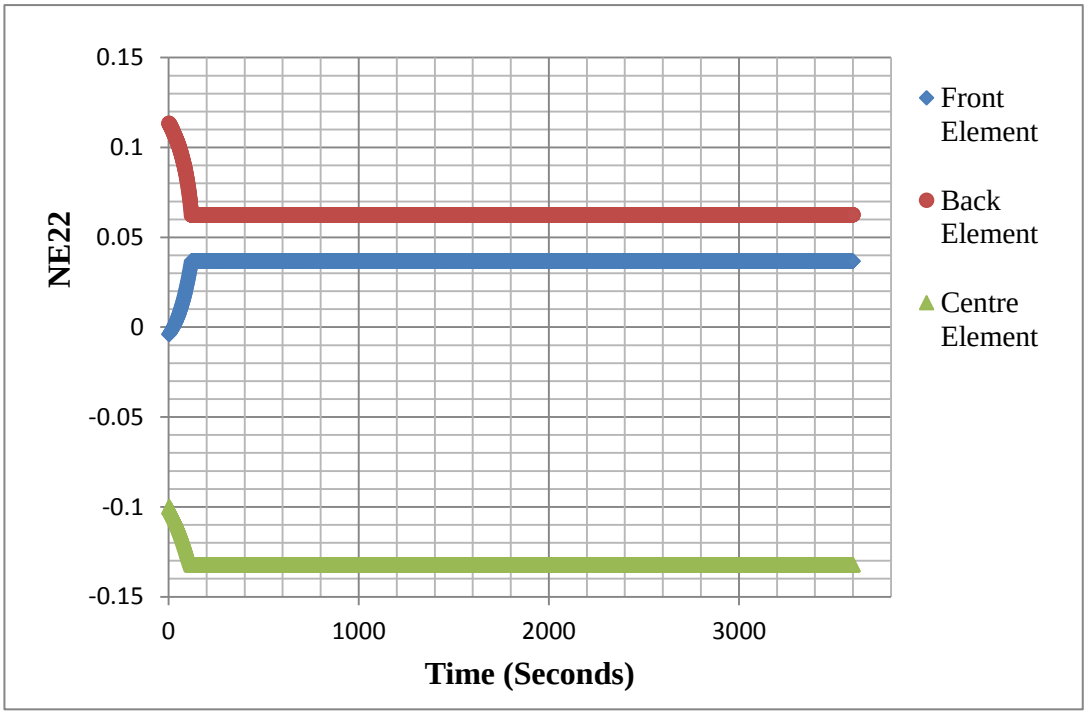

Figure 7.18 The evolution of nominal strain (NE_{22}) with time in three different elements across the O-ring cross-section during the decompression cycle.

The strain changes rapidly in the first few minutes and stays constant during the RGD cycle. The rapid change in strain during the first few minutes is due to the decrease in pressure exerted by the working fluid. The stress (S_{22}) in the front elements gradually dropped as the absorbed gas diffused out however the strain almost remains constant as the absorbed gas diffuses out.

Figure 7.19 shows the stress (S_{11}) distribution inside the O-ring and at this point the forces acting on the O-ring are compression force from the housing gland surfaces and stresses from thermal expansion. The stress (S_{11}) distribution is non-uniform some of the elements are under compression whilst elements in the centre region are under tension loading in the x-direction.

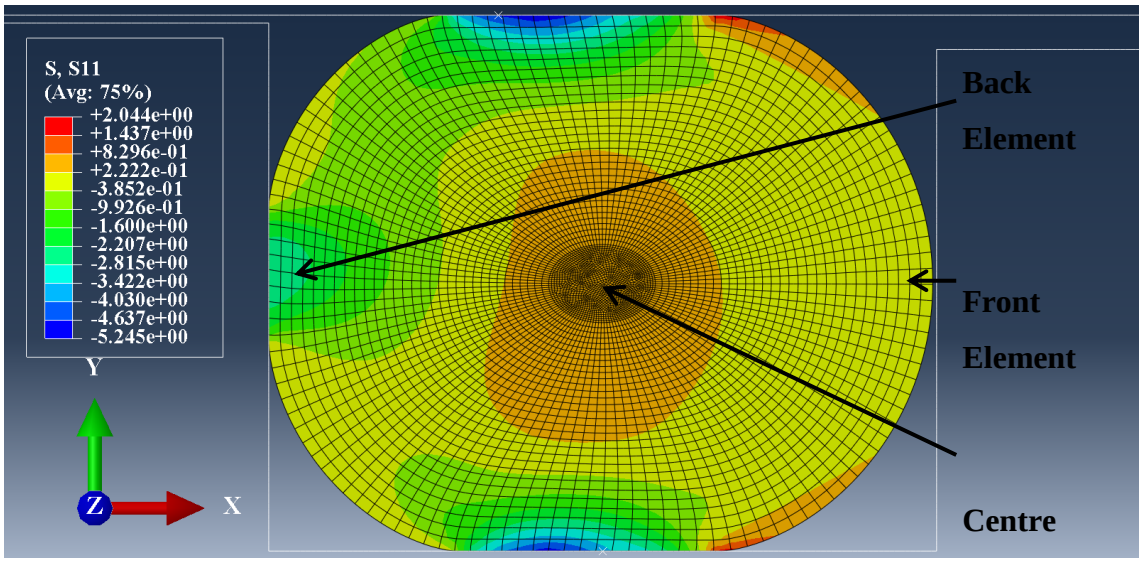

Figure 7.19 The stress distribution (S_{11}) inside the O-ring due to compression load from the housing gland surfaces and thermal expansion.

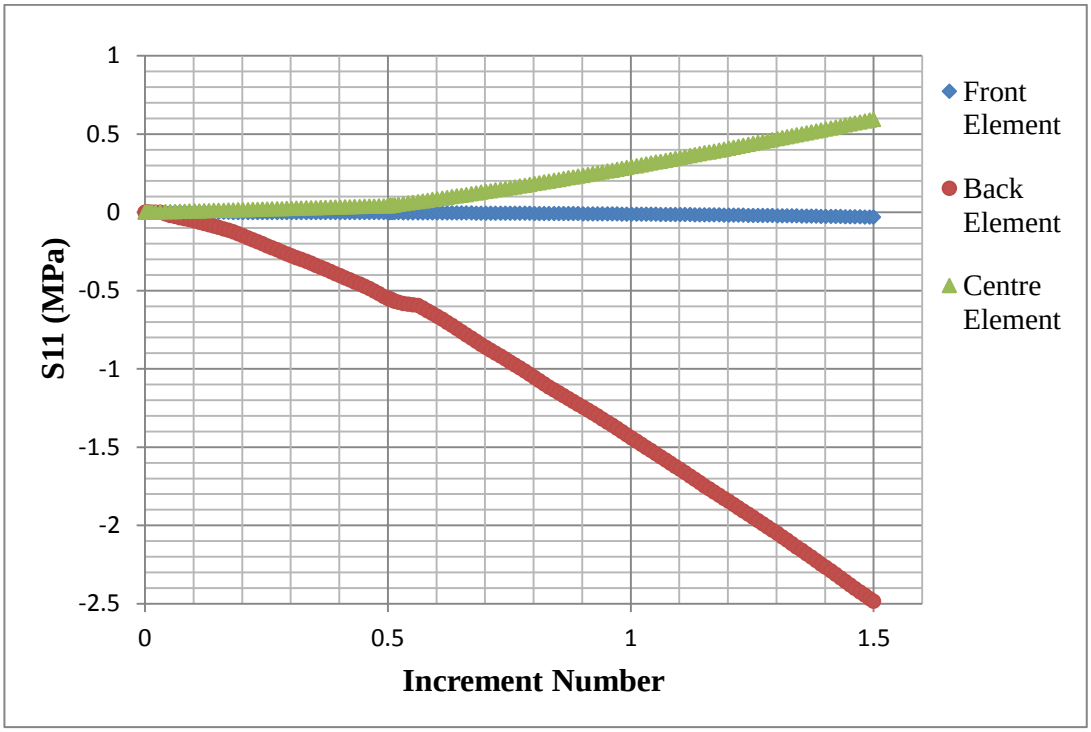

Figure 7.20 The evolution of stress (S_{11}) with time in three different elements across the O-ring cross-section during the decompression cycle.

Figure 7.20 shows the evolution of stress (S_{11}) in three different elements across the O-ring cross-section as shown in Figure 7.19. The values in Figure 7.20 represent integration point values averaged at the centroid of each element. Figure 7.20 confirms the phenomena observed in Figure 7.19, most elements in the centre region are under tensile stress in the x- direction.

Figure 7.21 shows stress (S_{11}) inside the O-ring after 1 second during the decompression cycle. At this stage the forces acting on the O-ring are:

- Compression force from the housing gland surfaces,
- Stresses due to thermal expansion,
- Pressure from the external working fluid and,
- Internal pressure from the absorbed gas.

Most of the elements in the O-ring are under compression in the x-direction. However as the external pressure from the working fluid is reduced most of the elements will experience a stress state change from compression ($-S_{11}$) to tension (S_{11}).

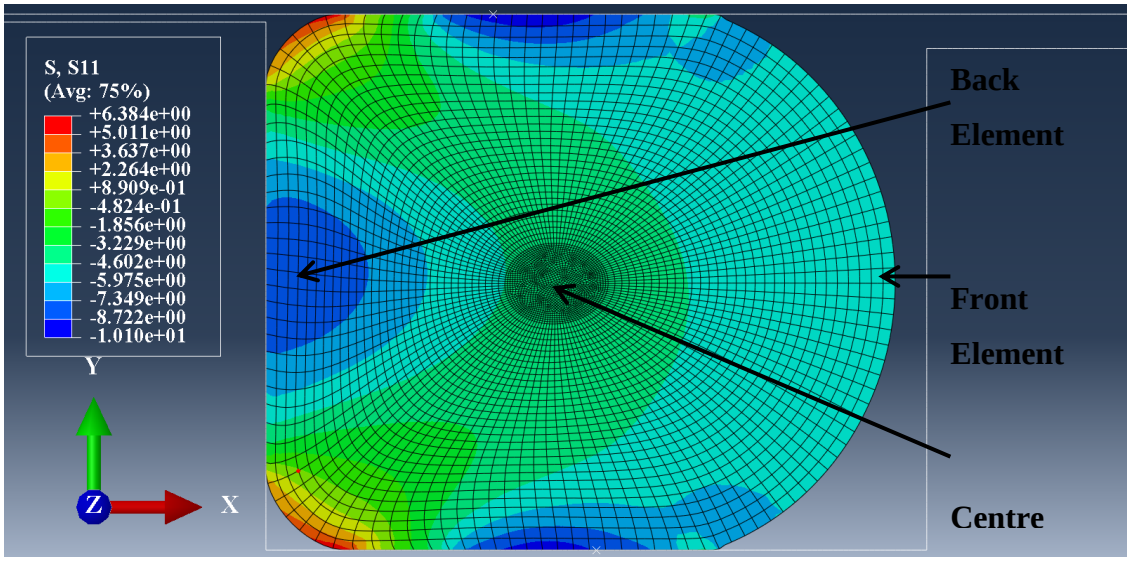

Figure 7.21 The stress distribution (S_{11}) inside the O-ring after 1 second during the decompression cycle.

Figure 7.22 shows the evolution of stress (S_{11}) with time in three different elements across the cross-section of the O-ring. There is a stress-state change in all the elements, from compression to tension during the first few minutes of the decompression cycle. In the three elements compared, the centre elements show the highest tensile stress (S_{11}).

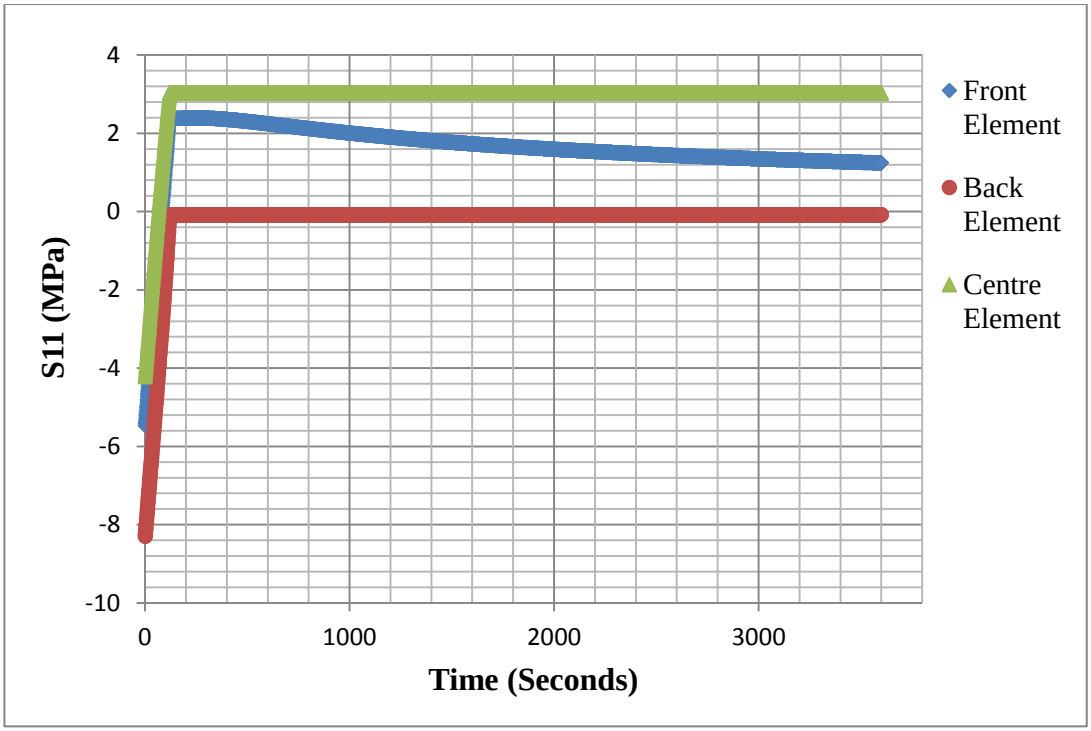

Figure 7.22 The evolution of stress (S_{11}) with time in three different elements across the O-ring cross-section during the decompression cycle.

Figure 7.23 shows the stress distribution inside the O-ring after an hour during the decompression cycle. Most of the elements in the O-ring are under tensile stress in the x-direction with elements in the centre region experiencing higher tensile stresses.

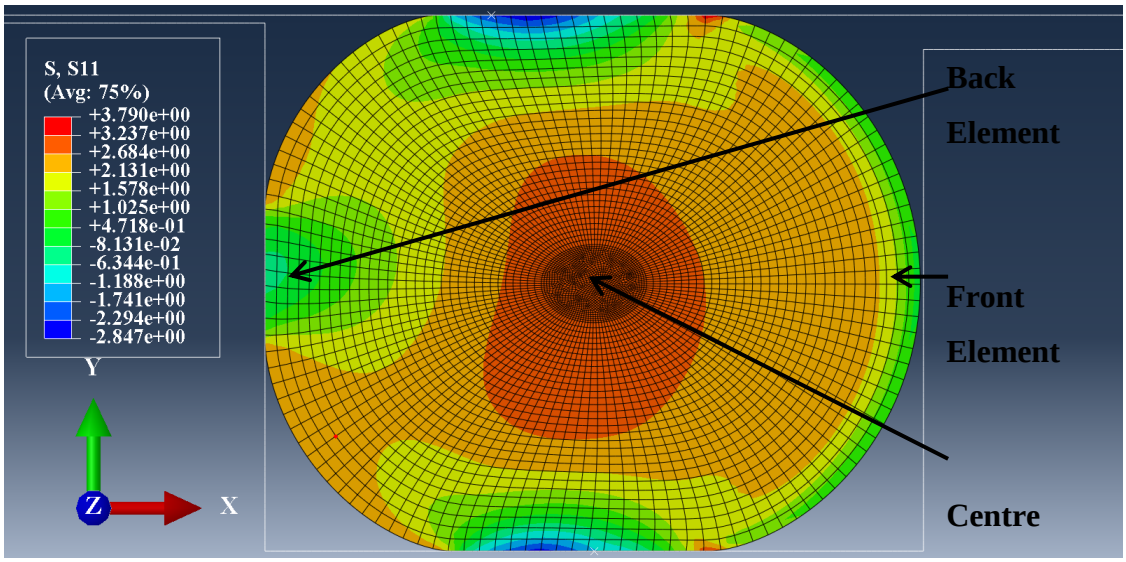

Figure 7.23 The stress distribution (S_{11}) inside the O-ring after an hour during the decompression cycle.

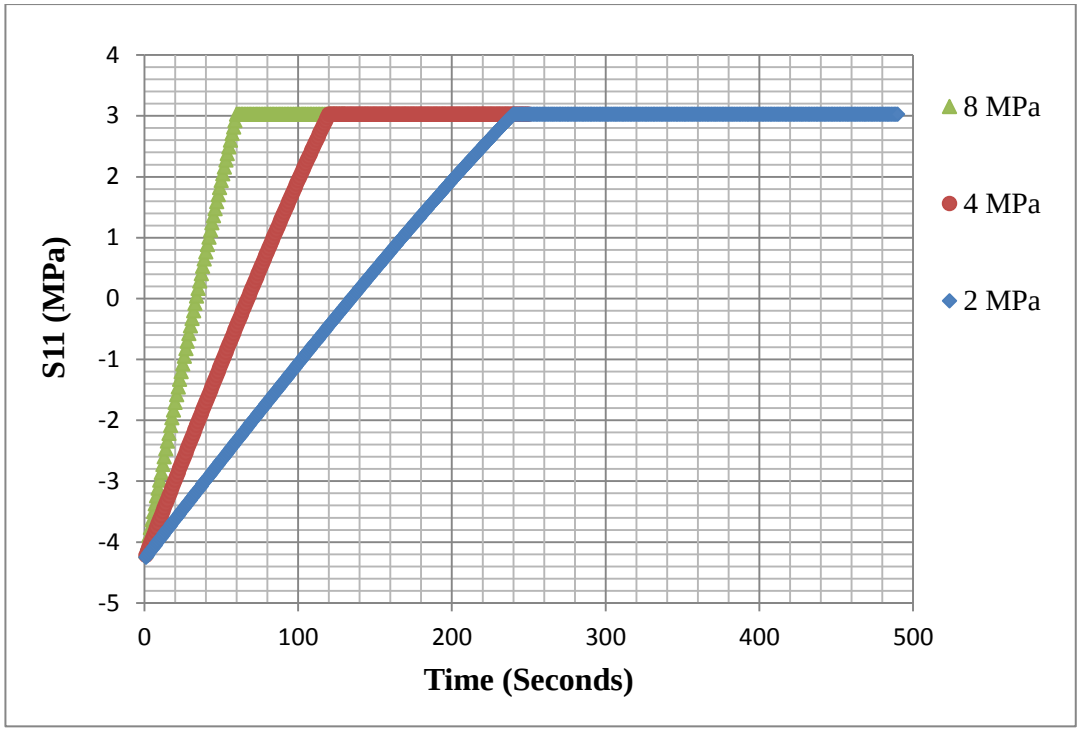

Figure 7.24 The evolution of stress (S_{11}) with time in a centre element during the decompression cycle at three different decompression rates.

Figure 7.24 shows the evolution of stress (S_{11}) with time in a centre element at different decompression rates. The stress rate is dependent on the decompression rate, the higher the decompression rate, the higher the stress rate.

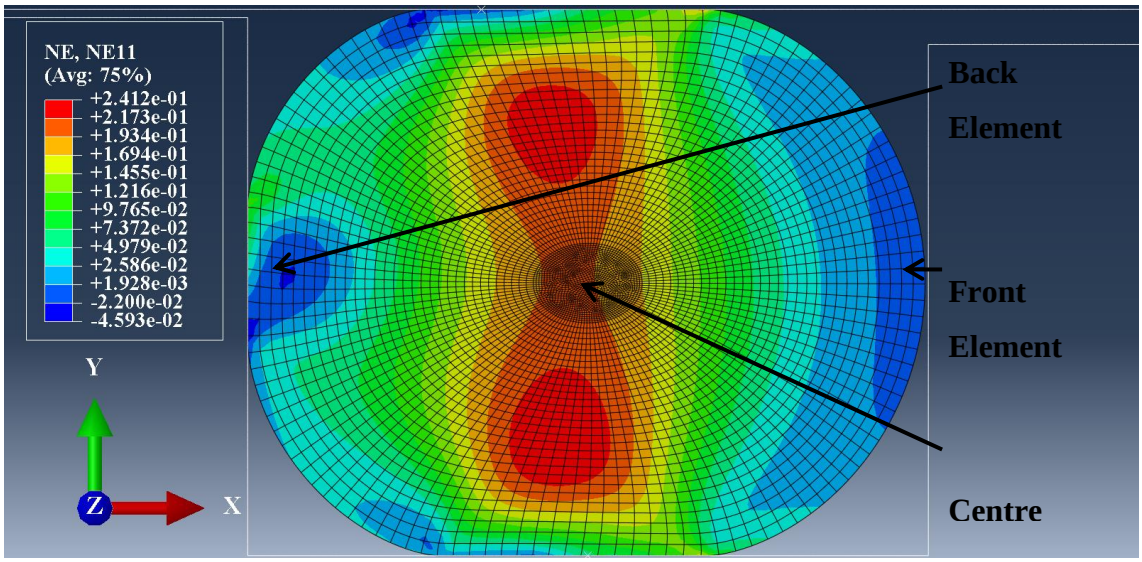

Figure 7.25 The nominal Strain (NE_{11}) distribution inside the O-ring after an hour during the decompression cycle.

Figure 7.25 shows the nominal strain NE_{11} distribution inside an O-ring after an hour during the decompression cycle. The elements in the centre region experience the highest tensile strain in the x-direction, whilst elements in the front and back of the O-ring cross-section show the least tensile strains (NE_{11}). The combination of high tensile strains (NE_{11}), tensile stresses (S_{11}) and a high concentration of voids is probably the reason cracks tend to initiate and propagate in the centre region and normal to the external pressure as observed in the RGD experiments and as noted by Rispin (1985).

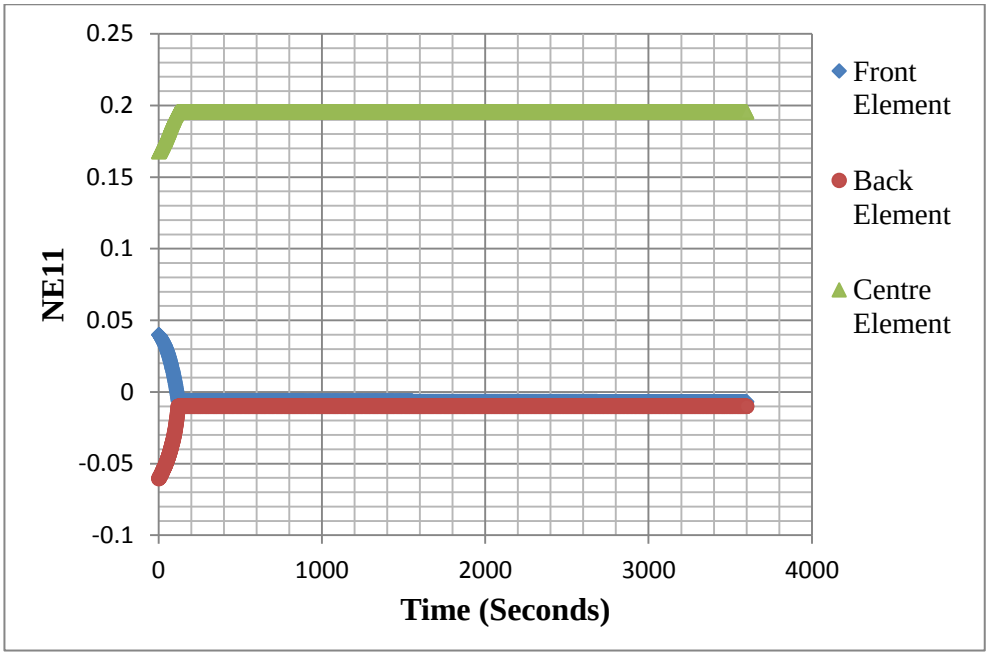

Figure 7.26 The evolution of nominal strain (NE_{11}) with time in three different elements across the O-ring cross-section during the decompression cycle.

Figure 7.26 shows the evolution of nominal strain with time in three different elements across the O-ring cross-section during the decompression cycle. Figure 7.26 also shows that NE_{11} does not significantly change as the absorbed gas diffuse out of the O-ring as observed for S_{11} especially in the front elements.

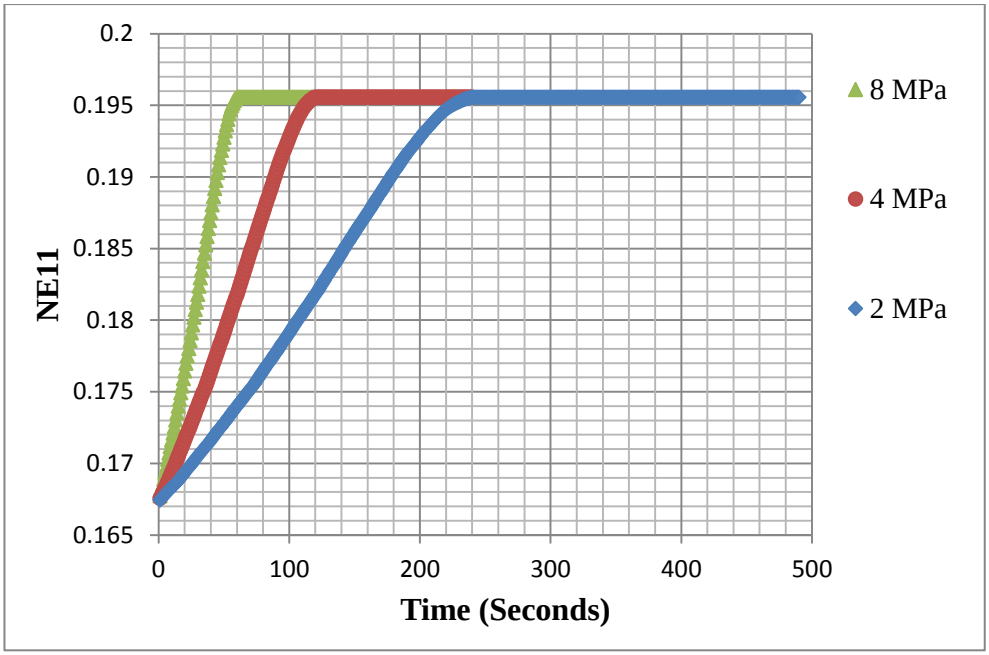

Figure 7.27 The evolution of nominal strain (NE_{11}) with time in a centre element during the decompression cycle at three different decompression rates.

Figure 7.27 shows the evolution of nominal strain with time in a centre element during the decompression cycle at three different decompression rates. Figure 7.27 also shows that the higher the decompression rate, the higher the strain rate during the first few minutes. This trend was also observed for stress and strain in the y-direction. This behaviour is why O-rings are more likely to fracture when the external pressure is released at a faster rate.

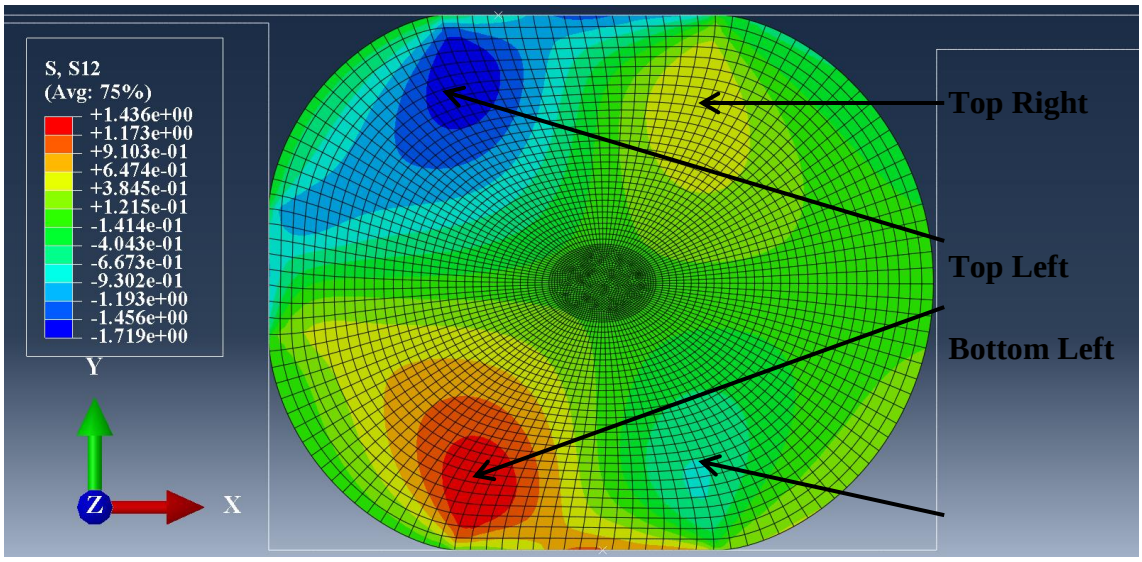

Figure 7.28 The stress distribution (S_{12}) inside the O-ring after 1 second during the decompression cycle.

Figure 7.28 shows the shear stress distribution inside the O-ring after one second during the decompression cycle. Figure 7.29 shows the evolution of shear stress (S_{12}) with time for four representative elements shown in Figure 7.28. The shear stresses are not greatly affected by the absorbed gas during the decompression cycle. However the shear stresses are affected by the compression force from the external working fluid.

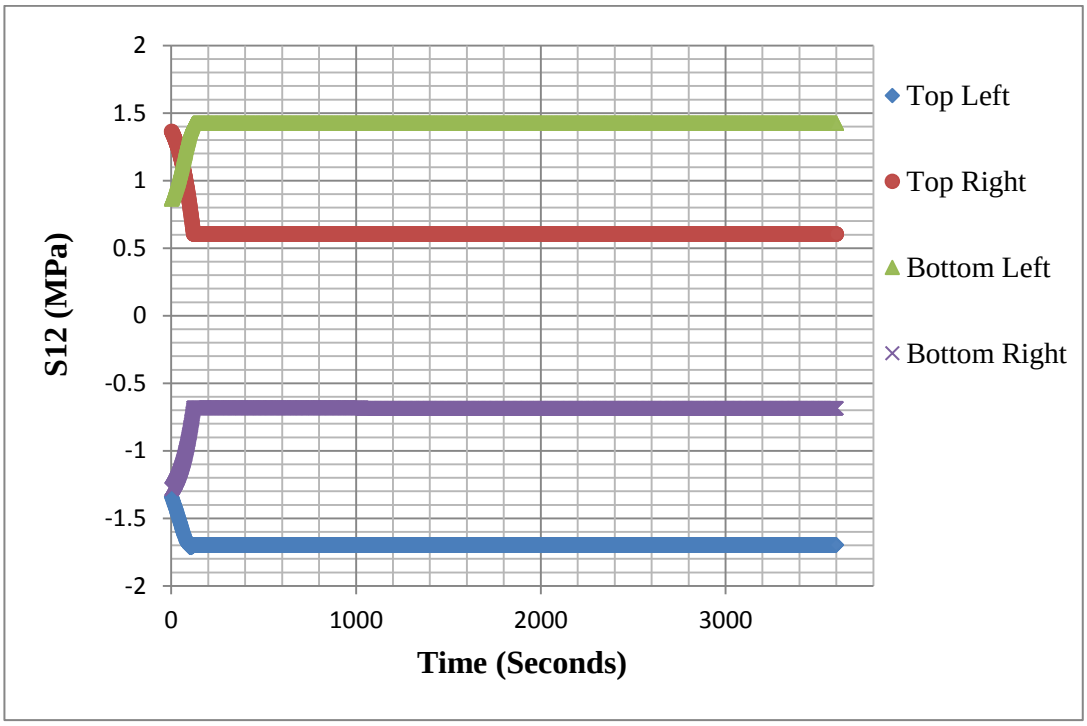

Figure 7.29 The evolution of shear stress (S_{12}) with time for four representative elements.

7.4. Numerical Model Results and Discussion Summary

A sequentially coupled structural – mass diffusion model has been proposed to model the behaviour of elastomer O-rings exposed to rapid gas decompression in the presence of CO_2 in order to evaluate the local mechanical fields and to understand the conditions necessary for damage initiation and propagation. The coupling between mass diffusion and structural deformation of the O-ring was achieved by employing the Peng-Robinson equation of state. The equation of state was used to evaluate the pressure exerted by the expanding gas inside the O-ring. User-subroutines were used to sequentially couple the mass diffusion of the absorbed gas and the structural deformation of an O-ring due to the pressure exerted by the absorbed gas.

The model has been used to evaluate the stress and strain distribution inside the O-ring during rapid gas decompression. The stress and strain distribution was shown to be affected by the external compressive stresses from the working fluid and the housing gland surfaces and by the internal tensional stresses form the expanding absorbed fluid. It has been shown that S_{11} and S_{22} go through a stress-state change from compression to tension during the decompression cycle. This stress state change is probably the reason for the formation of hackle lines on the fracture surfaces of failed O-rings and spring seals after being exposed to RGD conditions.

The FEA model revealed that elements in the centre region of the O-ring's cross-section experience the highest tensile strains and stresses in the x-direction. Computerised Tomography also revealed that there is a higher void concentration in the centre on the O-rings. The combination of high tensile strains (NE_{11}), tensile stresses (S_{11}) and a high concentration of voids is probably the reason cracks tend to initiate and propagate in the centre region and normal to the external pressure as observed in the RGD experiments and as noted by Rispin.

The strain rate during the stress-state change is dependent upon the decompression rate, the higher the decompression rate, the higher the strain rate. Rapid gas decompression experiments have shown that fracture in elastomer O-rings is more likely to occur at higher decompression rates compared to lower decompression rates.

Shear stresses (S_{12}) were mainly affected by the external force from the working fluid and the housing gland surfaces however not significantly affected by the expansion of the absorbed fluid.

8. Hybrid O-rings Results

This chapter shows the results for the hybrid O-rings. However before constructing hybrid O-rings it was important to understand how the addition of a second phase material affected the static and dynamic behaviour of the hybrid structures. This chapter contains results from experiments conducted to analyse how the addition of a second phase material affected the static and dynamic behaviour of the hybrid seals.

8.1. Tearing Strength Results

Tearing tests were conducted on hybrid crescent tearing samples and the aim of the test was to investigate how the geometry and location of the second phase material affected the structure's tearing strength. Figure 8.1, Figure 8.2 and Figure 8.3 show the failed specimens of control samples and hybrid samples 1 and 2 respectively. In Figure 8.1 cracks initiated perpendicular to the loading direction and continued to propagate until the sample failed. In Figure 8.2 the cracks initiated in the HNBR101 region and propagated perpendicular to the loading direction. When the cracks reached the LRCM888 layer, the cracks stopped and their propagation direction changed and propagated along the loading direction which was the chain realignment direction. In Figure 8.3 there was no specific crack propagation direction and the crack paths in all three specimens were different and this was mainly because cracks found it more difficult to propagate once they initiated in the LRCM888 region.

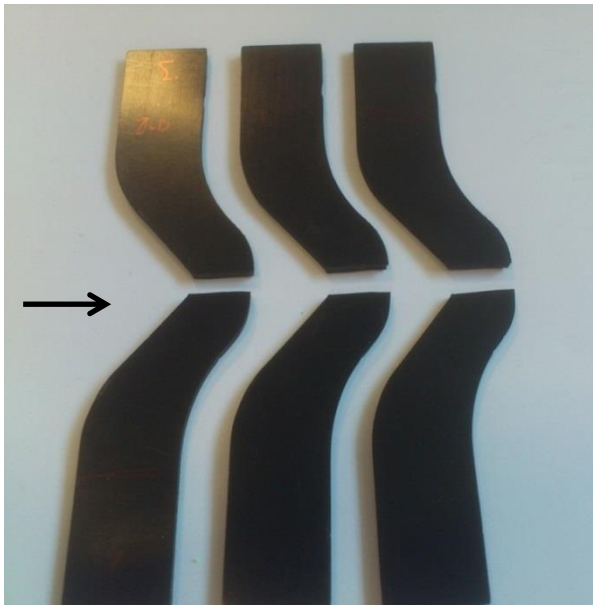

Figure 8.1 Broken sample of the control tear specimen (HNBR101).

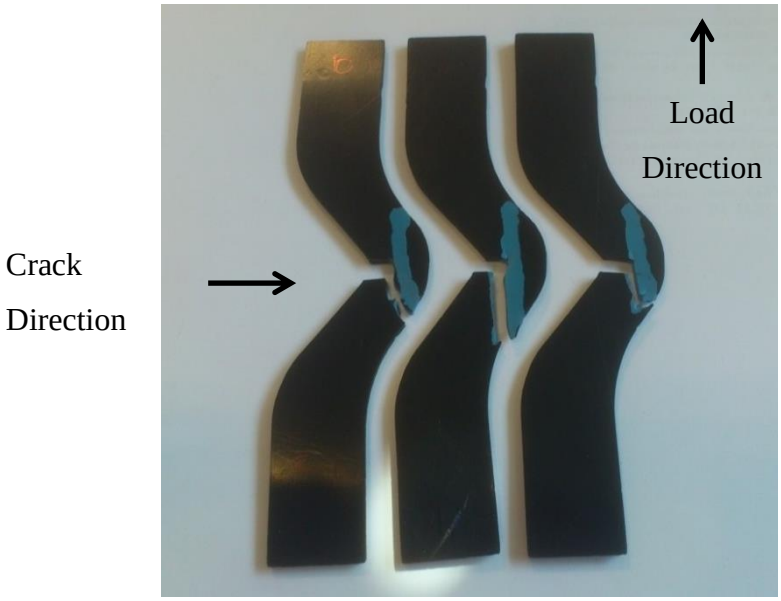

Figure 8.2 Failed specimens of hybrid 1 tearing strength sample (HNBR101 and LRCM888). Cracks initiated in HNBR101 but stopped and changed direction of propagation when the crack reached the LRCM888 layer.

Figure 8.3 Failed specimens of hybrid 2 tearing strength sample (HNBR101 and LRCM888) cracks found it more difficult to propagate once they initiated in the LRCM888 layer.

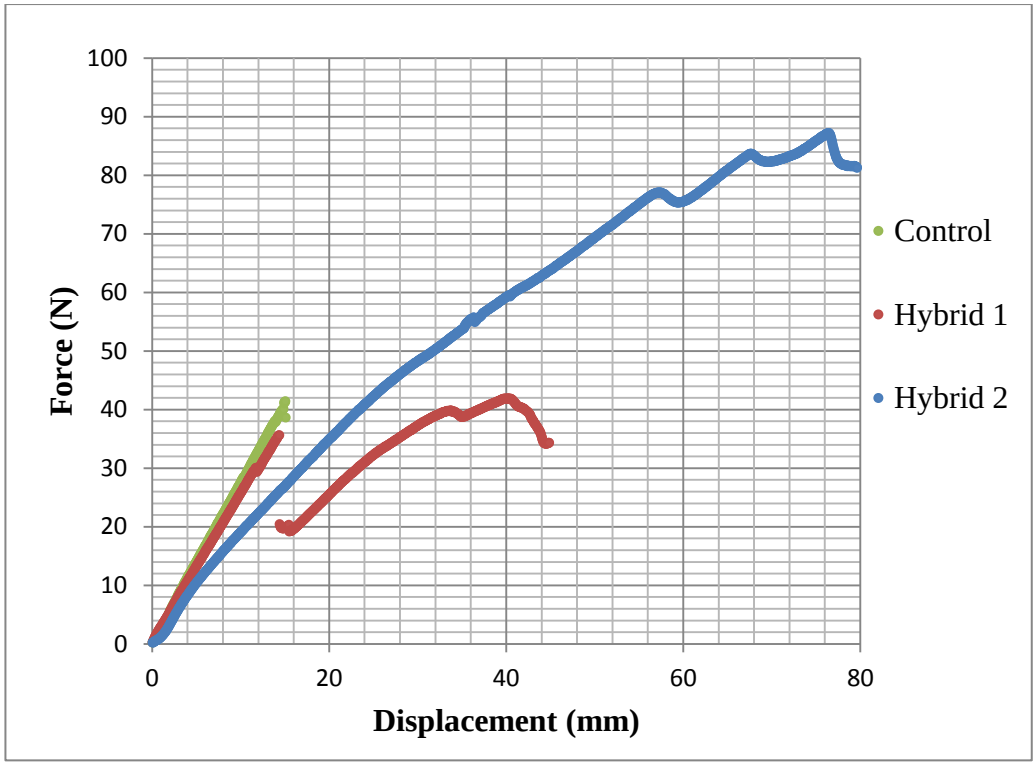

Figure 8.4 Tear test results showing the evolution of force with displacement for three different tear sample configurations.

Figure 8.4 shows the evolution of force with displacement for the control, hybrid 1 and hybrid 2 tearing strength samples. In hybrid sample 1, the crack initiated in the HNBR101 region and propagated perpendicular to the loading direction and when the crack reached the LRCM888 layer the crack arrested and changed direction. The point of crack initiation in hybrid sample 3 is shown by the sudden drop of force in Figure 8.4 and the point of crack arrest is shown by the increase in force after the sudden drop. The area under the force-displacement graph for hybrid sample 1 is higher than that of the control sample indicating a higher strain energy density before failure and this is an improvement in performance. Despite the improvement in performance in hybrid sample 1, cracks initiated at a lower force and displacement compared to the control sample. This shows that the overall work done by the hybrid specimen can be increased, however inserting the second phase material in a non-suitable region can lead to premature crack initiation.

For the same loading and displacement, hybrid sample 2 had the lowest strain energy density. However at failure, hybrid sample 2 had the highest strain energy when compared to all the other hybrid tear samples tested. The tearing strength of hybrid

sample 2 increased by more than 100 % compared to the control tear sample. Also the location of the second phase material did not result in any premature crack initiation. This indicates the highest improvement in performance. Three samples were tested for each test and the raw data is contained in Appendix J.

8.2. Fatigue Test Results

In the fatigue tests, all the control fatigue samples failed after a number of cycles less than 1500 hence the hybrid fatigue samples were tested only up to 2000 cycles. However, a few hybrid samples were left running up until failure in order to record the maximum number of cycles they could reach. Table 8.1 shows the average number of cycles and the maximum number of cycles for four different fatigue specimen designs.

Table 8.1 The average number of cycles and maximum number of cycles reached by four different fatigue specimens.

	Average Number of Cycles	**Maximum Number of Cycles**
Control	553 Cycles	1365 Cycles
Hybrid 1 Fatigue Sample	Over 2000 Cycles	3017 Cycles
Hybrid 2 Fatigue Sample	Over 2000 Cycles	23000 Cycles
Hybrid 3 Fatigue Sample	1 Cycle	2 Cycles

Figure 8.5 is a display of broken fatigue control samples. Cracks initiated on one side of the specimens and propagated across the cross-section of the control samples. The fractured surface of the control specimens displayed no macroscopically visible plastic deformation and once the crack initiated, the crack rapidly propagated through the specimen. This is an indication of a high energy fracture surface. Figure 8.6 displays the evolution of force against time for the control sample, the graph shows how the maximum force drops from 122 N to less than 100 N in the first few cycles. This drop was due to stress softening in the material and the force continues to drop gradually with time.

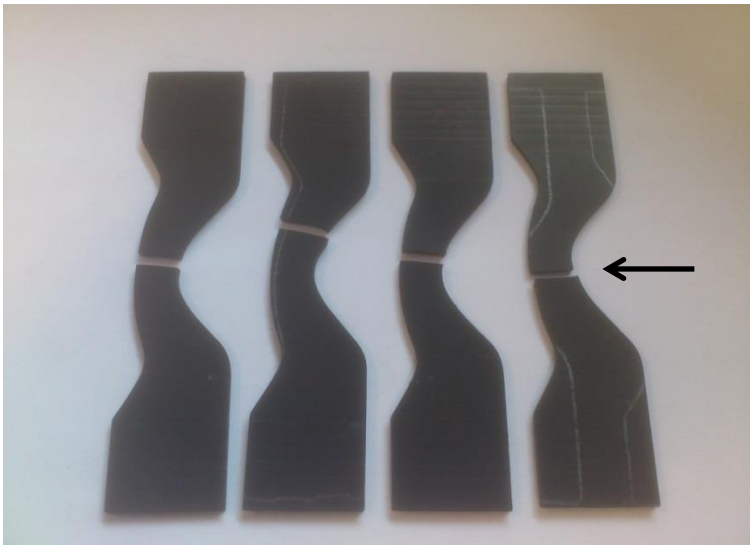

Figure 8.5 The fractured fatigue control samples with no second phase material.

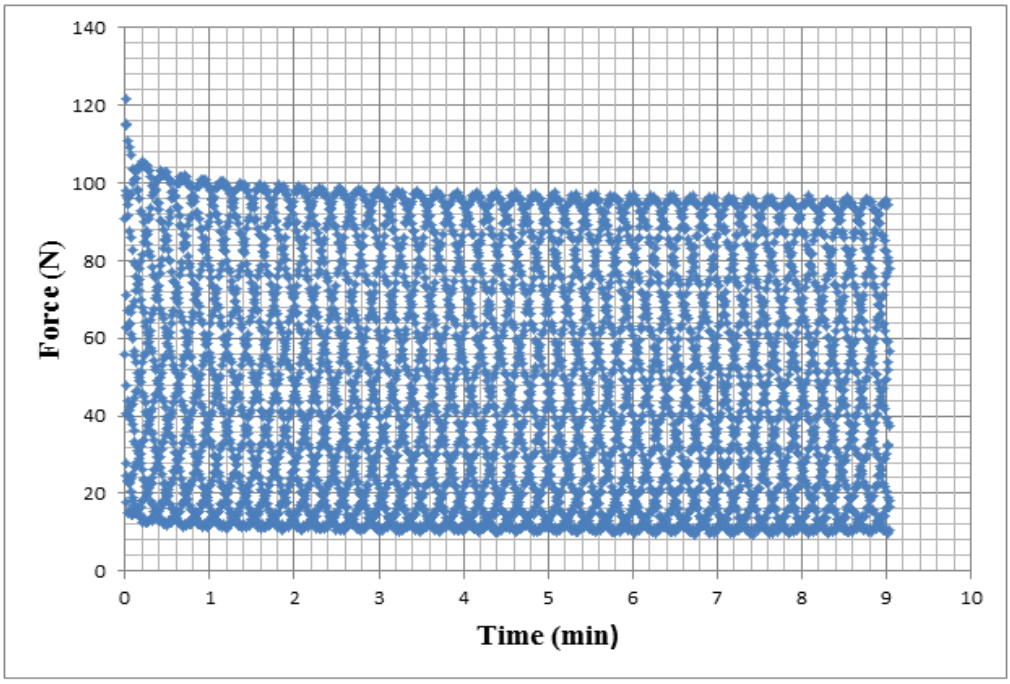

Figure 8.6 The progression of uniaxial force against time for the control fatigue specimen.

Figure 8.7 is a display of fractured hybrid 1 fatigue samples with a second phase material strip located behind the crack initiation point. The aim of this configuration was to investigate whether the second phase material is capable of stopping a crack from propagating, thereby increasing the fatigue life of the component. In Figure 8.7 cracks initiated on one side of the hybrid samples in the HNBR101 region, and propagated across the sample. When the cracks reached the LRCM888 layer, the cracks arrested and started propagating parallel to the loading direction. Cracks found it

difficult to propagate across a layer of LRCM888, however found they found it easier to propagate parallel to the loading direction (polymer chain realignment direction). The hybrid samples continued to support a load however the overall stiffness of the sample was greatly reduced.

Figure 8.8 shows the progression of uniaxial force against time for the hybrid fatigue samples shown in Figure 8.7. The graph shows the point of crack initiation, which is represented by a sudden drop in force and the point of crack arrest which is the point where force changed from dropping rapidly to dropping gradually with time. The graph also reveals a loss in overall stiffness after a few cycles. The hybrid fatigue samples shown in Figure 8.7 contained varying thicknesses of the reinforcing second phase material and it was observed that cracks initiated earlier in samples with thicker sections of the second phase material.

Figure 8.7 Display of fractured hybrid 1 fatigue samples with a second phase material located behind the crack initiation point.

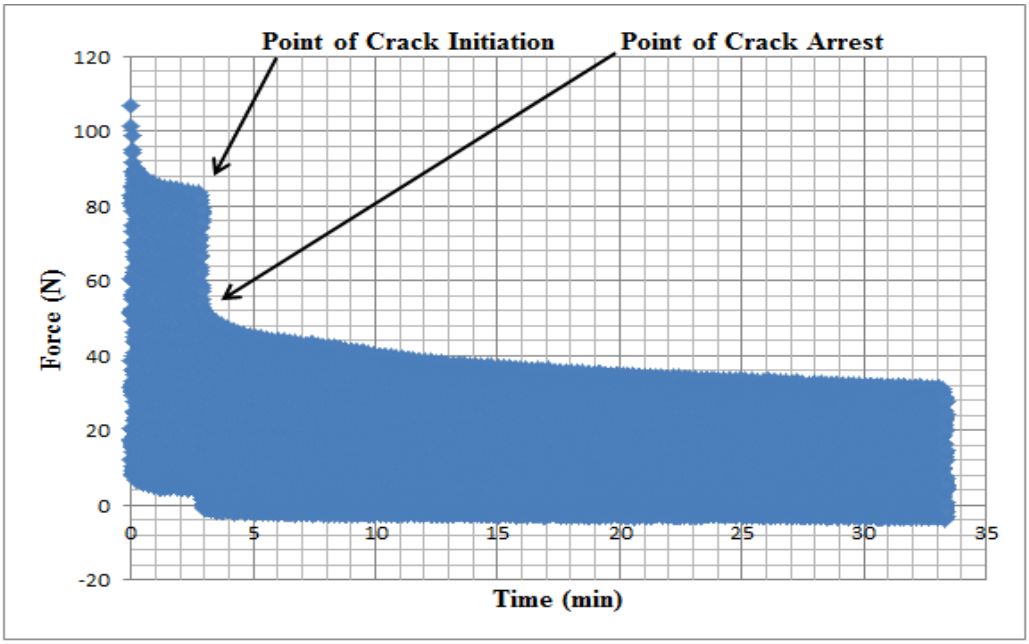

Figure 8.8 The progression of uniaxial force against time for the hybrid fatigue samples with second phase material strip below the initiation point.

Figure 8.9 is a display of hybrid samples with a second phase material strip located at the point of high stress concentration after being fatigued. None of these samples failed below 2000 cycles and the highest number of cycles recorded for one of these samples was 23000 cycles. The aim of this configuration was to investigate the effect of LRCM888 in delaying crack initiation in hybrid samples after they are subjected to dynamic loading.

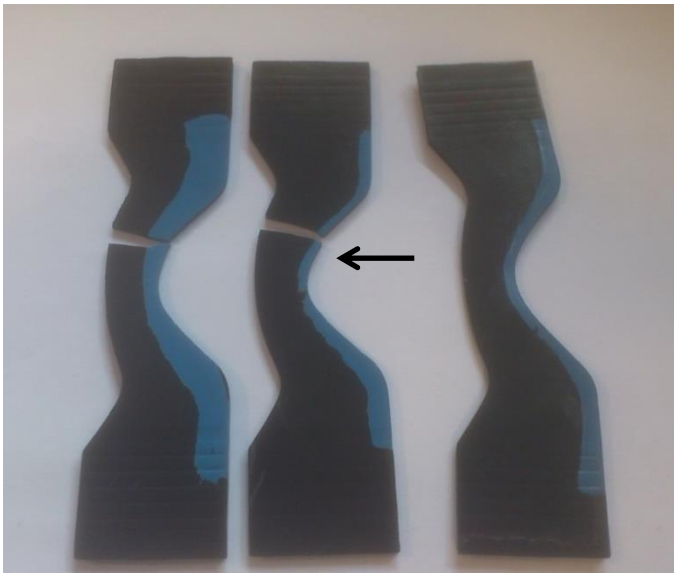

Figure 8.9 Display of fractured hybrid 2 fatigue samples with a second phase material strip located at the point of high stress concentration.

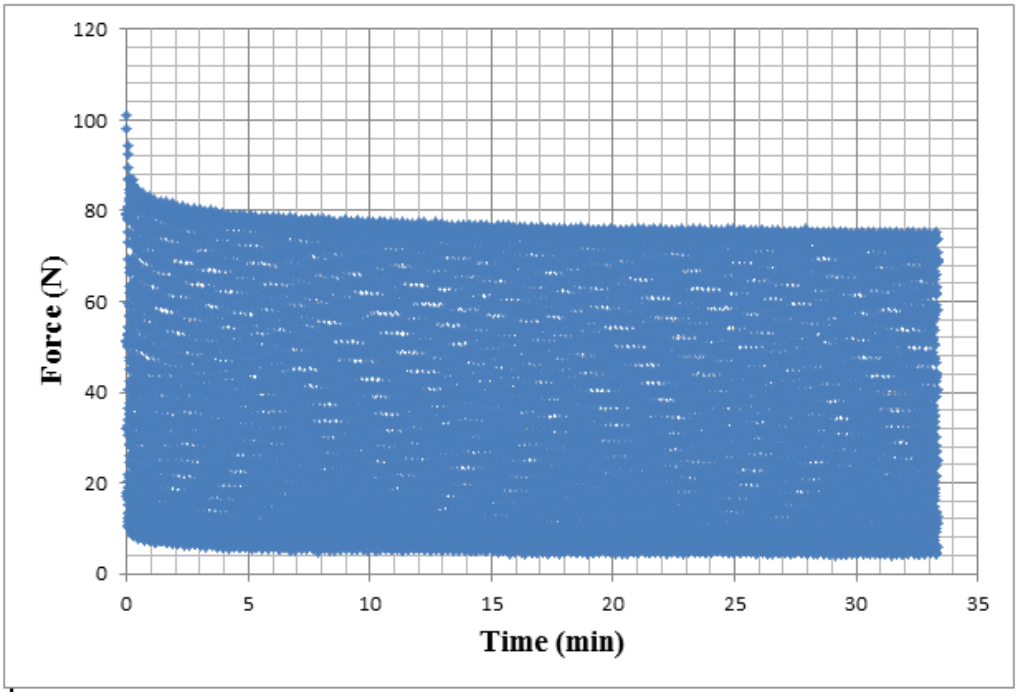

Figure 8.10 The progression of uniaxial force against time for the hybrid fatigue samples with the second phase material strip located at the point of high stress concentration.

Figure 8.10 displays the evolution of uniaxial force against time for the hybrid fatigue samples with the second phase material strip located at the point of high stress concentration. The graph shows how the maximum force drops from 100 N to less than 80 N in the first few cycles. This was due to stress softening and the force continues to drop gradually with time.

Figure 8.11 is a display of the fractured hybrid fatigue samples with the second phase material located at the point of crack initiation and in the direction of crack propagation. These samples failed after 1 or 2 cycles, and the reason for these poor results was simply down to poor design.

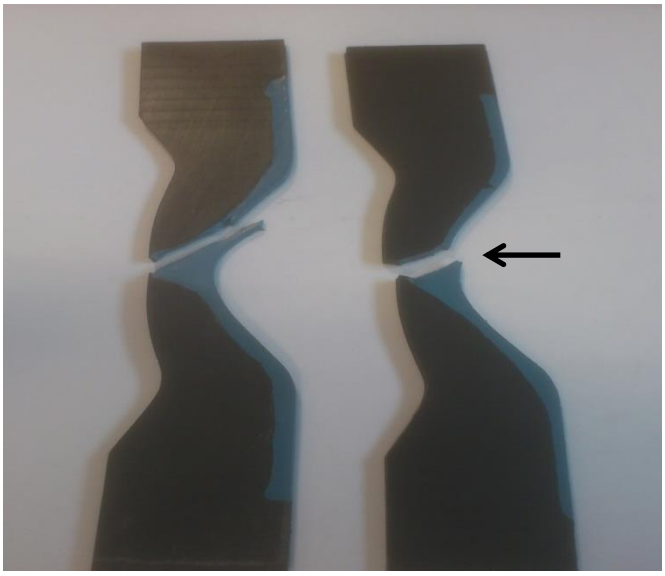

Figure 8.11 Display of the fractured hybrid design 3 fatigue samples with the second phase material located at the point of crack initiation and in the direction of crack propagation.

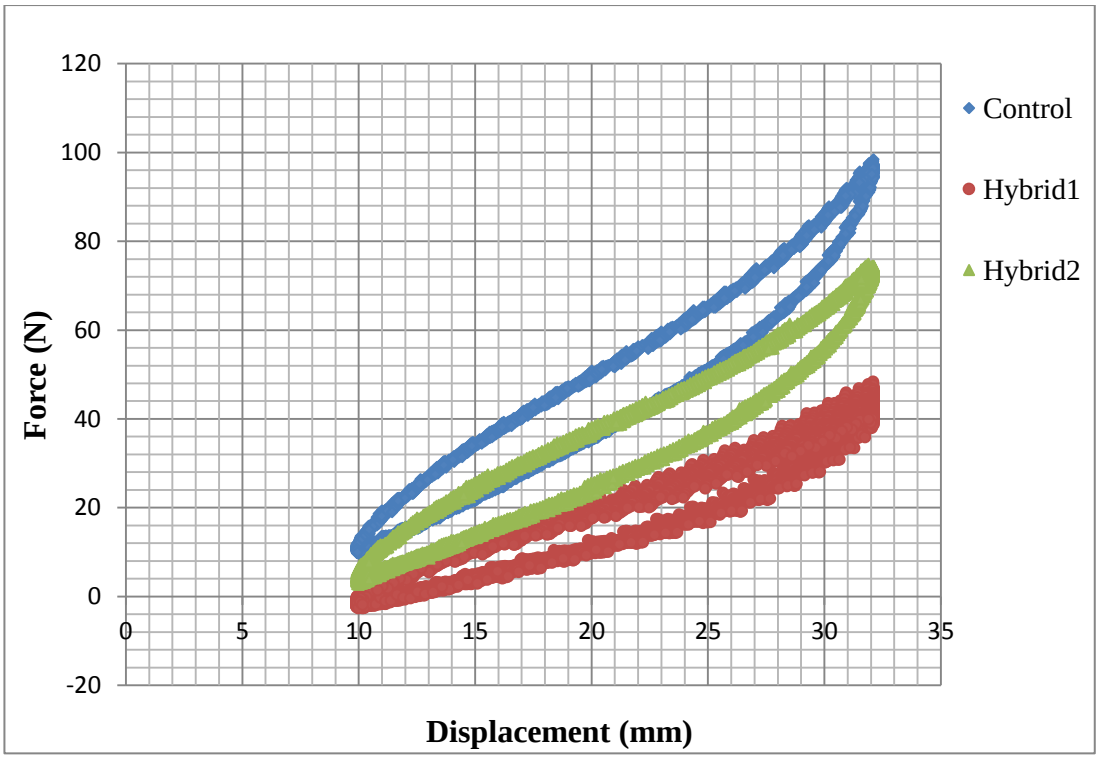

Figure 8.12 The evolution of force against displacement during fatigue testing, for the control sample and two different types of hybrid fatigue samples.

Figure 8.12 shows the loading and unloading cycles of three different fatigue samples. The addition of a second material reduced the overall stiffness of each specimen. The maximum average uniaxial force was measured for three different fatigue designs at the maximum displacement.

Table 8.2 The maximum average force for three different fatigue sample designs.

	Maximum Displacement (mm)	**Maximum Average Force (N)**
Control Sample	32	95
Hybrid 1 Fatigue Sample	32	48
Hybrid 2 Fatigue Sample	32	73

The control sample had the highest stiffness when compared to the other two fatigue samples. Out of the two hybrids, hybrid 2 offered the highest stiffness and the maximum average uniaxial force was 20 % less than the control sample, whilst the maximum average force in hybrid 1 was 63 % less than the control sample. Since this design technique will be applied to O-rings and spring seals it is important to understand how the addition of the second phase material affects the overall stiffness of the component.

8.3. FEA Hybrid O-rings Results

Before making hybrid O-rings, it was essential to analyse how the addition of a second phase material affected the stress and strain distribution in the O-ring. Tearing and fatigue test results revealed that the insertion of a second phase material reduces the stiffness of the hybrid structure. Therefore it was crucial to investigate how the addition of the second phase material affected the O-ring's sealing abilities. This was conducted by evaluating how the addition of the second phase material affected the contact pressure between the O-ring and the O-ring housing gland surfaces.

Tearing and fatigue tests revealed that the performance of a component can be improved by incorporating the second phase material in regions of high stress concentration. However the location of the second phase material can also lead to premature crack initiation by introducing new higher stress concentration areas. Results from previous chapters revealed that the combination of high tensile strains (NE_{11}), tensile stresses (S_{11}) and a high concentration of voids is probably the reason cracks tend to initiate and propagate in the centre region and normal to the external pressure as observed in the RGD experiments. Therefore the FEA model analysed how the addition of the second phase material affected the S_{11} and NE_{11} distribution and also the contact pressure between the O-ring and the housing gland surfaces. The aim was to reduce and

redistribute stress and strain thereby avoiding high tensile stresses and strains in the centre region whilst maintaining acceptable sealing performance. The LRCM888 layer was inserted in the centre region of the O-ring because during RGD this was the region where cracks usually initiate and propagate from. Initially three different configurations of the LRCM888 insert were investigated. The configurations consisted of a circular insert and oval insert. Circular and oval inserts were selected to avoid introducing high stress concertation regions in the O-rings. The oval insert was initially analysed oriented horizontal to the top housing surface and in the subsequent analysis the oval insert was inserted oriented perpendicular to the top housing surface. This section shows results from the FEA analysis on hybrid O-ring structures.

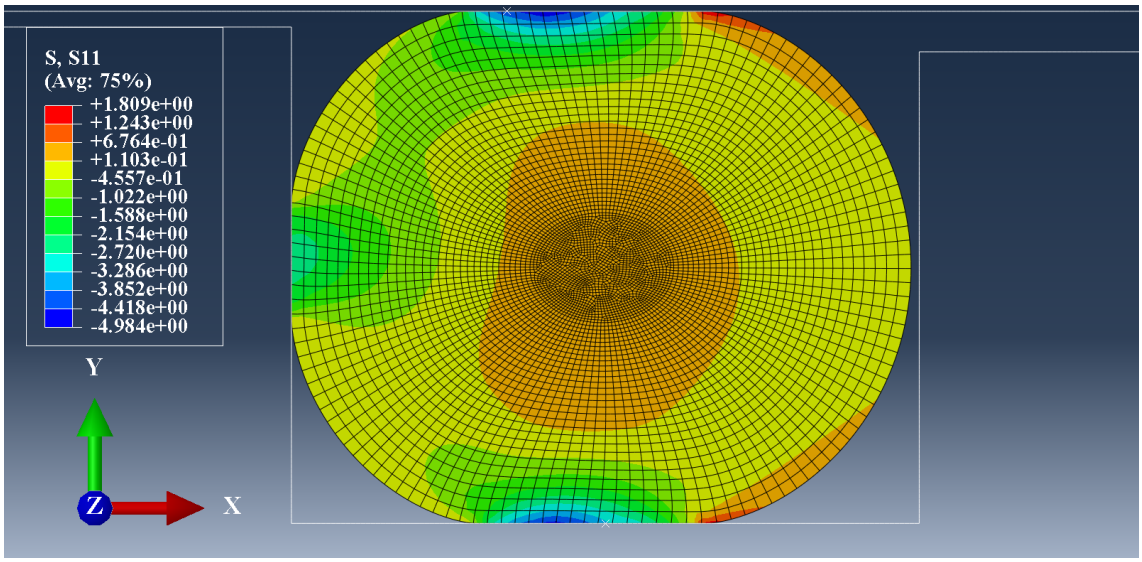

Figure 8.13 The stress S_{11} distribution inside the control O-ring after compression from housing gland surfaces, high tension stress in the centre region.

Figure 8.13 shows the stress S_{11} distribution inside the control O-ring containing only HNBR101 and no second phase material. Most of the elements in the O-ring section are under compressive stress in the x-direction apart from elements in the centre region and the front top and bottom edges of the O-ring. Figure 8.14 shows the strain NE_{11} distribution inside the control O-ring. High tensile strains are experienced by elements in the centre region of the O-ring. The highest tensile strains were reaching up to 21 %.

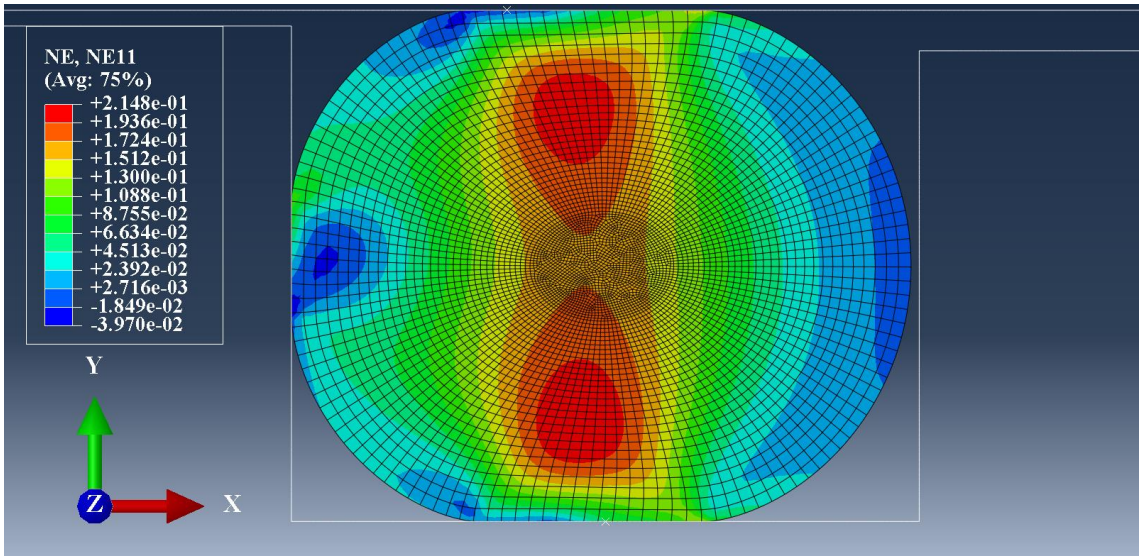

Figure 8.14 The strain NE_{11} distribution inside the control O-ring after compression from its housing gland surfaces, high tension strains are experienced in the centre region.

Figure 8.15 shows the stress S_{11} distribution inside a hybrid O-ring with a circular second phase material located in the centre region of the O-ring cross-section. This configuration introduced areas of high stress concentration at the boundaries between the less stiff LRCM888 and the stiffer HNBR101. The size of the region with high tensile stresses in the HNBR material is smaller compared to the one from the control O-ring. However the magnitude of stress is higher in the hybrid sample.

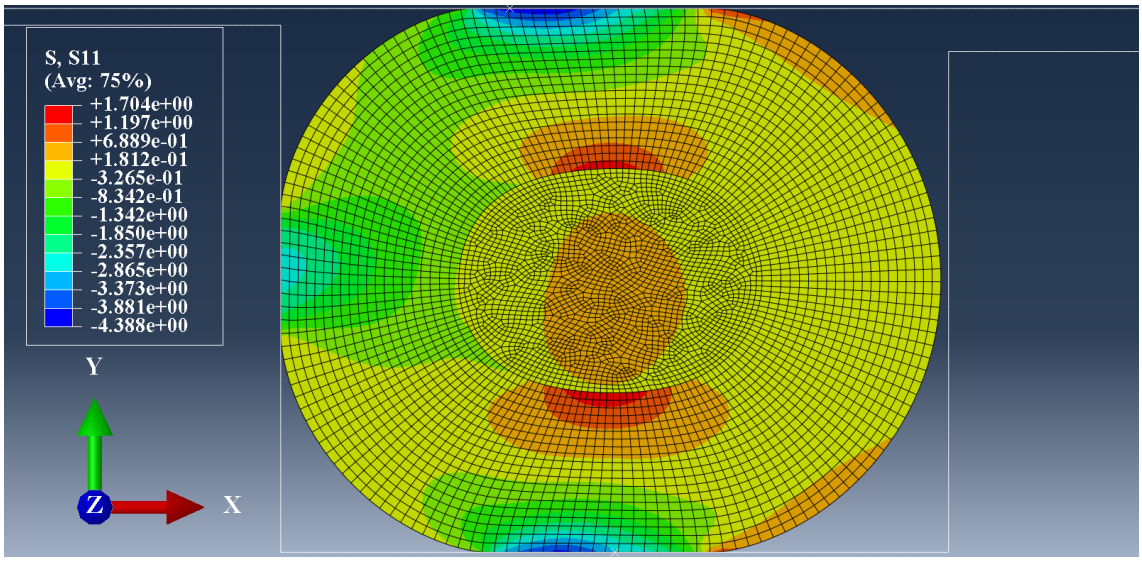

Figure 8.15 The stress S_{11} distribution inside hybrid_1 O-ring with a circular second phase material located in the centre region of the O-ring.

Figure 8.16 shows the strain NE_{11} distribution inside a hybrid O-ring with a circular second phase material inserted in the centre region of the O-ring. The addition of the second phase material reduced the size of the region with high tensile strains in the HNBR101 component. The second phase material absorbed most of the tensile strains which otherwise would have been experienced by HNBR101. However elements in the HNBR101 layer at the boundaries with LRCM888 are still under high tensile strains and this could lead to premature crack initiation.

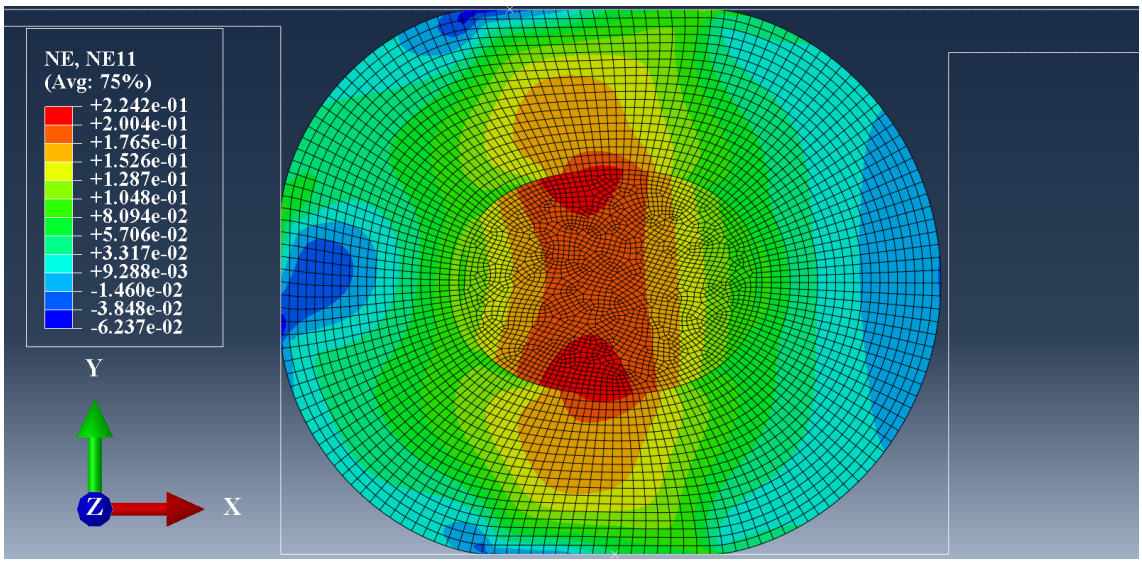

Figure 8.16 The strain NE_{11} distribution inside hybrid_1 O-ring with a circular second phase material located in the centre region of the O-ring.

Figure 8.17 shows the stress distribution inside a hybrid O-ring with a horizontal oval second phase material inserted in the centre region. This configuration shows the same distribution as the one shown by the hybrid O-ring with a circular second phase material in the centre region. The second phase material absorbs most of the tensile stresses, and reduces the amount of tensile stress experienced by the HNBR101 layer. However the HNR101 layer still experiences high tensile stresses in the centre region. Figure 8.18 shows the strain distribution inside a hybrid O-ring with a horizontal oval second phase material inserted in the centre region of the O-ring. The second phase material absorbs most of the tensile strains, and reduces the amount of tensile strains experienced by HNBR101. However HNBR101 still experiences high tensile strains in the centre region where cracks usually initiate and propagate from. Therefore this configuration could still lead to premature crack initiation.

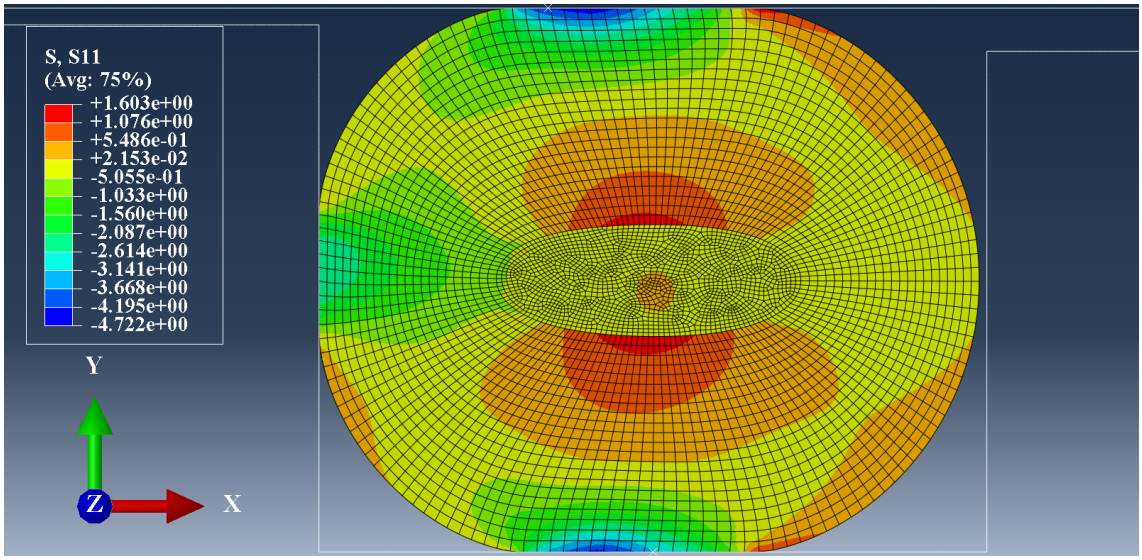

Figure 8.17 The stress S_{11} distribution inside hybrid_2 O-ring with a horizontal oval second phase material located in the centre region of the O-ring.

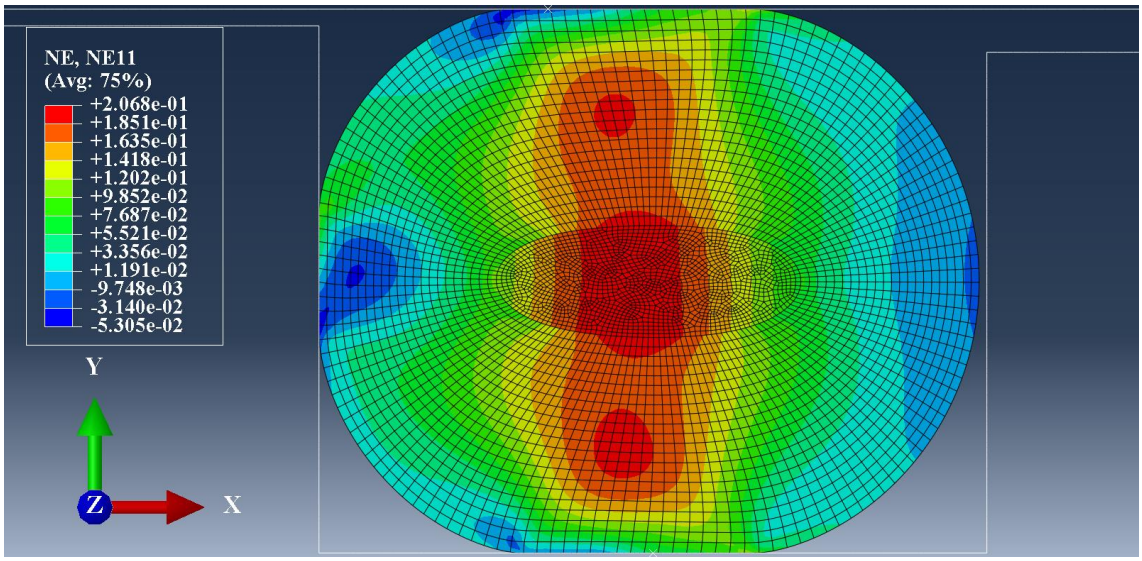

Figure 8.18 The strain NE_{11} distribution inside hybrid_2 O-ring with a horizontal oval second phase material located in the centre region of the O-ring.

Figure 8.19 shows the stress distribution inside a vertical oval second phase material inserted in the centre region of the O-ring. This configuration introduced areas of high stress concentration at the boundaries between LRCM888 and HNBR101. The area of the region with high tensile stresses S_{11} in the HNBR101 material is smaller compared to the one from the control specimen and the other two hybrid O-rings. Figure 8.20 shows the strain distribution inside a hybrid O-ring with a vertical oval second phase material located in the centre region of the O-ring. The second phase material absorbs

most of the tensile strains NE_{11} which otherwise would have been experienced by the HNBR material.

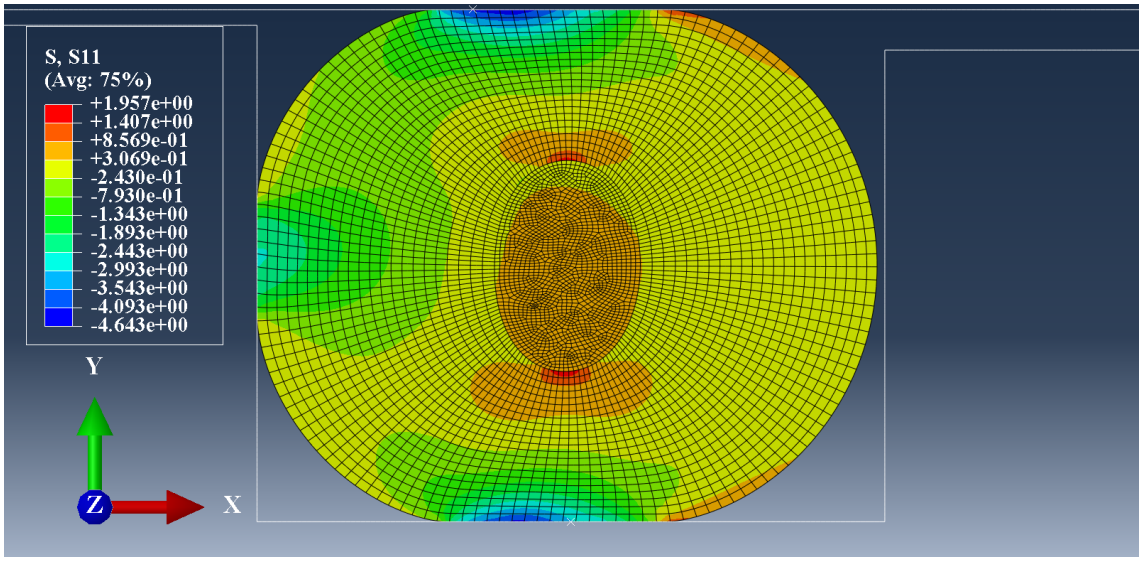

Figure 8.19 The stress S_{11} distribution inside hybrid_3 O-ring with a vertical oval second phase material located in the centre region of the O-ring.

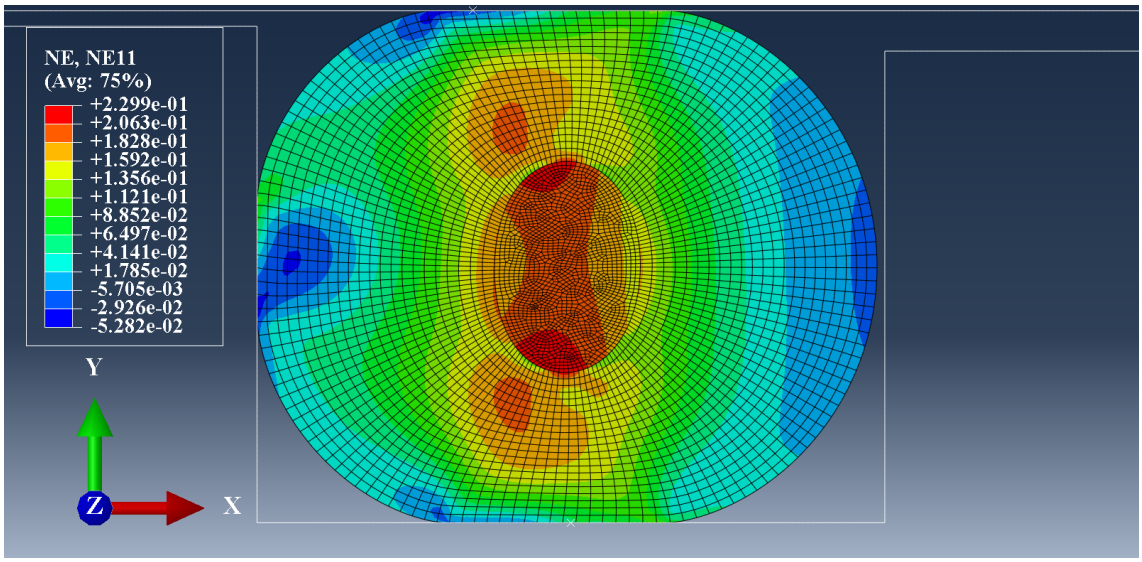

Figure 8.20 The strain NE_{11} distribution inside hybrid_3 O-ring with a vertical oval second phase material located in the centre region of the O-ring.

The three hybrid configurations discussed so far are capable of absorbing the stresses and strains which otherwise would have been experienced by the HNBR101 material. Of all the hybrid O-ring configurations, the hybrid O-ring configuration with a vertical oval second phase insert absorbed most of the tensile stresses in the O-ring structure. All the hybrid O-ring configurations are still introducing areas of high stress

concentration at the border between the stiffer HNBR101 and the less stiff LRCM888. These areas are located in the centre region of the O-ring, where cracks are known to initiate and propagate during RGD. These designs could then lead to premature crack initiation. An X-shaped second phase material insert was proposed. The aim of this design was to absorb the tensile stresses and strains in the O-ring structure without introducing areas of high stress concentration in the centre region of the O-ring.

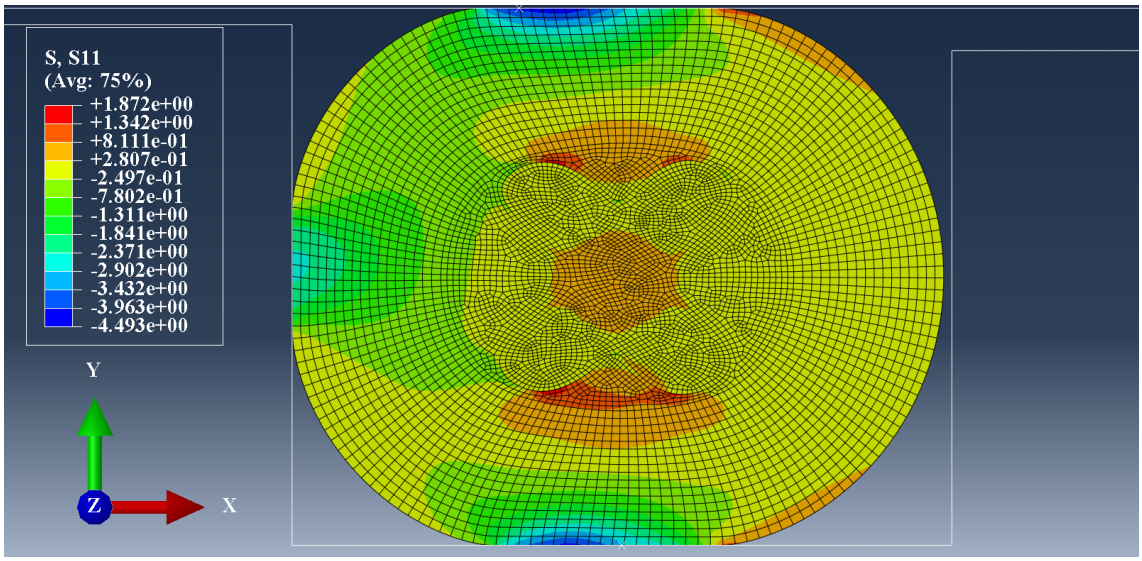

Figure 8.21 The stress S_{11} distribution inside hybrid_4 O-ring with an X-shape second phase material located in the centre region of the O-ring.

Figure 8.21 shows the stress S_{11} distribution inside an O-ring with an X-shape second phase material in the centre region. This configuration introduced areas of high stress concentration at the border between HNBR101 and LRCM888. These areas are however not located in the centre region like the other hybrid O-ring configurations. Therefore using this type of design, the amount of stress in the HNBR101 layer can be reduced whilst taking the stress concentration areas away from the centre region where crack initiation is likely to occur. Figure 8.22 shows the strain NE_{11} distribution inside a hybrid O-ring with an X-shaped second phase material insert. The reinforcing insert absorbs most of the tensile strains which otherwise would have been experienced by the HBR101 structure. Of all the hybrid configurations analysed, the X-shaped hybrid O-ring avoids introducing areas of high stress concentration in the centre region making this configuration the most promising. However the shape of the insert makes the hybrid O-ring difficult to manufacture.

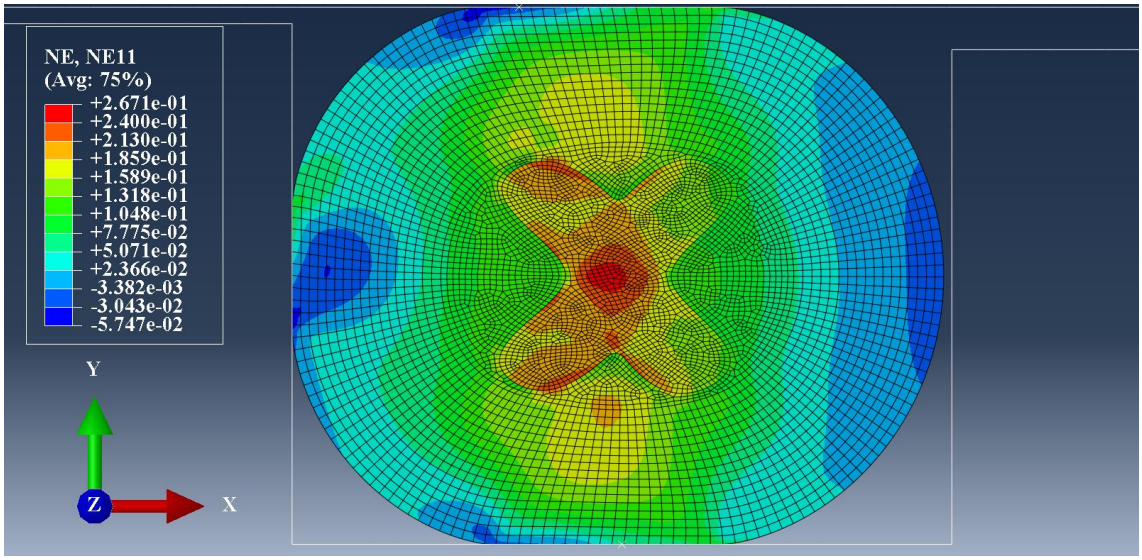

Figure 8.22 The strain NE_{11} distribution inside hybrid_4 O-ring with an X-shape second phase material located in the centre region of the O-ring.

Table 8.3 shows the contact pressure between different hybrid O-rings and their housing glands surfaces and the reduction in contact pressure due to the addition of a second layer. Hybrid_2 showed the least reduction in contact pressure between the O-ring and its housing gland surfaces and Hybrid_1 showed the highest reduction. The decrease in contact pressure between the hybrid O-ring and its housing gland surfaces can be reduced by decreasing the size of the second phase material.

Table 8.3 Contact pressure between different hybrid O-rings and their housing glands surfaces, and the reduction in contact pressure due to the addition of a less stiff LRCM888 layer.

FEA Model	**CPRESS (MPa)**	**Reduction in CPRESS (%)**
Control O-ring	4.61	
Hybrid_1 O-ring	3.95	14
Hybrid_2 O-ring	4.32	6
Hybrid_3 O-ring	4.18	9
Hybrid_4 O-ring	4.04	12

8.4. Hybrid O-rings Results

After curing the hybrid O-rings, it was difficult to assess whether the second phase material maintained its shape and did not flow during the curing process. The only way

to assess whether the hybrid O-rings kept their intended profile shape is to cut them open and analyse the internal structure. Figure 8.23, Figure 8.24 and Figure 8.25 show three cross-sections of hybrid O-rings after they were cured and before post cure, these were manufactured using the first technique discussed in Section 3.3.4. The cut specimens revealed that the second phase material was flowing and losing its shape during the curing process. The second phase material was especially flowing towards the flash line on both the inner and outer diameter of the O-ring.

Figure 8.23 Hybrid_1 O-ring with a circular second phase material located in the centre region of the O-ring.

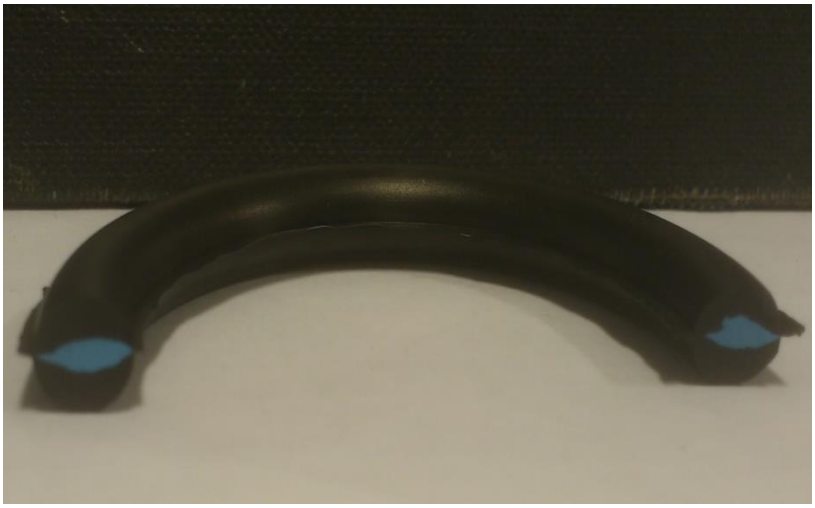

Figure 8.24 Hybrid _2 O-ring with a horizontal oval second phase material located in the centre region of the O-ring.

Figure 8.25 Hybrid _3 O-ring with a vertical oval second phase material located in the centre region of the O-ring.

Figure 8.26 shows the cross-sections of hybrid O-rings containing a horizontal oval second phase material located in the centre region. The hybrid O-rings shown in Figure 8.26 were manufactured using the pre-cure method described in Section 3.3.4. The LRCM888 insert maintained its profile shape however the position of the second phase material shifted thereby upsetting the profile shape of the hybrid O-ring.

Figure 8.26 Hybrid _2 O-ring with a horizontal oval second phase material located in the centre region of the O-ring, manufactured using the pre-curing technique.

8.5. Hybrid O-rings Results and Discussion Summary

Tearing and fatigue tests were conducted on two phase hybrid samples. The aim was to investigate how the location and geometry of the second phase material affected the components tearing strength and dynamic behaviour.

Inserting the second phase material just behind the crack initiation region increased the work done on hybrid tearing sample 1 before failure. However, cracks initiated prematurely in hybrid 1 samples and this was because the position and orientation of the second phase material resulted in high stress concentration regions. This indicates the importance of location and orientation of the second phase material.

Inserting the second phase material in the crack initiation region resulted in the hybrid tearing strength sample 2 containing the highest tearing strength and strain energy density at failure compared to all other samples, indicating the highest improvement in performance.

Hybrid fatigue samples were made to investigate the dynamic behaviour of hybrid rubber components. Hybrid 1 fatigue samples contained a second phase material just behind the crack initiation region. Hybrid 1 fatigue samples had improved fatigue lives when compared to the fatigue control samples however, the overall structural stiffness was greatly reduced by 63 %. This large reduction in stiffness was due to a cracks initiating only after a few cycles and propagating across the sample's cross-section only to be stopped by the presence of the LRCM888 layer. Even though the fatigue samples would continue to carry a load for many cycles to come, its structural stiffness was greatly reduced. The reason for premature crack initiation in hybrid 1 fatigue samples was because the location of the reinforcing material layer resulted in the introduction of high stress concentration regions. This was also observed in the hybrid 1 tearing strength sample, indicating how important the location and geometry of the second phase material has on the overall dynamic and static performance of rubber structures.

Hybrid 2 fatigue samples had the highest fatigue lives, however there was a 20 % reduction in the components overall stiffness when compared to the fatigue control sample. This design confirmed that, by inserting a less stiff, high toughness material in regions of high stress concentration can improve the rubber components dynamic behaviour.

FEA was conducted on hybrid O-rings and the aim was to analyse how the addition of a second phase material affected the stress and strain distribution in the O-ring and the O-ring's sealing abilities. The O-ring's sealing ability was analysed by evaluating how the addition of a second phase material affected the contact pressure between the O-ring and the O-ring housing gland surfaces. The hybrid O-ring configurations were designed based on the results from the scanning electron microscopy, computational tomography, tearing and fatigue tests and the coupled structural-mass diffusion FEA model.

The addition of a second phase material resulted in the LRCM888 material absorbing most of the stresses and strains which otherwise would have been experienced by the HNBR101 material. However the addition of a second phase material resulted in high stress concentration areas being introduced at the boundaries between the less stiff LRCM888 layer and the stiffer HNBR101 layer. For this reason, an X-shaped second phase material insert was proposed. The aim of this design was to absorb the tensile stresses and strains in the O-ring structure whilst avoiding introducing areas of high stress concentration in the centre region. Of the entire hybrid configurations tested, the X-shape insert was the most promising, however it was not possible to manufacture the X-shaped hybrid O-ring with the manufacturing technics available. Also it was shown that the sealing abilities on the O-ring are reduced with the introduction of a second phase material.

Two different techniques were attempted to manufacture hybrid O-rings. However after inspecting the hybrid O-rings, it was found that the second phase insert was flowing and losing its profile shape. In the second technique the second phase insert maintained its profile shape however, the second phase shifted from its position thereby upsetting the profile shape of the whole hybrid O-ring.

9. Conclusions and Future Work

Damage resistance of elastomer O-rings and spring seals exposed to rapid gas decompression (RGD) has been investigated using both experimental and numerical methods.

9.1. RGD Fracture Analysis

Experimental methods included using scanning electron microscopy to analyse fractured surfaces of O-rings and spring seals after exposure to RGD. Microcracks were found to initiate from microvoids or inherent flaws present in the centre region of all the O-rings and spring seals tested. These microcracks would propagate slowly towards the inner and outer circumference of the seals and when the crack reached a critical size, the crack rapidly accelerated resulting in a catastrophic brittle fracture. The fracture surfaces of all O-rings and spring seals, displayed a more pronounced relatively stable crack growth towards the inner circumference. This indicates that higher stress levels were experienced on this side of the seal during RGD, or this region maybe a point of weakness in the seals structure.

All flaws in the spring seals were located in the centre region and this indicates that these flaws could have been introduced during the manufacturing process and were not necessarily inherent flaws contained in the elastomer raw material. The fracture surfaces of both O-rings and spring seals specimens contained pits on the surface and these pits were a result of reinforcing agglomerates, coming out of the matrix. These loose agglomerates in the matrix can act as stress raisers offering an easy path for a tear to follow thereby reducing the overall strength of the material.

Computerised tomography (micro-CT) was conducted on elastomer O-rings and the aim was to investigate the void density and distribution. The micro-CT images revealed multiple randomly distributed voids of varying dimensions from 30 – 60 micrometres along the length of the O-ring sections scanned. All the voids had various shapes and dimensions and they could have been introduced during the manufacturing process or contained in the elastomer raw material. The O-ring sections also contained smaller multiple voids which were only visible in binary images or after zooming in on the raw images.

The binary mode images revealed that all 2D cross-section images of the O-rings contained a high void density in the centre region. This distribution of small voids could be one of the reasons why cracks in HNBR101 O-rings always initiate and propagate through the centre region. This is because during service there is a higher concentration of absorbed gas at the centre of the O-ring due to high void density in this region. When the external pressure suddenly drops during RGD, higher stress levels are experienced in this region due to the high concentration of compressed gas expanding.

9.2. RGD Numerical Model

The experimental work was complimented with a numerical model. A sequentially coupled FEA structural–mass diffusion model was developed to evaluate the behaviour of elastomer O-rings exposed to rapid gas decompression, in the presence of CO_2. The coupling between mass diffusion and the structural deformation of the O-ring was achieved by employing the Peng – Robinson equation of state and two user-subroutines to evaluate the pressure exerted by the rapidly expanding gas.

The RGD numerical model was used to evaluate the stress and strain distribution inside an O-ring during RGD. Elements in the O-ring experienced a stress-state change from compression to tension during the decompression cycle. The strain rate during the stress-state change was shown to be dependent upon the decompression rate. The higher the decompression rate, the higher the strain rate. This could explain why fracture in elastomer O-rings usually occur at higher decompression rates compared to lower decompression rates as observed during RGD experiments.

The RGD numerical model also revealed that elements in the centre region of the O-ring's cross-section experience the highest tensile strains and stresses in the direction normal to the external pressure gradient. The combination of high tensile strains (NE_{11}), tensile stresses (S_{11}) and a high concentration of voids is probably the reason cracks tend to initiate and propagate in the centre region and normal to the external pressure as observed in the RGD experiments and as noted by Rispin.

9.3. Hybrid O-rings

Before constructing hybrid O-rings, tearing strength and fatigue tests were conducted on two phase hybrid samples. The aim was to investigate how the location and geometry of the second phase material affected the components tearing strength and dynamic behaviour.

Inserting the second phase material behind the crack initiation region increased the work done before failure, indicating an improvement in performance. The presence of a LRCM888 layer stopped cracks from propagating through the sample. However cracks initiated prematurely in hybrid 1 specimens and this was because the position and orientation of the second phase material resulted in high stress concentration areas being introduced. This indicates the importance of location and orientation of the second phase material.

Inserting the second phase material in the crack initiation region resulted in hybrid 2 specimen containing the highest tearing strength and strain energy density at failure compared to all other samples, indicating the biggest improvement.

Hybrid fatigue samples which contained a second phase material just behind the crack initiation region had improved fatigue lives when compared to the control fatigue samples. However the overall stiffness of the structure was greatly reduced by up to 63 %. This large reduction in stiffness was due to cracks initiating only after a few cycles and propagating across the sample's cross-section only to be stopped by the presence of the LRCM888 layer. The reason for premature crack initiation in these hybrid fatigue samples was because the location of the reinforcing material layer resulted in high stress concentration areas in the structure. This was also observed in the hybrid tearing strength sample with a second phase material insert just behind the crack initiation region. This indicates the importance of the location and geometry of the second phase.

Inserting the second phase material in the crack initiation region resulted in hybrid 2 fatigue samples displaying the highest fatigue cycles. However, there was a 20 % reduction in the components overall stiffness when compared to the fatigue control samples. This design confirmed that, by inserting a less stiff high hysteresis material in regions of high stress concentration can improve the rubber components dynamic behaviour.

FEA analysis was conducted on hybrid O-rings and the aim was to analyse how the addition of a second phase material affected the stress and strain distribution in the O-ring and the O-ring's sealing abilities. The O-ring's sealing ability was analysed by evaluating how the addition of a second phase material affected the contact pressure between the O-ring and the O-ring's housing gland surfaces. The hybrid O-ring configurations were designed based on the results from scanning electron microscopy, computational tomography, tearing strength and fatigue tests and the coupled structural-mass diffusion FEA model.

The addition of a second phase material in the O-ring structure, resulted in the LRCM888 material absorbing most of the stresses and strains which otherwise would have been experienced by the HNBR101 material. However the addition of a second phase material resulted in high stress concentration areas being introduced at the boundaries between the less stiff LRCM888 layer and the stiffer HNBR101 layer. For this reason, an X-shaped second phase material insert was proposed. The aim of this design was to absorb the tensile stresses and strains in the O-ring structure whilst avoiding introducing areas of high stress concentration in the centre region. Of the entire hybrid configurations tested, the X-shape insert was the most promising.

Two different techniques were adopted to manufacture different hybrid O-rings. The two techniques involved extruding two different O-ring layers separately and combining them to form hybrid O-rings. After constructing the hybrid O-rings they were inspected by cutting the O-rings into separate sections and checking whether the hybrid O-rings maintained their profile shape. In the first technique it was found that the second phase insert was flowing and losing its profile shape. In the second technique the second phase insert maintained its profile shape however shifted from its original position thereby upsetting the profile shape of the whole hybrid O-ring.

9.4. Concluding Remarks

This research has shown that it is possible to improve the static and dynamic fracture resistance of rubber components using hybrid structures. Tear strength and fatigue tests have shown that it is possible to delay fracture initiation and propagation by carefully inserting a "high fracture toughness" layer to create hybrid components. FEA showed how this concept can be applied to elastomer O-rings. The stress and strain distribution

in an O-ring can be manipulated by inserting a carefully designed second phase material thereby improving areas of high stress concentration.

The SEM analysis revealed that fracture in elastomer O-rings and spring seals initiated and from the centre region and propagated towards the outer and inner circumference of the seal. Results from SEM analysis prompted for the need to carry out micro-CT analysis on virgin O-rings. The binary images from the micro-CT results showed that there is a high void density ratio in the centre region of the O-rings. This void distribution was most likely introduced during the manufacturing process.

An FEA model was proposed to evaluate the behaviour of elastomer O-rings exposed to RGD conditions in the presence of Carbon Dioxide. The FEA model was used to evaluate the stress and strain distribution inside the O-rings during rapid gas decompression. It was shown that the nominal stresses go through a stress-state change from compression to tension during the decompression cycle and the strain rate during the stress-state change is dependent upon the decompression rate. The FEA model revealed that the elements in the centre region of the O-ring's cross-section experience high tensile strains and stresses during each decompression cycle.

The FEA results together with results from SEM and micro-CT experiments were used to design new hybrid O-ring structures. Unfortunately the two different techniques used to construct the hybrid O-rings did not yield successful results. In the first technique, the LRCM888 material was flowing and losing its profile shape. In the second technique the LRCM888 material maintained its profile shape however shifted from its original position thereby upsetting the profile shape of the whole hybrid O-ring.

9.5. Future Work

A sequentially coupled structural – mass diffusion model was proposed to evaluate the interaction between rapidly expanding gas and the structural deformation on an O-ring. The time taken for carbon dioxide to diffuse out of the O-ring in the FEA model was not accurately representative of the actual time it takes for carbon dioxide to diffuse out of the O-ring in the experiments. This is because the permeation data used in this thesis was measured at different conditions than those experienced during the RGD process. The model can be further improved by evaluating the permeation data at conditions

representative of the actual RGD conditions. Conditions such as temperature, pressure and the stress state in the material. These conditions vary during the RGD cycle therefore it will be more accurate to evaluate the permeation data as a function of temperature and pressure.

Also the model proposed in this thesis is a sequentially coupled model, meaning that data is exchanged at the end of each simulation analysis. To further improve the accuracy of the numerical model, a co-simulation coupling can be used to couple the structural deformation of the O-ring and mass diffusion of absorbed gas. In a co-simulation, data is exchanged at each increment during the simulation step. Using a co-simulation will allow the boundary conditions for both analyses to be updated at each increment. Also since stress and strain cannot be used as a damage criterion for rubber products, to predict fracture in elastomer O-rings during RGD, the numerical model proposed in this thesis can be coupled with a J-integral method to predict crack propagation.

Tearing strength and fatigue tests on hybrid components have shown that it is possible to improve the static and dynamic fracture resistance of rubber components using hybrid structures. FEA analysis has also shown that it is possible to apply this concept to improve fracture resistance of elastomer O-rings. However, the hybrid O-rings proposed were not easy to manufacture using the manufacturing techniques available. The two manufacturing techniques proposed resulted in either the LRCM888 layer flowing during the curing process and losing its profile or the LRCM888 layer keeping its profile however, shifting from its original position. Therefore more research should be performed to find better efficient techniques for constructing hybrid O-rings.

10. References

Abaqus (2011). Abaqus Documentation, Dassault Systèmes, Providence, RI, USA

Agarwal, K. et al. (2005) Scanning Electron Microscopy Study on the Influence of Temperature on tear Strength and Failure Mechanism of Natural Rubber Vulcanizates. Polymer Testing. 24, pp. 781 – 789.

Anderson L. D. (1989) Thermodynamics and Equations of State. In, Theory of the Earth. Boston: Blackwell Scientific Publications, pp 82.

Arruda, E. M. and Boyce, M. C. (1993) A Three Dimensional Constitutive Model for the Large Stretch Behaviour of Rubber Elastic Materials. J Mech Phys, Solids. 41(2), pp. 389 – 412.

ASM International (2003) Characterization and Failure of Plastics. Pp 404: Available from: www.asminternational.org [Accessed 16th December 2014].

Bale, H. et al. (2012) Characterizing Three-Dimensional Textile Ceramic Composites Using Synchrotron X-ray Micro-Computed-Tomography. J. AM, Ceram. Soc. 95(1), pp. 392 – 402.

Beattie, A. J. and Bridgeman, C. (1928) A New Equation of State for Fluids. Proceedings of the American Academy of Arts and Sciences, 63(5), pp. 229 – 308.

Bever, A. (1992) Literature Survey: Dynamic Behaviour of Rubber and Rubberlike Material. WFW-report 92.006.

Blatz, P. J. and Ko, W. L. (1962) Application of Finite Elastic Theory to the Deformation of Rubbery Materials. Transactions of the Society of Rheology. VI, pp. 223 – 253.

Boyce M. C. and Arrudda M. E. (2000) Constitutive Models of Rubber Elasticity: A Review. Rubber Chemistry and Technology, 73 pp 504 – 523.

Briscoe, B. J. et al (1994) Explosive Decompression Failure of Rubbers: A Review of the Origins of Pneumatic Stress Induced Rupture in Elastomers. 67(3). Pp. 384 – 416.

British Standards Publications (2012). Rubber, vulcanized or thermoplastic – Determination of permeability to gases. Part 1: Differential-pressure methods. BS ISO 2782-1

Bruker Micro-CT (2013) CT-Analyser Version 1.13: The User's Guide, pp 3.

Bugani, S. et al. (2008) X-ray Computed Tomography as a Non-Destructive Tool for Stone Conservation. 9th International Conference on NDT of Art, Jerusalem.

Busse, W. F. (1934) Tear Resistance and Structure of Rubber. Industrial and Engineering Chemistry. 26(11), pp 1194 – 1199.

Chang, J. H. and Ye, J. B. (1997) Calculation of J2-Intergral for 2-D Cracks in Rubbery Materials. Engineering Fracture Mechanics. 59(5), pp. 683 – 695.

Chiesura, S. (2015) A Micro-Computed Tomography Technique to Study the Quality of Fibre Optics in Composite Materials. Sensors, ISSN. 1424(8220), pp. 10852 – 10871.

Collyer, A. A. (1994) Rubber Toughened Engineering Plastics. Springer-Science-Business, Media, First Edition. Pp 124.

Cox, V. A. (1985) A User's View of Explosive Decompression in Oilfield Elastomers. Proceedings of Conference on Offshore Engineering with Elastomers, paper 19. (London, Plastics and Rubber Institute).

Cox, V. A. (1985) Service Failures – A Users View of Explosive Decompression in Oilfield Elastomers. Discussion Forum and Exhibition on Offshore Engineering with Elastomer. 19. (London, Plastics and Rubber Institute)

Crank, J. (1956) The Mathematics of Diffusion. Clarendon Press, Oxford.

Daynes, H. A (1920) The Process of Diffusion Through a Rubber Membrane. Proc. R. Soc. Lond. A. 97, pp 286 – 307.

Deans, S. R. (2000) Radon and Abel Transforms: The Transforms and Applications Handbook. Second Edition, Boca Raton: Press LLC.

Deans, S, R. (1983) The Radon Transform and Some of its Applications. John Wiley and Sons.

Edmond, K. (2003) Elastomer Fatigue Testing for Explosive Decompression Cycling Prediction. 17th International Conference on Fluid Sealing, BHR Group, pp 241 – 250.

Edmond, K. et al. (2001) Comparison of Explosive Decompression Test Protocols for Seals in High Pressure Gas Service. Symposium T-1G, Corrosion Paper Number 01109.

Egwaikhide, A. P. et al. (2013) Rheological and Mechanical Properties of Natural Rubber Compounds Filled with Carbonized Palm Kernel Husk and carbon Black. Science Journal of Chemistry. 1(5), pp. 50 – 55.

Embury, P. (2004) High Pressure Gas Testing of Elastomer Seals and a Practical Approach to Designing for Explosive Decompression Service. Sealing Technology.

Feldkamp, L. A. et al. (1984) Practical Cone-Beam Algorithm. J. Opt. Soc AM, 1(6), pp. 612 – 619.

Flitney, R. K. (1999) Prediction of Explosive Decompression Damage in Elastomer Seals. The Reliability of Rotating Machinery Sealing Systems Conference, IMechE, London. Pp. 191 – 198.

Gdoutos, E. E. et al. (2013) Tearing Energy of Tire Rubber Under Mode I and Mode III Loading. ICF11, Italy 2005.

Gent, A. N. and Tomkins, D. A. (1969) Nucleation and Growth of Gas Bubbles in Elastomers. Journal of Applied Physics, 40(6), pp. 2520 – 2525.

Greenhalgh, S. E. (2009) Delamination – Dominated Failures in Polymer Composites. In: Failure Analysis and Fractography of Polymer Composites. Woodhead Publishing Limited. Pp 170.

Griffith, A. A. (1920) The Phenomena of Rupture and Flow in Fluids. Philosophical Transactions of the Roya Society of London A: Mathematical, Physical and Engineering Sciences 221.582 – 593(1921), pp. 163 – 198.

Guo, Z and Sluys, L. J. (2008) Constitutive Modelling of Hyperelastic Rubber – Like Materials. Heron, 53(3) pp 109 – 132.

Hamzah, M. N and Razao, A. A (2013) Nonlinear Visco-Hyperelastic Constitutive Modelling for Filled Elastomeric Materials. AL-Qadisiya Journal for Engineering Sciences, 6(4) pp 369 – 382.

Harara, W. (2008) Digital Radiography in Industry. Atomic Energy Commission, 17th World Conference on non-Destructive Testing, Shanghai, China. Pp. 25 – 28.

Hayes, D. M. et al (2015) Fractography in Failure Analysis of Polymers. Elsevier, pp 2.

Heidemann, R. A. and Prausnitz (1976) A Van Der Waals-Type Equation of State for Fluids with Associating Molecules. Applied Physics Sciences. 73(6), pp. 1773 – 1776.

Ho, E. (1993) Theoretical and Computational Modelling Polymer Seal Life. PhD Thesis, Cranfield Institute of Technology.

Ho, E. (2006) Elastomeric Seals for Rapid Gas Decompression Applications in High Pressure Services. Research Report 485, BHR Group Limited, The Fluid Engineering Centre, Cranfield.

International Standard Rubber – Determination of Frictional Properties, BS ISO 15113, Second Edition 2005.

ISO 23936-2: Petroleum Petrochemical and Natural Gas Industries – Non-Metallic Materials in Contact with Media Related to Oil and Gas Production – Part: Elastomers.

ISO Standard Test Method, Vulcanized Rubber and Thermoplastic Elastomers-Tension. D412-06. 2008.

James Walker & Co. Ltd and Oil and Gas Products. HNBR 101- Elastomeric Seals and Components for Oil and Gas Industry. Issue 9, pp 26.

Ju. M. et al. (2014) A Comparison Among Polynomial Model, Reduced Polynomial Model and Ogden Model for Polyurethane Foam. Advanced Materials Research, Trans Tech Publications, Material Science and Engineering Technology II. Pp 169 – 175.

Kim, B. et al. (2011) A Comparison Among Neo-Hookean Model, Mooney Rivlin Model and Ogden Model for Chloroprene Rubber. International Journal of Precision Engineering Manufacturing. 13(5), pp. 759 – 764.

Kim, B. H. and Joe, C. R. (1989) Single Specimen Method for Determining Fracture Energy (JC) of Highly Deformable Materials. Engineering Fracture Mechanics. 32(1), pp. 155 – 161.

Knag, T. L. and McKetta, J. J. (1961) Application of Benedict-Webb-Rubin of State to Sulphur Dioxide. Journal of Chemical and Engineering Data. 6(2), pp. 227 – 228.

Kontaxakis, G. and Strauss, L. G. (1998) Maximum Likelihood Algorithms for Image Reconstruction in Positron Emission Tomography. Mediterra Publishers, Athens. Pp. 73 -106.

Kumar, S. S. R and Nijasure, A. M. (1997) Vulcanization of Rubber – How to Alter Molecular Structure and Influence Physical Properties. Resonance, pp 55 – 59.

Kurian, J. et al. (1989) Scanning Electron Microscope Studies on Tension Fatigue of High Density Polyethylene Filled Natural Rubber Vulcanizates. Int. J. Fatigue. 2, pp. 129 – 133.

Leslie, S. A. and Mitchell, J. C. (2007) Removing Gold Coating from SEM Samples. Palaeontology. 50(6), pp. 1459 – 1463.

Li, Q. et al. (2009) Fatigue Life Prediction of Rubber Mount Based on Tests of Materials properties and Finite Element Analysis. Engineering Failure Analysis, 16, pp 2305 – 2310.

Lindley, P. B. (1984) Engineering Design with Natural Rubber. The Malaysians Rubber Producers, Research Association, pp 6

Lorge, O. et al (1999) Gas Induced Damage in Poly(Vinylidene Fluoride) Exposed to Decompression. 40(11). Pp. 2981 – 2991.

Luong, R. et al. (2007) Damage Initiation Mechanism in Rubber Sheet Composites During the Static Loading. Archives of Materials Science and Engineering. 28(1), pp. 19 – 26.

Machado, G. et al (2010) Analysis of the Isotropic Model of the Mullins Effect Based on Filled Silicone Rubber Experimental Results. Mechanics of Materials. 42, pp. 841 – 851.

Mansouri, M. R. and Darijani, H. (2014) Constitutive Modelling of isotropic Hyperelastic Materials in an Exponential Framework Using a Self-Contained Approach. International Journal of Solid and Structures. 51, pp. 4316 – 4326.

Mathew, N. M. and De, S. K. (1983a) Scanning Electron Microscopy Studies on Tear Fractures of Natural Rubber. Polymer, 23, pp. 632 – 634.

Mathew, N. M. and De, S. K. (1983b) Scanning Electron Microscopy Studies on Flexing and Tension Fatigue of Rubber. INT. J. Fatigue, pp 23 – 28.

Mathew, N. M. et at (1982) Scanning Electron Microscopy on Tensile Rupture of Rubber. Journal of Materials Science. 17, pp. 2594 – 2598.

Mezger, M. et al. (2005) HNBR Advanced Technology: The new Low Molecular Weight Polymer. High Performance and Speciality Elastomers 2005(18), pp. 181 – 195.

Monaghan, K. J. et al. (2006) Specification of Elastomeric Materials for Rapid Gas Decompression Applications. Oilfield Engineering with Polymers 2006, London.

Mooney, M. (1940) A Theory of Large Elastic Deformation. Journal of Applied Physics. 11(9) pp 582 – 592.

MSC, Software Whitepaper. (2010) Nonlinear Finite Element Analysis of Elastomers [online], pp 4. Available from: http://www.mscsoftware.com/Submitted- Content/ Resources/WP_Nonliear_FEA-Elastomers.pdf [Accessed 14th July 2014].

Mullins, L. (1969) Softening of Rubber by Deformation. Rubber Chem Technol. 42 pp 339-362.

Nace TMO 192-98. Evaluating Elastomers Materials in Carbon Dioxide Decompression Environments.

Nagdi, K (1993) Rubber as an Engineering Material Guideline for Users. Hauser Publishers, Munich, Vienna, New York, Barcelona.

Norsok M-CR-710 Rev.1 (1994) Qualification of Non-metallic Sealing Materials and Manufacturers.

Norsok Standard M-710 Rev. 2, Qualification of Non-Metallic Sealing Materials and Manufacturers. 2001.

Ogden, R. W. (1972) Large Deformation Isotropic Elasticity – On the Correlation of Theory and Experiment For Incompressible Rubberlike Solids. Proceedings of the Royal Society of London, Series A, Mathematical and Physical Sciences. 326(1567) pp 565 – 584.

Oh, H. L (1976) A Simple Method for Measuring Tearing Energy of Nicked Rubber Strips. Mech of Cracked Growth, ASTM STP 590, pp. 104 – 114.

Omnes, B. et al (2010) FE-Implementation of a Constitutive Model to Simulate the Behaviour of Seals in Explosive Decompression.

Ozkaya, N. et al. (2012) Mechanical Properties of Biological Tissues. In Fundamentals of Biomechanics: Equilibrium, Motion and Deformation, Springer Science + Business Media. Pp. 221.

Peeters, F. J. H and Kussner, M. (1999) Material Law Selection in the Finite Element Simulation of Rubber-Like Materials and its Practical Application in the Industrial Design Process. In: Dorfmann, A. and Muhr, A. (1999) Constitutive Models for Rubber. Netherlands, A. A. Balkema. Pp 29 – 63.

Peng, D and Robinson, D. B. (1976). A New Two Constant Equation of State. IND. ENG. Chem., Fundam, 15(1), pp 59 – 64.

Perkin Elmer, INC. (2007) Expansion Coefficient of Polymeric Materials Using DMA 8000. Available from: http://www.perkinelmer.com/Catalog/Product/ID/N5330101 [Accessed 12th September 2014].

Ping-Sung L. et al. (2007) A Fast Algorithm For Multilevel Thresholding. Journal of Information Science and Engineering. 17, pp. 713 – 727.

Raghavan, V. (1998) Material Science and Engineering, 4th Edition. Prentice- Hall of India, pp. 396.

Rattanasom, N. et al. (2009) Comparison of Mechanical Properties at Similar Hardness Level of Natural Rubber Filled with Various Reinforcing-Fillers. Polymer Testing. 28, pp. 8 – 12.

Rice, J. R. (1968) A Path-Independent Integral and the Approximate Analysis of Strain Concentration by Notches and Cracks. J. Appl. Mech. 35, pp. 379 – 386.

Rispin, A. (1985) Elastomeric Materials to Resist Explosive Decompression.

Rivlin, R. S and Saunders, D. W. (1951) Large Elastic Deformations of Isotropic Materials VII. Experiments on The Deformation of Rubber, PHI, Trans Soc. London Series A, 243(865) pp 251 – 288.

Rivlin, R. S. and Thomas, A. G. (1953) Rupture of Rubber- Characteristic Energy for Tearing. J. Polymer Science. 10, pp. 291 – 318.

Rothon, R. N (2001) Particulate Filers for Polymers. Rapra Review Reports, 12(9), pp 23

Routh, J. and Ho, E. (1997) Modelling of Decompression in Elastomeric Systems. Sealing Technology. 1997(47), pp. 10 – 12.

Routh, J. M. (1999) Prediction of Explosive Decompression Damage in Elastomer Seals. PhD Thesis, University of Cranfield.

Schwartz, T. H. (2001) Compatibility of Sealing Materials with Sour Gas. Economos Austria GmbH.

Schubert, G and Harrison, P. (2015) Equi-biaxial tension tests on magneto-rheological elastomers. Smart Mater. Struct. 25.

Setua, D. K. and De, S. K. (1983) Scanning Electron Microscopy Studies on Mechanism of Tear Fracture of Styrene-Butadiene Rubber. Journal of Material Science. 18, pp 847 – 852.

Setua, D. K. and De, S. K. (1984) Short Silk Fibre Reinforced Nitrile Rubber Composites. Journal of Materials Science. 19, pp. 983 – 999.

Simo, J. C. and Pister, K. S. (1984) Remarks on Rate Constitutive Equations for Finite Deformation Problems: Computational Implications. Computer Methods in Applied Mechanics and Engineering. 46, pp. 201 – 215.

Span, R. and Wagner (1994) A New Equation of State for Carbon Dioxide Covering the Fluid Region for the Triple-Point Temperature to 1100 K Pressure up to 800 MPa. J. Phys. Chem. Ref. Data. 25(6), pp. 1509 – 1596.

Susmita, B. et. al. (1993) Properties and Degradation of Nitrile Rubber. in: N. P, Cheremisinoff (Ed.) Elastomer Technology Handbook. Morganville, New Jersey. SciTech Technical Services. pp 525.

Taylor, H. F. et al (2015) A New Method to Identify Void Constrictions in Micro-CT Images of Sand. Computers and Geotechnics. 69(2015), pp. 279 – 290.

Thavamani, P. and Bhowmick, A. K. (1992) Dynamic Mechanical Properties of Hydrogenated Nitrile Rubber: Effect of Cross-Link Density, Curing System, Filler and Resin. Journal of Materials Science, 27(1992), pp. 3243 – 3253.

The British Standard, Rubber, Vulcanized or Thermoplastic – Determination of Tear Strength. Part 2: Small (Delft) Test Pieces, BS ISO 34 – 2: 2011.

The British Standards Plastics – Determination of Dynamic Mechanical Properties. Part 1: General Principles, ISO 6721 – 1, 2011.

Totalfina SP-TCS-142 Appendix H. Elastomer O-ring Seals Explosive Decompression Type Testing Procedure.

Treloar, L. R. (1975) The Physics of Rubber Elasticity. Oxford University Press

Van Der Waals, J. D. (1873) On the Continuity of the Gaseous and Liquid States. PhD Thesis, University Leiden.

Wang, N. M. (1973) Finite Element Analysis of Cut-Growth in Sheets of Highly Elastic Materials. International Journal of Solids and Structures. 9(10), pp. 1211 – 1223.

Yeoh, O. H. (1993) Some Forms of Strain Energy Function for Rubber. Rubber Chem. Technol. 66, pp 754 – 771.

Zhang, Y. et al. (2001) Effect of Carbon Black and Silica Fillers in Elastomer Blends. Macromolecules, 34(20) pp 7056 – 7065.

11. Appendices

11.1. Appendix A: Fractured Surfaces (SEM)

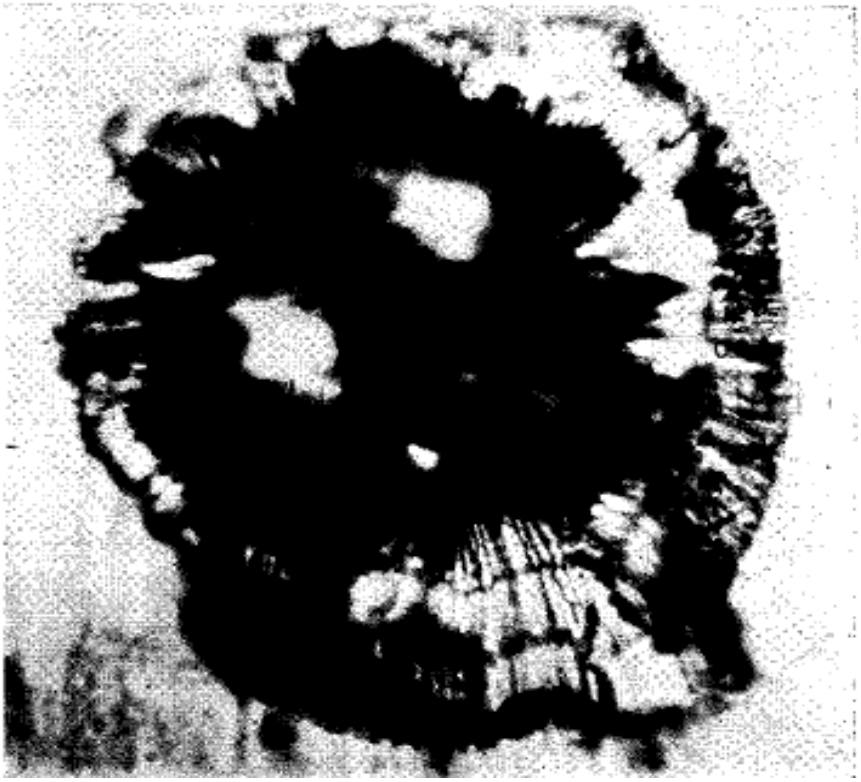

Figure 1 Bubble cross-section after collapse from experiments conducted by A. N Gent and D. A Tomkins: Original magnification × 500, shown here × 200, SBR2, Carbon dioxide (P_o about 14 kg/cm$^{2)}$, 25 °C.

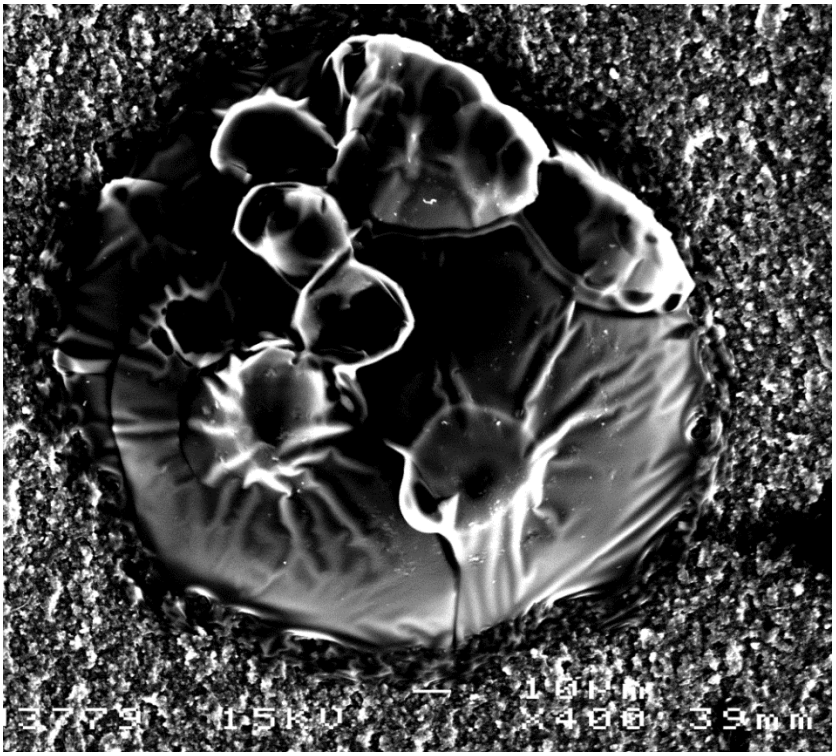

Figure 2 A flaw in a Teesele™ which was initially thought to be an inherent flaw either introduced during manufacturing or contained in the raw elastomer material.

Initially the flaw in the Teesele™ was thought to be an inherent flaw contained in the raw elastomer material or introduced during the manufacturing process. However after close inspection, the flaw shows similarities to a flaw of a collapsed bubble due to RGD from A. N Gent and D. A. Tomkins.

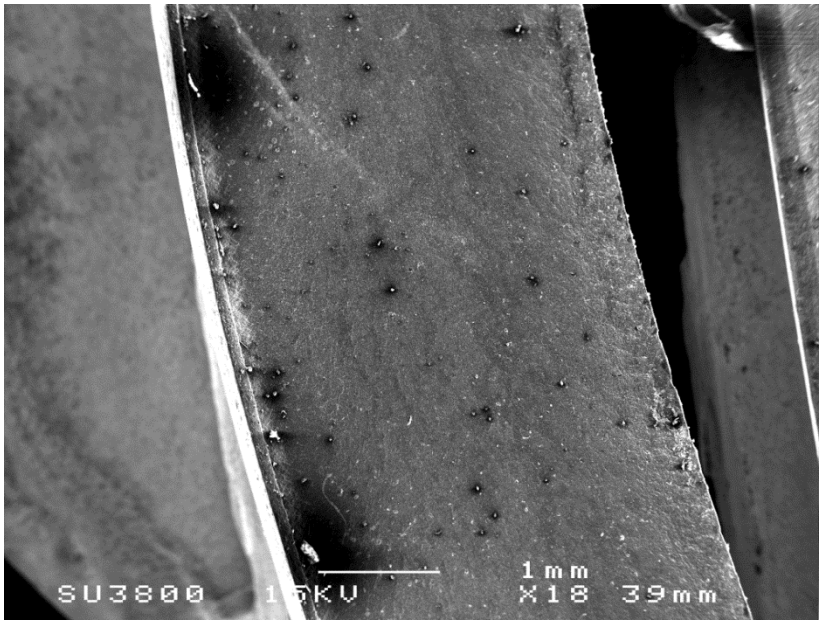

Figure 3 An SEM image of fractured Teesele™ containing debris on the fractured surface and a tear line running along the edge of the seal.

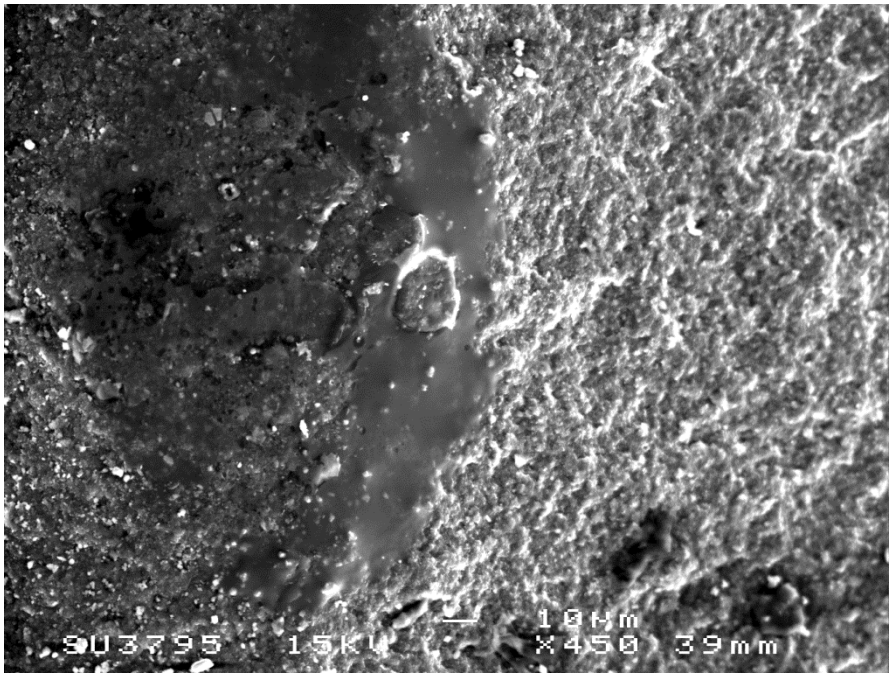

Figure 4 An SEM image of fractured surface from a Teesele™ after exposure to RGD, the fractured surface contains two different surface textures. The different surface texture could have been a result of RGD.

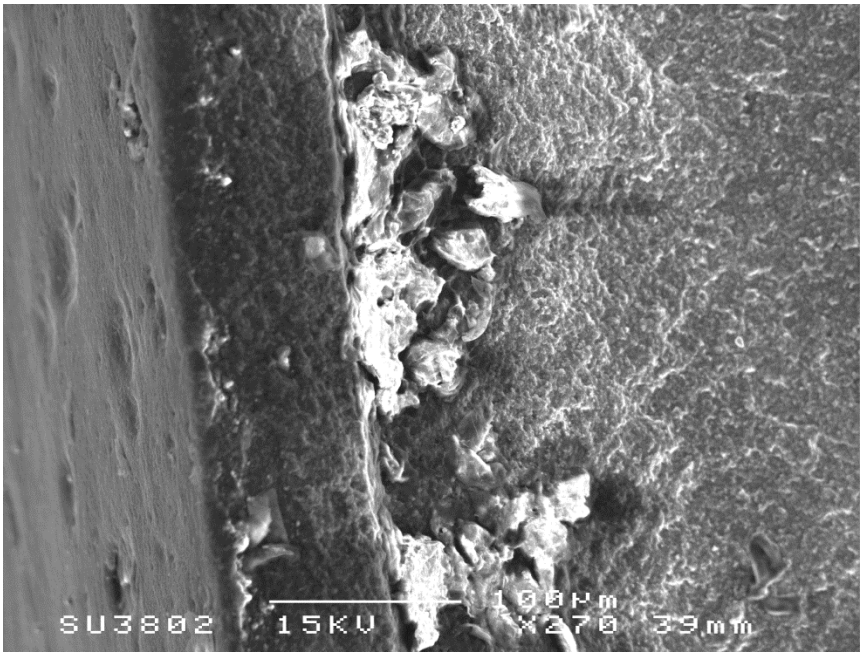

Figure 5 An SEM image of fractured Teesele™ showing part of a tear line containing material tearing, indicating ductile fracture. Image also contains bumps on the outside of the Teesele™.

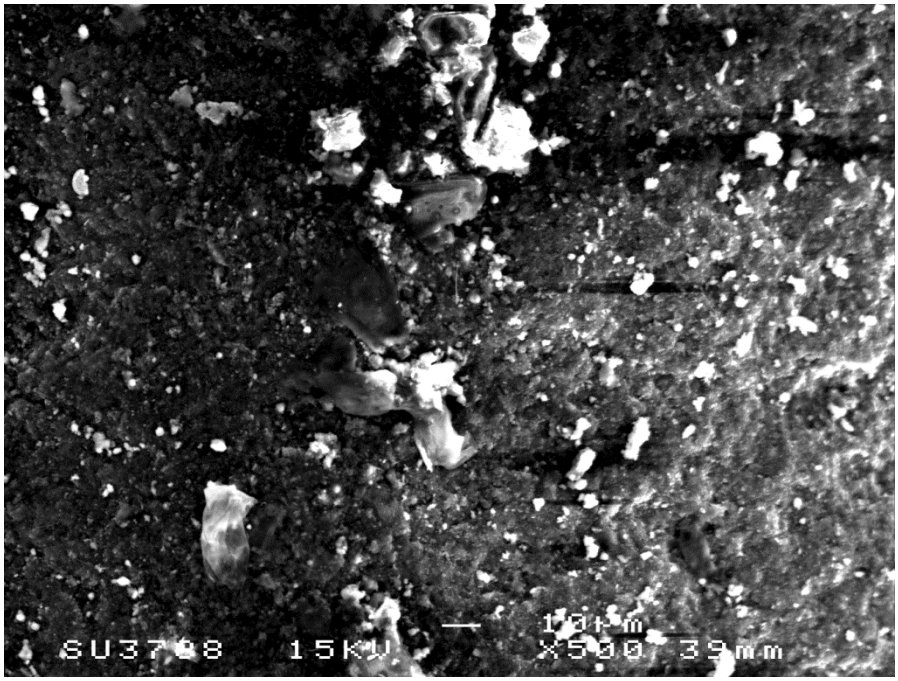

Figure 6 Fractured surface of a Teesele™ containing surface debris.

11.2. Appendix B: Computed Tomography Images

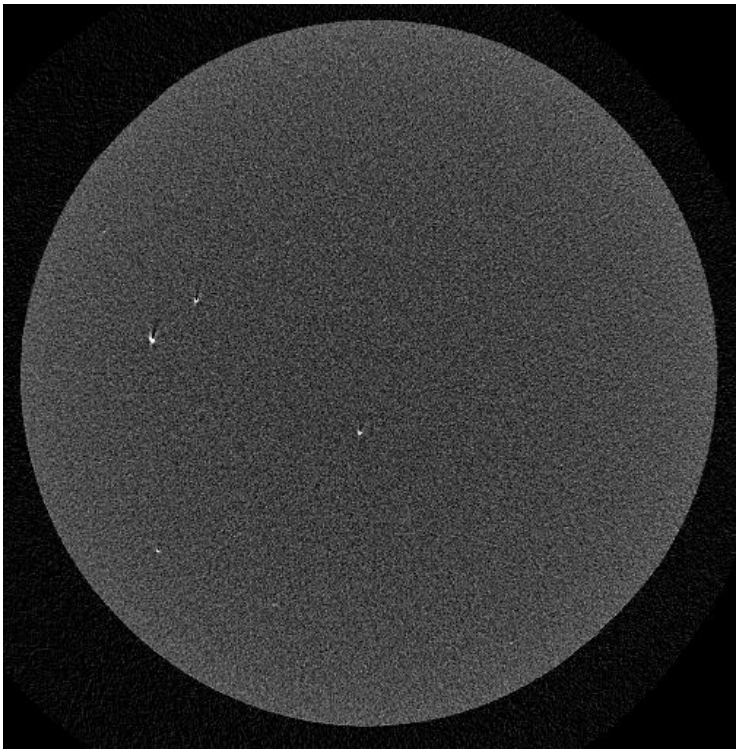

Figure7 Display of a 2D image of a standardly manufactured O-ring_1. The image contains visible voids distributed randomly in the image.

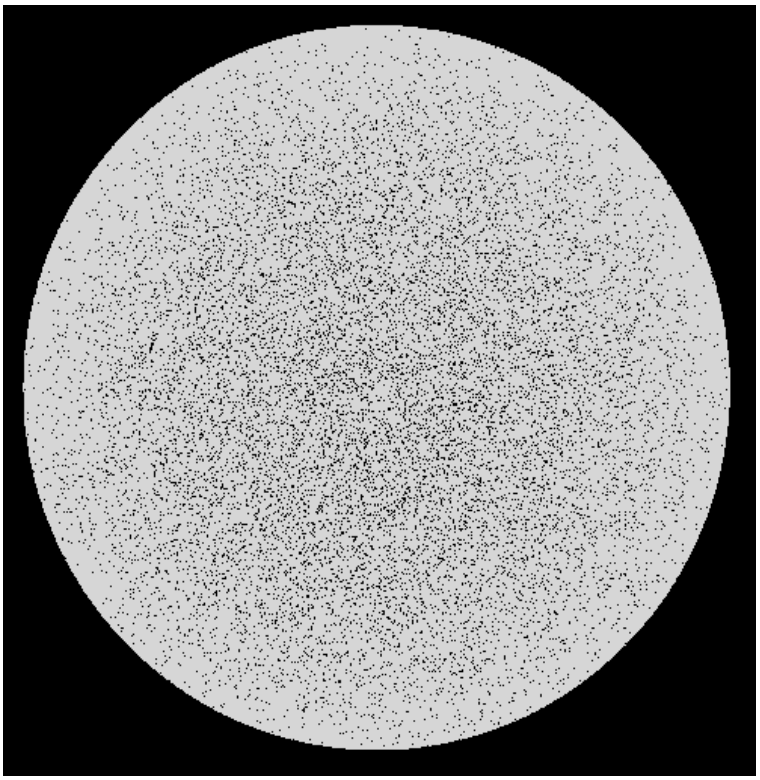

Figure 8 Binary image of a 2D image shown in Figure 7. The image has a total porosity of 7.06%.

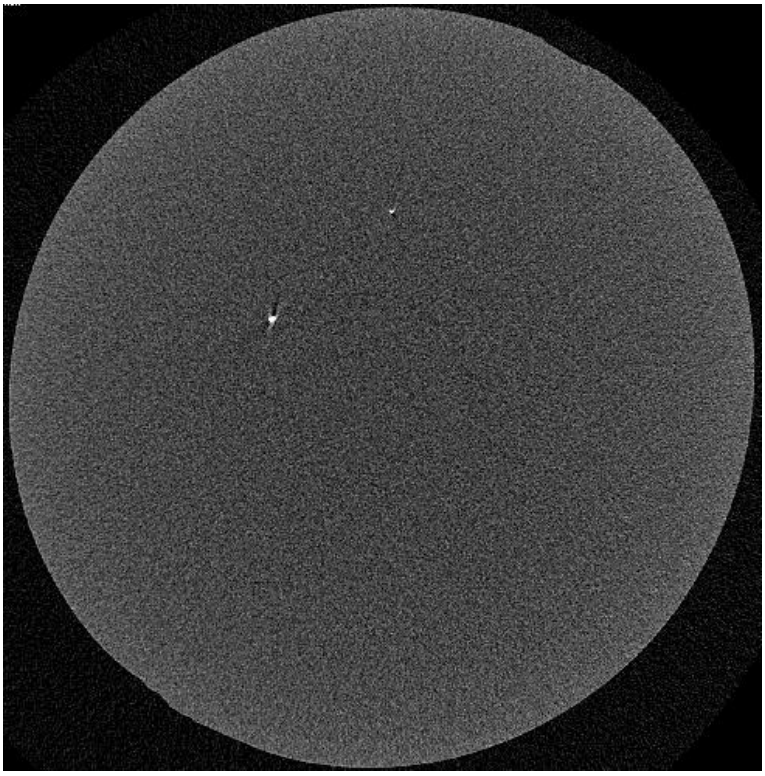

Figure 9 Display of a 2D image of a standardly manufactured O-ring_2. The image contains a visible void in the centre region of the image.

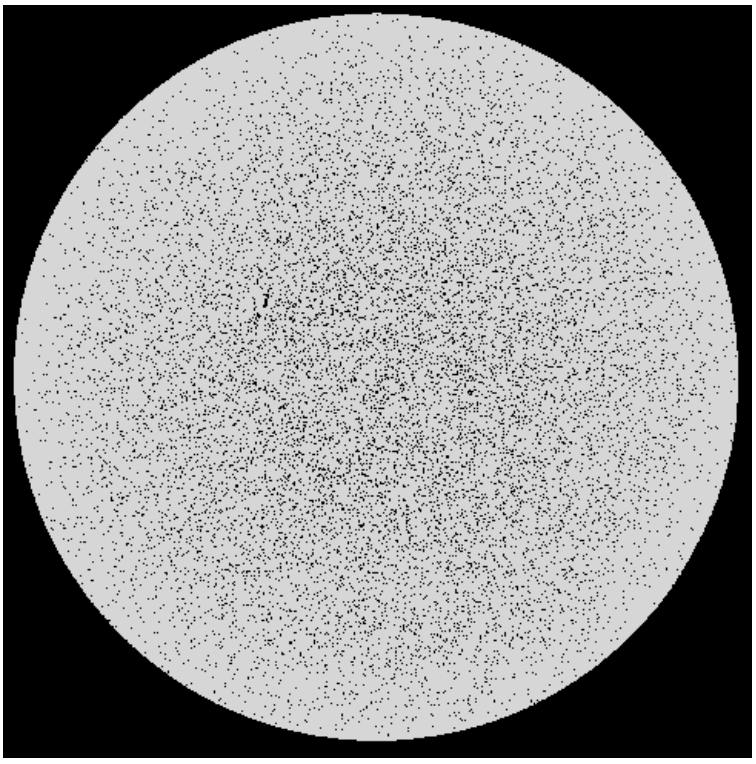

Figure 10 Binary image of a 2D image shown in Figure 9. The image has a total porosity of 6.38%.

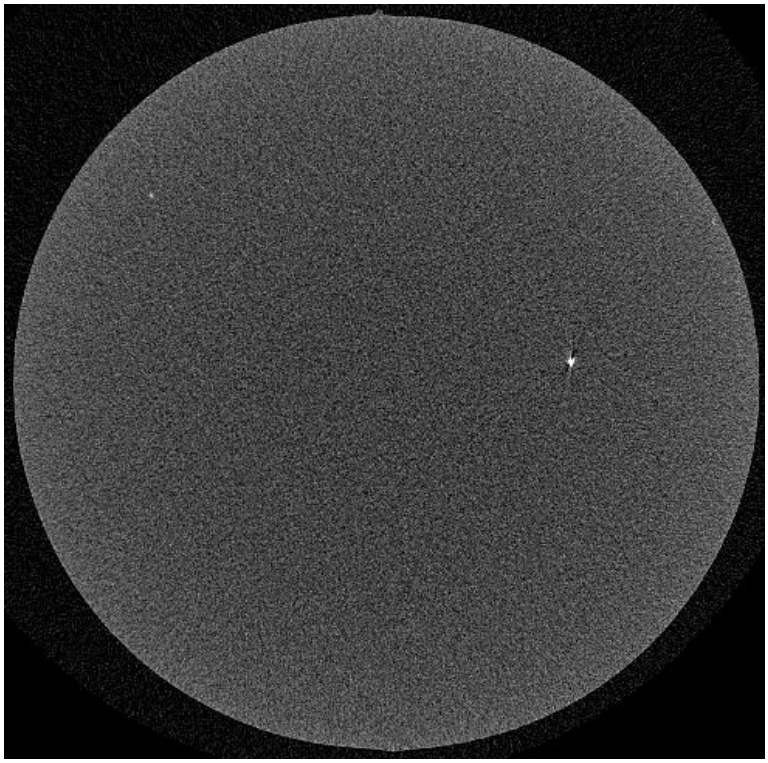

Figure 11 Display of a 2D image of a further processed O-ring_1. The image contains a visible void in the centre region of the image.

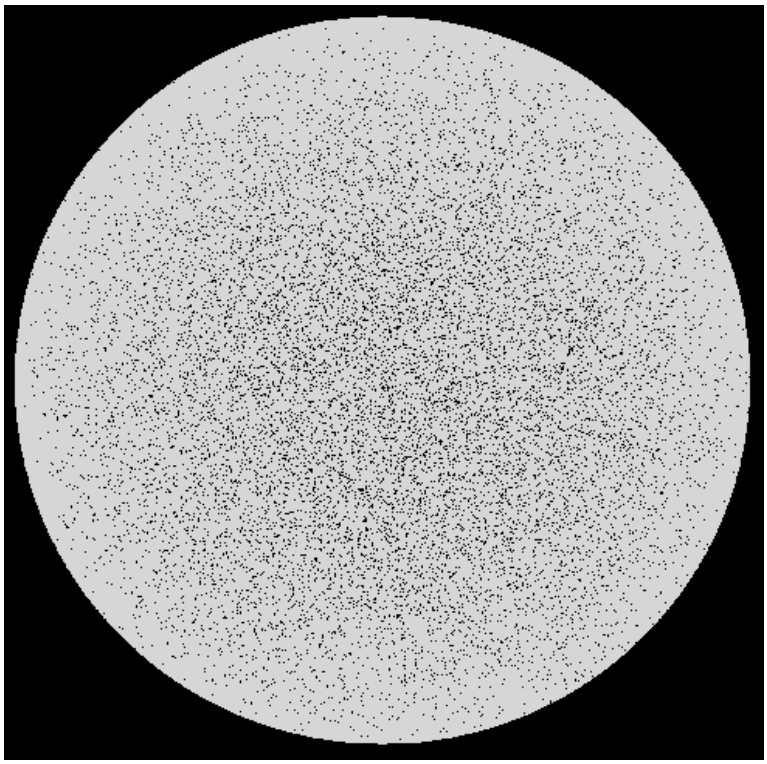

Figure 12 Binary image of a 2D image shown in Figure 10. The image has a total porosity of 6.28%.

11.3. Appendix C: URDFIL Subroutine

```
SUBROUTINE URDFIL (LSTOP, LOVRWRT, KSTEP, KINC, DTIME, TIME)

    INCLUDE 'ABA_PARAM.INC'

    DIMENSION ARRAY(513),JRRAY(NPRECD,513),TIME(2)
    EQUIVALENCE (ARRAY(1),JRRAY(1,1))
    Real :: ELNUM(1,180),CONC(180) ! ELNUM and CONC are arrays containing
    Element numbers and Concentration values respectively.

    open(unit=101,file= 'InputData') ! File containing output data
    x = 0
    y = 0
    key = 0

    JRCD=0
    DO 110 K1 = 1,200
    IF  (KINC == K1)  THEN
    CALL POSFIL(KSTEP,KINC,ARRAY,JRCD) ! Subroutine called to read results
    at specified Increment and Step.

    write (101,1) kinc,TIME(1)
    1 format (i6,t9,f7.3)

    ELSE IF (KINC .NE.K1) THEN
    GO TO 110

    END IF
    DO 100 K2=1,99999

    CALL DBFILE(0,ARRAY,JRCD)! Subroutine called to read records from the
    results file.

        if (JRCD .NE. 0) GO TO 100

            KEY=JRRAY(1,2)

        if (key == 38) then ! Record to be read in the results file.

             x=x+1

            CONC(x) = array(3)

        end if

        if (key == 1) then  ! Record to be read in the results file.

             y = y+1
```

```
                ELNUM (1,y) = jrray(1,3)
            end if
        100 Continue
        do i = 1,180
        write (101,2)ELNUM (1,i), CONC(i) ! Write records to an external file.
2       format (f10.2,f11.6)
        end do
        110 CONTINUE
end
```

11.4. Appendix D: DLOAD Subroutine

```
SUBROUTINE DLOAD (F, KSTEP, KINC, TIME, NOEL, NPT, LAYER, KSPT, COORDS, JLTYP, SNAME)
    INCLUDE 'ABA_PARAM.INC'
    DIMENSION COORDS(3)
    CHARACTER*80 SNAME

Real :: Ru, T, Tc, Pc, w, alpha, a, b
real, dimension (59626800) ::CONC          ! Array containing concentration values.
Integer, dimension (59626800) :: ELNUM  ! Array containing element numbers.
real, dimension (19872000) ::P,v           ! Arrays containg Pressure and molar volume respectively.
integer :: i, K1,K2,K3,K4,K,IOC,K5,x

open (101, file='InputData', status='old')      ! File containing Input data.
open(102, file= 'Results', status='old')  ! File containing output data.

Ru = 8.314        ! Universal Gas Constant kPa.m^3/kmol.K.
T = 373           ! Temperature K.
w = 0.225         ! Accentric Factor m^3/kmol.
Tc = 304.21       ! Critical Temperature K.
Pc = 7377         ! Critical Pressure kPa.

alpha = (1 + (0.37464 + 1.54226*w - 0.26992*w**2)*(1-(sqrt(T/Tc))**2))
a = (0.457236*alpha*(Ru**2)*(Tc**2))/Pc
b = (0.0777961*Ru*Tc)/Pc

   do 4 K2 = 1,19875600
   read (101,1, IOSTAT =IOC )ELNUM(K2),CONC(K2) ! read input file from mass diffusion analysis containing element numbers and concentration values.
   if (IOC /= 0) then
   go to 60
      stop
```

```
      end if
   4 end do
   60 continue
! code below locates specified step, increment number, element number, surface and load intergration point and applies the specified pressure to that surface
if (KSTEP == 4) then
do K4 = 1,3600
if (KINC == K4) then
do x = 1,5520
K = 5520*(K4-1)+K4+x
if (NOEL == ELNUM(x)) then
do y = 21,24
if (JLTYP == y) then
do z = 1,3
if (NPT == z) then
if (CONC(K) == 0)then
v(K) = 0
else
v(K) = 1/(CONC(K)*1000000)
end if
if (v(K) == 0) then
P(K)  = 0
else
P(K) = ((Ru*T)/(v(K)-b)- (a)/((v(K)**2)+2*v(K)*b - b**2))/1000
end if
F = -P(K) ! Pressure is applied as a negative since its pushing onto the elastomer walls.
write (102,5)ELNUM(K),CONC(K),P(K),NOEL,KINC, NPT, JLTYP, K
```

```
5 format (i7,tr3,f15.12,tr5,f6.3,tr2,i5,tr2,i3,i3,i3,tr3,i5)
end if
end do
end if
end do
end if
end do
end if
end do
end if
1  format (i7,tr5,f15.12)
Return
End
```

11.5. Appendix E: Coefficient of Friction Calculations

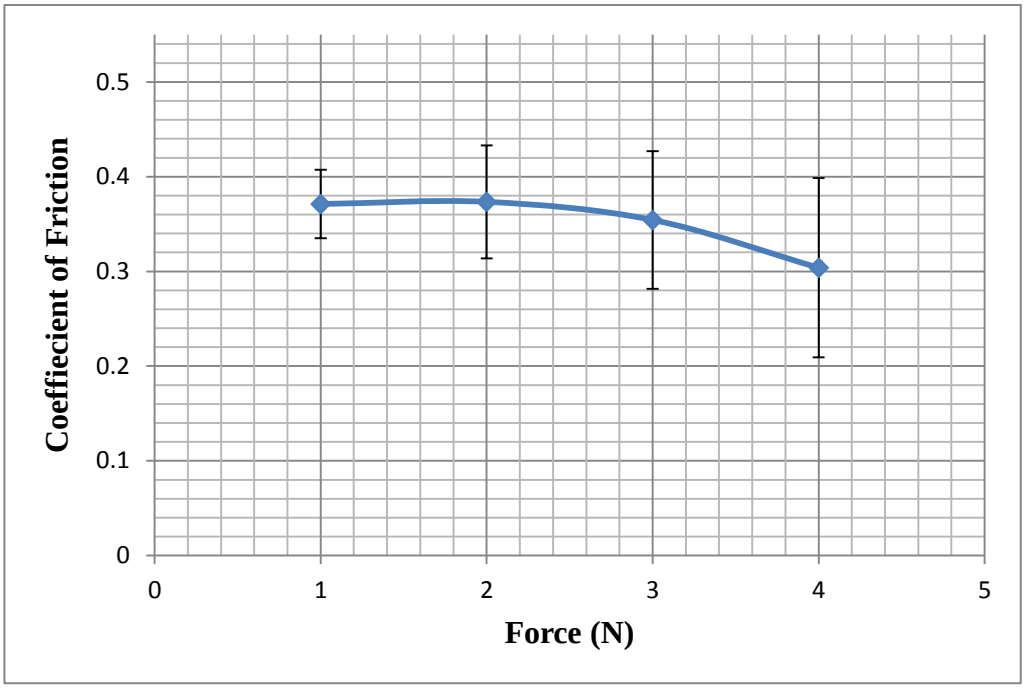

Figure 13 Plot of average coefficient of friction vs force, the coefficient of friction decreases with force.

The coefficient of friction was evaluated as described in Section 3.7. The error bars represent the standard deviation of the mean value from the measured results. The standard deviation error increases as the force is increased. This increase is likely a result of the complexity of evaluating the coefficient of friction of elastomers. At high forces and temperature, it is likely that the elastomer surface is deformed as the other surface slides across the elastomer surface. This phenomenon is probably the reason why the coefficient of friction varies more with increasing force. However since the FEA model is used to evaluate the maximum reaction force, the highest coefficient of friction at lower forces was chosen, since it contributes more to the maximum reaction force value in the FEA model.

Table 1 Raw data from 3 experiments to evaluate the friction coefficient between rubber and steel.

Force (N)	Test 1	Test 2	Test 3	Average	Standard deviation
1	0.400933	0.381624	0.330899	0.371152	0.036173
2	0.43715	0.364454	0.318663	0.373422	0.07268
3	0.430501	0.346744	0.285735	0.354327	0.07268
4	0.412327	0.238885	0.260477	0.303896	0.094522

11.6. Appendix F: Solubility and Diffusion calculations

The mass diffusion coefficient evaluated from:

$$D = \frac{d^2}{6\theta} \quad [1]$$

where

D is the gas diffusion coefficient (m^2/s);

Θ is the delay time obtained from the gas transmission curve (s);

d is the thickness of the test piece, which was found to be 2.817mm.

Θ was evaluated from the plot of pressure vs time, which was evaluated by Smithers Rapra and was found to be equal to 34 hours (122400 seconds). Using the diffusion equation and the value of *Θ*:

$$D = 1.081e^{-5}\,\frac{mm^2}{s} \quad [2]$$

The permeability was given in (m^2/Pa.s) units, however in this thesis it was essential to convert the permeability units to [mol·m/ (m^2·s·Pa)]. To achieve this, the permeability was divided by the molar volume according to BS ISO 2782: 2012 standards to find the number if moles of test gas passing through a test piece per unit area, per unit time, with a unit partial-pressure difference between the two sides of the test piece.

The permeability which was provided by Smithers Rapra as 2.57 e^{-17} m^2/Pa.s was divided by 0.0027 m^3/mol to give 1.1321e^{-15} mol·m/ (m^2·s·Pa).

The solubility coefficient was calculated from:

$$Q = SD \quad [3]$$

where

Q is the gas permeability coefficient [mol·m/ (m^2·s·Pa)];

D is the gas diffusion coefficient (m^2/s);

S is the solubility coefficient [mol/ (m^3·Pa)]

The solubility coefficient was found to be 1.0473e^{-7} mol/ (m^3·Pa)

The initial concentration of gas absorbed onto the O-ring's surface can then be calculated using Henry's law:

$$C = Sp \quad [4]$$

where

C is the gas concentration [mol/mm^3]

S is the solubility coefficient [mol/ (m^3·Pa)]

p is the partial pressure of the gas [Pa]

The initial gas concentration absorbed at the surface of the O-ring was found to be 8.378e^{-7} mol/mm^3.

11.7. Appendix G: Creep Test Data

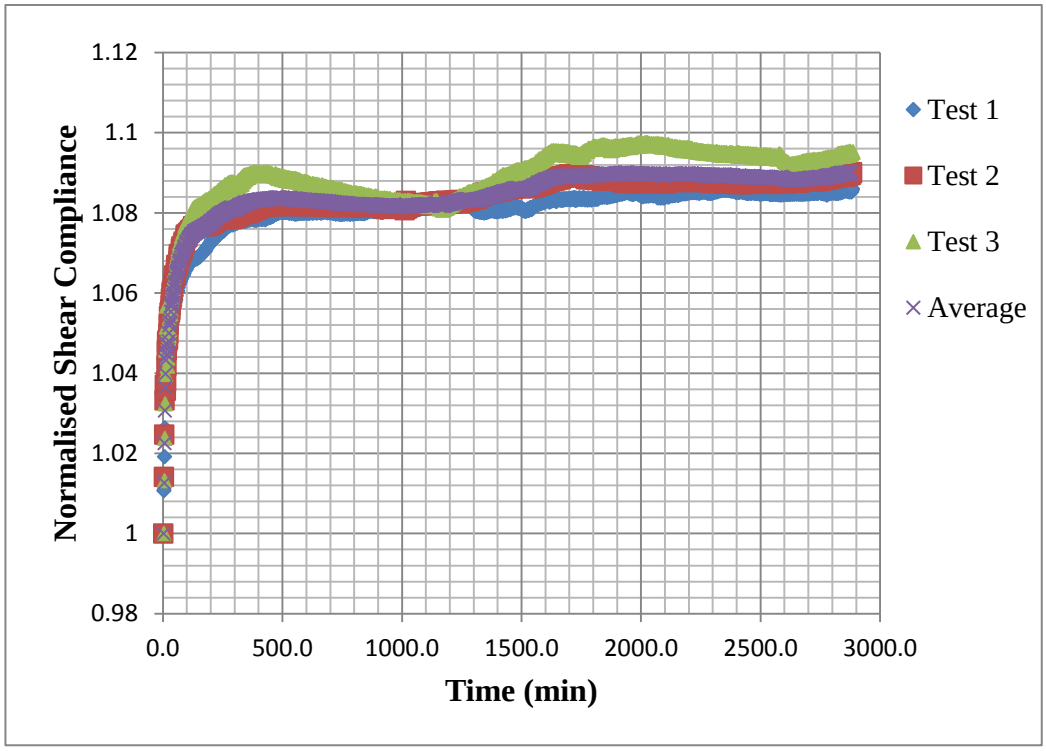

Figure 14 Evolution of normalised shear compliance with time for HNBR101.

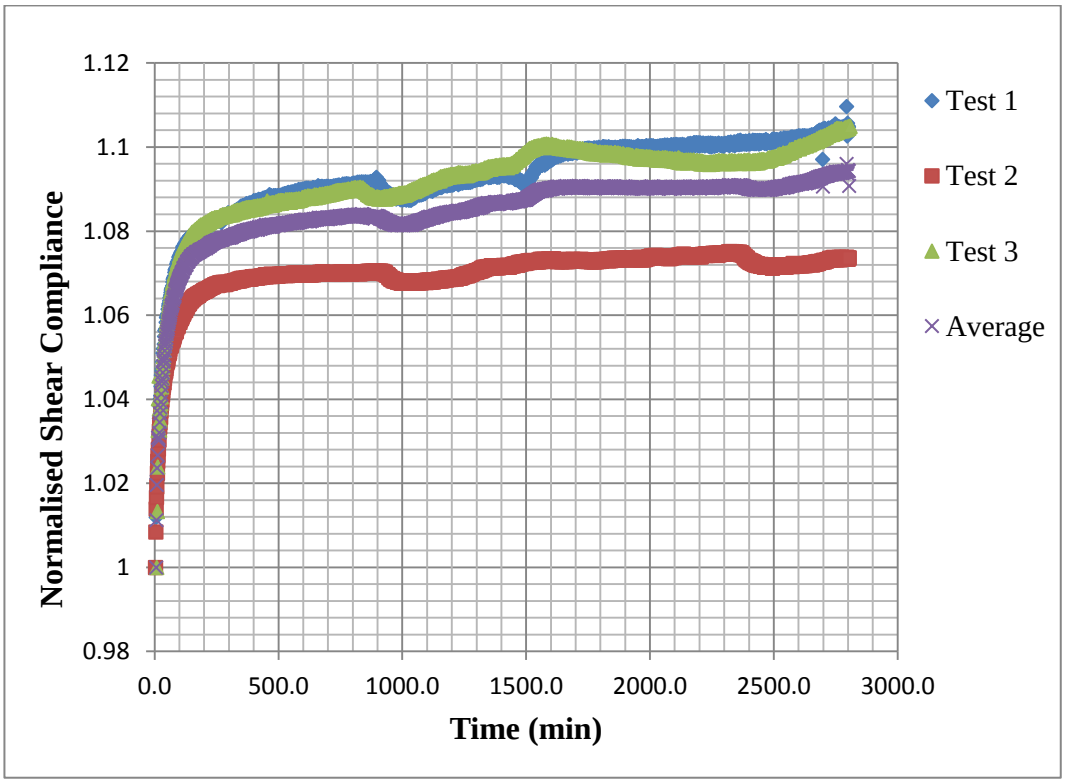

Figure 15 Evolution of normalised shear compliance with time for HNBR101.

Figure 14 and Figure 15 show the processed data from creep tests conducted on both HNBR101 and LRCM888. The two graphs show that HNBR101 had a smaller standard deviation compared to LRCM888.

11.8. Appendix H: Glass Transition Temperature and Loss Factor

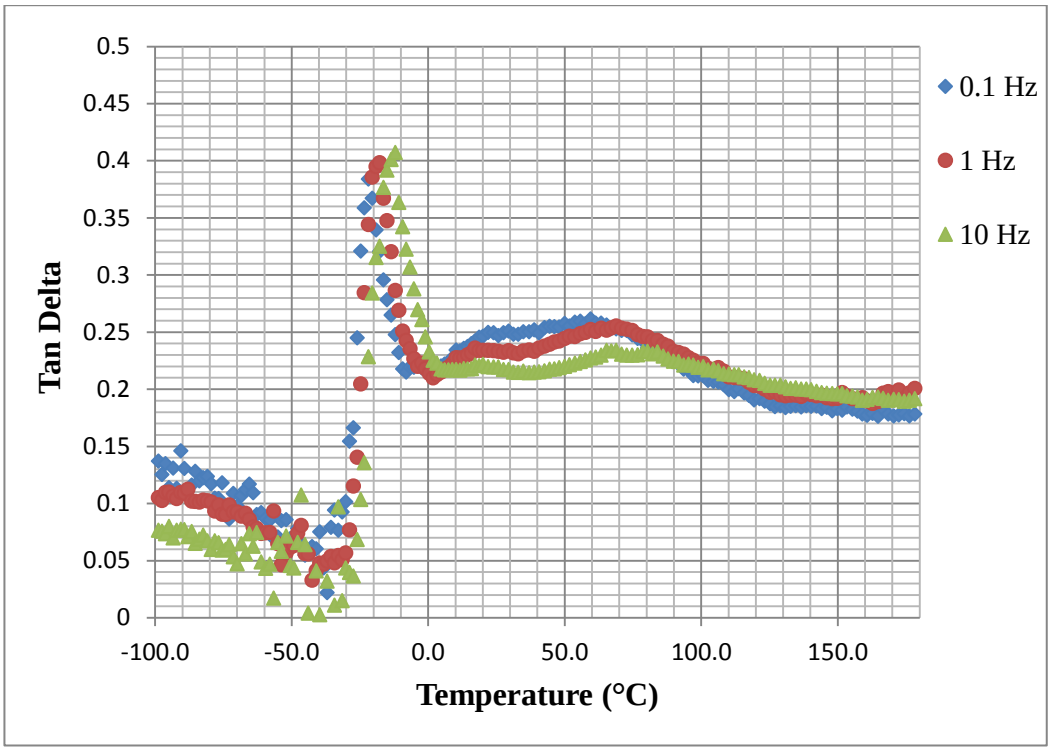

Figure 16 Evolution of loss factor with temperature at multiple frequencies for HNBR101, the glass transition temperature is dependent on the frequency.

Figure 16 and Figure 17 show the evolution of loss factor with temperature at multiple frequencies for HNBR101 and LRCM888 respectively. The glass transition temperature is dependent on the frequency of the tests.

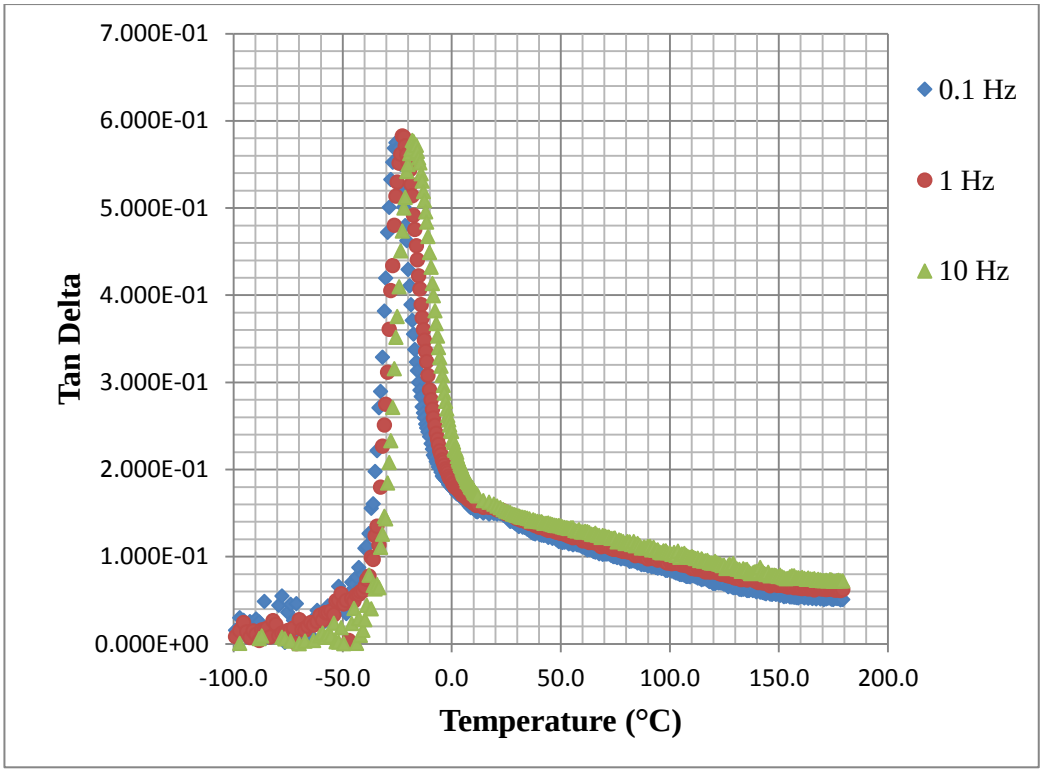

Figure 17 Evolution of loss factor with temperature at multiple frequencies for LRCM888, the glass transition temperature is dependent on the frequency.

11.9. Appendix I: Hyperelastic Material Data

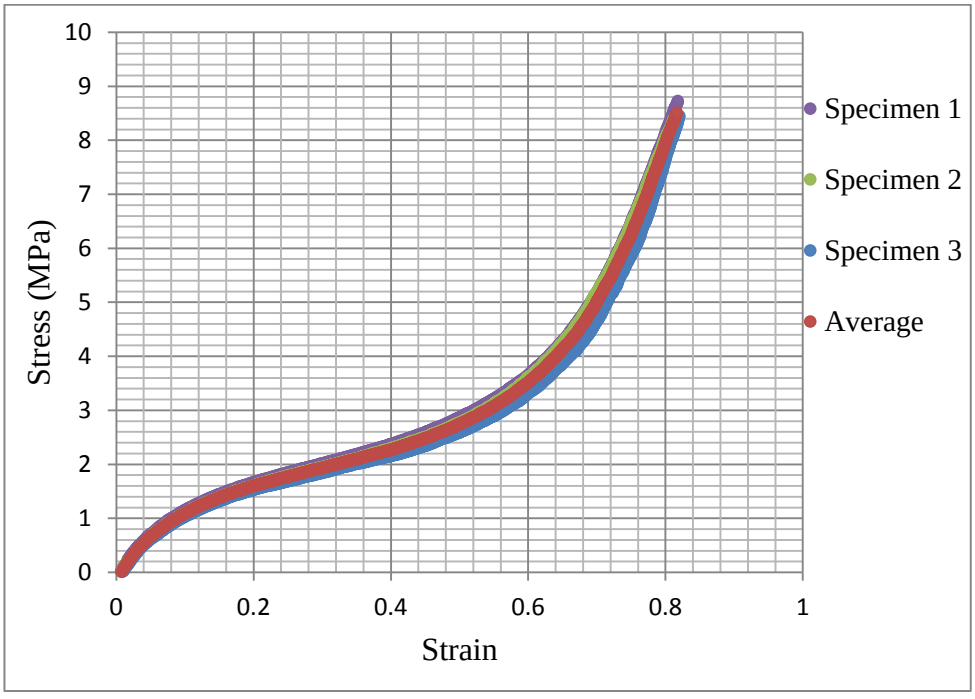

Figure 18 Uni-axial stress-strain results for HNBR101.

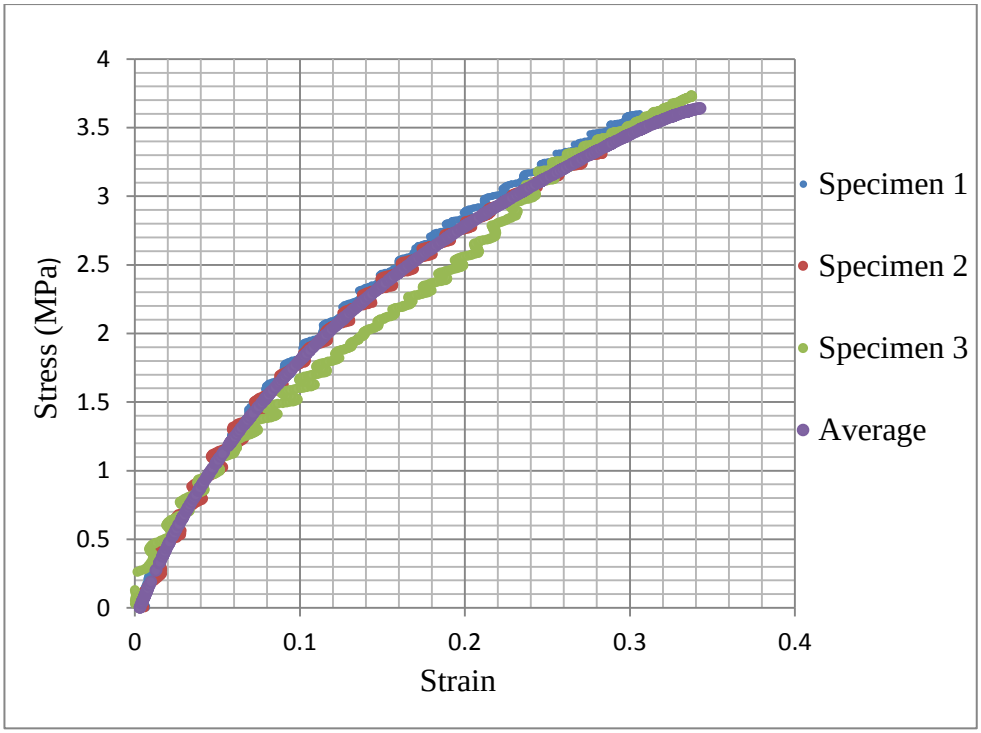

Figure 18 Planar shear stress-strain results for HNBR101.

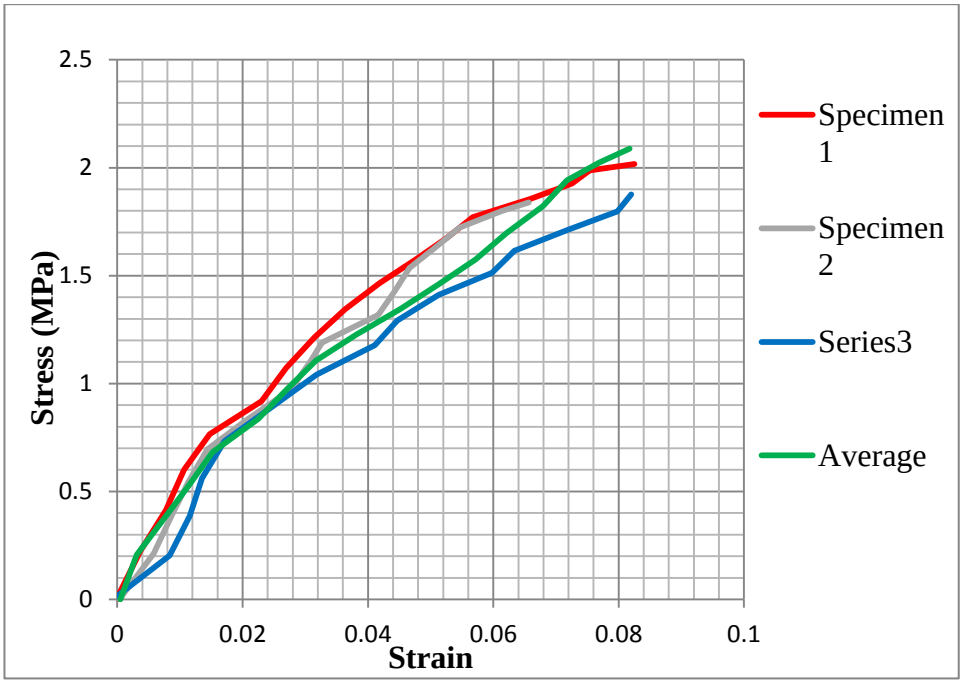

Figure 18 Equibiaxial stress-strain results for HNBR101.

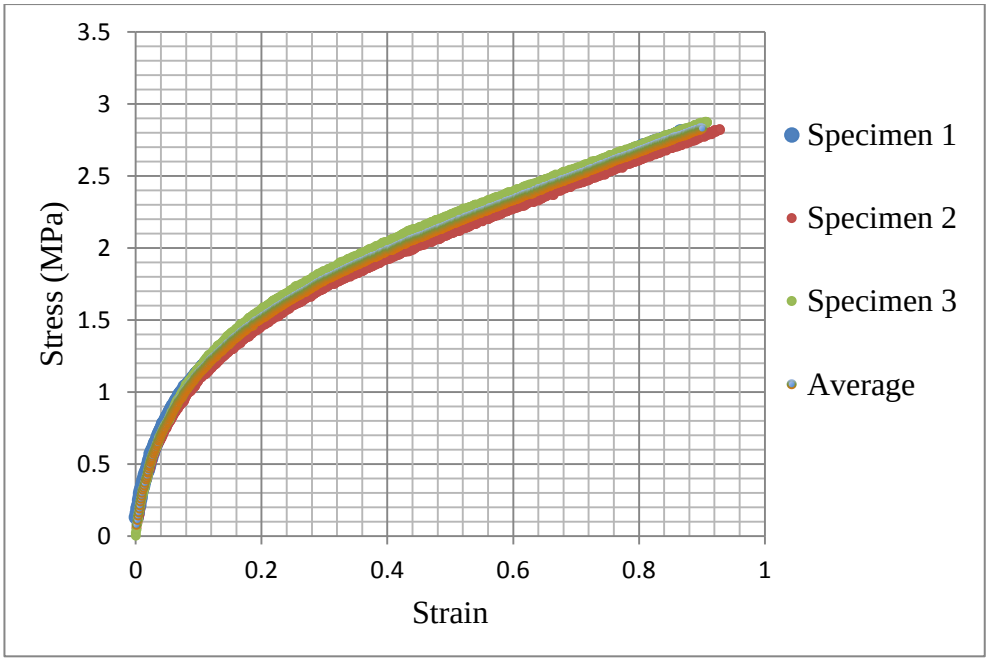

Figure 18 Uni-axial stress-strain results for LRCM888.

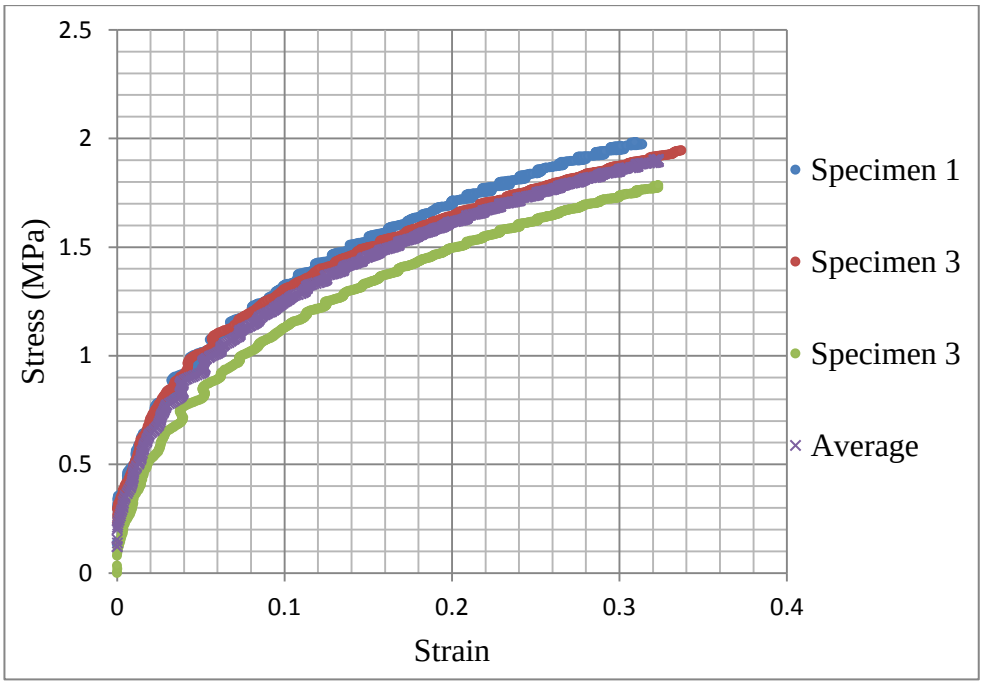

Figure 18 Planar shear stress-strain results for LRCM888.

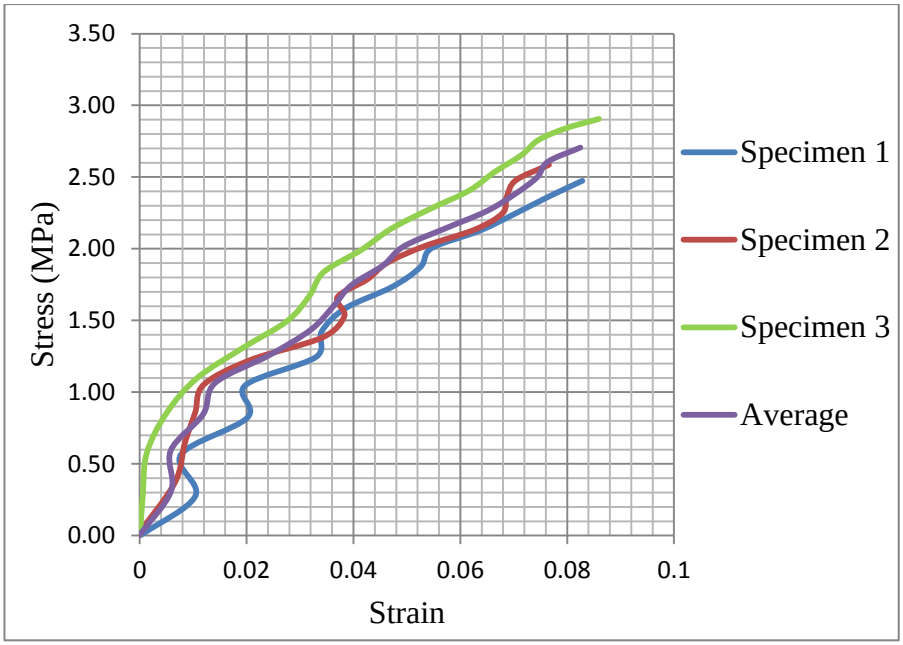

Figure 18 Equibiaxial stress-strain results for LRCM888.

11.10. Appendix J: Tearing Strength Results

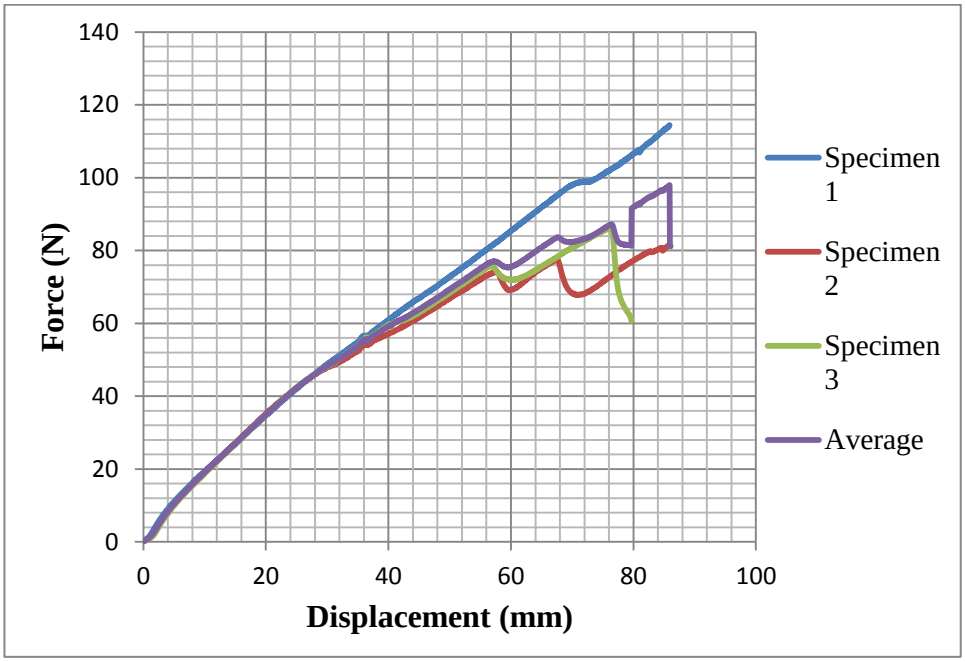

Figure 19 Raw data for Hybrid 1 tearing strength specimens showing the evolution of force with displacement.

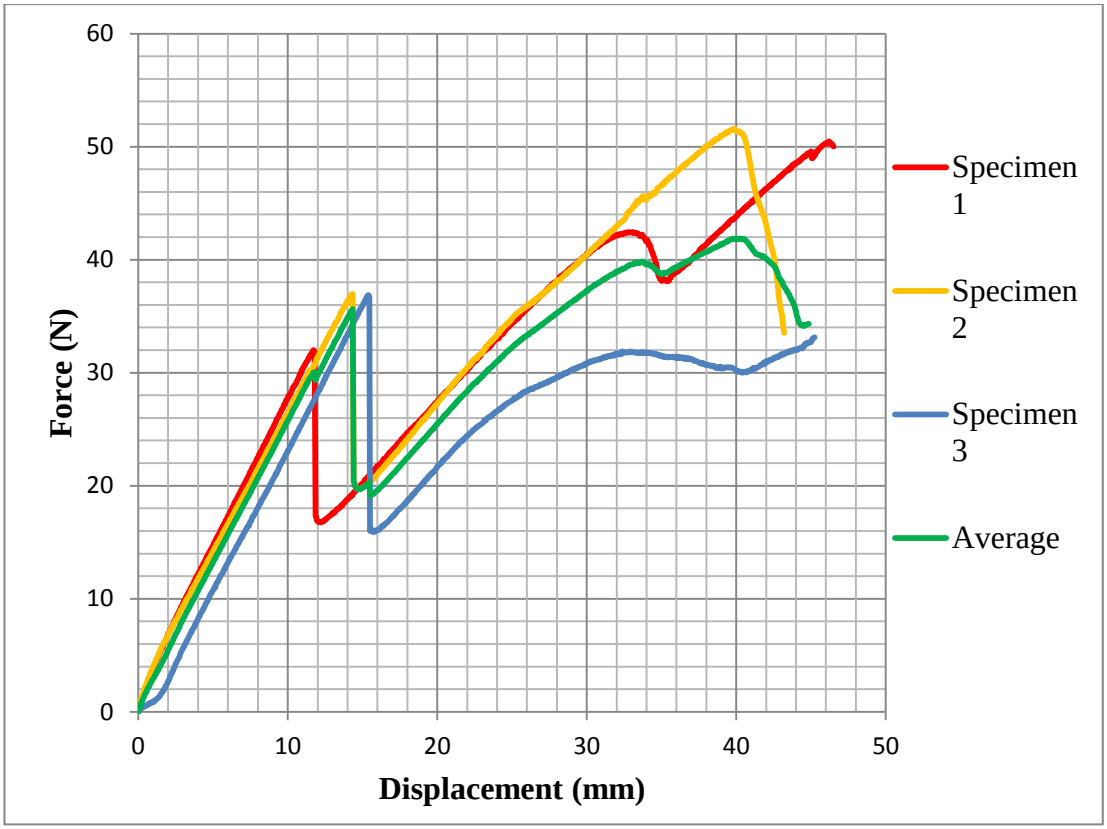

Figure 20 Raw data for Hybrid 2 tearing strength specimens showing the evolution of force with displacement.

11.1. Appendix K: Compression Test Results

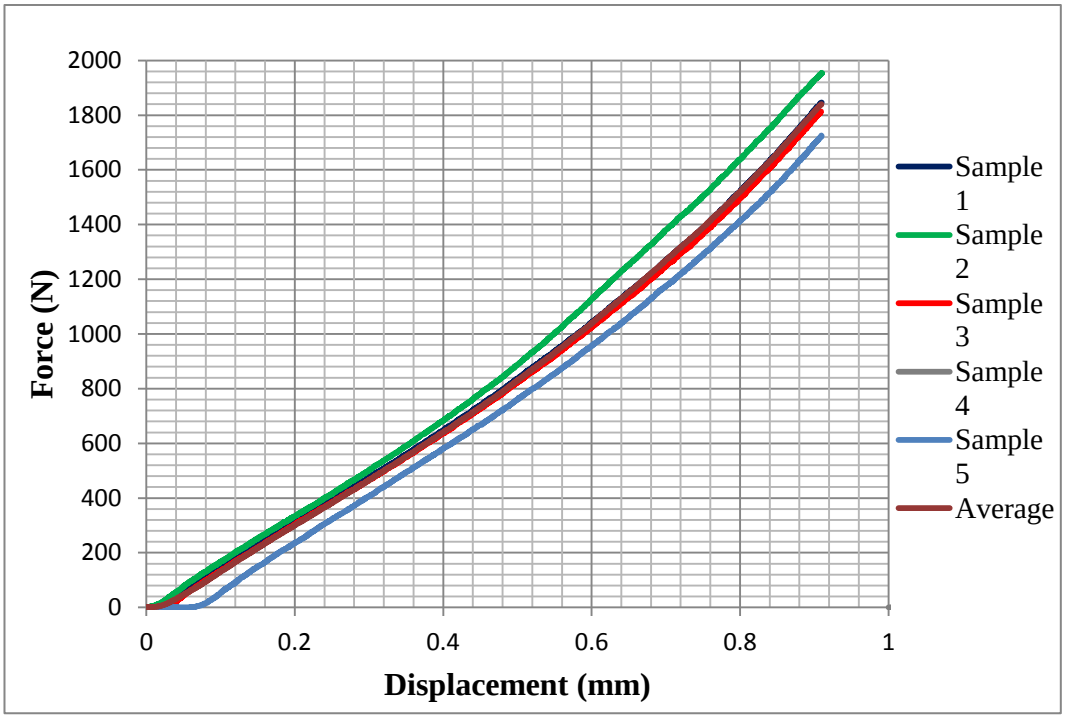

Figure 21 Evolution of force with displacement for an O-ring under compression from its housing gland surfaces the graph is an average of five tests.